Cover Page

The following handle holds various files of this Leiden University dissertation:
http://hdl.handle.net/1887/63086

Author: Chuang, K.J.
Title: The formation of complex organic molecules in dense clouds : sweet results from the laboratory
Issue Date: 2018-06-20

The Formation of Complex Organic Molecules in Dense Clouds

Sweet Results from the Laboratory

Ko-Ju Chuang

The Formation of Complex Organic Molecules in Dense Clouds

Sweet Results from the Laboratory

Proefschrift

ter verkrijging van
de graad van doctor aan de Universiteit Leiden
op gezag van de Rector Magnificus prof. mr. C. J. J. .M. Stolker,
volgens besluit van het College voor Promoties
te verdedigen op woensdag 20 juni 2018
klokke 10:00 uur

door

Ko-Ju Chuang
geboren te Hsinchu, Taiwan
in 1987

Promotiecommissie

Promotores	Prof. dr. H. V. J. Linnartz	
	Prof. dr. E. F. van Dishoeck	
Co-promotores	Dr. S. Ioppolo	Queen Mary University of London
	Dr. G. Fedoseev	INAF— Catania Astrophysical Observatory
Overige leden	Prof. dr. H. J. A. Röttgering	
	Prof. dr. A. G. G. M. Tielens	
	Prof. dr. M. R. Hogerheijde	
	Prof. dr. H. M. Cuppen	Radbound University Nijmegen
	Prof. dr. S. D. Price	University College London
	Prof. dr. S. Yamamoto	The University of Tokyo

To see a World in a Grain of Sand,
And Heaven in a Wild Flower,
Hold Infinity in the palm of your hand,
And Eternity in an hour.

Auguries of Innocence by William Blake (1863)

CONTENTS

INTRODUCTION

Everything in our daily life, such as the Sun we see, the soil we stand on, the water we drink, and even the molecules we are made of, all of these have had their origin in the interstellar medium (ISM). This highly dilute environment, spaced between stars, consists of ~99% gas and 1% dust by mass (~10^{-12} by number with respect to the element hydrogen). The gas composes ~89% atomic hydrogen, ~9% helium, and ~2% heavier elements. The dust that is typically submicron in size (~ 0.1 μm) comprises iron— or magnesium—bearing silicates, and carbonaceous material (Draine & Lee 1984; Henning & Mutschke 1997). The gas and dust are not homogeneously distributed in space, but rather concentrated in certain regions, known as interstellar clouds. According to the different physical and chemical conditions (density, temperature, visual extinction (A_V), and chemical composition), interstellar clouds can be categorized following three different stages; (1) diffuse clouds, (2) translucent clouds, and (3) dense dark clouds.

In diffuse clouds, the density and temperature are extremely low, i.e., $n_H \approx 10^2$ cm^{-3} and T<80 K, which allows optical and UV-photons from the interstellar radiation field (ISRF), to fully penetrate the cloud, and to intensively irradiate the gas and the dust grains ($A_V \leqslant 1$). The energetic UV-photons dissociate and ionize most molecules into atomic and ionic form. Diffuse clouds are the first stage in complex process ultimately resulting in the formation of new stars and planets. A disturbance, such as a supernova shock, turbulence, cloud-cloud collisions, winds from old stars, outflows from young stars, and on larger galaxy scales spiral density waves, can compress a diffuse cloud. The resulting translucent clouds have a some-what higher density of ~10^3 cm^{-3}. In this stage, the optical and UV-photons are partially shielded by dust grains ($1 \leqslant A_V \leqslant 5$). Dust temperatures drop to ~15 K. Ionized carbon atoms transfer into their neutral form C and CO molecules in the gas phase (van Dishoeck & Black 1989). When $A_V \geqslant 3$, H_2O ice starts forming through the sequential hydrogenation of atomic and molecular oxygen on grain surfaces (Whittet et al. 1988; Boogert et al. 2015; Wakelam et al. 2017).

Further contraction leads to dark clouds with densities of ~10^{4-5} cm^{-3} ($A_V \geqslant 10$), and the temperature decreases to ~10 K. In this stage, known as the prestellar core phase, most of the gaseous species are in molecular form and they accrete onto the pre-formed H_2O ice mantle at 10 K, with the exception of H_2 and He. This cloud can be maintained for some time by the combination of thermal, turbulent and magnetic pressure, but eventually gravity takes over and the cloud collapses. Initially the cloud stays very cold because the molecules radiate the gravitational energy away, but ultimately the innermost region becomes opaque and warm, i.e., no radiative energy escapes. The core then becomes a protostar in which nucleosynthesis

does not yet happen, but which does emit a continuum of infrared radiation. The entire collapsing object is called a Young Stellar Object (YSO). Due to the conservation of the angular momentum, the rotating spheres of gas and dust can lead to the formation of a protoplanetary disk with bipolar outflows perpendicular to the disk (Shu et al. 1991). The dust and gas in the disk plane will eventually evolve in the formation of planets, their moons and other celestial bodies. When the temperature of the protostar is sufficiently high to initiate nuclear fusion, the new star, 'sun', is born. Depending on its mass, a star can live several billion years. Once it starts running out of fusion material, a number of processes are triggered, resulting in the collapse of the inner core, while the outer layer regions will be expelled as blown away, resulting in a planetary nebula. This fertilizes the ISM with chemically enriched material to be included in a next generation of stars and planets.

1.2   INTERSTELLAR MOLECULES

To date (Spring 2018), astronomical observations have resulted in the identification of some 200 different molecular species in the ISM or circumstellar shells, not including isotopologues and isotopomers, (CDMS:https://www.astro.uni-koeln.de/cdms/molecules), mainly by rotational (radio-astronomy), but also vibrational (infrared), and electronic (UV-VIS) spectroscopy. The list with interstellar molecules comprises various types of species, such as inorganics (e.g., H_2O, CO, CO_2, and NH_3), organics (e.g., CH_4, CH_3OH, and H_2CO), anions (e.g., $C_{2n}H^-$; n = $2-4$), cations (e.g., H_3^+, HCO^+, N_2H^+), unsaturated hydrocarbon chain radicals (e.g., C_nH; n = $2-8$), fullerenes (e.g., C_{60}, C_{70}, and C_{60}^+), and aromatic hydrocarbons (e.g., c-C_6H_5CN). Molecular hydrogen, H_2 is the most abundant molecule, at four orders of magnitude higher concentration than the second most abundant species CO. Over the last decades also much has been understood of the involved formation mechanisms that range from reactions in the gas-phase and solid state to gas-grain surface interactions (Herbst & Klemperer 1973; Tielens & Hagen 1982; Garrod et al. 2009; Wakelam et al. 2010; Aikawa et al. 2012; Taquet et al. 2012; Herbst & van Dishoeck 2009; Walsh et al. 2014a,b; Ruaud et al. 2016).

In interstellar clouds, ion-molecule reactions dominate the gas-phase chemistry, and successfully explain the observed abundances of simple hydrocarbons, protonated species, unsaturated species, as well as the relatively high fraction of deuterated species (Herbst 1997; Geballe & Oka 1996; Wootten 1987; Millar et al. 1989). The key processes in the gas-phase are through reactions between ionized species (e.g., H_2^+ produced by cosmic rays interacting with the gas) and neutral molecules (e.g., H_2) to form ions (e.g., H_3^+). H_3^+ can subsequently react with another species "X" resulting in XH^+ through proton transfer. CO^+, via C^++OH, meets H_2 producing HCO^+, which further reacts with an electron giving neutral CO through dissociative recombination. Gas-phase reactions cannot reproduce all the observed abundances, such as the most abundant molecule H_2, fully saturated molecules (e.g., H_2O, NH_3, CH_3OH), lager complex organics, or species only produced in acid-base reactions (e.g., NH_4^+). For this, grain surface reactions and gas-grain interactions are required. The underlying solid-state formation mechanisms have been extensively studied, theoretically, in laboratory studies and through astrochemical models (Tielens & Hagen 1982; D'Hendecourt et al. 1985; Tielens & Allamandola 1987; Charnley et al. 2001; Garrod et al. 2008; Cuppen et al. 2009; Vasyunin & Herbst 2013a; Linnartz et al. 2015; Öberg 2016).

1.2.1 *Formation of icy dust grains*

At low temperatures and sufficiently high densities, the submicron—sized dust grains form a perfect place for gaseous species to accrete, meet, react, and eventually desorb. In translucent and dense dark clouds, the optical and UV extinction is relatively high, and temperature values drop down to $10 - 15$ K. In this temperature regime, atoms and molecules start accreting forming a so-called "ice mantle" (the term ice refers to any species frozen in the solid state). The interstellar ice mantle acts as a molecule reservoir, where the chance of particles to interact is much larger than in the gas phase. Upon reaction, excess energy is released to the surrounding ice, offering a third body (and chemical catalyst) to stabilize new molecules that are formed through exothermic reactions. In dense clouds, the flux of molecular and atomic hydrogen arriving on a dust grain is expected to be $\sim 10^8$ molecules cm^{-2} s^{-1}, and $\sim 10^4$ atoms cm^{-2} s^{-1}, respectively. The accretion of H_2 and H-atoms on a single grain (radius ~ 0.1 μm) happens about once every 10 seconds, and once a day, respectively. At the low H-atom flux that is realized at 10 K, an H-atom can visit all sites on the grain surface (coverage of 10^6 sites) many times before desorption, or react with another reactant forming new species before the next H-atom impacts. The layers with deposited and produced molecules can be as thick as 0.01 μm (Boogert et al. 2015).

1.2.2 *Interstellar ice composition*

Within the solid state, molecules cannot freely rotate. As a consequence, interstellar ices are usually studied through the infrared (IR) absorption spectrum, monitoring typical vibrational modes. This is realized by observing embedded young stellar objects, or along line of sight to a background star. In the IR, ground based observations are strongly hindered by the Earth's atmosphere, due to polluting H_2O and CO_2 absorptions. Consequently, air-borne and space observations have been used to derive interstellar ice compositions, their chemical environment, abundances, and temperature history (van Dishoeck & Blake 1998). The Infrared Space Observatory (ISO, see Whittet et al. 1996; Gibb et al. 2000, 2004) and the Spitzer Space Telescope (SST, see Boogert et al. 2008; Pontoppidan et al. 2008; Bottinelli et al. 2010; Öberg et al. 2011b) in the range of $2.4 - 200$, and $5 - 35$ μm, respectively, revealed many astonishing ice features which are classified into three different groups; (1) H_2O, CO, CO_2, CH_3OH, NH_3, and CH_4 for secure identification, (2) H_2CO, OCN^-, and OCS for likely identification, and (3) HCOOH, CH_3CH_2OH, CH_3CHO, $HCOO^-$, SO_2, and NH_4^+ for possible identification (see review Boogert et al. 2015).

A typical IR spectrum in the range of $2 - 80$ μm for a massive YSO is shown in Figure 1.1. An interpretation of these astronomical features in terms of molecule identification and environmental conditions, such as ice mixing ratios and ice temperature, is possible because of systematic laboratory investigations of IR spectra of a large number of pure and mixed ices recorded for different temperature settings and ice preparations (Tielens et al. 1991; Hudgins et al. 1993; Gerakines et al. 1995; Baratta & Palumbo 1998; Cuppen et al. 2011; Boogert et al. 2015; Terwisscha van Scheltinga et al. 2017). For example, a comparison between observational (ESO Very Large Telescope and Keck telescope) and laboratory results shows that interstellar ices are partially layered, starting with a H_2O-rich layer and a CO-rich layer coated on top of this H_2O layer (Tielens et al. 1991; Pontoppidan et al. 2003). As solid-state formation schemes are linked to specific molecules, this also means that some species will be more abundant in the water rich and other species in the CO rich environments. This spectroscopic confirmation is fully consistent with the picture of interstellar cloud evolution; in translucent clouds, O (O_2) and H-atoms accrete on a grain surface forming a polar H_2O-rich layer with other minor
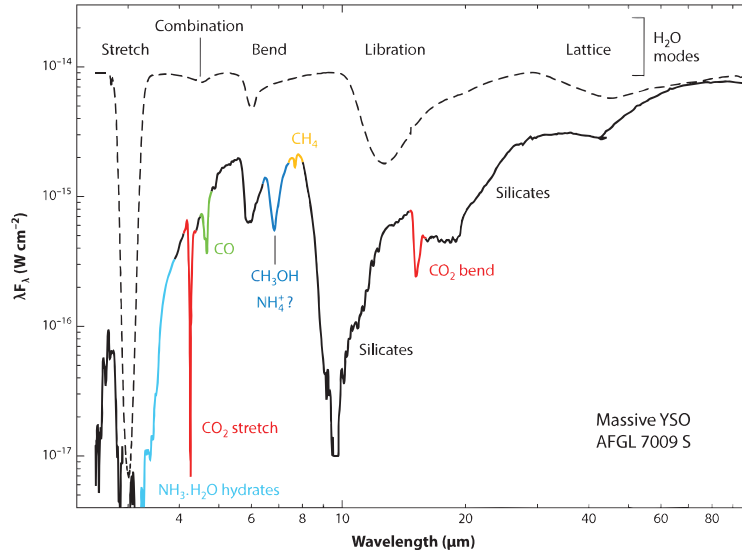
Figure 1.1: The strongest ice and dust features in the massive YSO AFGL 7009S obtained from Infrared Space Observatory (ISO) (Dartois et al. 1998). The figure is taken from Boogert et al. (2015).

hydrogenated species, e.g., NH_3, and CH_4. When the density increases to 10^{4-5} cm^{-3}, the abundant gaseous CO starts dominating the accretion process (Pontoppidan 2006), resulting in an apolar (non-polar) ice layer and offering a reservoir for the formation of complex organic molecules. The observed ice abundances for these different environments are summarized in Table 1.1.

The formation of COMs is linked to the question: does life has its building blocks in space? Observational searches in the mid-infrared (MIR) range, especially at $5-10$ µm, are essential to complement ice evolution studies and to link laboratory and modeling studies that investigate the formation of organic species on grain surfaces. The James Webb Space Telescope (JWST), with extremely high detection sensitivity, very high spatial and relatively high spectral resolution, will further add to the understanding whether life had a cold start on interstellar dust grains.

1.2.3   Interstellar COMs: complex organic molecules

Among the observed interstellar molecules, there are about 50 species that contain six or more atoms and at least one carbon atom. These species are the so-called interstellar Complex Organic Molecules (COMs) (Herbst & van Dishoeck 2009; Herbst 2017). It is important to note that the term 'complex' directly relates to the ISM, as for Earthly conditions most of the interstellar molecules are considered to be rather simple species. Moreover, in this thesis, a more restrictive definition for COMs is used, limiting this class of molecules to species possessing more than six atoms and at least two carbon/nitrogen atoms. As a direct consequence, CH_3OH is not regarded to be a COM. The first detections of COMs e.g., CH_3CN, NH_2CHO, CH_3CHO, and CH_3CCH, was in massive (high)—mass star-forming regions, such as Orion and Sgr B, through rotational spectroscopy at $100-200$ K (Solomon et al. 1971; Rubin et al. 1971; Gottlieb 1973; Buhl & Snyder 1973). However, COM detections are not limited

Table 1.1: Interstellar ice species

Molecule	%[H_2O] Massive YSO	Low-YSO	Comets
Securely identified			
H_2O	100	100	100
CO	$3-26$	$(<3)-85$	$0.4-30$
CO_2	$11-27$	$12-50$	$4-30$
CH_3OH	$(<3)-31$	$(<1)-25$	$0.2-7$
NH_3	~ 7	$3-10$	$0.2-1.4$
CH_4	$1-3$	$1-11$	$0.4-1.6$
Likely identified			
OCN^-	$0.1-0.9$	$(<0.1)-11$	-
OCS	$0.03-0.16$	1.6	$0.1-0.4$
H_2CO	$\sim 2-7$	~ 6	$0.11-1$
Possibly identified			
HCOOH	$(<0.5)-6$	$(<0.5)-4$	$0.06-0.14$
CH_3CH_2OH	$(<0.5)-6$	-	-
$HCOO^-$	$0.3-1$	~ 0.4	-
CH_3CHO	$3.3-11$	-	-
NH_4^+	$9-34$	$4-25$	-
SO_2	$(<0.9)-1.4$	~ 0.2	0.2
PAH	~ 8	-	-
HNCO	$<0.3-0.7$	-	$0.02-0.1$
NH_2CHO	<1.5	-	0.002

Table reproduced from Table 2 and 3 of Boogert et al. (2015)

to high-mass protostars. Meanwhile, a great number of COMs are reported toward low-mass protostars, such as IRAS 16293-2433, NGC1333 IRAS2A, and NGC1333 IRAS4A (Jørgensen et al. 2016; Taquet et al. 2015; Coutens et al. 2015). The interstellar sugar, i.e., glycolaldehyde, which is an important ingredient for ribonucleic acid (RNA) and was first observed in Sgr B2 by Hollis et al. (2000), has now been detected in a solar—mass protostar (IRAS 16293-2422). The formation mechanisms of COMs are traditionally thought to take place on icy grain surfaces, both upon non-energetic and energetic triggers. COM synthesis, for example, can be realized through energetic particles (UV photons, free electrons or cosmic rays) dissociating species to form radicals that can recombine through thermal diffusion. Eventually, the heavier species will desorb into the gas—phase when temperatures reach $\sim 100-150$ K. However, observations showing gaseous COMs in dark cloud and pre-stellar cores challenge the "warm ice" formation scenario (Marcelino et al. 2007; Bacmann et al. 2012; Öberg et al. 2010, 2011a; Cernicharo et al. 2012; Vastel et al. 2014; Jiménez-Serra et al. 2016). Alternative formation channels for explaining the presence of COMs in the early phase of dense cloud have been proposed and discussed in the literature and are at the core of this thesis (Balucani et al. 2015; Fedoseev et al. 2015a; Butscher et al. 2015; Chapter 2; Chapter 3; Chapter 4).

1.3 PHYSICAL AND CHEMICAL PROCESSES IN INTERSTELLAR ICES

In a number of recent studies, partly summarized in this thesis, it has become clear that solid-state chemistry triggered by non-energetic and energetic processes on icy grain surfaces is key in the formation mechanism of hydrogenated species and COMs that contain two, three, or even more carbon elements. Further studies, characterizing the physical and chemical pa-

rameters governing solid-state chemistry, e.g., deposition (binding energy and sticking coefficient), migration (diffusion energy), reaction (activation energy), and desorption mechanism (energy dissipation), under different vacuum, surface material, and cryogenic conditions, provide insight in the actual processes taking place. The details of non-energetic and energetic processes in dense dark clouds are discussed in the next subsections (1.3.1 and 1.3.2). Generally, in surface reactions, radical—molecule and radical—radical reactions typically have small activation barriers or are even barrierless. This makes non—energetic processes - typically atom addition reactions —a possible dominating mechanism resulting in the formation of heavier species at very low temperatures. This also offers a non-thermal low temperature (∼10 K) desorption pathway, (Garrod et al. 2007; Minissale et al. 2016; Chapter 6). In addition, the moderate flux of UV-photons or electrons induced by cosmic rays (CR) interacting with hydrogen can trigger energetic processes, to enhance the concentration of radicals in the ice mantle, and to non—thermally desorb the solid-state species into the gas phase. In a later stage of star formation, the interstellar ice will be exposed to higher temperatures and violent UV radiation from the forming (proto)star. More intense chemical reactions can occur, thermally induced, in the 'warm' ice mantle leading to species with high molecular complexity (Schutte et al. 1993; Butscher et al. 2015; Fresneau et al. 2015). Beside sublimation of volatile species due to heat, molecules will be locked in icy grains as these move to the mid-plane of the protoplanetary disk, and become ingredients available for planet and comet formation. Instruments on the *ROSETTA* mission to the comet 67P/Churyumov-Gerasimenko (67P/C-G) studied *in situ* the pristine interstellar ices on the surface and in the coma, and found a remarkable level of molecular complexity, such as glycolaldehyde (interstellar sugar), and even glycine (the simplest amino acid), as well as large amounts of frozen oxygen (Bieler et al. 2015; Le Roy et al. 2015; Goesmann et al. 2015; Altwegg et al. 2016, 2017).

1.3.1   *Non-energetic processes*

Three major processes dominate surface reactions. These follow (1) a Langmuir-Hinshelwood (L-H), (2) an Eley-Rideal (E-R), or (3) a Hot-Atom (H-A) mechanism, as illustrated in Figure 1.2. In the Langmuir-Hinshelwood mechanism, two reactants that are thermally equilibrated on the surface in two different binding sites, diffuse around the available sites and finally meet each other resulting in a new species. In the Eley-Rideal mechanism, one of the reactants directly accretes from the gas phase on top of an absorbed reactant, and the reaction takes place immediately before reaching thermal equilibrium. The Hot-Atom mechanism is somewhat situated between the previous two; the reactant lands on the surface, migrates a considerable distance, and associates with another reactant without thermal equilibrium. The surface is crucial for product synthesis as a way for excess energy dissipation, and the stabilization of the newly formed species.

In dense clouds, H-atom addition, e.g., so-called hydrogenation reactions, are considered to be most prominent due to the substantial abundance of hydrogen in the Universe. The L-H mechanism is the main route to associate two species, since (1) in dense clouds, the temperature of gaseous species and dust grains is ∼10 K, and therefore hot-atoms barely exist, and (2) the flux of H-atoms is too low to support reactions through an E-R mechanism. In a laboratory setting, E-R and H-A are hard to distinguish. This is due to the non-negligible temperature difference between H-atom and the absorbed species, as well as the considerable H-atom flux that is normally $8 - 10$ orders of magnitude larger in the laboratory than the flux in dense clouds, in order to achieve a comparable fluence in a relatively short time. For this reason it is important to involve modeling simulations, to bridge experiments in the lab with
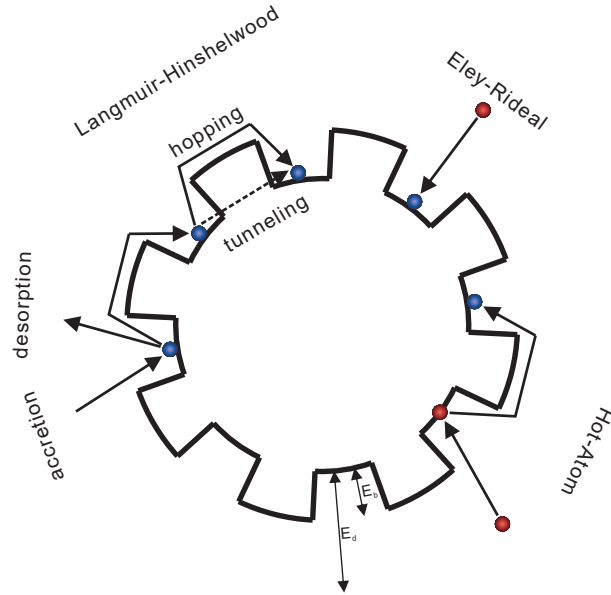
Figure 1.2: Three mechanisms for surface reaction on the grain surface: Langmuir-Hinshelwood, Eley-Rideal, and Hot-atom mechanism. The blue particles are thermalized species and red particles are non-thermalized. E_d is an activation barrier of desorption; E_b is an activation barrier of the diffusion form one surface site to another.

'real' astronomical conditions, compensating for the difference in timescales and to derive the reaction rate constant under interstellar conditions (Cuppen et al. 2009).

Some important hydrogenation routes that result in the formation of abundant interstellar molecules, e.g., H_2, H_2O, CO_2, CH_3OH, and NH_3, are shorty discussed here. H_2 formation is one of the most well studied examples of radical-radical reactions on various surfaces in the laboratory (Islam et al. 2007; Vidali 2013; Wakelam et al. 2017). In dense clouds, two H-atoms accreted on a grain surface diffuse and meet each other forming molecular hydrogen through an L-H mechanism. Molecular hydrogen is also formed through other mechanisms during different stellar evolutionary stages. Due to the extremely low binding energy ($\sim$100 K) of accumulating H_2, multilayer H_2 ice is very unlikely to form under interstellar cloud conditions. Newly formed H_2, therefore, will quickly be released into the gas phase. H_2O is the most abundant ice species. The formation of H_2O mainly starts in translucent clouds by means of the interaction between H-atoms and oxygen allotropes, i.e., O, O_2, and O_3, as shown in Figure 1.3 (Ioppolo et al. 2008; Miyauchi et al. 2008; Linnartz et al. 2015). A similar pathway can be applied to explain the solid-state formation of CH_4 and NH_3 (Hidaka et al. 2011; Fedoseev et al. 2015b). CO_2 ice can be formed in different ways. An efficient channel is through the reaction CO + OH, as shown in Figure 1.3. Alternatively, direct addition of atomic oxygen to CO is another possible channel, but with a typically high H/O ratio in dense dark clouds this reaction competes with the barrierless O + H channel that forms the OH radical.

The solid state formation of oxygen-bearing organic ice species, such as CH_3OH, was first proposed by Tielens & Hagen (1982), and confirmed by modeling and laboratory work, as shown in the left panel of Figure 1.3 (Charnley 1997; Cuppen et al. 2009; Chang & Herbst 2012; Hiraoka et al. 1994; Watanabe & Kouchi 2002; Zhitnikov & Dmitriev 2002; Fuchs et al. 2009).
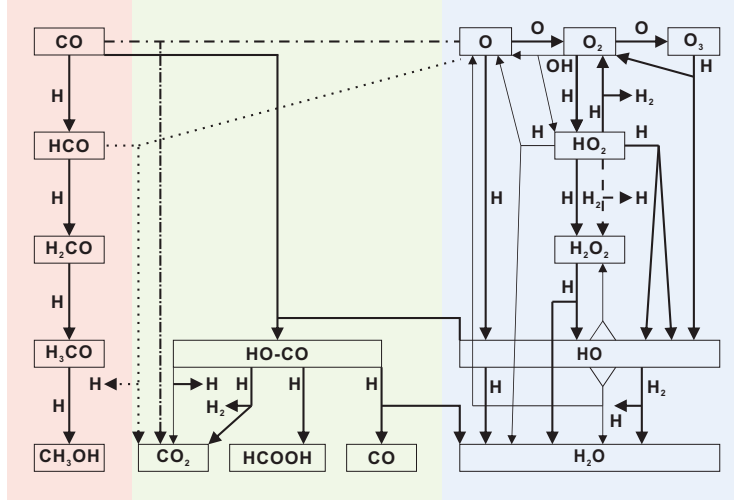
Figure 1.3: A schematic representation of the reaction network for CH_3OH (left), H_2O (right), and CO_2 (middle) on grain surfaces. The figure is taken from Linnartz et al. 2015.

In prestellar cores ($n_H \approx 10^5$ cm^{-3} and T$\approx$10 K), gaseous CO catastrophically freezes out on the grain surface, and reacts with impacting H-atoms through along the sequence:

$$CO \xrightarrow{+H} HCO \xrightarrow{+H} H_2CO \xrightarrow{+H} CH_3O(CH_2OH) \xrightarrow{+H} CH_3OH \tag{1}$$

The first and third H-atom addition reactions, forming HCO, and CH_2OH/CH_3O, have a similar activation energy of $\sim$2400 K, reported in the gas-phase. Later, isotope laboratory studies with D-atoms showed that the deuteration of CO forms similar products, but in the corresponding deuterated form. The derived reaction rate constant for deuteration is about ten times less than the rate constant for hydrogenation indicating that the reaction barrier of H + CO and D + CO takes place through tunneling (Hidaka et al. 2007). Clearly, solid-state reactions may result in H/D abundances that deviate from natural values.

   Beside H-atom addition reactions, also H-atom abstraction reactions play an important role (Tielens & Hagen 1982). Laboratory studies demonstrate that the H-D substitution for H_2CO and CH_3OH is through H abstraction reactions, and results in H_2CO-d$_n$ (n = 1 − 2) and CH_3OH-d$_m$ (m = 1 − 3) formation, respectively, as shown in Figure 1.4 (Nagaoka et al. 2005; Hidaka et al. 2009). In this Thesis it is shown that the formation of oxygen-bearing complex organic molecules involves recombination of radicals that are formed both in addition and abstraction reactions in the CO-H_2CO-CH_3OH hydrogenation chain (Woods et al. 2013; Fedoseev et al. 2015a; Chapter 2; Chapter 3). Barrierless radical-radical recombinations on grain surfaces open a new door to form COMs starting from the simple species CO in the very early stages of dense dark cloud formation.
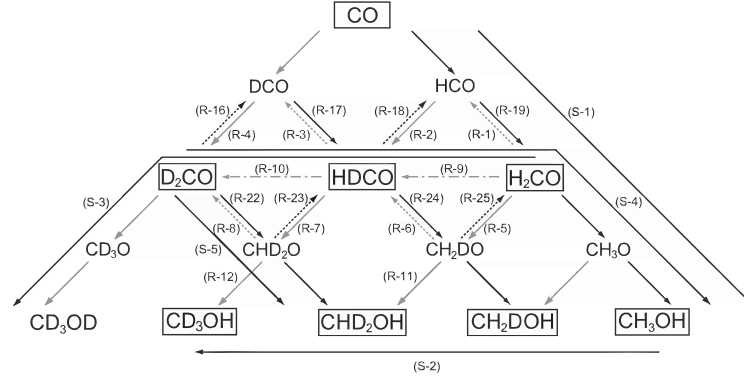
Figure 1.4: Surface reaction network of CO exposed to H and D atoms. The solid arrows refer to for atom addition reactions; the dashed arrows indicate atom abstraction reactions. Molecules in rectangular frame are astronomically observed. The figure is taken from Hidaka et al. (2009)

1.3.2   Energetic processes

In dense dark clouds, the interstellar radiation field (ISRF) is blocked by the abundant dust grains as a result of absorption or scattering. However, cosmic rays, i.e., highly energetic particles (proton, charged helium, and heavy metal nuclei), are able to affect the inner dense cloud and interact with gaseous H_2 and dust particles along their path, resulting in (secondary) UV-photons (typically at Ly-α and H_2 emission wavelengths) and electrons. The flux of the CR induced UV field is $(1-10)\times 10^3$ photons cm^{-2} s^{-1}, for a CR dissociation rate of $\sim 10^{-17}$ s^{-1} (Prasad & Tarafdar 1983; Mennella et al. 2003; Shen et al. 2004). Although the UV-photon (and electron) flux is lower than that of the dominating H-atoms, these energetic particles can easily penetrate the entire ice mantle, and react with accreted molecules that originated from the gas phase, e.g., CO, or new species formed through surface hydrogenation, such as H_2O, CH_4, NH_3 and CH_3OH.

Several laboratory studies have focused on the role of energetic processes, i.e., UV-photons, electrons, X-rays, and protons, and showed the efficient formation of COMs in ice mantles (Greenberg et al. 1995; Bernstein et al. 2002; Muñoz Caro et al. 2002; Meierhenrich 2005; Nuevo et al. 2008; Öberg et al. 2009; Öberg 2016; Modica & Palumbo 2010; Chen et al. 2013; Boamah et al. 2014; Maity et al. 2015; Paardekooper et al. 2016a). In the earlier studies, relatively high energetic fluences, and thick ices containing multiple observed interstellar species were used, and GC-MS analysis of the refractory residue after UV-photon processing led to the discovery of biologically relevant compounds, including various amino acids. In the more recent studies, the focus has been moved on pure, binary, and tertiary ices, to allow a characterization of the involved reactions. Moreover, these studies are all *in situ* without the need to isolate a residual.

1.3.3   Non-thermal desorption mechanisms

The astronomical gas-phase observations showing unexpectedly high abundances of simple species and complex molecules ($\sim 10^{-8}$–10^{-9} n_H) in dense clouds seem to contradict the concept that at such low temperature (10 K) all species must be frozen out on the grain surfaces, forming ice mantles, except H_2 and He due to their extremely low binding energy. In dense

clouds, the temperature of grain surfaces is too low to sublimate the condensed molecules; thermal desorption is forbidden in this stage. Thus, different non-thermal desorption mechanisms have been proposed to explain the net transfer of frozen molecules from the solid state into the gas phase, such as photo-desorption and reactive desorption.

UV-photon irradiation studies of simple species, e.g., CO, CO_2, H_2O, and CO:N_2 ice mixture, have been investigated and discussed to offer an efficient non-thermal desorption pathway. Broad band UV-light of H/H_2 emissions in a microwave discharge H_2 flowing lamp (MDHL) was used, or narrow-band (but tunable) UV light using a synchrotron source (Öberg et al. 2007; Muñoz Caro et al. 2010; Fayolle et al. 2011; Chen et al. 2014; Fillion et al. 2014; Paardekooper et al. 2016b). However, for molecules like CH_3OH, which is abundantly detected in the gas phase ($\sim 10^{-9}$ n_H), photon-dissociation becomes a dominant channel leading to photo-fragmentation, forming CH_3O, CH_2OH, and CH_3 (Bertin et al. 2016; Cruz-Diaz et al. 2016). The reported upper limit desorption rate, i.e., $< 10^{-6}$ molecules photon^{-1}, is too small to substantially transfer CH_3OH into gas phase. It is expected that this also holds for other organic species larger than CH_3OH.

Alternatively, reactive desorption, i.e., desorption following the exothermic formation of species, may contribute to the gas-phase enrichment of both simple molecules, e.g., CO, and complex species, e.g., CH_3OH. Upon formation, excess energy, typically a few eV, can release bound molecules into the gas phase. Up to recently, laboratory studies of reactive desorption of CO-H_2CO-CH_3OH hydrogenation scheme in multi-layered CO-rich interstellar ice analogues are lacking. Therefore, the reactive desorption fraction, i.e., the efficiency of product desorption from the surface after reaction, is usually handled in astronomical models as a free parameter in the range of $0.01 - 0.10$ to account for the steady state gas-phase abundances of simple species observed in dense clouds (Garrod et al. 2007; Vasyunin & Herbst 2013b). Garrod et al. (2007) showed that models including chemical desorption require a reactive desorption fraction of 0.03 to optimally represent the observed gaseous CH_3OH abundances.

All these non-thermal desorption studies, including investigation of exothermic energy dissipation, reactive desorption, photo-absorption cross-sections, and photo-desorption, are crucial to understand how interstellar molecule transfer from solid state to gas phase is influenced by non-energetic and energetic processes (Fayolle et al. 2011; Cruz-Diaz et al. 2014a,b; Fredon et al. 2017). In this thesis, reactive desorption is studied for reactions taking place along the CO hydrogenation chain.

1.4   INTERSTELLAR ICE IN LABORATORY

In this section the experimental setup is described to simulate the processes described above. To comprehensively study the involved processes and to understand the dependency on the physical and chemical processes at play, it is important to experimentally mimic realistic surface scenarios under dense cloud conditions as good as possible. Experiments are therefore performed under ultra-high vacuum (UHV; $\leqslant \sim 10^{-9}$ mbar) and at cryogenic conditions, incorporating both energetic and non-energetic triggers. Simulating interstellar conditions on a much shorter time scale than usual in space is a challenging task for an experimentalist and not only because of experimental limitations; different processes will be at play at the same time and unraveling their relative importance is a time consuming job that is fortunately possible because in the laboratory conditions can be varied very systematically (Watanabe et al. 2007; Henderson & Gudipati 2015). This allows to compare, for example, the competition between ice fragments (i.e., radicals and atoms) and H-atom accretion from the gas-phase (Chapter 4; Chapter 5).
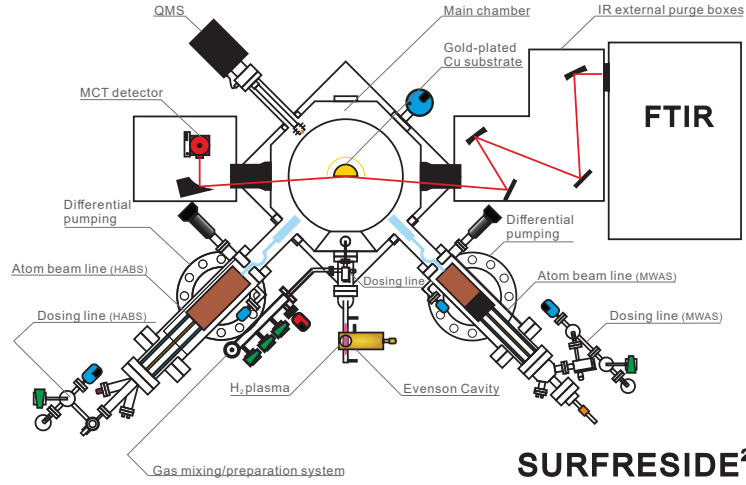
Figure 1.5: Schematic top-view of SURFRESIDE^2. Figure is adapted from Ioppolo et al. (2013).

1.4.1 *Experimental Setup*

The laboratory studies presented in this thesis are performed in the Sackler Laboratory for Astrophysics using SURFRESIDE^2 (Surface Reaction Simulation Device 2), an ultra-high vacuum system fully optimized to study atom addition/abstraction reactions in interstellar ice analogues under dense interstellar cloud conditions. A top-view of the setup is shown in Figure 1.5. This upgraded system is operational since 2012, and has been further extended in the past few years to simulate more sophisticatedly the ice chemistry in environments relevant for interstellar studies. Details are available from Ioppolo et al. (2013). This setup consists of a main chamber and two atom source chambers, which are all differentially pumped to $10^{-10} - 10^{-9}$ mbar (i.e., $\sim 10^6 - 10^7$ cm^{-3}) by turbomolecular pumps and rotary vane vacuum forepumps. At UHV, the residual gas is mainly H$_2$ with a negligible amount of H$_2$O contamination on a cold substrate ($\leqslant 4 \times 10^{13}$ molecules cm^{-2} for 1 hr). A gold-plated copper substrate is centered in the main chamber and cooled by a closed-cycle helium cryostat (Cold-Edge model: CH-204, supported by a Compressor: HC-4), which allows for manipulation of the substrate temperature between 8 and 450 K using resistive heating wire. Two silicon diode thermal sensors (LS-DT-640B CU) installed right behind the substrate and on the second stage of the cold finger are used to monitor the temperature with 0.5 K absolute accuracy.

Two atom beam lines, incorporated in separate differentially pumped vacuum chambers, are connected with UHV shutter valves to the main chamber at angles of 45 degree in order to study different atom addition/abstraction reactions based on different atom generation methods; (1) Hydrogen Atom Beam Source (HABS, Dr. Eberl MBE-Komponenten GmbH, see Tschersich 2000) producing H- or D-atoms by thermal (2100 K) cracking of precursor H$_2$ and D$_2$ through a tungsten filament, and (2) Microwave Atom Source (MWAS, Oxford Scientific Ltd, see Anton et al. 2000) capable of producing H-atoms, D-atoms, and other atoms, e.g., O-, N-atoms, and various radicals (like OH) using a microwave discharge (275 W at 2.45 GHz). A nose-shape quartz pipe is placed along the exit path of both beam lines to efficiently quench and thermalize excited atoms and non-dissociated molecules through multiple collisions with
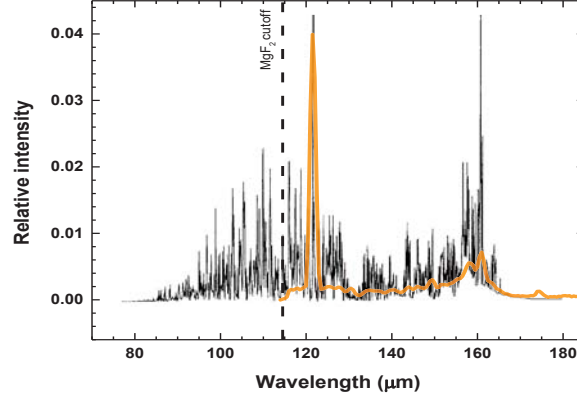
Figure 1.6: UV spectrum (yellow) of the MDHL used in this thesis, which is obtained from Ligterink et al. (2015). The background line (black) is the calculated spectrum of UV photons induced by CR interacting with H_2 molecules in dense clouds, which is obtained from Gredel et al. (1989). The MgF_2 window cutoff is indicated (dashed line).

the walls of the pipe. This quartz pipe also shields the ice sample from UV light ($\lambda \leqslant 200$ nm) generated in the MWAS plasma. Typical atomic beam line fluxes vary (depending on the precursor). Typical H-fluxes are in the range $\sim(1-10) \times 10^{12}$ atoms cm^{-2} s^{-1}, and can be simultaneously operated to further increase the H-atom flux.

UV-photons generated by a Microwave Discharge Hydrogen-flow Lamp (MDHL) are guided through an MgF_2 window, and directed on the substrate at normal incidence. The lamp is mounted in between the two atomic beam lines. The customized quartz lamp is 'F' shaped, $\sim$1.3 cm in diameter and $\sim$20.0 cm in length, and combined with a commercial Evenson coaxial Cavity (Opthos). The distance between the UHV sealed MgF_2 window and the substrate is about 30 cm. Without a collimating tube, the UV-beam spot covers the entire substrate area (2.5×2.5 cm^2). The microwave power generator (Sairem-GMS200W, 2.45 GHz) is used to discharge H_2 flowing gas at a pressure of $\sim$1 mbar, generating H_2 plasma and UV light. In Figure 1.6, the UV spectrum ranging between 114 and 180 nm is shown to consist of a main peak at 121.6 nm (Ly-α, $\sim$33% of the total flux) and a series of other peaks between 155 and 165 nm (H_2 emission, $\sim$20% of the total flux) superposed on a broad continuum ($\sim$47% of the total flux). The total UV flux is estimated to be $\sim$6×10^{12} photons cm^{-2} s^{-1}. Details are available in Ligterink et al. (2015).

Gaseous molecules are prepared in an oil-free gas-mixing/preparation high vacuum ($\leqslant 10^{-5}$ mbar) system, which is pumped by a turbomolecular pump backed with a scroll forepump, and stored in two separate reservoir dosing lines. The dosing pressure is monitored by a mass independent gauge in the range of mbar to bar. These vapor species are introduced into the main chamber through one of two capillary tubes controlled by high-precision leak valves, such that they deposit onto the pre-cooled substrate under an angle of +22° (or -22°) from the surface normal. The typical deposition pressure is in the range of $\sim$10$^{-10} - 10^{-8}$ mbar, and ices are grown with sub-monolayer precision in thickness ranges from few ML to several tens of ML. Here 1 monolayer (ML) is defined to be 1×10^{15} molecules cm^{-2}.

Two different ice grows techniques are commonly applied in the experiments described in this thesis; pre-deposition and co-deposition. In the pre-deposition experiments, molecules are

first deposited on the pre-cooled substrate resulting in a pre-grown ice sample before atoms or UV-photons start interacting. Once the ice is bombarded with atoms and/or irradiated with UV-photons, the kinetics of the pre-deposited species and the newly formed products can be obtained. These time-resolved data can be fitted with rate equations to determine the chemical characteristics, e.g., reaction rates and activation energy. In the atom addition/abstraction experiments, the penetration depth is limited to only the upper layers of the pre-deposited ice leading to relative low formation yields. Moreover, the active intermediate radicals formed during the chemical reactions are quickly converted into stable products.

In the co-deposition experiments molecules and atoms (and UV photons) are simultaneously deposited onto the pre-cooled substrate with a specific deposition-flux calibrated in advance. This technique has the ability to study various ratios between the molecular reactants and the atomic species simulating the different ISM density (flux) conditions. Moreover, co-deposition experiments are more representative of the actual processes taking place under dense cloud conditions, where atoms and molecules continuously adsorb onto dust grains. Matrix techniques can be exploited in co-deposition experiments using overabundant molecule depositions to preserve the intermediate radical products, which generally recombine immediately with incoming atoms through barrierless reactions. In this case, the final yield of products is proportional to the co-deposition time, resulting in a more secure identification of the analytical methods used.

1.4.2 *Analytical techniques*

RAIRS: The ice composition and abundance are monitored in situ by means of Reflection-Absorption InfraRed Spectroscopy (RAIRS) using the external IR path from a Fourier Transform Infrared Spectrometer (FTIR; Agilent Technologies Cary 600 Series), and a Mercury Cadmium Telluride (MCT) detector cooled by liquid nitrogen. The IR absorbance spectrum is obtained by taking the common logarithm of the ratio of substrate and ice sample single-beam spectra, i.e., $Abs(\nu) = \log(I_{\text{substrate}}(\nu)/I_{\text{sample}}(\nu))$, which covers the range of $4000 - 700$ cm^{-1} typically with 1 cm^{-1} resolution. As RAIR spectra are continuously recorded, these allow to monitor changes compared with the spectrum for the initially deposited and unprocessed parent species; this allows not only to investigate which species are formed, but also how effectively this process takes place. The icy constituents are identified by their characteristic vibrational modes that are directly connected to different functional groups. The vibrational modes shift when isotopes are used. In general, RAIRS has a higher sensitivity than transmission IR spectroscopy, because (1) the geometry of the IR path in the ice is at least two times longer than in transmission, i.e., the incident sample path before reaching the substrate and the reflecting sample path after hitting the substrate, and (2) the glancing angle $\sim10°$ to the substrate plane) of IR light enhances the p-polarized electric field at the gold surface resulting in higher sensitivity. It should be noted, though, that the reported IR band strengths available from the literature are generally derived from transmission experiments and these cannot be directly used to quantify RAIR data.

In order to overcome this issue, (setup-specific) RAIR band strengths need to be determined. Therefore, experiments have been performed to separately derive the RAIR band strength values for the most commonly studied species in this Thesis, i.e., CO, H_2CO, and CH_3OH, by using the laser interference technique. A HeNe laser beam hits the gold-plated substrate, at an incident angle of $\sim3°$ with respect to the surface normal incidence, and the reflecting laser beam intensity is monitored by a photodiode. Simultaneously, the pure ice is introduced onto

the pre-cooled substrate forming ice layers in a constant deposition rate over time. For pure ice, the absolute column density is calculated (molecules cm^2) with the equation:

$$N = \frac{d \cdot \rho \cdot N_a}{M} \tag{2}$$

where d is the thickness of ice in cm, ρ is the density in g cm^{-3}, N_a is Avogadro's constant $(6.022 \times 10^{23}$ mol^{-1}), and M is the molar mass of the species. The ice thickness, d, is experimentally determined by laser refractive interference:

$$d = \frac{k \cdot \lambda \cdot 10^{-7}}{2n \cdot \cos(\theta_f)} \tag{3}$$

where λ = 632.8 nm is the HeNe laser wavelength, n is the refractive index of a specific ice, $\theta_f = 3°$ is the angle of refraction in the ice in degrees and k is the number of involved fringes (Hollenberg & Dows 1961; Westley et al. 1998). The ice growth on the substrate is monitored by RAIRS for the first few minutes (Figure 1.7 right-hand panel) before RAIR signal saturation. To keep a constant deposition rate for the entire measurement (~hours), a relatively high gas sample pressure is used in the gas-mixing and dosing reservoir lines. The IR absorbance area obtained from the integration of the IR signal is correlated to the absolute column density derived from the laser interference pattern (Figure 1.7 left-hand panel). The correlation is described by the modified Beer-Lambert Law:

$$N = \frac{\log 10 \cdot \int Abs(\nu)d(\nu)}{A'} \tag{4}$$

where $Abs(\nu)$ is the IR absorbance intensity, and A' is the RAIR band strength value. By linear fitting the data (middle panel Figure 1.7), the A' RAIR value can be derived for all relevant modes of the involved molecules. The band strength for CO (2142 cm^{-1}), H_2CO (1497 cm^{-1}), and CH_3OH (1030 cm^{-1}) is derived as: $(5.2\pm0.3)\times10^{-17}$, $(3.2\pm0.3)\times10^{-17}$, and $(7.1\pm0.6)\times10^{-17}$ cm $molecule^{-1}$, respectively.

The identification of specific molecules in RAIR spectra is based on the full ensemble of fingerprint features. Typically, the larger the molecule, the larger the number of vibrational modes that can be seen, and the more specific a functional group, the easier is an unambiguous identification. For example, glycolaldehyde (GA, CH_2OHCHO) contains a hydroxymethyl (-CH_2OH) and an aldehyde (-CHO) group, showing very strong O-H, C-O, and C=O stretching vibration modes at ~3340, ~1750, and ~1110 cm^{-1}, respectively. When bands with these wavelengths are found with SURFRESIDE[2], comparable to molecular fingerprints available from literature, it is very likely that glycolaldehyde is present in the ice. However, it should be noted that in the case that GA is formed in the ice, e.g., upon hydrogenation of CO-ice, it is possible that other molecules with similar functional groups are formed as well, yielding spectra with similar features.

This is part of the discussions in Chapter 2; CO hydrogenation experiments not only give glycolaldehyde, but also yield isomeric species, e.g., methyl formate (MF, CH_3OCHO), and the fully hydrogenated species, e.g., ethylene glycol (EG, $CH_2(OH)CH_2OH$). In this case, the hydroxymethyl (-CH_2OH) and the aldehyde (-CHO) groups are not represented by glycolaldehyde alone, so this complicates the qualitative species identification and quantitative abundance estimation (Figure 1.8). The use of isotopically labeled precursors may help in the identification, but it is also possible to use a complementary detection method.
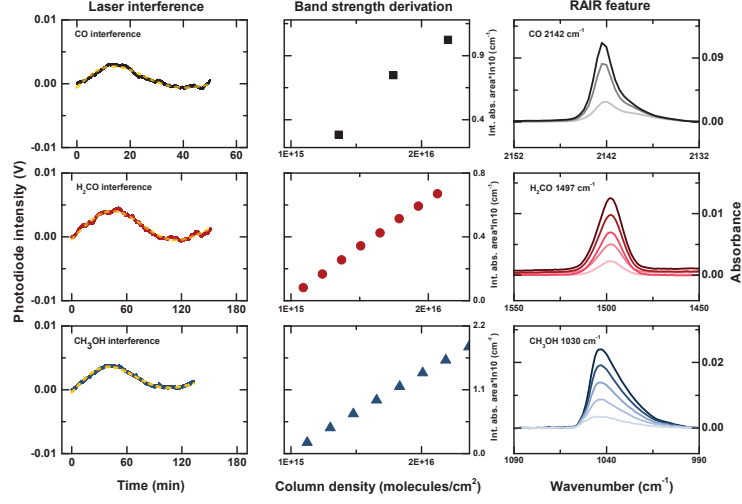
Figure 1.7: Left: typical examples of the obtained interference fringes as function of time and their corresponding sinusoidal fittings (yellow dashed line) deposition of pure CO, H_2CO, and CH_3OH. Right: the RAIR absorbance feature different times for deposited CO (2142 cm^{-1}), H_2CO (1497 cm^{-1}), and CH_3OH (1030 cm^{-1}). Middle: the integrated absorption as a function of column density of each species for the first few minutes of deposition.
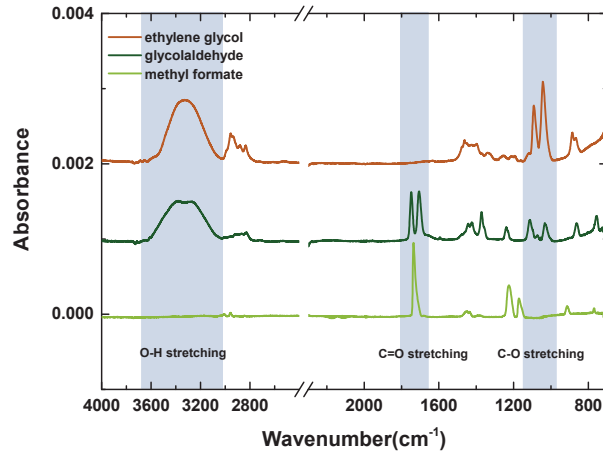
Figure 1.8: IR absorbance spectra of methyl formate, glycolaldehyde, and ethylene glycol in the range of $4000 - 700$ cm^{-1}.
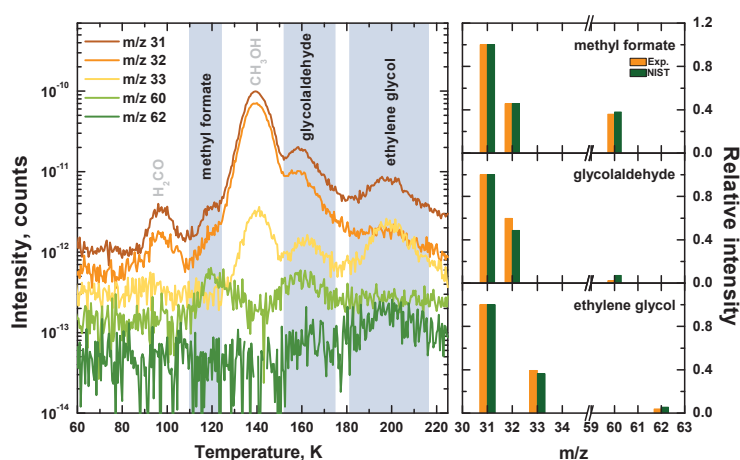
Figure 1.9: Left: TPD mass spectra obtained from a codeposition experiment of H_2CO and H-atoms. The thermal desorption temperatures of methyl formate (m/z = 31, 32, and 60), glycolaldehyde (m/z = 31, 32, 33, and 60), and ethylene glycol (m/z = 31, 33, and 62) are at 120, 160, and 180 K, respectively. Right: comparison of the fragmentation patterns of these COMs with the corresponding NIST[1.1] database.

TPD: During a Temperature Programmed Desorption (TPD) experiment an ice sample, which consists of initially deposited species and newly formed products, is linearly and slowly heated to a preset (high) temperature value, typically with a rate of the order of $1 - 10$ K min^{-1}. At specific temperatures specific molecules can thermally desorb in the gas phase and this is recorded sensitively by Quadrupole Mass Spectrometry (QMS; MKS Microvision-plus). In the QMS desorbed species are ionized by electrons, which are emitted from a hot filament on the tip of the QMS. The ionized molecules are accelerated and guided into the quadrupole mass filter, which consists of four cylindrical rods oppositely connected to RF voltage with a DC offset voltage in two pairs. Only the ions with certain mass-to-charge ratio (m/z) can reach the detector for a given voltage ratio, and the other ions with different m/z will eventually collide with rods before detection. Two types of detectors can be used in the used QMS for different sensitivities: (1) a Faraday detector for high ion intensity, and (2) a Channel Electron Multiplier (CEM) for trace ion signals ($\geqslant 5 \times 10^{-14}$ mbar).

The desorption temperature for each species is another characteristic that depends on the species' binding energy to the surface. Therefore, measuring this characteristic offers a complementary tool to distinguish reaction products that share very similar functional groups. For example, in Figure 1.9, the MF, GA, and EG desorption peaks are located at 120, 160, and 180 K, respectively, in the mass spectrum using the TPD experiment.

The electrons emitted from the ionizing source have an energy of 70 eV, which is sufficient to break COMs, resulting in typical mass fragmentation patterns. This mass fragmentation

---

[1.1] NIST Mass Spec Data Center, S.E. Stein, director, 'Mass Spectra' in NIST Chemistry WebBook, NIST Standard Reference Database Number 69, Eds. P.J. Linstrom and W.G. Mallard, National Institute of Standards and Technology, Gaithersburg MD, 20899, http://webbook.nist.gov.

pattern offers another fingerprint for each species due to the different molecular structures that correspond with different binding energies. For example, in the right panel of Figure 1.9, the mass fragmentation for MF, GA, EG from a H_2CO hydrogenation experiment is in agreement with the NIST database values. Normally, three typical mass fragments, that is, the total molecular weight, the most abundant signal, and a unique mass, are chosen in order to make a confident species identification.

Under sufficient gas pumping speed, the recorded QMS signal ($I(t)$) for the selected m/z is proportional to the species desorption rate (dN/dt), and can be described by the Polanyi-Wigner equation:

$$I(t) \propto dN/dt = \nu(N,T) \cdot N^n \exp\left(\frac{-E_{des}(N,T)}{k_b T}\right) \qquad (5)$$

where ν is the pre-exponential factor, N is the surface coverage, n is the kinetic desorption order, E_{des} is the activation energy for desorption, k_B is the Boltzmann constant, and T is the surface temperature. This equation is perfect for describing 'pure' species desorption behavior on surfaces, and allows to derive binding energies for various surfaces (Brown & Bolina 2007; Fayolle et al. 2016). However, in most of the experiments described in this thesis, interstellar ice analogues are 'dirty', containing multiple species in the ice mantle and this leads to more than one binding energy value. Moreover, volatile species may exhibit multiple desorption peaks from co-desorbing with less-volatile species. Therefore, it is not trivial to accurately derive species abundances by fitting TPD peaks in the mass spectrum using equation (5). However, the area of the desorption peak obtained from integration of the QMS signals ($I(t)$) over time is representative of the species' abundance (N) on the surface. This can be used as a tool to quantify branching ratios for each of the newly formed products.

Care needs to be taken when analyzing the peak area for a given m/z, since this is dependent on several factors: (1) the electronic ionization cross-section ($\sigma^+(mol)$) as a function of energy, which is available for most stable molecules in the literature, (2) the fraction of ionized molecules with charge z ($I_F(z)$), which is unity when z = 1, (3) the fraction of mass fragmentation ($F_F(m)$), which is available in the literature, and (4) the mass sensitivity ($S(m/z)$), which is setup dependent, as shown in Figure 1.10. The species abundance can be estimated by carefully calibrating the above factors using the equation (Martín-Doménech et al. 2015):

$$N(molecule) = k_{QMS} \cdot \frac{A(m/z)}{\sigma^+(molecule) \cdot I_F(z) \cdot F_F(m) \cdot S(m/z)} \qquad (6)$$

where k_{QMS} is the proportionality constant, which is independent of the species assuming relatively constant pumping speed for all formed products, and need to be independently measured using other techniques. For the relative abundance, it can be derived by the equation:

$$\frac{N_1(molecule1)}{N_2(molecule2)} = \frac{A_1(m/z)}{A_2(m/z)} \cdot \frac{\sigma_2^+(molecule2) \cdot I_{F2}(z) \cdot F_{F2}(m) \cdot S_2(m/z)}{\sigma_1^+(molecule1) \cdot I_{F1}(z) \cdot F_{F1}(m) \cdot S_1(m/z)} \qquad (7)$$

The TPD experiments thus give a second complementary tool to further constrain the formation of surface reaction products. Obviously, TPD cannot probe species at the temperatures for which the reactions take place. Moreover, during the heating, additional surface reactions could happen. Ice destruction is an intrinsic property of TPD. In many of the experiments that are described in this thesis, RAIRS and TPD are applied simultaneously.
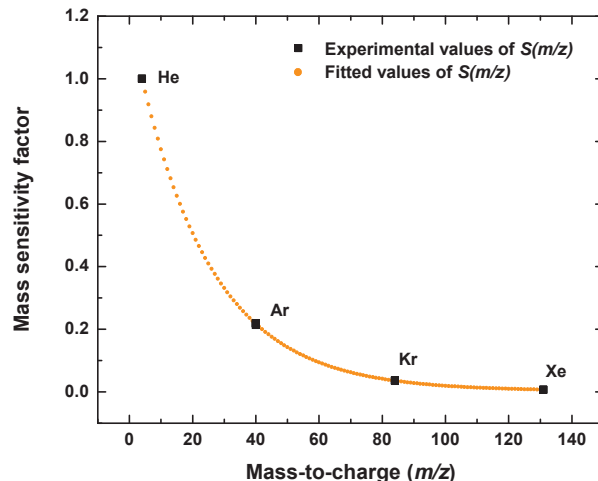
Figure 1.10: QMS detection sensitivity for different mass channels obtained from noble gas calibration experiments.

1.5   THIS THESIS

Interstellar ice mantles consist of simple molecules, e.g., CO, accreting from the gas phase, and of complex species, e.g., CH_3OH and COMs (likely), formed on dust grains. To understand interstellar ice evolution, complementary approaches, i.e., astronomical observations, theoretical/astrochemical models, and laboratory studies, are needed.

The motivation of this thesis is to have a more comprehensive picture of the interactions of CO-hydrogenation products with abundant H-atoms and moderate UV-photons on the grain surfaces under dense cloud conditions. The recent gas-phase discovery of COMs at low temperatures challenges the conventional COM formation scenarios where CH_3OH undergoes intensive UV-photon irradiation, CR bombardment, and 'warm' ice chemistry forming complex organics in the gravitationally collapsing stage. The primary goal of this thesis is to understand how simple solid-sate species transform to COMs without such energetic processes focusing on the CO catastrophically freeze-out stage at temperatures as low as 10 K and to explain the 'cold' COM detections. Moreover, the net transfer of the newly formed species, especially partially or fully hydrogen saturated molecules on the grain surfaces, into the gas phase through non-thermal desorption is currently unconstrained, and is a free parameter in astrochemical models. To this end, experimental studies systematically investigate CO ice hydrogenation, and expand our understanding of the CO-H_2CO-CH_3OH formation network to more complex organics, which contain two, three or even more carbon atoms, such as glycolaldehyde (an interstellar sugar), ethylene glycol, and glycerol (sugar alcohol). The interactions of CO with other interstellar relevant species, e.g., NO and H_2, under moderate UV irradiation are experimentally studied to address the formation of CN-bearing, and of H_nCO (n$\geqslant$1) species in dense clouds. The utilization of SURFRESIDE[2], an UHV and cryogenic setup in the Sackler Laboratory for Astrophysics, makes it possible to explore molecular complexity and to understand details of the physical/chemical properties on icy grain surfaces. The ex-

perimental findings are summarized below.

Chapter 2 focuses on the formation of oxygen-bearing complex organic molecules, e.g., methyl formate (HC(O)OCH$_3$), glycolaldehyde (HC(O)CH$_2$OH) and ethylene glycol (H$_2$C(OH)CH$_2$-OH), upon hydrogenation and without the influence of energetic particles (e.g., UV-photons and electrons) or embedded energy source under dense dark cloud conditions. The solid-state synthesis mechanisms are realized by the recombination of the intermediate radicals, i.e., HCO, CH$_2$OH, and CH$_3$OH, which are produced in the hydrogenation scheme of CO-H$_2$CO-CH$_3$OH. We confirm that the interaction of H$_2$CO with H-atoms not only leads to the hydrogenated species, i.e., CH$_3$OH, but also results in dehydrogenated species, i.e., CO, through HCO radical. A similar mechanism is also found in abstraction reactions involving CH$_3$OH to form H$_2$CO. The simultaneous forward (addition) and backward (abstraction) reactions of stable molecules enhance the lifetime of active radicals on grain surfaces compared to previous assumptions, which consider addition reactions only. The experimental findings unambiguously prove complex organic molecule formation during the early phase of the catastrophic CO freeze-out stage and without the need of UV photolysis or cosmic ray bombardment. The solid-state COM formation network is proposed.

Chapter 3 aims to extend the COM formation network presented in Chapter 2 to three-carbon oxygen-bearing species. Under prestellar core conditions, CO hydrogenation is the dominant pathway leading to H$_2$CO and CH$_3$OH formation through successive H-atom addition reactions. The recombination of intermediate radicals with single- and double-carbon containing backbones is experimentally demonstrated to explain the formation of biologically relevant compounds, e.g., glyceraldehyde (HOCH$_2$CH(OH)-CHO), a three-carbon simple sugar, and glycerol (HOCH$_2$CH(OH)-CH$_2$OH), a three-carbon sugar alcohol. The three-carbon sugar plays a key role in energy transfer in living organisms, and the three-carbon sugar alcohol is an important ingredient for membranes of modern living cells. The proposed formation mechanisms have much potential to form complex sugar alcohols and sugars, which can be delivered by comets or other celestial bodies to planets. The resulting reaction scheme can be further extended to form even larger COMs.

Chapter 4 presents the first systematic experimental study that compares quantitatively hydrogenation and UV-induced reactions as well as their cumulative effect in interstellar relevant CO:CH$_3$OH=4:1 ice analogues. We focus on three COMs, i.e., methyl formate (HC(O)O-CH$_3$), glycolaldehyde (HC(O)CH$_2$OH) and ethylene glycol (H$_2$C(OH)CH$_2$OH), which are most commonly produced in '(non-)energetic' processes. In the pure hydrogenation experiments, the derived abundances and the abundance fractions are dependent on the ratio of H-atoms/CO:CH$_3$OH and on the accretion rate of the involved species. The abundance fractions for methyl formate: glycolaldehyde: ethylene glycol are $0:(0.2-0.4):(0.8-0.6)$ for pure hydrogenation, and 0.2:0.3:0.5 for UV involving experiments. In experiments where both hydrogenation and UV irradiation are applied, the overall absolute yields drop to 50% of those found in the pure UV experiments. However, the COM abundance fractions are identical to the fractions in the pure UV experiments. The COM ratios obtained from the laboratory findings can be used as a diagnostic tool to derive the chemical origin of these species. The GA/EG ratios in the laboratory $(0.3-1.5)$ compare well with observations toward various comets and solar-mass protostars suggesting a solid-state formation pathway.

Chapter 5 presents the formation of N-C bearing species obtained from the sequence of NO:CO:H-atom accretion and UV-photon irradiation as well as the simultaneous codeposi-

tion of NO:CO:H-atoms and UV irradiation on grain surfaces. Ice mixtures of NO and hydrogenated CO ices, i.e., comprising H_2CO and CH_3OH, are studied. The UV-irradiation results in NH_2 through photodissociation of NH_2OH, which is the main product of NO hydrogenation. The NH_2 radical plays a key role in the formation of species with an N-C bond, such as HNCO, OCN^-, and NH_2CHO. The formation scheme of N-C bearing species is proposed, and the astronomical implications are discussed.

Chapter 6 presents the reactive desorption fraction of the species along the $CO-H_2CO-CH_3OH$ hydrogenation scheme under prestellar core conditions. The net transfer of solid-state species into the gas phase at very low temperatures, i.e., for settings in which all molecules should be condensed on the grain surface, is experimentally triggered through exothermic reactions with H-atoms in the laboratory. The reactive desorption efficiency for the overall hydrogenation network is derived by precisely measuring the solid-state element carbon budget at $10-14$ K. This results in an upper limit of 0.24 ± 0.02. The corresponding effective desorption fraction for each hydrogenation step and for each H-atom induced reaction (i.e., addition and abstraction) is $\leqslant 0.07$ and $\leqslant 0.02$, respectively. These values favor the lower range of the reactive desorption efficiencies of $0.01-0.10$, which are currently used as a free parameter in astrochemical models.

Chapter 7 investigates whether additional hydrogenation events can take place upon UV irradiation of a $CO:H_2$ ice mixture under prestellar core conditions. The experimental findings show unambiguously that hydrogenated species, e.g.., HCO and H_2CO, are formed after UV-irradiation on the pre-deposited $CO:H_2$ ice mixture. A possible formation mechanism is discussed, through a reaction between photo-excited CO and H_2 molecules resulting in HCO and free H-atoms. Moreover, the newly formed H-atoms can further react with CO along a regular addition step. The HCO production shows a strong temperature dependence for the studied $8-20$ K temperature range, which is directly linked to the H_2 sticking coefficient. Isotope experiments in a $CO:D_2$ ice mixture present a similar trend for the temperature-dependent DCO formation rate, but the overall DCO production efficiency only reaches $\leqslant 25\%$ of the HCO yield at 8 K. Clearly, UV-photon induced hydrogenation enriches interstellar ices with HCO radicals that can further react with other radicals or molecules ultimately also increasing the formation efficiency of COMs. The astrochemical implications are discussed.

The main take-home massage of this thesis is that the building blocks of life are already formed on the grain surfaces at low temperatures before the emerging of the protostar. In dense clouds, the chemical complexity of non-energetic processes is beyond our imagination. The two scenarios of COM formation, i.e., non-energetic and energetic processes, do not conflict each other. Moreover, their product fractions offer a diagnostic potential to derive the formation origin of COMs in different star evolutionary stages. It is therefore expected the upcoming JWST with high spectral resolution and detection sensitivity at mid-infrared wavelengths will greatly increase our knowledge of the interstellar COM evolution from dense cloud to solar system.

BIBLIOGRAPHY

Aikawa, Y., Wakelam, V., Hersant, F., Garrod, R. T., & Herbst, E. 2012, Astrophys. J., 760, 40
Altwegg, K., Balsiger, H., Bar-Nun, A., et al. 2016, Science Advances, 2, e1600285
Altwegg, K., Balsiger, H., Berthelier, J. J., et al. 2017, Mon. Not. R. Astron. Soc., 469, S130
Anton, R., Wiegner, T., Naumann, W., et al. 2000, Review of Scientific Instruments, 71, 1177

Bacmann, A., Taquet, V., Faure, A., Kahane, C., & Ceccarelli, C. 2012, Astron. Astrophys., 541, L12

Balucani, N., Ceccarelli, C., & Taquet, V. 2015, Mon. Not. R. Astron. Soc., 449, L16

Baratta, G. A. & Palumbo, M. E. 1998, Journal of the Optical Society of America A, 15, 3076

Bernstein, M. P., Dworkin, J. P., Sandford, S. A., Cooper, G. W., & Allamandola, L. J. 2002, Nature, 416, 401

Bertin, M., Romanzin, C., Doronin, M., et al. 2016, Astrophys. J. Lett., 817, L12

Bieler, A., Altwegg, K., Balsiger, H., et al. 2015, Nature, 526, 678

Boamah, M. D., Sullivan, K. K., Shulenberger, K. E., et al. 2014, Faraday Discussions, 168, 249

Boogert, A. C. A., Gerakines, P. A., & Whittet, D. C. B. 2015, Ann. Rev. Astron. Astrophys., 53, 541

Boogert, A. C. A., Pontoppidan, K. M., Knez, C., et al. 2008, Astrophys. J., 678, 985

Bottinelli, S., Boogert, A. C. A., Bouwman, J., et al. 2010, Astrophys. J., 718, 1100

Brown, W. A. & Bolina, A. S. 2007, Mon. Not. R. Astron. Soc., 374, 1006

Buhl, D. & Snyder, L. E. 1973, in Molecules in the galactic environment

Butscher, T., Duvernay, F., Theule, P., et al. 2015, Mon. Not. R. Astron. Soc., 453, 1587

Cernicharo, J., Marcelino, N., Roueff, E., et al. 2012, Astrophys. J. Lett., 759, L43

Chang, Q. & Herbst, E. 2012, Astrophys. J., 759, 147

Charnley, S. B. 1997, Mon. Not. R. Astron. Soc., 291, 455

Charnley, S. B., Rodgers, S. D., & Ehrenfreund, P. 2001, Astron. Astrophys., 378, 1024

Chen, Y.-J., Chuang, K.-J., Muñoz Caro, G. M., et al. 2014, Astrophys. J., 781, 15

Chen, Y.-J., Ciaravella, A., Muñoz Caro, G. M., et al. 2013, Astrophys. J., 778, 162

Coutens, A., Persson, M. V., Jørgensen, J. K., Wampfler, S. F., & Lykke, J. M. 2015, Astron. Astrophys., 576, A5

Cruz-Diaz, G. A., Martín-Doménech, R., Muñoz Caro, G. M., & Chen, Y.-J. 2016, Astron. Astrophys., 592, A68

Cruz-Diaz, G. A., Muñoz Caro, G. M., Chen, Y.-J., & Yih, T.-S. 2014a, Astron. Astrophys., 562, A119

Cruz-Diaz, G. A., Muñoz Caro, G. M., Chen, Y.-J., & Yih, T.-S. 2014b, Astron. Astrophys., 562, A120

Cuppen, H. M., Penteado, E. M., Isokoski, K., van der Marel, N., & Linnartz, H. 2011, Mon. Not. R. Astron. Soc., 417, 2809

Cuppen, H. M., van Dishoeck, E. F., Herbst, E., & Tielens, A. G. G. M. 2009, Astron. Astrophys., 508, 275

Dartois, E., Cox, P., Roelfsema, P. R., et al. 1998, Astron. Astrophys., 338, L21

D'Hendecourt, L. B., Allamandola, L. J., & Greenberg, J. M. 1985, Astron. Astrophys., 152, 130

Draine, B. T. & Lee, H. M. 1984, Astrophys. J., 285, 89

Fayolle, E. C., Balfe, J., Loomis, R., et al. 2016, Astrophys. J. Lett., 816, L28

Fayolle, E. C., Bertin, M., Romanzin, C., et al. 2011, Astrophys. J. Lett., 739, L36

Fedoseev, G., Cuppen, H. M., Ioppolo, S., Lamberts, T., & Linnartz, H. 2015a, Mon. Not. R. Astron. Soc., 448, 1288

Fedoseev, G., Ioppolo, S., & Linnartz, H. 2015b, Mon. Not. R. Astron. Soc., 446, 449

Fillion, J.-H., Fayolle, E. C., Michaut, X., et al. 2014, Faraday Discussions, 168, 533

Fredon, A., Lamberts, T., & Cuppen, H. M. 2017, Astrophys. J., 849, 125

Fresneau, A., Danger, G., Rimola, A., et al. 2015, Molecular Astrophysics, 1, 1

Fuchs, G. W., Cuppen, H. M., Ioppolo, S., et al. 2009, Astron. Astrophys., 505, 629

Garrod, R. T., Vasyunin, A. I., Semenov, D. A., Wiebe, D. S., & Henning, T. 2009, Astrophys. J. Lett., 700, L43

Garrod, R. T., Wakelam, V., & Herbst, E. 2007, Astron. Astrophys., 467, 1103

Garrod, R. T., Widicus Weaver, S. L., & Herbst, E. 2008, Astrophys. J., 682, 283

Geballe, T. R. & Oka, T. 1996, Nature, 384, 334

Gerakines, P. A., Schutte, W. A., Greenberg, J. M., & van Dishoeck, E. F. 1995, Astron. Astrophys., 296, 810

Gibb, E. L., Whittet, D. C. B., Boogert, A. C. A., & Tielens, A. G. G. M. 2004, Astrophys. J. Suppl. Ser., 151, 35

Gibb, E. L., Whittet, D. C. B., Schutte, W. A., et al. 2000, Astrophys. J., 536, 347

Goesmann, F., Rosenbauer, H., Bredehöft, J. H., et al. 2015, Science, 349

Gottlieb, C. A. 1973, in Molecules in the Galactic Environment, 181

Gredel, R., Lepp, S., Dalgarno, A., & Herbst, E. 1989, Astrophys. J., 347, 289

Greenberg, J. M., Li, A., Mendoza-Gomez, C. X., et al. 1995, Astrophys. J. Lett., 455, L177

Henderson, B. L. & Gudipati, M. S. 2015, Astrophys. J., 800, 66

Henning, T. & Mutschke, H. 1997, Astron. Astrophys., 327, 743

Herbst. 2017, International Reviews in Physical Chemistry, 36, 287

Herbst, E. 1997, in IAU Symposium, Vol. 170, IAU Symposium, ed. W. B. Latter, S. J. E. Radford, P. R. Jewell, J. G. Mangum, & J. Bally, 71–78

Herbst, E. & Klemperer, W. 1973, Astrophys. J., 185, 505

Herbst, E. & van Dishoeck, E. F. 2009, Ann. Rev. Astron. Astrophys., 47, 427

Hidaka, H., Kouchi, A., & Watanabe, N. 2007, J. Chem. Phys., 126, 204707

Hidaka, H., Watanabe, M., Kouchi, A., & Watanabe, N. 2009, Astrophys. J., 702, 291

Hidaka, H., Watanabe, M., Kouchi, A., & Watanabe, N. 2011, Phys. Chem. Chem. Phys., 13, 15798

Hiraoka, K., Ohashi, N., Kihara, Y., et al. 1994, Chemical Physics Letters, 229, 408

Hollenberg, J. L. & Dows, D. A. 1961, J. Chem. Phys., 34, 1061

Hollis, J. M., Lovas, F. J., & Jewell, P. R. 2000, Astrophys. J. Lett., 540, L107

Hudgins, D. M., Sandford, S. A., Allamandola, L. J., & Tielens, A. G. G. M. 1993, Astrophys. J. Suppl. Ser., 86, 713

Ioppolo, S., Cuppen, H. M., Romanzin, C., van Dishoeck, E. F., & Linnartz, H. 2008, Astrophys. J., 686, 1474

Ioppolo, S., Fedoseev, G., Lamberts, T., Romanzin, C., & Linnartz, H. 2013, Review of Scientific Instruments, 84, 073112

Islam, F., Latimer, E. R., & Price, S. D. 2007, The Journal of chemical physics, 127, 064701

Jiménez-Serra, I., Vasyunin, A. I., Caselli, P., et al. 2016, Astrophys. J. Lett., 830, L6

Jørgensen, J. K., van der Wiel, M. H. D., Coutens, A., et al. 2016, Astron. Astrophys., 595, A117

Le Roy, L., Altwegg, K., Balsiger, H., et al. 2015, Astron. Astrophys., 583, A1

Ligterink, N. F. W., Paardekooper, D. M., Chuang, K.-J., et al. 2015, Astron. Astrophys., 584, A56

Linnartz, H., Ioppolo, S., & Fedoseev, G. 2015, International Reviews in Physical Chemistry, 34, 205

Maity, S., Kaiser, R. I., & Jones, B. M. 2015, Phys. Chem. Chem. Phys., 17, 3081

Marcelino, N., Cernicharo, J., Agúndez, M., et al. 2007, Astrophys. J. Lett., 665, L127

Martín-Doménech, R., Manzano-Santamaría, J., Muñoz Caro, G. M., et al. 2015, Astron. Astrophys., 584, A14

Meierhenrich, U. J. 2005, Angew. Chem. Int. Ed., 44, 5630

Mennella, V., Baratta, G. A., Esposito, A., Ferini, G., & Pendleton, Y. J. 2003, Astrophys. J., 587, 727

Millar, T. J., Bennett, A., & Herbst, E. 1989, Astrophys. J., 340, 906

Minissale, M., Moudens, A., Baouche, S., Chaabouni, H., & Dulieu, F. 2016, Mon. Not. R. Astron. Soc., 458, 2953

Miyauchi, N., Hidaka, H., Chigai, T., et al. 2008, Chemical Physics Letters, 456, 27

Modica, P. & Palumbo, M. E. 2010, Astron. Astrophys., 519, A22

Muñoz Caro, G. M., Jiménez-Escobar, A., Martín-Gago, J. Á., et al. 2010, Astron. Astrophys., 522, A108

Muñoz Caro, G. M., Meierhenrich, U. J., Schutte, W. A., et al. 2002, Nature, 416, 403

Nagaoka, A., Watanabe, N., & Kouchi, A. 2005, Astrophys. J. Lett., 624, L29

Nuevo, M., Auger, G., Blanot, D., & D'Hendecourt, L. 2008, Origins of Life and Evolution of the Biosphere, 38, 37

Öberg, K. I. 2016, Chemical Reviews, 116, 9631

Öberg, K. I., Boogert, A. C. A., Pontoppidan, K. M., et al. 2011a, Astrophys. J., 740, 109

Öberg, K. I., Bottinelli, S., Jørgensen, J. K., & van Dishoeck, E. F. 2010, Astrophys. J., 716, 825

Öberg, K. I., Fuchs, G. W., Awad, Z., et al. 2007, Astrophys. J. Lett., 662, L23

Öberg, K. I., Garrod, R. T., van Dishoeck, E. F., & Linnartz, H. 2009, Astron. Astrophys., 504, 891

Öberg, K. I., van der Marel, N., Kristensen, L. E., & van Dishoeck, E. F. 2011b, Astrophys. J., 740, 14

Paardekooper, D. M., Bossa, J.-B., & Linnartz, H. 2016a, Astron. Astrophys., 592, A67

Paardekooper, D. M., Fedoseev, G., Riedo, A., & Linnartz, H. 2016b, Astron. Astrophys., 596, A72

Pontoppidan, K. M. 2006, Astron. Astrophys., 453, L47

Pontoppidan, K. M., Boogert, A. C. A., Fraser, H. J., et al. 2008, Astrophys. J., 678, 1005

Pontoppidan, K. M., Fraser, H. J., Dartois, E., et al. 2003, Astron. Astrophys., 408, 981

Prasad, S. S. & Tarafdar, S. P. 1983, Astrophys. J., 267, 603

Ruaud, M., Wakelam, V., & Hersant, F. 2016, Mon. Not. R. Astron. Soc., 459, 3756

Rubin, R., Swenson Jr, G., Benson, R., Tigelaar, H., & Flygare, W. 1971, Astrophys. J., 169, L39

Schutte, W. A., Allamandola, L. J., & Sandford, S. A. 1993, Science, 259, 1143

Shen, C. J., Greenberg, J. M., Schutte, W. A., & van Dishoeck, E. F. 2004, Astron. Astrophys., 415, 203

Shu, F. H., Ruden, S. P., Lada, C. J., & Lizano, S. 1991, Astrophys. J. Lett., 370, L31

Solomon, P., Jefferts, K., Penzias, A., & Wilson, R. 1971, Astrophys. J., 168, L107

Taquet, V., Ceccarelli, C., & Kahane, C. 2012, Astron. Astrophys., 538, A42

Taquet, V., López-Sepulcre, A., Ceccarelli, C., et al. 2015, Astrophys. J., 804, 81

Terwisscha van Scheltinga, J., Ligterink, N. F. W., Boogert, A. C. A., van Dishoeck, E. F., & Linnartz, H. 2017, ArXiv e-prints

Tielens, A. G. G. M. & Allamandola, L. J. 1987, in Astrophysics and Space Science Library, Vol. 134, Interstellar Processes, ed. D. J. Hollenbach & H. A. Thronson, Jr., 397–469

Tielens, A. G. G. M. & Hagen, W. 1982, Astron. Astrophys., 114, 245

Tielens, A. G. G. M., Tokunaga, A. T., Geballe, T. R., & Baas, F. 1991, Astrophys. J., 381, 181

Tschersich, K. G. 2000, Journal of Applied Physics, 87, 2565

van Dishoeck, E. F. & Black, J. H. 1989, Astrophys. J., 340, 273

van Dishoeck, E. F. & Blake, G. A. 1998, Ann. Rev. Astron. Astrophys., 36, 317

Vastel, C., Ceccarelli, C., Lefloch, B., & Bachiller, R. 2014, Astrophys. J. Lett., 795, L2

Vasyunin, A. I. & Herbst, E. 2013a, Astrophys. J., 762, 86

Vasyunin, A. I. & Herbst, E. 2013b, Astrophys. J., 769, 34

Vidali, G. 2013, Chemical reviews, 113, 8762

Wakelam, V., Bron, E., Cazaux, S., et al. 2017, Molecular Astrophysics, 9, 1

Wakelam, V., Smith, I. W. M., Herbst, E., et al. 2010, Space Science Reviews, 156, 13

Walsh, C., Herbst, E., Nomura, H., Millar, T. J., & Weaver, S. W. 2014a, Faraday Discussions, 168, 389

Walsh, C., Millar, T. J., Nomura, H., et al. 2014b, Astron. Astrophys., 563, A33

Watanabe, N. & Kouchi, A. 2002, Astrophys. J. Lett., 571, L173

Watanabe, N., Mouri, O., Nagaoka, A., et al. 2007, Astrophys. J., 668, 1001

Westley, M. S., Baratta, G. A., & Baragiola, R. A. 1998, J. Chem. Phys., 108, 3321

Whittet, D. C. B., Bode, M. F., Longmore, A. J., et al. 1988, Mon. Not. R. Astron. Soc., 233, 321

Whittet, D. C. B., Schutte, W. A., Tielens, A. G. G. M., et al. 1996, Astron. Astrophys., 315, L357

Woods, P. M., Slater, B., Raza, Z., et al. 2013, Astrophys. J., 777, 90

Wootten, A. 1987, in IAU Symposium, Vol. 120, Astrochemistry, ed. M. S. Vardya & S. P. Tarafdar, 311–318

Zhitnikov, R. A. & Dmitriev, Y. A. 2002, Astron. Astrophys., 386, 1129

2

H-ATOM ADDITION AND ABSTRACTION REACTIONS IN MIXED CO, H_2CO AND CH_3OH ICES —AN EXTENDED VIEW ON COMPLEX ORGANIC MOLECULE FORMATION

Complex organic molecules (COMs) have been observed not only in the hot cores surrounding low- and high-mass protostars, but also in cold dark clouds. Therefore, it is interesting to understand how such species can be formed without the presence of embedded energy sources. We present new laboratory experiments on the low-temperature solid state formation of three complex molecules —methyl formate ($HC(O)OCH_3$), glycolaldehyde ($HC(O)CH_2OH$) and ethylene glycol ($H_2C(OH)CH_2OH$)— through recombination of free radicals formed via H-atom addition and abstraction reactions at different stages in the CO-H_2CO-CH_3OH hydrogenation network at 15 K. The experiments extend previous CO hydrogenation studies and aim at resembling the physical—chemical conditions typical of the CO freeze-out stage in dark molecular clouds, when H_2CO and CH_3OH form by recombination of accreting CO molecules and H-atoms on ice grains. We confirm that H_2CO, once formed through CO hydrogenation, not only yields CH_3OH through ongoing H-atom addition reactions, but is also subject to H-atom-induced abstraction reactions, yielding CO again. In a similar way, H_2CO is also formed in abstraction reactions involving CH_3OH. The dominant methanol H-atom abstraction product is expected to be CH_2OH, while H-atom additions to H_2CO should at least partially proceed through CH_3O intermediate radicals. The occurrence of H-atom abstraction reactions in ice mantles leads to more reactive intermediates (HCO, CH_3O and CH_2OH) than previously thought, when assuming sequential H-atom addition reactions only. This enhances the probability to form COMs through radical-radical recombination without the need of UV photolysis or cosmic rays as external triggers.

2.1   INTRODUCTION

CO is the second most abundant molecule in the interstellar medium (ISM) after H$_2$ (Ohishi et al. 1992). It is formed in the gas phase and despite its high volatility, carbon monoxide accretes on the surfaces of grains in the dense and cold parts of molecular clouds. After water, CO is the second most abundant component of interstellar ices (Pontoppidan 2006). Observational data show that rather than mixing with H$_2$O, the bulk of the CO accretes on top of a previously formed H$_2$O-rich polar ice, forming an apolar CO-rich ice layer (Tielens et al. 1991; Öberg et al. 2009, 2011b; Boogert & Ehrenfreund 2004; Gibb et al. 2004; Mathews et al. 2013; Boogert et al. 2015). The resulting CO-coating, in turn, is thought to react with impacting H-atoms, producing H$_2$CO via the HCO intermediate radical and subsequently CH$_3$OH through CH$_3$O or, possibly, CH$_2$OH radical intermediates. This surface formation route is generally considered to be the chemical pathway explaining the observed abundance of methanol in dense clouds, both in the solid state and in the gas phase. The process has been subject of numerous experimental (Hiraoka et al. 1994; Zhitnikov & Dmitriev 2002; Watanabe & Kouchi 2002; Fuchs et al. 2009), theoretical and modelling (Tielens & Hagen 1982; Shalabiea & Greenberg 1994; Cuppen et al. 2009; Vasyunin & Herbst 2013) studies. For a recent review, see also Linnartz et al. (2015). Moreover, combined laboratory and observational data show that CO and CH$_3$OH are intimately mixed in interstellar ices. This is fully consistent with a common chemical history (Cuppen et al. 2011).

Solid methanol, in turn, has been proposed as a starting point for the formation of complex organic molecules (COMs). Experiments involving energetic processing, e.g., UV photolysis (Öberg et al. 2009; Henderson & Gudipati 2015), soft X-ray irradiation (Chen et al. 2013), high-energy electron (Bennett et al. 2007; Maity et al. 2015) and ion (Moore et al. 1996; de Barros et al. 2011) bombardment, and low-energy electron radiolysis (Boamah et al. 2014) of solid methanol ice, show that COMs form upon recombination of dissociation products. This is in line with a number of astronomical observations (for recent reviews see Herbst & van Dishoeck 2009; Caselli & Ceccarelli 2012). However, these experiments do not explain the recent detection of COMs in dark clouds where icy grains are not exposed to strong UV fields or have been heated. In particular, methyl formate, acetaldehyde, dimethyl ether and ketene have been detected in the cold pre-stellar core L1689B (Bacmann et al. 2012). The same species have also been seen in the cold pre-stellar core B1-b (Cernicharo et al. 2012), in the cold outer envelopes of low-mass protostars (Öberg et al. 2010), and in outflow spots in dark clouds where the ice mantles are liberated by shocks (Arce et al. 2008; Öberg et al. 2011a). Acetaldehyde and ketene were also detected in the cold pre-stellar core L1544 (Vastel et al. 2014). These observations clearly hint for a scenario in which COMs also form at temperatures below 15 K. Recent work by Fedoseev et al. (2015) demonstrated non-energetic routes to form COMs by surface hydrogenation of CO molecules.

An efficient pathway, creating a C-C backbone without the involvement of energetic processing, has the potential to form COMs earlier than expected during the chemical evolution of interstellar clouds and moreover will increase the chemical diversity. The solid state formation of various two- or even three-carbon bearing species was already suggested in a number of astrochemical models. Charnley et al. (2001) and Charnley & Rodgers (2005) studied C-atom addition reactions to HCO and HCCO radicals, whereas Garrod et al. (2008) and Woods et al. (2012) worked on a backbone extension through recombination of various carbon-bearing intermediates, such as CH$_3$, HOCO and the CO hydrogenation intermediates; HCO, CH$_3$O and CH$_2$OH. Some of these reactions were already proposed quite some time ago, i.e., by Agarwal et al. (1985) and Schutte (1988), to explain results obtained after energetic processing of ices. Up to now, however, experimental studies verifying the formation of COMs along

non-energetic pathways have been largely lacking, with exception of the above mentioned study by Fedoseev et al. (2015) who showed that glycolaldehyde (HC(O)CH$_2$OH) and ethylene glycol (H$_2$C(OH)CH$_2$OH) form at low temperatures in CO + H deposition experiments. In their study, Fedoseev and co-workers combined molecule specific desorption temperatures and ionization fragmentation patterns for the newly formed species to conclude that recombination of HCO radicals yields glyoxal (HC(O)CHO) that is subsequently converted to glycolaldehyde and ethylene glycol upon two or four consecutive H-atom additions, respectively. They also suggested a possible formation route of methyl formate (HC(O)OCH$_3$) through recombination of HCO and CH$_3$O radicals, but it was not possible to experimentally confirm this.

The concept of non-energetic H-atom abstraction reactions is not new. Tielens & Hagen (1982) presented modelling calculations that emphasized the importance of H-atom abstraction reactions in grain-surface hydrogenation sequences. Experimental work by Nagaoka et al. (2005) investigated the exposure of methanol ice to D-atoms. They found that partially deuterated methanol (CH$_2$DOH, CHD$_2$OH and CD$_3$OH) is quickly formed upon D-atom exposure of solid CH$_3$OH at 10 K. Following results from ab initio calculations, the authors proposed that one of the possible H-D substitution pathways takes place via H-atom abstraction from the methyl side of methanol to form the hydroxymethyl radical (CH$_2$OH), after which D-atom addition forms CH$_2$DOH. Subsequently, Hidaka et al. (2009) proposed H-D substitution in H$_2$CO to also originate from an H-atom abstraction yielding HCO followed by D-atom addition to form HDCO. In both studies, the existence of abstraction reactions is crucial to explain the formation of deuterated molecules. Similar H-atom abstraction reactions may be triggered by H-atoms as well, i.e., instead of D-atoms, which would effectively increase the total amount of HCO, CH$_3$O and CH$_2$OH radicals formed in the ice, increasing the probability that recombination reactions result in COM formation.

The aim of this study is to verify the formation of COMs through H$_2$CO+H and CH$_3$OH+H, extending on Fedoseev et al. (2015) by focusing on the influence of H-atom induced abstraction reactions along with H-atom addition events. We experimentally investigate hydrogenation of pure ice samples (H$_2$CO or CH$_3$OH) as well as ice mixtures (H$_2$CO+CO, CH$_3$OH+CO, or H$_2$CO+CH$_3$OH). Both the existence of abstraction reactions involving H$_2$CO and CH$_3$OH and the possible formation of COMs are discussed. Special care is taken to verify that the COMs are products formed during codeposition, and not the result of thermally induced chemistry upon heating or due to contaminations.

2.2 EXPERIMENTAL PROCEDURE

2.2.1 *Description of the setup*

All experiments are performed under ultra-high vacuum (UHV) conditions, using the SURFRESIDE[2] setup that has been described in detail by Ioppolo et al. (2013). This setup consists of three distinct UHV chambers: a main chamber with base pressure of $\sim$10^{-10} mbar and two beam line chambers with base pressures in the range of 10^{-9}-10^{-10} mbar. These chambers are separated by shutters, allowing independent operation of the individual parts. In the main chamber, a rotatable gold-coated copper substrate is mounted on the tip of a cold head of a closed-cycle helium cryostat. Accessible temperatures range from 13 to 300 K and ice samples are deposited on the substrate with monolayer precision (where 1 ML is assumed to be $\sim$1$\times$ 10^{15} molecules cm^{-2}). The absolute temperature is accurate to better than 2 K, while the relative precision is better than 0.5 K.

The beam line chambers comprise different atom sources: a Hydrogen Atom Beam Source (HABS, Dr. Eberl MBE-Komponenten GmbH; see Tschersich 2000) generating H- or D-atoms by thermal cracking H$_2$ and D$_2$, and a Microwave Atom Source (MWAS, Oxford Scientific Ltd; see Anton et al. 2000) capable of producing H-, D-, O-, or N-atoms as well as various radicals by cracking selected parent molecules in a capacitively coupled microwave discharge (275 W at 2.45 GHz). Here only the MWAS is used, as the HABS chamber may contain CO contaminations when operated at high temperatures of the tungsten filament. Typical atom fluxes amount to roughly 6×10^{14} atoms cm^{-2} min^{-1}. Along the path of both beam lines, a nose-shape quartz pipe is placed behind the shutter to efficiently quench excited atoms and non-dissociated molecules through collisions with the wall of the pipe. In addition, two separate dosing lines in the main chamber are used for deposition of molecular components of the ice, i.e., CO, H$_2$CO and CH$_3$OH. The individual gas samples are prepared by introducing single gases into a distinct well prepumped ($<1\times10^{-4}$ mbar) full-metal reservoir. By means of a high-precision full-metal leak valve gas vapours are introduced into the UHV chamber with normal and $68°$ incidence angles to the sample. Degassed liquid CH$_3$OH (Sigma- Aldrich 99.9 per cent) is used to obtain CH$_3$OH vapour and solid paraformaldehyde powder (Sigma-Aldrich 95 per cent) warmed to $60-80°$ under vacuum to generate H$_2$CO vapours. Residuals are typically shorter oligomers of formaldehyde and water. A CO gas cylinder (Linde 2.0, residuals: ^{13}CO, N$_2$ and CO$_2$) is used for the preparation of carbon monoxide containing ice samples.

The ice diagnostics are performed by using either Fourier transform infrared absorption spectroscopy (FT-RAIRS) or temperature-programmed desorption quadrupole mass spectrometry (TPD QMS). The first method allows in situ studies of species embedded, formed or consumed in the ice, but has limited sensitivity and selectivity. The FT-RAIRS covers the range between 4000 and 700 cm^{-1} with a spectral resolution of 1 cm^{-1}. A modified Lambert-Beer's law is used to derive number densities of CO and H$_2$CO on the substrate using absorbance strength as described in Ioppolo et al. (2013). The absorbance strength values of CO, CH$_3$OH and H$_2$CO are obtained from transmission absorbance strength values as described by Watanabe et al. (2004). After completion of a codeposition and RAIRS experiment, a TPD QMS experiment is performed with a typical rate of 5 K/min to monitor thermally desorbing ice species. The TPD QMS is a more sensitive technique and combines known desorption temperatures with dissociative ionization fragmentation patterns upon electron impact in the head of the QMS. This makes it a strong diagnostic tool to recognize newly formed species, but obviously this technique comes with the thermal processing and ultimately destruction of the ice. See also Ioppolo et al. (2014) and Linnartz et al. (2015) for further technical details.

2.2.2   *Experimental methods*

Three distinct sets of experiments are performed and systematically listed in Table 2.1. Each of them addresses a specific goal.

1) Verification of CO and H$_2$CO formation by H-atom abstraction from H$_2$CO and CH$_3$OH, respectively; exps 1.1-1.11. H-atom-induced abstraction reactions from H$_2$CO and CH$_3$OH yielding CO and H$_2$CO, respectively, are verified by codepositing pure H$_2$CO or CH$_3$OH samples and H-atoms for different settings. The applied codeposition technique has the advantage that penetration depth issues into the bulk of the ice can be circumvented, as two or more species can be deposited simultaneously rather than sequentially. The latter has been a problem in previous pre-deposition experiments (Watanabe et al. 2003; Fuchs et al. 2009) in which only the top few layers were involved in H-atom-induced reactions. In a codeposi-

Table 2.1: Overview of the performed experiments.

Hydrogenation of pure H_2CO and CH_3OH

No.	Experiment	T_{sample} (K)	Ratio	$Flux_{Molecule}$ ($cm^{-2}\ min^{-1}$)	$Flux_H$ ($cm^{-2}\ min^{-1}$)	Time (min)
1.1	H_2CO+H	15	1:30	2×10^{13}	6×10^{14}	360
1.2	H_2CO	15	-	2×10^{13}	-	360
1.3	H	15	-	-	6×10^{14}	360
1.4	no deposition	15	-	-	-	360
1.5	CH_3OH+H	15	1:30	2×10^{13}	6×10^{14}	360
1.6	CH_3OH	15	-	2×10^{13}		360
1.7	$^{13}CH_3OH+H$	15	1:20	3×10^{13}	6×10^{14}	360
1.8	$^{13}CH_3OH$	15	-	3×10^{13}		360
1.9	H_2CO+H	25	1:30	2×10^{13}	6×10^{14}	360
1.1	H_2CO+H	50	1:30	2×10^{13}	6×10^{14}	360
1.11	H_2CO+H	15	1:30	2×10^{13}	6×10^{14}	850

Hydrogenation of CO, H_2CO, CH_3OH mixtures

No.	Experiment	T_{sample} (K)	Ratio	$Flux_{Molecule(1)}$ ($cm^{-2}\ min^{-1}$)	$Flux_{Molecule(2)}$ ($cm^{-2}\ min^{-1}$)	$Flux_H$ ($cm^{-2}\ min^{-1}$)	Time (min)	MF	GA	EG
									Relative abundance	
2.1	$CO+H_2CO+H$	15	1:1:30	2×10^{13}	2×10^{13}	6×10^{14}	360	0.46	0.15	0.49[a]
2.2	$CO+H_2CO$	15	1:1	2×10^{13}	2×10^{13}	-	360	-	-	-
2.3	$CO+CH_3OH+H$	15	1:1:30	2×10^{13}	2×10^{13}	6×10^{14}	360	0	0.14	0.00[a]
2.4	$CO+CH_3OH$	15	1:1	2×10^{13}	2×10^{13}	-	360	-	-	-
2.5	H_2CO+CH_3OH+H	15	1:1:30	2×10^{13}	2×10^{13}	6×10^{14}	360	0.56	0.2	0.13[a]
2.6	H_2CO+CH_3OH	15	1:1	2×10^{13}	2×10^{13}	-	360	-	-	-
2.7	H_2CO+H	15	1:15	4×10^{13}	-	6×10^{14}	360	1	1	1.00[a]
2.8	$CO+H$	15	1:15	4×10^{13}	-	6×10^{14}	360	0	0.33	0.30[a]

Control experiments

No.	Experiment	T_{sample} (K)	Ratio	$Flux_{H_2CO}$ ($cm^{-2}\ min^{-1}$)	$Flux_{CH_3OH}$ ($cm^{-2}\ min^{-1}$)	Time (min)
3.1	H_2CO+CH_3OH	15	1:3.5	17×10^{13}	59×10^{13}	50
3.2	H_2CO+CH_3OH	15	1:0.3	16×10^{13}	4×10^{13}	50
3.3	H_2CO+CH_3OH	15	1:0.1	16×10^{13}	2×10^{13}	50

Note. All of the relative abundances are based on values in Figure 2.7

MF=HC(O)OCH$_3$, GA=HC(O)CH$_2$OH, and EG=H$_2$C(OH)CH$_2$OH

[a] These values are obtained after subtraction of the control experiment accounting for the influence

of thermal processing of the ice and contaminations (i.e., red columns in the upper panel of Figure 2.7

tion experiment, gas mixing ratios are easily varied and the consequent use of a high enough abundance of H-atoms compared to the molecules of interest guarantees that they all become available for encounters with H-atoms. Moreover, the formed products are trapped in the growing ice lattice and this prevents them from further interactions with H-atoms. Furthermore, codeposition mimics the actual processes taking place on an interstellar grain in space when the outer layer starts accreting CO molecules together with impacting H-atoms (Cuppen et al. 2009). The newly formed species are monitored *in situ* for the full time of a 360 min codeposition experiment by means of RAIRS. After completion of the codeposition, a TPD QMS experiment is performed. Control experiments comprise pure H$_2$CO and CH$_3$OH depositions without H-atoms (exps 1.2 and 1.6), H-atom deposition without H$_2$CO or CH$_3$OH molecules (exp. 1.3), and a blank experiment without any deposition (exp. 1.4). The formation of H$_2$CO in CH$_3$OH+H is further verified using ^{13}C-labelled methanol.

2) Verification of COM formation via radical-radical interactions in the aforementioned system; exps 2.1-2.8. The hydrogenation experiments described in the previous section are further extended by performing codeposition experiments of binary ice mixtures, H$_2$CO+CO, CH$_3$OH+CO and H$_2$CO+CH$_3$OH with H-atoms. In the next section, it is shown that, for these experiments, COMs can be detected, specifically methyl formate (HC(O)OCH$_3$), glycolaldehyde (HC(O)CH$_2$OH) and ethylene glycol (H$_2$C(OH)CH$_2$OH). TPD QMS is used as the main diagnostic tool to detect these COMs because of (significant) spectral overlap of the stronger vibrational modes with H$_2$CO and CH$_3$OH infrared absorption features (Öberg et al. 2009).

3) The final set of TPD QMS experiments (exps 3.1-3.3) is specifically designed to rule out the possibility that any COMs are found due to contaminations in the depositing gas samples or as a result of thermally induced reactions during TPD. For this purpose, a series of depositions with mixed H$_2$CO:CH$_3$OH ices is followed by a regular TPD QMS experiment without any H atoms impacting. In these control experiments, the used H$_2$CO:CH$_3$OH ratios are chosen to cover the entire range of values as obtained in the hydrogenation experiments after 6 h of codeposition. This allows for a systematic comparison between the TPD QMS peak intensities of HC(O)OCH$_3$, HC(O)CH$_2$OH and H$_2$C(OH)CH$_2$OH found in the hydrogenation experiments and the corresponding results from the control experiments.

2.3   RESULTS

2.3.1   *CO formation upon codeposition of H and H$_2$CO*

In Figure 2.1, RAIRS data (exps 1.1 and 1.2) for a 15 K codeposition experiment of H$_2$CO+H (upper spectrum) and only H$_2$CO (lower spectrum), i.e., without hydrogenation, are presented. The spectral signatures of the originally deposited H$_2$CO are found around 1727 cm^{-1} as well as at 1499 and 1253 cm^{-1}; an H$_2$CO band around 1178 cm^{-1} is harder to discriminate. In the H-atom addition experiment, new peaks at 1031 and 1423 cm^{-1} can be assigned to the C-O stretching and O-H bending vibrational modes of CH$_3$OH, respectively (Falk & Whalley 1961). A clearly visible peak at 2138 cm^{-1} is due to the stretching mode of CO. The formation of CH$_3$OH is consistent with previous studies of successive hydrogenation of CO and H$_2$CO (Hiraoka et al. 1994; Watanabe & Kouchi 2002; Hidaka et al. 2004; Fuchs et al. 2009). The simultaneous appearance of the 2138 cm^{-1} band indicates that along with the H-atom addition reactions to formaldehyde, resulting in the formation of CH$_3$OH, also a sequence of two H-atom abstraction reactions takes place, yielding CO. Spectral features of the intermediate radicals, i.e., HCO and CH$_3$O/CH$_2$OH are not observed, consistent with previous studies concluding that their abundance is low. This is due to the higher reactivity of these
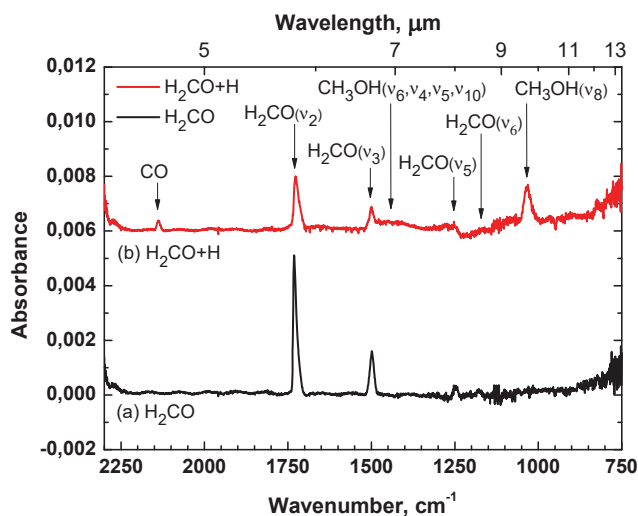
Figure 2.1: RAIR spectra obtained after 360 min (co)deposition at 15 K of (a) H_2CO and (b) H_2CO with H-atoms in a ratio H_2CO:H = 1:30 and an H-atom flux of 6×10^{14} atoms cm^{-2} min^{-1}.

intermediates to H-atoms via barrierless reactions compared to the stable species that have to bypass activation barriers (Watanabe & Kouchi 2002; Fuchs et al. 2009).

The main experimental finding here is that interaction of H-atoms with H_2CO molecules at 15 K not only leads to the formation of methanol but also of carbon monoxide. This is in agreement with the experimental findings of Hidaka et al. (2004).

2.3.2 H_2CO formation upon codeposition of H and CH_3OH

The results of a CH_3OH+H 15 K codeposition experiment as well as reference data obtained for a pure CH_3OH deposition (exps 1.5 and 1.6) are shown in Figure 2.2. In the left-hand panel, the wavelength domain that covers the strongest (RAIR) absorption band of H_2CO, i.e., its C-O stretching vibration mode, is shown (see also Figure 2.1); neither this band nor any other H_2CO features can be found. The left shoulder of a broad band around 1652 cm^{-1} could be due to the C-O stretching mode of formaldehyde, but given the absence of the other H_2CO bands the full absorption feature is more likely due to polluting H_2O that results from con-tamination in the H-atom beam. A similar band is also present in Figure 2.1, but hard to see given the less accurate intensity scale used there.

More sensitive TPD QMS data are presented in the right-hand panel of Figure 2.2, which confirm H_2CO formation. The two strongest m/z signals of H_2CO, i.e., HCO^+ (29 amu) and H_2CO^+ (30 amu) exhibit both a peak centred at 95 K. This desorption temperature as well as the m/z = 30 to m/z = 29 ratio of 0.6 are consistent with literature data (Fuchs et al. 2009, NIST database[2.1]).

[2.1] NIST Mass Spec Data Center, S.E. Stein, director, 'Mass Spectra' in NIST Chemistry WebBook, NIST Standard Reference Database Number 69, Eds. P.J. Linstrom and W.G. Mallard, National Institute of Standards and Technology, Gaithersburg MD, 20899, http://webbook.nist.gov.
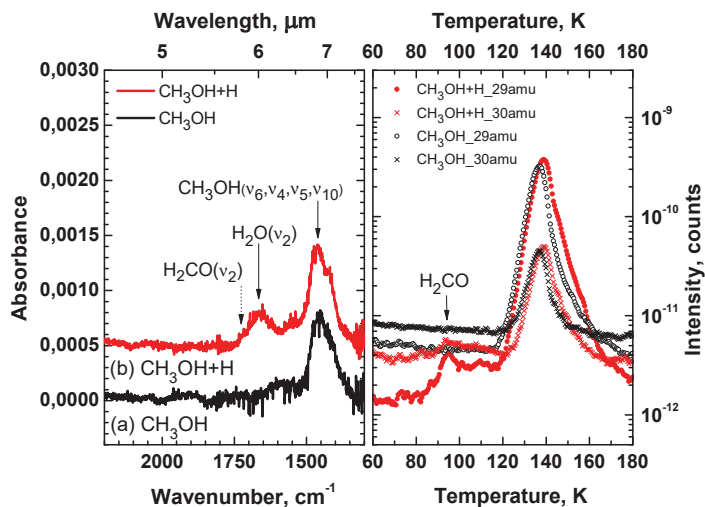
Figure 2.2: The left-hand panel shows RAIR spectra of 360 min (co)deposition at 15 K of (a) CH_3OH and (b) CH_3OH with H-atoms in a ratio $CH_3OH:H = 1:30$ and an H-atom flux of 6×10^{14} atoms cm^{-2} min^{-1}. The shown wavelength domain corresponds to the region where the strongest absorption features of H_2CO should be visible. The right-hand panel presents parts of the TPD QMS spectra obtained after these two experiments for m/z = 29 and 30 amu. Peaks at T~95 and 140 K correspond to formaldehyde and methanol desorption, respectively.

To further constrain H_2CO formation from $H+CH_3OH$, the experiment is repeated for ^{13}C-labelled methanol (not shown in Figure 2.2). The TPD QMS shows the same peak at 95 K, but this time the maximum has an m/z value of 30 (as opposed to 29 for the regular ^{12}C isotope of H_2CO) and again a ratio of m/z = 31 to m/z = 30 of 0.6 is found. This is fully consistent with the conclusion that the species desorbing at 95 K can be assigned to formaldehyde and that it forms through hydrogen abstraction from CH_3OH. This means that the network derived by Hidaka et al. (2009) can be further extended to include a two-step dehydrogenation process transferring CH_3OH into H_2CO. Also here, the intermediate CH_2OH radical is not observed because of its high reactivity.

2.3.3   *Formation of COMs: methyl formate, glycolaldehyde and ethylene glycol*

In Figure 2.3, the TPD QMS spectra (exps 1.1 and 1.2) are presented for a temperature range from 15 to 225 K taken after 360 min of H_2CO+H codeposition and H_2CO deposition at 15 K, respectively. In addition to the desorption peaks from the originally deposited H_2CO, its hydrogenation product CH_3OH and its abstraction product CO (not shown), there are three more desorption peaks showing up. The TPD QMS spectra provide two ways to identify the desorbing species; via their desorption temperature and via their dissociative ionization fragmentation pattern upon electron impact in the head of the QMS. The first sublimation peak is centred at 120 K, the centre of the second one is located around 160 K, and the last one is around 200 K. Based on available data reported by Öberg et al. (2009) and recent work by Fedoseev et al. (2015), the aforementioned three desorption temperatures can be attributed to methyl formate, glycolaldehyde, and ethylene glycol, respectively.
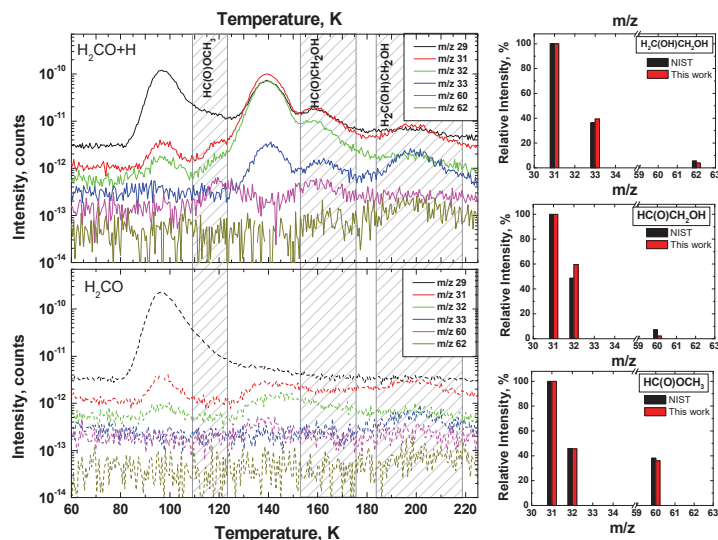
Figure 2.3: Left: the TPD mass spectra obtained after deposition of H_2CO (lower panel) and equal amounts of H_2CO and H-atoms (upper panel). The codepositions are performed at 15 K for 360 min, using a mixture of H_2CO:H = 1:30 and an H-atom flux equal to 6×10^{14} atoms cm^{-2} min^{-1}. Only relevant m/z numbers are shown. Right: comparison of the fragmentation patterns of the detected desorbing COMs with available literature values.

The assignments are further supported by the fragmentation patterns that are largely in agreement with the 70 eV patterns as available from the NIST database (see footnote 2.1). Relatively small inconsistencies in these patterns are likely due to the thermal codesorption of trapped H_2CO or CH_3OH with the aforementioned COMs, which have the same m/z values for some of the dissociative ionization fragments.

As mentioned before, these COMs could not be detected unambiguously by means of RAIRS, because there exists considerable overlap between the strongest IR absorption features of methyl formate, glycolaldehyde, and ethylene glycol with those of H_2CO and CH_3OH that have higher abundances in the ice. Furthermore, an attempt to detect these COMs through the molecule specific but weaker C-C stretching mode of glycolaldehyde and ethylene glycol or the O-CH_3 stretching mode of methyl formate were unsuccessful due to the low final yield of these species. Nevertheless, important information can be derived from spectroscopic data. Figure 2.4 presents RAIR spectra obtained at 15 K after 850 min of H_2CO hydrogenation with excess of atomic hydrogen in a H_2CO:H = 1:30 ratio and compared with the results from an experiment in which H_2CO and CH_3OH are deposited in a 1:1 ratio (exps 1.11 and 2.6). The two left-hand panels show zoom-ins of wavelength domains that cover the strongest absorption features of HCO and CH_2OH. The two right-hand panels coincide with the strongest absorption features of glycolaldehyde. Moreover, a RAIR spectrum obtained after 1 ML deposition of pure glycolaldehyde, as reported by Öberg et al. (2009), is included for a direct comparison. From this, it becomes clear that while the strongest absorption features of HCO and CH_2OH cannot be seen (left-hand panel), those of $HC(O)CH_2OH$ can be observed in the ice, despite substantial overlap with H_2CO and CH_3OH features. For example, the ~1748 cm^{-1} peak of glycolaldehyde is positively identified in the left shoulder of the $H_2CO_{(\nu2)}$ band obtained

after codeposition of H_2CO with H-atoms, since this absorption band is not present in the spectra of pure $H_2CO:CH_3OH$ ice mixtures. Similarly, no contradiction is found with the possible presence of the $\sim 1112\ cm^{-1}$ absorbance feature of $HC(O)CH_2OH$ on the spectrum obtained in the H_2CO+H experiment. This provides a strong argument that glycolaldehyde is formed already at 15 K among other products in a H_2CO+H codeposition experiment, and that detection of COMs during the TPD by means of the QMS is not the result of recombination of radicals trapped in the lattice of the ice at higher temperatures.

Furthermore, repeating the H_2CO codeposition with H-atoms at higher temperatures, i.e., at 25 and 50 K, does not result in COM detections. This is not surprising since the H-atom lifetime on the surface drops significantly at higher temperatures, which results in a drastic decrease of reactivity of H_2CO with H-atoms at 25 K and a complete inhibition at 50 K. A similar decrease of reaction rates with temperature was observed by Fuchs et al. (2009) and Hidaka et al. (2007) upon CO hydrogenation.

2.3.4   *Establishing the types of involved intermediate radicals*

In an attempt to reveal in more detail the reaction mechanisms responsible for the formation of methyl formate, glycolaldehyde and ethylene glycol, several additional experiments are performed. Since different kinds of intermediate radicals are formed upon H-atom exposure of CO and CH_3OH, i.e., HCO and possibly CH_2OH (Nagaoka et al. 2007), two-component binary mixtures of CO with H_2CO, CO with CH_3OH, and H_2CO with CH_3OH are codeposited with H-atoms at 15 K (exps 2.1, 2.3 and 2.5). Subsequently, relative COM abundances are examined in each of the experiments (see Table 2.1). To facilitate direct comparisons among these experiments, a 1:1 ratio is used for the molecular constituents, while the total applied ratio, including H-atoms, amounts to 1:1:30 to guarantee that (de)hydrogenation effects will be clearly visible.

The formation of all three COMs is observed in each of the experiments with the exception of $CO+CH_3OH+H$, where methyl formate cannot be detected. Figure 1.5 shows the comparison between the H_2CO+H and $CO+CH_3OH+H$ experiments for selected TPD QMS spectra and the relevant *m/z* values. In the H_2CO+H codeposition (left-hand panel), a desorption peak centred around 120 K is clearly seen and assigned to $HC(O)OCH_3$ according to the QMS fragmentation shown in Figure 2.3. However, in the $CO+CH_3OH+H$ ice mixture experiment (right-hand panel), there are no mass signals that can be assigned to methyl formate. This is an important finding which shows that only the abundant presence of H_2CO in the sample produces $HC(O)OCH_3$ molecules. Although some amount of H_2CO can be formed in the $CO+CH_3OH+H$ experiment by hydrogenation of CO molecules and by dehydrogenation of CH_3OH (see signal 29 *m/z* at ~ 96 K in Figure 2.5), this is not effective enough for our experimental settings to be transformed to a detectable amount of $HC(O)OCH_3$.

2.3.5   *Control experiments*

H_2CO is sensitive to its ice surrounding, and is chemically active upon thermal processing, when embedded in an H_2O, CH_3OH, and/or NH_3 environment (Schutte et al. 1993; Duvernay et al. 2014). Also, despite cleaning procedures, low-level pollutions may be involved that influence final outcomes. Therefore, in order to exclude any artefacts, three control experiments (exps 3.1-3.3) involving the deposition of different $H_2CO:CH_3OH$ ice mixtures (CH_3OH/H_2CO ratio = 0.1, 0.3 and 3.5) are performed and TPD QMS spectra are acquired. In Figure 2.6, the normalized integrated QMS signals are shown for each of the three COMs
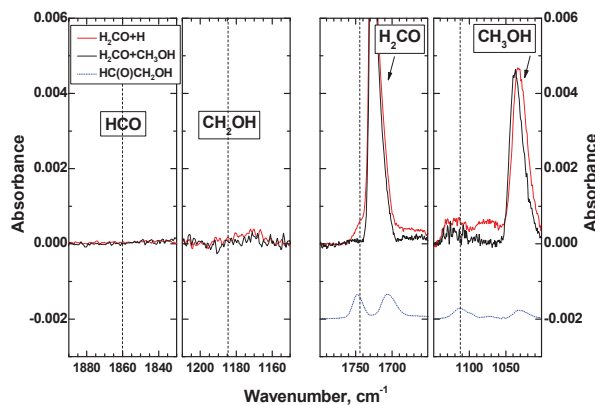
Figure 2.4: RAIR spectra obtained after codeposition of H_2CO and H-atoms for 850 min at 15 K using a ratio $H_2CO:H$ = 1:30 (exp. 1.11) and codeposition of H_2CO with CH_3OH using a 1:1 ratio (exp. 2.6). The two left-hand panels show the regions of the spectra where the most intense absorption features of HCO and CH_2OH are expected. The two right-hand panels show the spectral regions where the strongest absorption features from $HC(O)CH_2OH$ are present, scaled for the amount of H_2CO and CH_3OH, respectively. A spectrum of pure $HC(O)CH_2OH$ (blue) is presented for comparison.
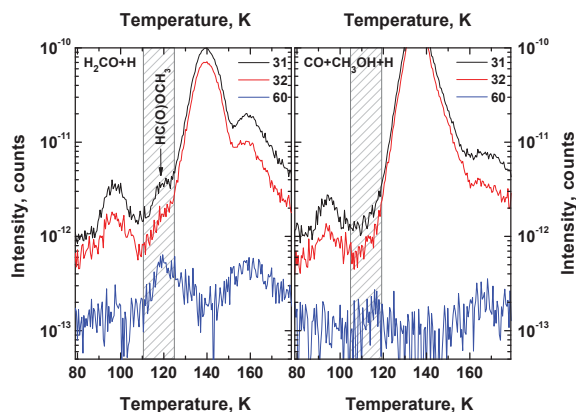
Figure 2.5: Left: the TPD QMS spectrum obtained after codeposition of H_2CO with H-atoms at 15 K for 360 min with $H_2CO:H$ = 1:30. Right: TPD QMS spectrum obtained after codeposition of CO, CH_3OH and H-atoms with $CO:CH_3OH:H$ = 1:1:30 for the same experimental conditions. The H-atom flux in both experiments is equal to 6×10^{14} atoms cm^{-2} min^{-1}. Only selected *m/z* values from the desorbing species are indicated. The desorption peak centred around 120 K and assigned to $HC(O)OCH_3$ is visible in the left-hand panel, while it is absent among the products of the experiment shown in the right-hand panel. The 140 and 160 K peaks are due to methanol and glycolaldehyde, respectively.

found here and for each of the used mixing rates. In the same figure, also the COM intensities are plotted as obtained in our hydrogenation experiments versus the final H_2CO and CH_3OH abundance ratio obtained after 6 h of codeposition. It should be noted that the ethylene glycol, glycolaldehyde and methyl formate abundances presented in Figure 2.6 are normalized with respect to the total amount of H_2CO and CH_3OH observed by RAIRS at the end of a codeposition experiment but before starting a TPD QMS experiment. The error bars represent instrumental errors and do not account for uncertainties resulting from the baseline subtraction procedure. The CO abundance is not taken into account here due to the expected chemical inertness of this species during thermal processing.

The comparison between hydrogenation and control experiments indicates that COMs are formed in the ice and cold surface H-atom addition and abstraction reactions are required to explain the observed COM abundances because the relative intensity of the newly formed COMs generally exceeds the one from the control experiments. However, there are some observations that need to be pointed out. For instance, in the case of $H_2C(OH)CH_2OH$ (top panel of Figure 2.6), some $H_2C(OH)CH_2OH$ is present in the control experiments and a clear growing trend with increasing CH_3OH is observed and fitted with a polynomial function. This can be explained by either the presence of ethylene glycol as a contamination in the CH_3OH sample or by thermally induced chemistry involving CH_3OH molecules. However, the intensity of the observed $H_2C(OH)CH_2OH$ produced by hydrogenation is significantly higher than that found in the control experiments for all hydrogenated ice mixtures except that with the highest CH_3OH abundance (exp. 2.3). For both $HC(O)CH_2OH$ and $HC(O)OCH_3$ molecules (middle and bottom panels of Figure 2.6), the observed intensities in the hydrogenation experiments cannot be reproduced in the control experiments, with the exception of the CO+CH_3OH+H and CO+H co-deposition experiments (exps 2.3 and 2.8), where the abundance of $HC(O)OCH_3$ is lower than the value obtained in the control experiments at the corresponding CH_3OH/H_2CO ratio.

To further understand the relative abundance of the produced COMs in all the performed experiments, the final COM abundances obtained after each experiment is normalized to the total amount of deposited carbon-bearing species, i.e., CO, H_2CO and CH_3OH. Results are presented in Figure 2.7 (black columns). Since a non-negligible amount of $H_2C(OH)CH_2OH$ is observed in all the control experiments (top panel of Figure 2.6), this has been taken into account and subtracted from the final $H_2C(OH)CH_2OH$ abundances observed in the hydrogenation experiments using a procedure described below. The control experiment data points (upper panel of Figure 2.6) are fitted with the polynomial function. Subsequently, the obtained coefficients –'$H_2C(OH)CH_2OH$(control exp.)'/'$H_2C(OH)CH_2OH$(hydrogenation exp.)'–are derived for all of the hydrogenation experiment data points. Consequently, the $H_2C(OH)CH_2OH$ abundances are reduced by the obtained coefficients and presented in Figure 2.7 (red columns in top panel of 2.7). The latter should be treated as a relative comparison of the lower formation limits of the observed COMs.

2.4   DISCUSSION

2.4.1   *Chemical network*

As described by Fedoseev et al. (2015), the formation COMs observed here can be explained by interaction of intermediate radicals that are formed upon H-atom addition and abstraction
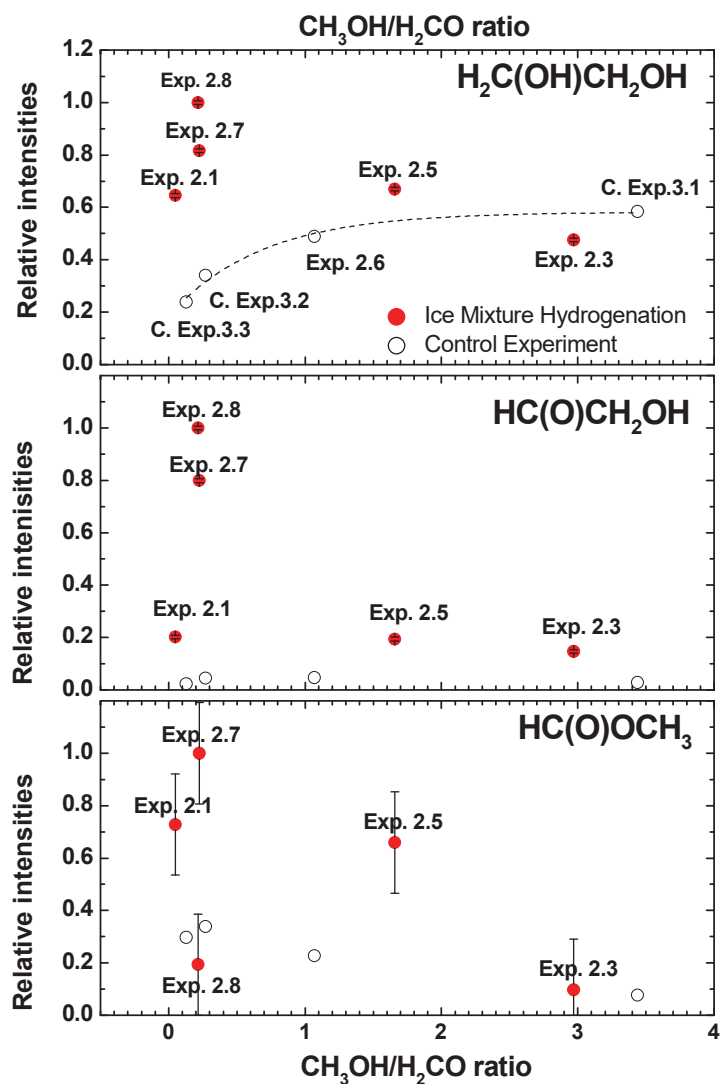
Figure 2.6: Normalized integrated TPD QMS intensities for each of the three COMs discussed here (upper panel = ethylene glycol, middle panel = glycolaldehyde and lower panel = methyl formate) as a function of the CH_3OH/H_2CO mixing ratio. The empty circles indicate the results of the control experiments, i.e., without hydrogenation. Solid circles show the result from the ice mixture hydrogenation experiments. The mass peaks used for the integration are m/z = 31, 31 and 60 for upper, middle and lower panel, respectively. The numbers are normalized with respect to the total amount of H_2CO and CH_3OH observed before the TPD experiment.
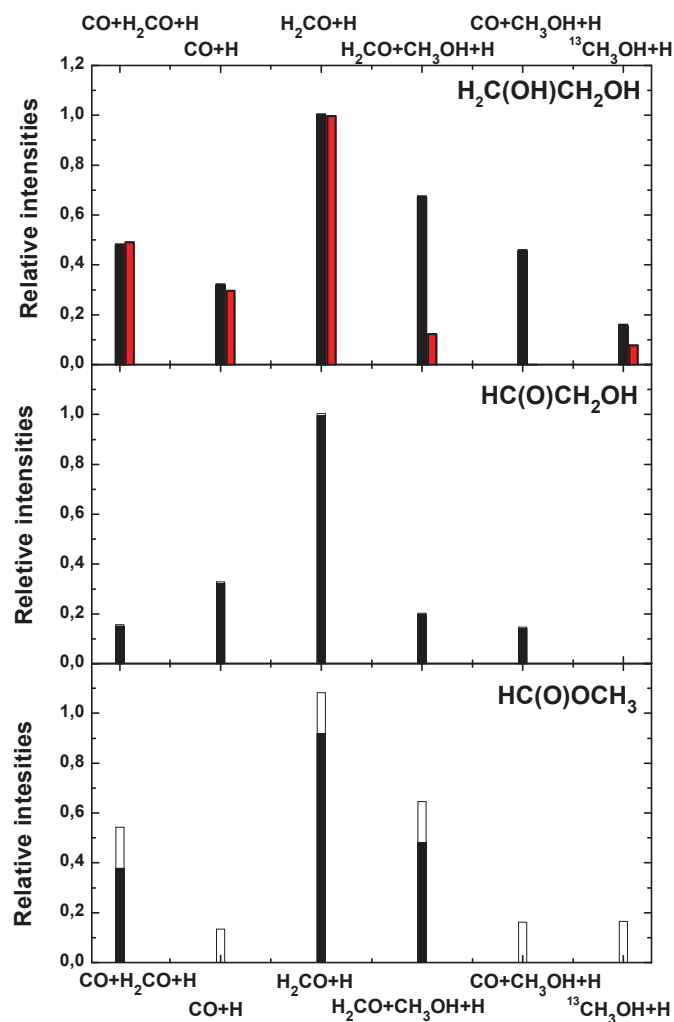
Figure 2.7: Relative comparison of the integrated intensities of ethylene glycol (upper panel), glycolaldehyde (middle panel), and methyl formate (lower panel) observed by means of TPD QMS and normalized for the total amount of carbon-bearing molecules observed before performing the TPD experiment. Black columns represent raw data. In the upper panel, red columns represent the data obtained after reduction of the control experiments shown in Figure 2.6 and should be treated as relative comparison of the lower formation limits observed in this study. White bars (mainly visible in the lower panel, but present in all the panels) represent instrumental errors.

reactions with H_2CO. These are CH_3O and possibly CH_2OH radicals formed in the reaction:

$$H_2CO + H \longrightarrow CH_3O \qquad \text{(8a)}$$

$$H_2CO + H \longrightarrow CH_2OH, \qquad \text{(8b)}$$

which then further yield methanol through the reaction:

$$CH_3O + H \longrightarrow CH_3OH, \qquad \text{(9a)}$$

$$CH_2OH + H \longrightarrow CH_3OH, \qquad \text{(9b)}$$

and HCO radicals formed through the reaction:

$$H_2CO + H \longrightarrow HCO + H_2, \qquad \text{(10)}$$

which is a necessary step to form CO through the reaction:

$$HCO + H \longrightarrow CO + H_2. \qquad \text{(11)}$$

Various reactions involving these intermediate radicals can directly yield glycolaldehyde and ethylene glycol following reaction (8b):

$$HCO + CH_2OH \longrightarrow HC(O)CH_2OH, \qquad \text{(12)}$$

$$CH_2OH + CH_2OH \longrightarrow H_2C(OH)CH_2OH, \qquad \text{(13)}$$
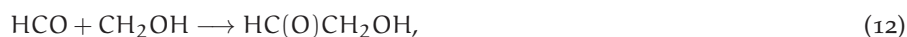
or methyl formate in case of reaction (8a):

$$HCO + CH_3O \longrightarrow HC(O)OCH_3. \qquad \text{(14)}$$

This scheme is also fully consistent with the formation route of ethylene glycol and glycolaldehyde through the sequence of reactions involving glyoxal proposed by Fedoseev et al. (2015):

$$HCO + HCO \longrightarrow HC(O)CHO, \qquad \text{(15)}$$

$$HC(O)CHO + 2H \longrightarrow HC(O)CH_2OH, \qquad \text{(16)}$$

$$HC(O)CH_2OH + 2H \longrightarrow H_2C(OH)CH_2OH. \tag{17}$$
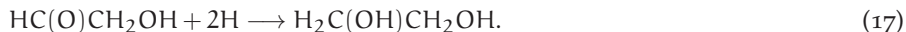
The presence of methyl formate among the products observed in this study indicates that reaction (8a, 8b) should at least partially result in the formation of CH$_3$O (instead of CH$_2$OH) to yield HC(O)OCH$_3$ through reaction (14). Methyl formate was not observed by Fedoseev et al. (2015); the use of CO as a starting point in that study resulted in considerably lower final yields of H$_2$CO and CH$_3$OH than in this work and, therefore, significantly lower amounts of formed CH$_3$O than required to yield methyl formate.

Interaction of H$_2$CO molecules with H-atoms results in both the formation of HCO and CH$_3$O radicals via H-atom abstraction and addition, respectively. The latter process can also lead to the formation of CH$_2$OH radicals in the case that the H-atom addition takes place on the oxygen side of the H$_2$CO molecule. The non-detection of HC(O)OCH$_3$ among the detected COMs in CO+CH$_3$OH+H implies that one of these radicals must play a crucial role in the formation of methyl formate. This cannot be HCO, as it can be produced by H-atom additions to CO molecules present in the ice mixture, thus it must be a reaction product of H-atom additions to H$_2$CO. Taking into account reaction (14), which describes HC(O)OCH$_3$ formation, this radical should be CH$_3$O. This, in turn, allows drawing an important conclusion: H-atom abstraction reactions from CH$_3$OH do not result in efficient formation of CH$_3$O radicals but yield primarily CH$_2$OH:

$$CH_3OH + H \longrightarrow CH_2OH + H_2, \tag{18}$$

as otherwise the presence of H$_2$CO would not be a pre-requisite. This conclusion is consistent with the result of Nagaoka et al. (2007) and Hidaka et al. (2009) obtained by studying deuterium substitution in methanol. Furthermore, H-atom addition reactions to H$_2$CO should result in considerable amounts of formed CH$_3$O through reaction (8), while the formation of CH$_2$OH in this reaction is expected to be a less efficient process.

The non-production of glycolaldehyde in the CO+CH$_3$OH+H codeposition experiment (exp. 2.3) obtained after subtraction of the control experiment data should be stressed here. This suggests that the H$_2$C(OH)CH$_2$OH formation mechanism through reactions (18) and (13) is overall less efficient than through reactions (12) and (17) or reactions (15—17). This may be an indication of a lower formation rate of CH$_2$OH in reaction (18) compared to the HCO formation rates in CO+H or in reaction (10).

Another reason why recombination of CH$_2$OH radicals to yield H$_2$C(OH)CH$_2$OH seems overall less efficient than recombination of HCO with HCO, CH$_3$O or CH$_2$OH radicals may be due to a geometrical properties of the species involved. The access to the unpaired electron of CH$_2$OH radical is significantly blocked by H-atoms bonded to carbon and oxygen atoms, while in the case of HCO radical the access to the unpaired electron will be easier. Thus, one can expect that the rate of CH$_2$OH radical recombination is less probable, or, alternatively, results in H-atom abstraction to form methanol and formaldehyde:

$$CH_2OH + CH_2OH \longrightarrow CH_3OH + H_2CO, \tag{19}$$

due to the easier access of H-atoms to C-H bonds.

The proposed COM formation network based on all investigated reaction routes is presented in Figure 2.8. From top to bottom, a chain of H-atom addition and abstraction reactions
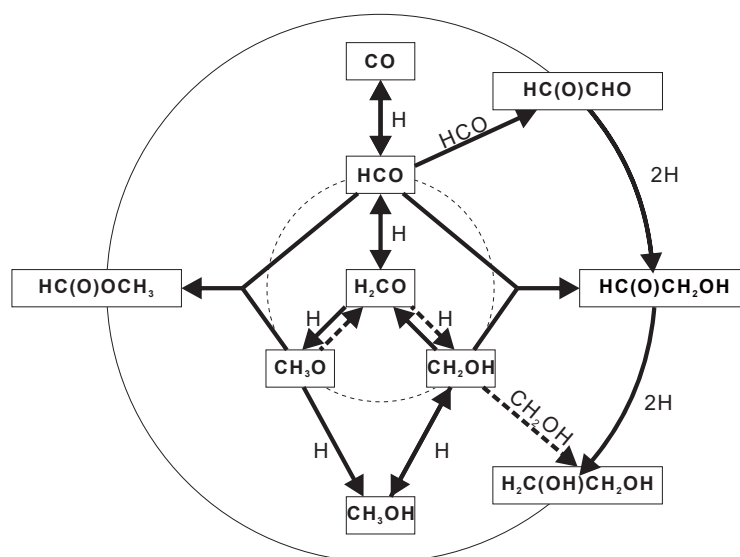
Figure 2.8: Extended COM formation network as obtained from the CO, H_2CO, and CH_3OH hydrogenation experiments. Solid arrows indicate the reaction pathways confirmed or suggested in this study. Dashed lines indicate the overall less efficient pathways.

leading to the formation of CH_3OH from CO is shown. As confirmed in this study, H_2CO can undergo an abstraction reaction induced by H-atoms to form HCO radicals, which successively can be dehydrogenated to form simple molecules, i.e., CO, thus increasing the total number of HCO formation events and its lifetime in the ice mantle. H_2CO also participates in addition reactions with H-atoms. Formation of the CH_3O radical is confirmed in this study by observing methyl formate; however, formation of CH_2OH radicals cannot be excluded, since all experiments involving H_2CO codeposition demonstrate relatively high yields of glycolaldehyde and ethylene glycol. In contrast, H-atom-induced abstraction reaction involving CH_3OH likely yield CH_2OH while no proof for CH_3O formation is found.

The barrier-less recombination of HCO intermediates yielding glyoxal followed by consequent hydrogenation, i.e., the mechanism investigated in Fedoseev et al. (2015), yields HC(O)-CH_2OH and $H_2C(OH)CH_2OH$ and is presented in the right-hand panel of the diagram. Alternatively, the intermediate HCO radicals can directly recombine with CH_3O or CH_2OH to form $HC(O)OCH_3$ and $HC(O)CH_2OH$, respectively. CH_2OH and CH_2OH recombination (dash arrows) seems to contribute less to the formation of $H_2C(OH)CH_2OH$. This may be explained by geometrical constraints or overall low efficiencies of abstraction reactions involving methanol.

From our experimental results, we cannot confidently determine whether diffusion of the intermediate radicals is involved in the formation of the observed methyl formate, ethylene glycol and glycolaldehyde at 15 K. In the simulations reported by Fedoseev et al. (2015), high activation barriers are used for HCO and CH_3O diffusion. This effectively immobilizes such species and only radicals formed next to each can recombine. Fedoseev et al. (2015) showed that the formation and reaction of adjacent radicals explains the observed results, offering an efficient formation pathway even at the low temperatures typical for dense dark clouds (~10 K). This is consistent with the laboratory detection of the three COMs discussed here.

It should be noted that a similar reasoning is often used to explain results obtained in photo-processing experiments, i.e., two consequent photodissociation events result in the formation of radicals that can recombine when located next to each other in the bulk of the ice (Öberg et al. 2009).

2.4.2   *Astrochemical implications and conclusions*

In dense molecular clouds, the reaction between CO molecules and H-atoms accreting on the grain surface does not only explain the abundance of interstellar methanol (Watanabe et al. 2006; Cuppen et al. 2009), but also its deuterium enrichment (Nagaoka et al. 2005; Hidaka et al. 2009). The latter can be realized through the series of H-atom abstraction reactions from the C-H ends of H_2CO and CH_3OH followed by D-atom additions, which take place faster than the corresponding D-atom abstraction reactions followed by substitution with H-atoms. HCO and CH_2OH are possible intermediates in these H-atom abstraction reactions.

In this work, we confirm that such H-atom-induced abstraction reactions take place by experimental observations of H_2CO formation upon H-atom exposure of CH_3OH and CO formation upon H-atom exposure of H_2CO for an astronomically relevant temperature of 15 K. This means that a CO hydrogenation mechanism leading to the formation of interstellar methanol in dark molecular clouds is not irreversible. CH_3OH as well as its formation intermediates can participate in sequences of consecutive H-atom addition and abstraction reactions, thus, once formed, H_2CO and CH_3OH molecules can be potentially dehydrogenated and become once again available for hydrogenation.

Interactions between reactive radicals such as those produced here are actively discussed in the literature as a source for COM formation, both theoretically and experimentally (Hudson & Moore 2000; Bennett et al. 2007; Garrod et al. 2008; Öberg et al. 2009; Woods et al. 2012; Garrod 2013). In these models, UV photon or cosmic-ray-induced dissociation of CH_3OH is usually taken as the external trigger responsible for the formation of these various intermediates. However, Fedoseev et al. (2015) experimentally showed that glycolaldehyde (HC(O)CH₂OH) and ethylene glycol (H₂C(OH)CH₂OH) can be equally efficiently formed just by cold surface hydrogenation of CO molecules without involvement of UV- or cosmic-ray energetic processing of interstellar ices at 15 K. Here, we report that in addition to glycolaldehyde and ethylene glycol formation also methyl formate (HC(O)OCH₃) production is observed. The suggested mechanism of HC(O)OCH₃ formation is the radical-radical recombination of HCO, formed either by H-atom addition to a CO molecule or H-atom abstraction from H_2CO, and CH_3O produced by H-atom addition to H_2CO. Furthermore, along with the formation of glycolaldehyde and ethylene glycol through the recombination of HCO radicals and the subsequent hydrogenation of glyoxal (Woods et al. 2013; Fedoseev et al. 2015), glycolaldehyde can be formed through the direct recombination of HCO and CH_2OH radicals, while ethylene glycol can form through the recombination of two CH_2OH radicals. However, the latter radical-radical reaction is found to be less efficient than the hydrogenation of glycolaldehyde under our experimental conditions.

Codeposition of H_2CO with H-atoms at 25 and 50 K results in a decrease of the efficiency of both abstraction and addition reactions; consequently, no formation of COMs is observed at these temperatures. This can be explained by a substantial drop in the life-time of H-atoms on the ice surface with increase of the temperature.

The direct consequence of both H-atom addition and abstraction reactions is to increase the number of interaction events as well as the timespan over which radicals reside in the ice. This should increase the overall reactivity and likely more COMs are formed through recombination of reactive intermediates than assumed so far. Clearly, the seemingly opposite

processes of H-atom addition and abstraction reactions will decrease the overall efficiency to form methanol directly from CO hydrogenation, essentially shifting the equilibrium point. The rates inferred by Fuchs et al. (2009) should therefore, be regarded as effective rates. In parallel, other processes become possible, increasing the overall efficiency with which COMs are formed. This process that is studied here only for a few temperature settings, is expected to be temperature dependent. The main take-home message from this work is that addition and abstraction reactions upon H-atom exposure of ice mantles can explain the formation of COMs in dense molecular clouds even when energetic external UV radiation or cosmic rays are lacking. It also means that solid state COM formation can start already at the beginning of the CO freeze-out stage, well before CH_3OH containing ices are thermally and energetically processed by the heating and radiation of the emerging protostar. It should be mentioned, that diffusion related processes will be different for the long astrochemical time-scales at play and can enhance the overall efficiency in comparison with the short laboratory time-scales. This provides further support of the COM formation mechanisms discussed in this work. This has important implications in astrobiology; glycolaldehyde is the simplest representative of the aldoses family to which sugars like glycose, ribose and erythrose belong, while ethylene glycol is the simplest polyol among which the triol glycerin is well known. As such, the non-energetic processes discussed here provide an important alternative to the formation of these prebiotically relevant species at an early stage in the chemical evolution of dark interstellar clouds.

The recent gas phase detection of COMs in pre-stellar cores, i.e., environments where temperatures are too low to initiate thermal desorption, raises questions concerning the efficiency of solid state formation of complex molecules and the process(es) responsible for their desorption. Typically, non-thermal desorption mechanisms, that is, upon impacting cosmic rays or irradiation by secondary UV photons, are expected to explain the effective transfer from solid state to gas phase (Bacmann et al. 2012; Cernicharo et al. 2012). In the case of CO, non-dissociative photodesorption explains the observed gas phase abundances (Fayolle et al. 2011), but for other species, like methanol, photodissociation seems to offer a competing scenario, (Öberg et al. 2009). However, larger species may be able to dissipate excess energy more effectively, due to the larger amount of vibrational modes that will help decreasing the dissociation efficiency. Another desorption mechanism that may be relevant is through cosmic ray induced impulsive spot heating. This process has been described in detail by Ivlev et al. (2015). The model presented by Garrod et al. (2007) shows that chemisorption offers another alternative mechanism; excess energy due to exothermicity of surface reactions offers a low temperature non-thermal desorption pathway. It is possible, given the nature of the reactions discussed in this work that COMs formed in CO-rich ices experience chemisorption. Moreover, intermolecular (van der Waals like) interactions with CO will be weak, compared to hydrogen bonds in water rich ices. At the moment, the nature of the process bridging the grain-gas gap is still unclear, and the work presented here offers good arguments for a further focus in future studies.

BIBLIOGRAPHY

Agarwal, V. K., Schutte, W., Greenberg, J. M., et al. 1985, Origins of Life, 16, 21

Anton, R., Wiegner, T., Naumann, W., et al. 2000, Review of Scientific Instruments, 71, 1177

Arce, H. G., Santiago-García, J., Jørgensen, J. K., Tafalla, M., & Bachiller, R. 2008, Astrophys. J. Lett., 681, L21

Bacmann, A., Taquet, V., Faure, A., Kahane, C., & Ceccarelli, C. 2012, Astron. Astrophys., 541, L12

Bennett, C. J., Chen, S.-H., Sun, B.-J., Chang, A. H. H., & Kaiser, R. I. 2007, Astrophys. J., 660, 1588

Boamah, M. D., Sullivan, K. K., Shulenberger, K. E., et al. 2014, Faraday Discussions, 168, 249

Boogert, A. C. A. & Ehrenfreund, P. 2004, in Astronomical Society of the Pacific Conference Series, Vol. 309, Astrophysics of Dust, ed. A. N. Witt, G. C. Clayton, & B. T. Draine, 547

Boogert, A. C. A., Gerakines, P. A., & Whittet, D. C. B. 2015, Ann. Rev. Astron. Astrophys., 53, 541

Caselli, P. & Ceccarelli, C. 2012, Astron. Astrophys. Rev., 20, 56

Cernicharo, J., Marcelino, N., Roueff, E., et al. 2012, Astrophys. J. Lett., 759, L43

Charnley, S. B. & Rodgers, S. D. 2005, in IAU Symposium, Vol. 231, Astrochemistry: Recent Successes and Current Challenges, ed. D. C. Lis, G. A. Blake, & E. Herbst, 237

Charnley, S. B., Rodgers, S. D., & Ehrenfreund, P. 2001, Astron. Astrophys., 378, 1024

Chen, Y.-J., Ciaravella, A., Muñoz Caro, G. M., et al. 2013, Astrophys. J., 778, 162

Cuppen, H. M., Penteado, E. M., Isokoski, K., van der Marel, N., & Linnartz, H. 2011, Mon. Not. R. Astron. Soc., 417, 2809

Cuppen, H. M., van Dishoeck, E. F., Herbst, E., & Tielens, A. G. G. M. 2009, Astron. Astrophys., 508, 275

de Barros, A. L. F., Domaracka, A., Andrade, D. P. P., et al. 2011, Mon. Not. R. Astron. Soc., 418, 1363

Duvernay, F., Danger, G., Theulé, P., Chiavassa, T., & Rimola, A. 2014, Astrophys. J., 791, 75

Falk, M. & Whalley, E. 1961, J. Chem. Phys., 34, 1554

Fayolle, E. C., Bertin, M., Romanzin, C., et al. 2011, Astrophys. J. Lett., 739, L36

Fedoseev, G., Cuppen, H. M., Ioppolo, S., Lamberts, T., & Linnartz, H. 2015, Mon. Not. R. Astron. Soc., 448, 1288

Fuchs, G. W., Cuppen, H. M., Ioppolo, S., et al. 2009, Astron. Astrophys., 505, 629

Garrod, R. T. 2013, Astrophys. J., 778, 158

Garrod, R. T., Wakelam, V., & Herbst, E. 2007, Astron. Astrophys., 467, 1103

Garrod, R. T., Widicus Weaver, S. L., & Herbst, E. 2008, Astrophys. J., 682, 283

Gibb, E. L., Whittet, D. C. B., Boogert, A. C. A., & Tielens, A. G. G. M. 2004, Astrophys. J. Suppl. Ser., 151, 35

Henderson, B. L. & Gudipati, M. S. 2015, Astrophys. J., 800, 66

Herbst, E. & van Dishoeck, E. F. 2009, Ann. Rev. Astron. Astrophys., 47, 427

Hidaka, H., Kouchi, A., & Watanabe, N. 2007, J. Chem. Phys., 126, 204707

Hidaka, H., Watanabe, M., Kouchi, A., & Watanabe, N. 2009, Astrophys. J., 702, 291

Hidaka, H., Watanabe, N., Shiraki, T., Nagaoka, A., & Kouchi, A. 2004, Astrophys. J., 614, 1124

Hiraoka, K., Ohashi, N., Kihara, Y., et al. 1994, Chemical Physics Letters, 229, 408

Hudson, R. L. & Moore, M. H. 2000, Icarus, 145, 661

Ioppolo, S., Fedoseev, G., Lamberts, T., Romanzin, C., & Linnartz, H. 2013, Review of Scientific Instruments, 84, 073112

Ioppolo, S., Öberg, K. I., & Linnartz, H. 2014, Laboratory Astrochemistry - FromMolecules Through Nanoparticles to Grains, Wiley, New York, 289

Ivlev, A. V., Padovani, M., Galli, D., & Caselli, P. 2015, Astrophys. J., 812, 135

Linnartz, H., Ioppolo, S., & Fedoseev, G. 2015, International Reviews in Physical Chemistry, 34, 205

Maity, S., Kaiser, R. I., & Jones, B. M. 2015, Phys. Chem. Chem. Phys., 17, 3081

Mathews, G. S., Klaassen, P. D., Juhász, A., et al. 2013, Astron. Astrophys., 557, A132

Moore, M. H., Ferrante, R. F., & Nuth, III, J. A. 1996, Planet. Space Sci., 44, 927

Nagaoka, A., Watanabe, N., & Kouchi, A. 2005, Astrophys. J. Lett., 624, L29

Nagaoka, A., Watanabe, N., & Kouchi, A. 2007, Journal of Physical Chemistry A, 111, 3016

Öberg, K. I., Boogert, A. C. A., Pontoppidan, K. M., et al. 2011a, Astrophys. J., 740, 109

Öberg, K. I., Bottinelli, S., Jørgensen, J. K., & van Dishoeck, E. F. 2010, Astrophys. J., 716, 825

Öberg, K. I., Garrod, R. T., van Dishoeck, E. F., & Linnartz, H. 2009, Astron. Astrophys., 504, 891

Öberg, K. I., van der Marel, N., Kristensen, L. E., & van Dishoeck, E. F. 2011b, Astrophys. J., 740, 14

Ohishi, M., Irvine, W. M., & Kaifu, N. 1992, in IAU Symposium, Vol. 150, Astrochemistry of Cosmic Phenomena, ed. P. D. Singh, 171

Pontoppidan, K. M. 2006, Astron. Astrophys., 453, L47

Schutte, W. 1988, Leiden: Rijksuniversiteit, 1988

Schutte, W. A., Allamandola, L. J., & Sandford, S. A. 1993, Science, 259, 1143

Shalabiea, O. M. & Greenberg, J. M. 1994, Astron. Astrophys., 290, 266

Tielens, A. G. G. M. & Hagen, W. 1982, Astron. Astrophys., 114, 245

Tielens, A. G. G. M., Tokunaga, A. T., Geballe, T. R., & Baas, F. 1991, Astrophys. J., 381, 181

Tschersich, K. G. 2000, Journal of Applied Physics, 87, 2565

Vastel, C., Ceccarelli, C., Lefloch, B., & Bachiller, R. 2014, Astrophys. J. Lett., 795, L2

Vasyunin, A. I. & Herbst, E. 2013, Astrophys. J., 762, 86

Watanabe, N. & Kouchi, A. 2002, Astrophys. J. Lett., 571, L173

Watanabe, N., Nagaoka, A., Hidaka, H., et al. 2006, Planet. Space Sci., 54, 1107

Watanabe, N., Nagaoka, A., Shiraki, T., & Kouchi, A. 2004, Astrophys. J., 616, 638

Watanabe, N., Shiraki, T., & Kouchi, A. 2003, Astrophys. J. Lett., 588, L121

Woods, P. M., Kelly, G., Viti, S., et al. 2012, Astrophys. J., 750, 19

Woods, P. M., Slater, B., Raza, Z., et al. 2013, Astrophys. J., 777, 90

Zhitnikov, R. A. & Dmitriev, Y. A. 2002, Astron. Astrophys., 386, 1129

3

FORMATION OF GLYCEROL THROUGH HYDROGENATION OF CO ICE UNDER PRESTELLAR CORE CONDITIONS

Observational studies reveal that complex organic molecules (COMs) can be found in various objects associated with different star formation stages. The identification of COMs in prestellar cores, i.e., cold environments in which thermally induced chemistry can be excluded and radiolysis is limited by cosmic rays and cosmic-ray-induced UV photons, is particularly important as this stage sets up the initial chemical composition from which ultimately stars and planets evolve. Recent laboratory results demonstrate that molecules as complex as glycolaldehyde and ethylene glycol are efficiently formed on icy dust grains via 'non-energetic' atom addition reactions between accreting H atoms and CO molecules, a process that dominates surface chemistry during the 'CO freeze-out stage' in dense cores. In the present study we demonstrate that a similar mechanism results in the formation of the biologically relevant molecule glycerol – $HOCH_2CH(OH)CH_2OH$ – a three-carbon-bearing sugar alcohol necessary for the formation of membranes of modern living cells and organelles. Our experimental results are fully consistent with a suggested reaction scheme in which glycerol is formed along a chain of radical-radical and radical-molecule interactions between various reactive intermediates produced upon hydrogenation of CO ice or its hydrogenation products. The tentative identification of the chemically related simple sugar glyceraldehyde – $HOCH_2CH(OH)CHO$– is discussed as well. These new laboratory findings indicate that the proposed reaction mechanism holds much potential to form even more complex sugar alcohols and simple sugars.

3.1   INTRODUCTION

With the increasing sensitivity of astronomical observing facilities, more and more complex organic molecules (COMs) have been identified in space (Halfen et al. 2015; Cernicharo et al. 2016; Jørgensen et al. 2016; McGuire et al. 2016). Gas-phase reactions are not efficient enough to explain many of the observed COM abundances, and it is generally accepted that such species form on the surfaces of icy dust grains by merging smaller species to larger and larger constituents. This idea, supported by numerous laboratory results and astrochemical simulations, indicates that surface reactions, triggered by accreting atoms, impacting cosmic rays and VUV photons, as well as by thermal processing, provide efficient pathways toward molecular complexity (Charnley & Rodgers 2008; Garrod et al. 2008; Herbst & van Dishoeck 2009; Vasyunin & Herbst 2013b; Walsh et al. 2014a,b; Linnartz et al. 2015; Öberg 2016).

Key in the formation of new COMs is the mechanism that extends, for interstellar conditions, the size of a carbon backbone of the precursor molecule with new C-C bonds. Subsequently, these larger species act as parents in new reactions, resulting in the formation of a whole set of other COMs with similar size properties. This holds until another C-C bond is added to one of these reaction products, yielding a parent species that acts as a precursor for another set of even larger COMs, etc. This repeatable process can be best illustrated by the reaction scheme introduced by Charnley et al. (2001) and Charnley & Rodgers (2008). During the 'catastrophic CO freeze-out' in dense cores, accreting CO molecules produce a layer of CO ice on the icy grain surfaces. Simultaneously, CO molecules undergo partial hydrogenation by accreting H atoms, producing CH_3OH in a series of H-atom addition and abstraction reactions that start with the formation of $H\dot{C}O$ radicals (Hiraoka et al. 1994; Watanabe & Kouchi 2002; Zhitnikov & Dmitriev 2002; Fuchs et al. 2009; Hidaka et al. 2009). Such 'non-energetic' atom addition reactions, i.e., reactions between species that are in thermalized equilibrium with the grain surface and, therefore, are not able to cross large reaction barriers, play a main role in dark cloud chemistry. The subsequent addition of C atoms to $H\dot{C}O$ results in the formation of ·CCHO and ·CCCHO radicals. The latter two intermediates are, in turn, proposed starting points in the formation of entire sets of new COMs through a sequence of H- and O-atom addition reactions. For example, acetaldehyde, ethanol, glyoxal, glycolaldehyde, and ethylene glycol are all produced through a series of atom or molecule additions to ·CCHO radicals. In a similar way, their 'three-carbon-bearing' analogues are produced from ·CCCHO intermediates.

The chemical concept of this C-atom addition scenario is straightforward, but requires a long sequence of 'site-selective' H-, C- and O-atom additions, making efficient formation of species like glyceraldehyde and ethylene glycol (in which each of the carbon atoms has one oxygen atom attached) unlikely. Moreover, in dense clouds most of the atomic carbon is locked in CO molecules, and fewer carbon atoms are available for accretion on the icy grain surface. Therefore, the formation of these two species has been addressed in another scenario that was experimentally verified by Fedoseev et al. (2015) and later extended by Butscher et al. (2015) and Chuang et al. (2016). In this reaction scheme, a carbon backbone increase is realized through recombination of various C(O)-bearing intermediate radicals that are produced along the CO to CH_3OH hydrogenation route (see figure 8 of Chuang et al. 2016). It was recently proven that direct recombinations of $H\dot{C}O$ and ·CH_2OH free radicals form glycolaldehyde, ethylene glycol, and, possibly, glyoxal. In this scheme, ethylene glycol may also be formed via two sequential H-atom additions to glycolaldehyde.

In an alternative 'energetic processing' scenario, reactive intermediates are formed upon irradiation of CH_3OH-rich ices by various energetic particles, including protons, electrons, X-rays, VUV photons, etc. Laboratory studies show that in this case COMs are efficiently formed

through recombination of carbon-bearing CH_3OH dissociation products (Allamandola et al. 1988; Hudson & Moore 2000; Öberg et al. 2009; Modica & Palumbo 2010; Jheeta et al. 2013; Henderson & Gudipati 2015; Maity et al. 2015; Abou Mrad et al. 2016; Paardekooper et al. 2016a; Chuang et al. 2017). Whereas the 'non-energetic' scenarios are thought to dominate in dark clouds, the latter ones will be more prominent during later stages of the star and planet formation process.

Efficient mechanisms increasing the number of C-C bonds are particularly interesting from an astrobiological point of view. Many of the basic chemical compounds required for the emergence of life consist of chains of carbon atoms with repeatable functional groups, such as (un)saturated fatty acids, simple sugars, and sugar alcohols. The two latter classes deserve special attention, as their smallest members, glycolaldehyde ($HOCH_2CHO$) and ethylene glycol ($HOCH_2CH_2OH$), have been successfully observed in the gas phase toward our Galactic center (Hollis et al. 2000, 2002), in solar-mass protostars (Jørgensen et al. 2012, 2016; Coutens et al. 2015; Taquet et al. 2015; Rivilla et al. 2017), and in cometary ices (Biver et al. 2014; Goesmann et al. 2015; Le Roy et al. 2015). It is possible that the mechanism responsible for the formation of glycolaldehyde and ethylene glycol also holds the potential to form the next larger members in these series, glyceraldehyde and glycerol. These molecules are needed in the synthesis of other sugars, sugar alcohols, amino acids, and even a nucleic acid, as proposed in one of the possible early Earth geochemical scenarios (Ritson & Sutherland 2012; Patel et al. 2015; Sutherland 2017). Thus, studying possible formation routes of this type of COM for conditions relevant to star-forming regions, at stages prior to the formation of planets, is particularly intriguing, assuming that at least a fraction of the original icy-dust material survives upon transfer to early planet surfaces.

3.2   PROPOSED REACTION SCHEME

In this work we experimentally verify an extension of the scenario in which COMs are formed through recombination of reactive carbon-bearing radicals produced along the CO to CH_3OH hydrogenation route. It illustrates that the mechanism resulting in the formation of glycolaldehyde and ethylene glycol is also capable of forming larger molecules with a $(-C(O)-)_n$ backbone, i.e., glyceraldehyde and glycerol (see Figure 3.1 for more details). Glycerol ($HOCH_2CH(OH)CH_2OH$) is one of the homologues in the sugar alcohol row, a subclass of linear polyols that can be described by the formula $HOCH_2(CH(OH))_nCH_2OH$. This class of chemical compounds comprises a chain of carbon atoms where each of the carbons is linked to the single hydroxyl (OH) group. With n=0 this formula is reduced to ethylene glycol, virtually the first representative in this row. The significant structural similarity between glycerol and ethylene glycol (the final product of glycolaldehyde hydrogenation) complicates the successive assignments of glycerol by means of IR spectroscopy, as the vibrational modes of glycerol are nearly identical to those of ethylene glycol and, to some extent, of CH_3OH. Broadening of absorption features due to hydrogen bonds further complicates spectroscopic assignments. In a similar way glyceraldehyde links to the series $HOCH_2(CH(OH))_nCHO$. In order to circumvent these problems, we use a combination of temperature programmed desorption (TPD) and quadrupole mass spectrometry (QMS). The methodology is described in the next section.

The experiments presented below are aimed at reproducing the 'CO freeze-out' stage in dense cores (Tielens et al. 1991; Pontoppidan 2006). At this stage external UV fields are to a large extent shielded by dust grains. This results in a significantly higher rate of H-atom accretion events on an ice surface in comparison to the number of impacting VUV photons or cosmic rays, e.g., H-atom flux $\sim 10^4$ atoms cm^{-2} s^{-1} versus UV flux of $\sim(1-10)\times 10^3$ photons cm^{-2} s^{-1} (Prasad & Tarafdar 1983; Chuang et al. 2017). Therefore, the CO hydro-
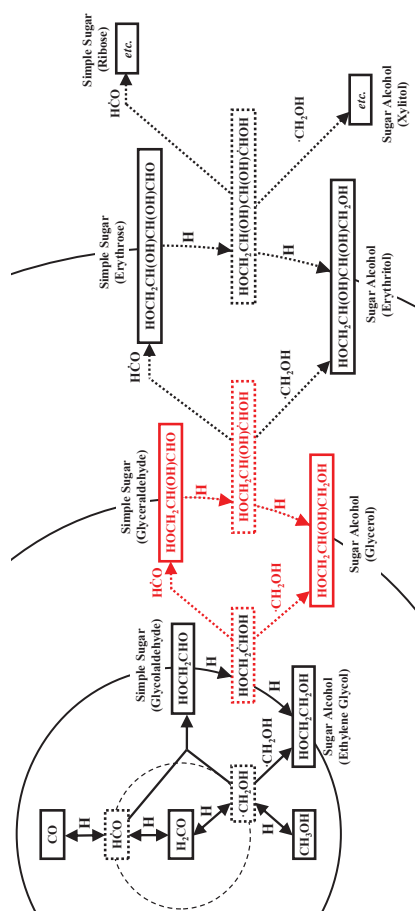
Figure 3.1: Proposed reaction scheme demonstrating the repetitive formation of various simple sugars and sugar alcohols starting from hydrogenation of CO molecules on the surface of interstellar grains. Solid line boxes represent stable molecules, while the intermediate radicals are shown in the dashed line boxes. In the case of more than one possible structural isomer, only the relevant one is depicted for simplicity, e.g., both ·CH$_2$OH and CH$_3$O· are formed, but only ·CH$_2$OH is relevant for this scheme. Solid arrows present the reaction pathways discussed in previous experimental studies. The dashed arrows show reaction routes made by extrapolation of these previously obtained results. The reaction routes investigated in the present study, resulting in the formation of glycerol and glyceraldehyde, are highlighted in red. Stereochemistry is omitted for simplicity.

genation composes the core of the reaction scheme presented in Figure 3.1. CH_3OH ice has been observed in dense clouds (Pontoppidan et al. 2003; Bottinelli et al. 2010; Boogert et al. 2015), and its abundance is in line with the predictions of theoretical and modeling work (Tielens & Hagen 1982; Shalabiea & Greenberg 1994; Geppert et al. 2005; Cuppen et al. 2009, 2011; Vasyunin & Herbst 2013a). Recent experimental and theoretical studies demonstrated that two-carbon-bearing COMs, i.e., glycolaldehyde and ethylene glycol, are also formed at this stage (Woods et al. 2012; Fedoseev et al. 2015; Butscher et al. 2015; Chuang et al. 2016). The key point in the formation of these species appears to be the recombination of free intermediate radicals, i.e., $H\dot{C}O$ or $\cdot CH_2OH$, produced in the sequence of H-atom addition and abstraction reactions along the aforementioned CH_3OH formation route (see figure 8 of Chuang et al. 2016 for more details). These experimentally verified reaction pathways compose the left part of the reaction scheme presented in Figure 3.1 and can be further extrapolated to form even larger species.

Both glycolaldehyde and ethylene glycol can participate in similar H-atom-induced reactions, producing two-carbon-bearing reactive intermediates, e.g., $HOCH_2\dot{C}HOH$. This radical, in turn, can participate in a barrierless recombination with $H\dot{C}O$ or $\cdot CH_2OH$, resulting in the formation of three-carbon-bearing species, i.e., glyceraldehyde and glycerol, the next simple sugar and sugar alcohol representatives in the $HOCH_2(CH(OH))_n$-CHO and $HOCH_2(CH(OH))_n$-CH_2OH rows, respectively. These formation routes are illustrated in the central part of Figure 3.1 and are experimentally verified in the present study. In an identical way, the same reaction sequence can be further extrapolated to form four-, five- and more-carbon-bearing representatives. Here, the consecutive increase of the $(-C(O)-)_n$ backbone by one segment is achieved each time when an $H\dot{C}O$ or $\cdot CH_2OH$ radical reacts with a three-, four-, or more-carbon-bearing precursor, as illustrated in the right part of the reaction scheme. In the figure solid lines represent experimentally verified reaction routes, while dashed lines show their further extrapolation as proposed in this study.

It is important to note that this reaction scheme explains the formation of simple sugars and sugar alcohols already at the cold dark cloud stage, i.e., earlier than in most other suggested chemical scenarios that require thermal heating or irradiation by photons and cosmic rays originating from the newly formed protostar (Garrod et al. 2006; Maity et al. 2015; Meinert et al. 2016; Paardekooper et al. 2016a; Taquet et al. 2016).

3.3 EXPERIMENTAL

The experiments are performed using SURFRESIDE[2], an ultra-high-vacuum (UHV) setup that has been described in much detail by Ioppolo et al. (2013). Updated information is available from Fedoseev et al. (2016). A gold-coated substrate is mounted onto the cold tip of an He close-cycle cryostat that is positioned in the center of a UHV main chamber with a typical base pressure of $\sim 10^{-10}$ mbar. The temperature of the substrate is regulated in the range between 13 and 330 K by means of resistive heating and monitored using two thermocouples. A LakeShore 340 temperature controller allows for a 0.5 K relative temperature precision. Two independently prepumped full-metal dosing lines are used for carbon monoxide and glycolaldehyde vapor deposition. The impacting H atoms are obtained through thermal cracking, using a Hydrogen Atom Beam Source (HABS; Tschersich 2000) or through dissociation of H_2 molecules in a capacitively coupled microwave discharge using a Microwave Atom Source (MWAS; Anton et al. 2000). The two sources are mounted in separate UHV chambers that are connected to the main chamber via UHV shutters. In both systems the produced H atoms and undissociated H_2 molecules remaining in the H-atom beam are thermalized through collisions inside a bent quartz pipe prior to their impact on the ice substrate in the main chamber.

This setting allows a fully independent operation of the individual deposition lines. The use of two different H-atom sources also allows for cross-reference of the obtained results. Both HABS and MWAS are commercial systems. Their fluxes are calibrated '*in situ*,' and the details of this procedure are available from Ioppolo et al. (2013). Typical H-atom fluxes used in the present study amount to 8×10^{12} atoms cm^{-2} s^{-1}.

Along the proposed reaction scheme a steady abundance decrease is expected with increasing COM size. Previously obtained experimental results show that hydrogenation of pure CO ice yields glycolaldehyde and ethylene glycol, but their final abundances were at the edge of the detection sensitivity. This will prohibit the detection of glyceraldehyde and glycerol in a similar setting. Therefore, here the glycolaldehyde content is artificially increased with respect to the amounts formed in the pure CO hydrogenation experiments. Our assumption is that if the formation yield of glycerol and glyceraldehyde from glycolaldehyde is comparable to that of glycolaldehyde and ethylene glycol starting from CO hydrogenation –HOCH$_2$CHO/H$_2$CO and HOCH$_2$CH$_2$OH/CH$_3$OH ratios of $\sim 0.01 - 0.09$ were found in Fedoseev et al. (2015) –then the laboratory detection of three-carbon-bearing molecules should be possible. Although this approach greatly enhances the relative yields of newly formed species with respect to the initial amount of CO, the yields of three-carbon-bearing COMs with respect to glycolaldehyde should not be significantly affected, and the successful detection of three-carbon-bearing COMs should validate the overall mechanism proposed here.

The experiments are performed using a 'co-deposition' technique. In this case, CO and HOCH$_2$CHO molecules, as well as the H atoms, are exposed to a clean and precooled substrate, resulting in the growth of a uniform ice. Typically $\sim 1.4 \times 10^{16}$ molecules cm^{-2} are deposited over the duration of a 360-minute co-deposition with a 1:1 ratio. The ice composition and the column densities are monitored *in situ* by means of Reflection Absorption Infrared (RAIR) spectroscopy. The band strengths (cm mol^{-1}) of CO, H$_2$CO, CH$_3$OH, and HOCH$_2$CHO signals are derived using laser (632.8 nm) interference methods, as previously described in Baratta & Palumbo (1998) and Paardekooper et al. (2016b). The values derived for the pure ices are then applied to the ice mixtures. In the experiments ^{13}CO (Sigma-Aldrich, 99% ^{13}C, $<5\%$ ^{18}O isotope), ^{13}C^{18}O (Sigma-Aldrich, 99% ^{13}C and 99% ^{18}O isotope), regular CO (Linde 2.0), and H$_2$ (Praxair 5.0) are used as gas supplies. The glycolaldehyde vapors are obtained by thermal decomposition of solid glycolaldehyde dimers (Sigma-Aldrich) under vacuum at ~ 80 K.

Upon completion of the co-deposition experiment, a TPD measurement is performed, typically with a 5 K min^{-1} rate. Sublimating species are recorded in the gas phase, as a function of the ice temperature, using a quadrupole mass spectrometer (QMS), applying 70 eV, i.e., 'hard,' electron ionization. Dissociative electron impact ionization occurring in the ion source of the QMS causes significant fragmentation of the parent species. The produced QMS spectra are compared with those available in the NIST database[3.1] for similar electron energies. This provides an additional diagnostic tool to the regular assignment based on the sublimation temperature of individual species. Dissociative ionization also comes with the advantage that it allows us to study isotope-labeled experiments, using ^{13}CO and ^{13}C^{18}O, to further constrain assignments by searching for the corresponding shifts in the mass spectra. In addition to the QMS measurements, sublimating ice species can also be monitored by acquiring RAIR difference spectra prior to and after desorption of each of the ice constituents.

[3.1] NIST Mass Spec Data Center, S.E. Stein, director, 'Mass Spectra' in NIST Chemistry WebBook, NIST Standard Reference Database Number 69, Eds. P.J. Linstrom and W.G. Mallard, National Institute of Standards and Technology, Gaithersburg MD, 20899, http://webbook.nist.gov.
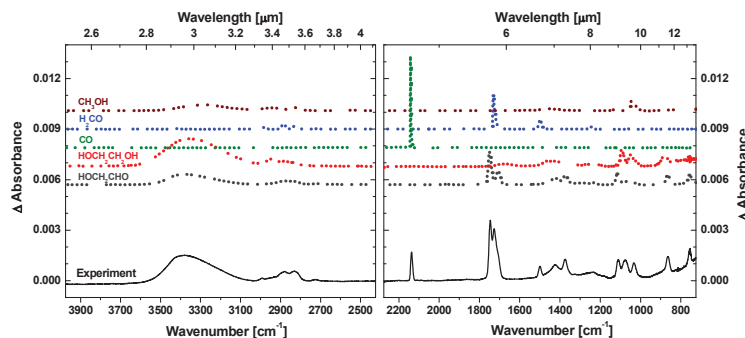
Figure 3.2: Solid line: RAIR spectra obtained after the co-deposition of a CO:HOCH$_2$CHO = 1:1 ice mixture with H atoms at 15 K. The total CO and HOCH$_2$CHO fluences amount to 7×10^{15} molecules cm^{-2}, while the total H-atom fluence is 2×10^{17} atoms cm^{-2}. Δabsorbance is normalized to 5×10^{15} deposited molecules. Dashed lines: reference spectra obtained after the deposition of pure HOCH$_2$CHO, HOCH$_2$CH$_2$OH, CO, H$_2$CO, and CH$_3$OH ices at 15 K. Each spectrum is normalized to 1×10^{15} deposited molecules.

All experiments have been performed using both HABS and MWAS and produce similar results. In the following only the HABS results are presented, as these have a lower content of background H$_2$O contamination. The chosen experiments are also repeated for faster TPD rates of 20 and 25 K min^{-1} to obtain higher signal-to-noise ratios for the COM signals. In the latter case, a regular 5 K min^{-1} rate is used in the range from 15 to 50 K to remove CO ice, and, subsequently, 20 or 25 K min^{-1} rates are applied above 50 K.

3.4 RESULTS AND DISCUSSION

In Figure 3.2 a typical example of an RAIR spectrum is presented, obtained after the co-deposition of HOCH$_2$CHO and CO molecules with H atoms at 15 K. This spectrum is normalized to 5×10^{15} deposited molecules and compared with five reference spectra recorded for pure HOCH$_2$CHO, HOCH$_2$CH$_2$OH, CO, H$_2$CO, and CH$_3$OH ices. The latter five spectra are each normalized to 1×10^{15} molecules. Along with the RAIR absorption features of the deposited HOCH$_2$CHO and CO molecules, the absorption bands of the three main hydrogenation products –HOCH$_2$CH$_2$OH, H$_2$CO and CH$_3$OH –can be identified. As discussed in Sections 3.2 and 3.3, the detection of the three-carbon-bearing sugar and sugar alcohol homologues, i.e., glycerol and glyceraldehyde, cannot be confirmed based solely on the RAIR data, due to spectral overlap with IR features of the two-carbon-bearing homologues and the relatively low formation yields. Below we address glycerol and glyceraldehyde formation based on the obtained QMS TPD data.

3.4.1 Glycerol

For the UHV conditions in SURFRESIDE^2, a desorption temperature of glycerol of around 240 K is expected (Kaiser et al. 2015; Paardekooper et al. 2016a). All recorded TPD QMS spectra, obtained after simultaneous deposition of HOCH$_2$CHO with CO molecules and H atoms, re-
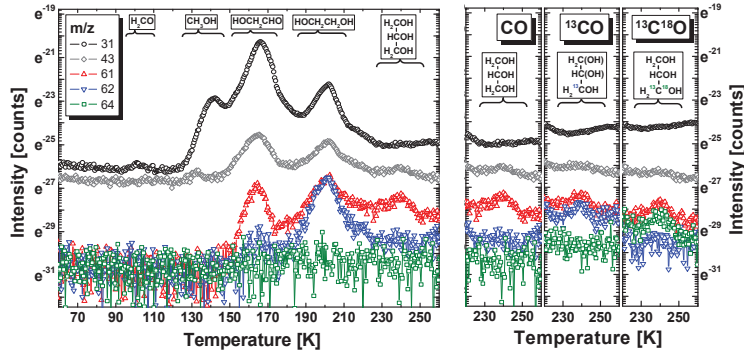
Figure 3.3: Left panel: QMS TPD spectra in the range from 60 to 260 K for five selected m/z values obtained after the co-deposition of a CO:HOCH$_2$CHO = 1:1 ice mixture with H atoms at 15 K. Right panel: comparison between the fragments of three QMS TPD spectra in the range from 220 to 260 K. The spectra are obtained after co-deposition at 15 K of HC(O)CH$_2$OH molecules with H atoms and naturally abundant CO (left spectrum), ^{13}CO (central spectrum), or ^{13}C^{18}O (right spectrum) labeled isotopes. All presented experiments are performed for identical experimental conditions. The total CO (^{13}CO, ^{13}C^{18}O) and HOCH$_2$CHO fluences amount to 7×10^{15} molecules cm^{-2}, while the total H-atom fluence is 2×10^{17} atoms cm^{-2}. The ordinate axis is presented in the natural logarithm scale for clarity.

veal the presence of a desorption peak at this temperature. The following evidence of glycerol assignment to this desorption feature can be provided.

In the left panel of Figure 3.3 an example of a typical TPD QMS spectrum is shown for a temperature range from 60 to 260 K. This spectrum is recorded after co-deposition at 15 K of HOCH$_2$CHO and CO molecules with H atoms for 360 minutes, where molecular deposition rates and H-atom flux amount to 3×10^{11} molecules cm^{-2} s^{-1} and 8×10^{12} atoms cm^{-2} s^{-1}, respectively. Five selected m/z values are plotted in the figure. These are the three characteristic QMS peaks of glycerol, i.e., 31–CH$_2$OH$^+$, 61–HOCH$_2$CHOH$^+$, and 43–C$_2$H$_2$OH$^+$. The two other m/z values at 62 and 64 are shown for comparison. The glycerol QMS spectrum does not reveal any signal at m/z = 92 –the 'parent' molecular mass (NIST database; Kaiser et al. 2015), reflecting near complete dissociative ionization of glycerol upon electron impact in the ion source of the QMS. Among the produced characteristic ions, CH$_2$OH$^+$ (m/z = 31) and HOCH$_2$CHOH$^+$ (m/z = 61) are obtained through the cleavage of C-C bonds in glycerol molecules. The m/z = 43 signal (C$_2$H$_2$OH$^+$) is the result of the subsequent loss of an H$_2$O unit from the HOCH$_2$CHOH$^+$ ion. The m/z signals at 61 and 43 clearly peak around 240 K, while the m/z = 31 signal is to a large extent obscured by the high baseline value that is caused by species desorbing at lower temperatures.

Besides the 240 K peak, four other distinct desorption features are observed in this diagram. Two peaks can be assigned to well-known CO hydrogenation products, i.e., H$_2$CO at ~100 K and CH$_3$OH at ~140 K (see Hiraoka et al. 1994; Watanabe & Kouchi 2002; Fuchs et al. 2009). Note that the m/z value at 31 corresponds to the parent mass of naturally occurring H$_2$^{13}CO. The intensity of the regular H$_2$CO isotope (m/z = 30, not shown here) is about two orders of magnitude higher, in accordance with the ^{12}C/^{13}C natural abundance ratio. Two other desorption peaks, at ~160 and ~200 K, can be respectively assigned to unprocessed glycolaldehyde, left over after co-deposition, and to HOCH$_2$CH$_2$OH, a known reaction product upon HOCH$_2$CHO hydrogenation (Burke et al. 2015; Fedoseev et al. 2015; Chuang et al.

2016; Maity et al. 2015). The detection of the formed H_2CO, CH_3OH, and $HOCH_2CH_2OH$ in addition to the low-volatile product desorbing at 240 K is fully consistent with the reaction scheme presented in Figure 3.1.

To further constrain the assignment of the glycerol desorption peak at 240 K, isotope-labeled experiments are performed. The co-deposition of $HOCH_2CHO$ with CO molecules and H atoms at 15 K is repeated for ^{13}CO and $^{13}C^{18}O$. In the case in which CO addition occurs at the edge of an $HOCH_2CHO$ molecule (see Figure 3.1), isotopically enriched glycerol molecules are formed: $HOCH_2CH(OH)^{13}CH_2OH$ and $HOCH_2CH(OH)^{13}CH_2{}^{18}OH$ for ^{13}CO and $^{13}C^{18}O$, respectively. To our knowledge, the electron-impact-ionization-induced QMS spectra of these two isotopologues have not been reported before, but it is possible to deduce these from the accessible QMS spectra of regular ^{12}C-containing species (NIST database; Kaiser et al. 2015) in the following way.

Glycerol is a symmetric molecule. Assuming that each of the symmetric chemical bonds has an equal probability to break upon 70 eV electron impact, the resulting distribution of m/z intensities can be interpreted. Take as an example the cleavage of C-C bonds of glycerol. As previously discussed, two of the most intense m/z values in the QMS spectrum of glycerol are 31 (CH_2OH^+) and 61 ($HOCH_2CHOH^+$). In the case in which only a single edge carbon or oxygen atom of the glycerol molecule is labeled by the isotope, half of the produced CH_2OH^+ ions should contain this isotope and half should not. On the contrary, in the case in which a central carbon or oxygen atom in the glycerol molecule is ^{13}C or ^{18}O labeled, no drop in m/z = 31 signal is expected. A similar conclusion can be deduced for the $HOCH_2CHOH^+$ ion where the same 1-to-1 distribution between isotopically labeled and unlabeled fragments should be obtained when the edge carbon or oxygen atom is isotopically labeled. In the case that the central carbon or oxygen is labeled, all resulting $HOCH_2CHOH^+$ ions will contain isotopically labeled atoms. Therefore, under the fair assumption that the dissociative ionization cross sections are nearly identical for isotopically labeled and nonlabeled glycerol, a 50% intensity drop at m/z = 61 is expected. The corresponding intensity increase at m/z = 62 or 64 should be observed for $HOCH_2CH(OH)^{13}CH_2OH$- or $HOCH_2CH(OH)^{13}CH_2{}^{18}OH$-labeled glycerol, respectively. These experiments have been performed, and the resulting TPD spectra obtained after co-deposition of $HOCH_2CHO$ with H atoms and CO, ^{13}CO, or $^{13}C^{18}O$ molecules are shown in the three right panels of Figure 3.3 in the range from 220 to 260 K. The measurements exhibit the predicted intensity shifts for m/z = 61, 62, and 64. None of the m/z = 62 and m/z = 64 signals exhibit a peak at 240 K for the regular glycerol isotope, whereas in the case of ^{13}C-labeled carbon monoxide, two peaks can be observed for m/z = 61 and m/z = 62 corresponding to the $HOCH_2CHOH^+$ and $HO^{13}CH_2CHOH^+$, respectively. In the case of $^{13}C^{18}O$, m/z = 61 ($HOCH_2CHOH^+$) and m/z = 64 ($H^{18}O^{13}CH_2CHOH^+$) peaks are observed, while no rise of m/z = 62 signals is detected.

By extrapolating the procedure described above to other ions observed in the QMS spectra of glycerol, the corresponding $HOCH_2CH(OH)^{13}CH_2OH$ and $HOCH_2CH(OH)^{13}CH_2{}^{18}OH$ spectra can be evaluated, from the natural 98.9% ^{12}C isotope QMS spectrum of glycerol available in the NIST database. The obtained QMS reference spectra are presented in the top panels of Figure 3.4. Two m/z ranges are chosen. In the left panel the previously discussed range between m/z = 60 and m/z = 64 is presented, while in the right panel the range between m/z = 43 and m/z = 47 is shown. In the bottom panels, the experimentally obtained intensities are presented for comparison. A good agreement between the evaluated QMS spectra of the different glycerol isotopes and the m/z intensities obtained from our experiments is found. A conclusive fit is obtained for the m/z = 60 − 64 range, while for the m/z = 43 − 47 range some discrepancies are observed. These are expected, however. Most of the ions in this range are formed by secondary fragmentation, e.g., H_2CCOH^+ (m/z = 43) is obtained by the loss of

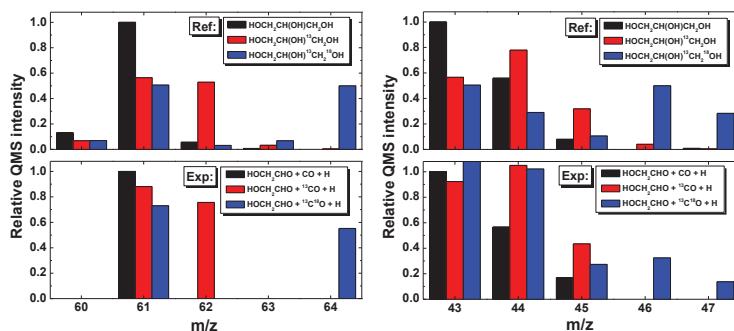Figure 3.4: Top left panel: 70 eV QMS spectra of three distinct glycerol isotopes HOCH$_2$CH(OH)CH$_2$OH (NIST database), and HOCH$_2$CH(OH)^{13}CH$_2$OH with HOCH$_2$CH(OH)^{13}CH$_2$^{18}OH (evaluated from the NIST database data in this study). The range from m/z = 60 to m/z = 64 is shown. Bottom left panel: comparison with the QMS intensities obtained at 240 K after the 15 K co-deposition of HOCH$_2$CHO molecules with H atoms and naturally abundant CO (black bars), ^{13}CO (red bars), or ^{13}C^{18}O (blue bars) labeled isotopes. The total CO (^{13}CO, ^{13}C^{18}O) and HOCH$_2$CHO fluences are equal to 7×10^{15} molecules cm^{-2}, while the total H-atom fluence amounts to 2×10^{17} atoms cm^{-2}. Right panels: same spectra in the range from m/z = 43 to m/z = 47, normalized to the m/z = 43 signal in a regular CO experiment.

an H$_2$O unit from HOCH$_2$CHOH$^+$ (m/z = 61). The latter ion lacks symmetry. Therefore, a deviation from a statistical 1-to-1 ratio is expected. Furthermore, some of the m/z signals can be caused by more than one ion, e.g., HOCH$_2$CH$^+$, HOCHCH$_2$$^+$, CO$_2$$^+$, etc., all have m/z = 44.

Based on the fit between the predicted and experimentally obtained glycerol QMS spectra presented in Figure 3.4, the formation of glycerol in our experiments is concluded. Moreover, the obtained fit confirms that CO addition occurs at the edge of the HOCH$_2$CHO molecules, constraining the mechanism shown in Figure 3.1. Assuming similar electron impact ionization cross sections and pumping rates of ethylene glycol (the two-carbon-bearing product of glycolaldehyde hydrogenation) and of glycerol (the three-carbon-bearing product), an HOCH$_2$CH(OH)CH$_2$OH/HOCH$_2$CH$_2$OH ratio of about 0.01 is derived from the TPD spectra presented in Figure 3.2. This indicates that for our experimental conditions, only a limited fraction of the HOCH$_2$CHO molecules contributes to a further extension of the carbon skeleton, as discussed in Section 3.3.

3.4.2 *Glyceraldehyde*

QMS spectra of isotopically labeled HOCH$_2$CH(OH)^{13}CHO and HOCH$_2$CH(OH)^{13}CH^{18}O cannot be extrapolated in a similar way to those in the case of glycerol, due to the lack of molecular symmetry of glyceraldehyde. Nevertheless, several experimental observations have been made. Two desorption temperatures have been reported for pure glyceraldehyde under UHV conditions (McManus 2014). These are 215 and 280 K, and these two desorption peaks were assigned to glyceraldehyde monomers and dimers in the adsorbed multilayers, respectively. Figure 3.5 shows the fragments of three TPD spectra in the $202 - 235$ K temperature range where thermal desorption of glyceraldehyde monomers is expected. These mass spectra
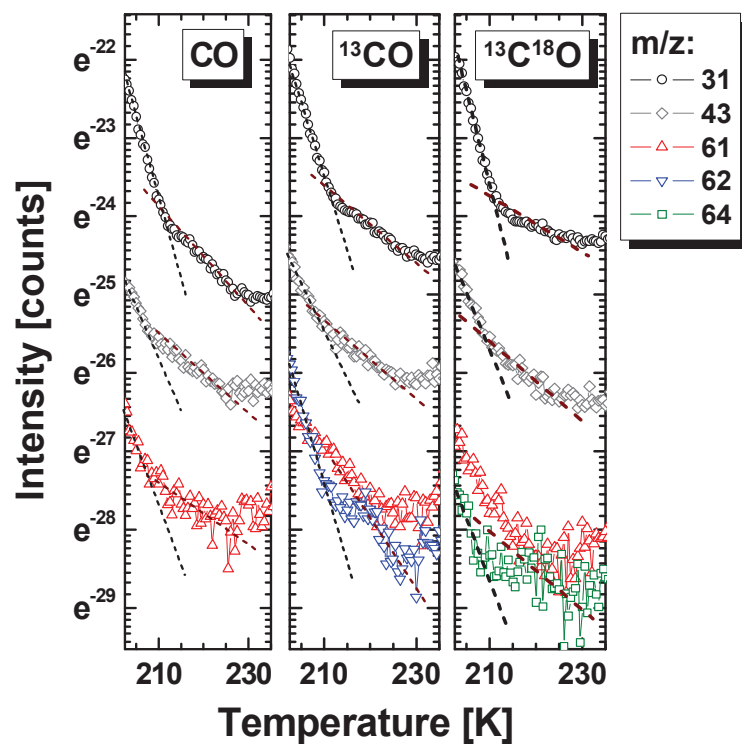
Figure 3.5: Comparison between the fragments of three QMS TPD spectra in the range from 202 to 235 K. The spectra are obtained after 15 K co-deposition of HOCH$_2$CHO molecules with H atoms and regular CO (left spectrum), ^{13}CO (central spectrum), or ^{13}C^{18}O (right spectrum) labeled isotopes. The total CO (^{13}CO, ^{13}C^{18}O) and HOCH$_2$CHO fluences amount to 7×10^{15} molecules cm^{-2}. The total H-atom fluence amounts to 2×10^{17} atoms cm^{-2}. The ordinate axis is presented as a natural logarithm, and an exponential decay should appear as a straight line. Dashed lines are added to highlight the presence of a distinct source of ions appearing at ~210 K, consistent with glyceraldehyde desorption.

are recorded after the co-deposition of HOCH$_2$CHO with H atoms and CO, ^{13}CO, or ^{13}C^{18}O molecules, respectively, discussed in the glycerol section. The results for the same m/z values as used before, i.e., 31, 43, 61, 62, and 64, are shown, where m/z = 31, 43, and 61 correspond to the most intensive peaks in the glyceraldehyde mass spectrum (NIST database; Brittain et al. 1971). For clarity, the ordinate axis is depicted as a natural logarithm scale, where exponential decay appears as a straight line. A clear deviation from a straight decay starting from 210 K for m/z = 31 and m/z = 43 (and possibly m/z = 61) plots is observed, indicating the appearance of a new species. In this case both the desorption temperature and the affected m/z values are in line with the desorption of glyceraldehyde monomers. Further evidence constraining the desorption of new species between 215 and 220 K is obtained in the ^{13}CO-labeled experiments, in which a clear desorption peak for m/z = 62 is observed, while in the ^{13}C^{18}O-labeled experiment a peak at m/z = 64 may be present. These observations point to the formation of glyceraldehyde in the performed experiments. However, an unambiguous assignment, as in the case of glycerol, is not possible at this stage and requires the use of more sensitive or selective techniques (Maity et al. 2015; Oba et al. 2016; Paardekooper et al. 2016a). However, given the positive identification of glycerol, following the reaction scheme shown in Figure 3.1, formation of glyceraldehyde is plausible with the observations presented here.

3.5   CONCLUSIONS AND ASTRONOMICAL RELEVANCE

Our laboratory results successfully demonstrate that in accordance with the reaction scheme presented in Figure 3.1, three-carbon-bearing COMs can be formed starting from simple accretion of H atoms and CO molecules on the surface of interstellar grains. Conclusive evidence for glycerol formation has been obtained in a set of selected isotope-labeled experiments. The formation of glyceraldehyde is shown to be plausible. The reaction scheme presented in Figure 3.1 is the extension of the well-studied CO + H hydrogenation chain, resulting in the formation of H$_2$CO and CH$_3$OH ice. This solid-state reaction chain is included in many astrochemical models, to explain solid and gas-phase CH$_3$OH observations in dark clouds and young stellar objects. Thus, the reaction routes investigated in this study can be used to extend already-existing astrochemical simulations. In this respect, the lattice-gas kinetic Monte Carlo simulations are the most promising, as they account for the specific lattice position for each of the intermediate radicals required to form COMs with two, three, and more carbon atoms (Cuppen et al. 2013; Vasyunin & Herbst 2013a; Chang & Herbst 2016; Garrod et al. 2017). However, the direct implications of the formation routes presented in Figure 3.1 require better knowledge of branching ratios and the activation barriers of various H-atom addition and abstraction reactions. Moreover, the correct implementation of quantum tunneling rate constants is of importance, as these also affect branching ratios for various H-atom addition and abstraction reactions (Lamberts et al. 2016). These issues can be partially overcome by extrapolating branching ratios and activation barriers from similar reactions investigated in previous studies (Fedoseev et al. 2015). In the latter case, the authors employed a model previously used to fit laboratory data of H$_2$CO and CH$_3$OH formation (Fuchs et al. 2009) and extrapolate the results to astrochemical timescales. H-atom abstraction reactions were omitted, and the effective reaction activation barrier for H-atom addition to the aldehyde group of HOCH$_2$CHO was assumed to be equal to the effective reaction activation barrier of H-atom addition to H$_2$CO as obtained in Fuchs et al. (2009). In a similar way, a first approximation could be made for H-atom addition to the aldehyde group of HOCH$_2$CH(OH)CHO. The R-ĊHOH/R-CH$_2$O· branching ratios obtained in these H-atom addition reactions can be set to 0.5 or 1 to provide estimates from above for the amount of formed COMs.

With increasing carbon chain length, the expected COM yields reduce strongly for each of the newly added -C(O)-segments. This complicates the assignment of larger species in the experiments starting from pure CO hydrogenation. The ice samples enriched with two-carbon-bearing precursors are used to confirm formation of the three-carbon-bearing COMs and further exploit the reaction scheme shown in Figure 3.1. In addition to the experimentally obtained $HOCH_2CH_2OH/CH_3OH$ ratio of $\sim 0.01 - 0.09$ previously reported by Fedoseev et al. (2015), an $HOCH_2CH(OH)CH_2OH/HOCH_2CH_2OH$ ratio of ~ 0.01 is reported in present study. It should be stressed, however, that this value is obtained under strong assumptions that include similar ionization cross sections and pumping rates of both molecules. Astrochemical simulations are needed to predict astronomically relevant abundance ratios.

Glycolaldehyde and ethylene glycol have been observed in solar-mass protostars. The present study shows that reactions of H and CO with glycolaldehyde can lead to large oxygen-rich COMs in cold dark clouds, i.e., without the need of 'energetic processing' of the ice mantle. Instead, 'non-energetic' H-atom addition and abstraction reactions provide the reactive intermediates to generate glycerol and likely glyceraldehyde. So far, similar results for oxygen-rich three-carbon-bearing COMs were only presented after VUV photon or cosmic-ray irradiation of CH_3OH-containing ices, where various reactive intermediates, i.e., $\cdot CH_2OH$, $CH_3O\cdot$, $\cdot CH_3$, $H\dot{C}O$, etc., are obtained by CH_3OH dissociation with impinging particles (Kaiser et al. 2015; Maity et al. 2015; Paardekooper et al. 2016a). The latter process is effective but lacks the selectivity of an H-atom-induced reaction scheme as shown in Figure 3.1. Furthermore, H-atom-induced reactions do not cause newly formed species to fragment, in contrast to impinging VUV photons or cosmic rays. It should be stressed, however, that the formation path for simple sugars and sugar alcohols as presented here does not contradict the 'energetic route' suggested in these studies. It rather complements these, showing that COMs of astrobiological importance can be formed as early as the cold dark cloud stage, during the CO freeze-out stage, and well before formation of the protostar and heating of the dust occurs. COMs produced on icy dust grains in this early stage of star formation can, in turn, be locked on the grain surface and participate in active 'energetic processing' during later stages, or even be released into the gas phase by shocks, heat, or photodesorption (Charnley & Rodgers 2008; Herbst & van Dishoeck 2009; Caselli & Ceccarelli 2012; Walsh et al. 2014a,b; Jiménez-Serra et al. 2016). Their efficient release into the gas phase by heat and photodesorption is unlikely, however, due to the low volatility of such complex species and a tendency of even the simplest COMs (e.g., CH_3OH) to photodissociate and desorb as fragments, rather than as an intact molecule (Bertin et al. 2016). As a consequence, these heavy-weight COMs have a higher chance to remain on grain surfaces during the later stages of ice evolution.

The astronomical importance of our experimental findings is emphasized by the astrobiological role of the obtained species. Glycerol is a necessary component of phospholipids (consisting of fatty acids, glycerol, and inorganic phosphate) composing the membranes of living cells. Glyceraldehyde is the simplest sugar that plays a key role in the energy transfer inside the cells of living organisms. Furthermore, the formation of glycerol and glyceraldehyde along the steps discussed here means that even larger sugar and sugar alcohols are expected to be formed by hydrogenation of accreting CO molecules, as shown in Figure 3.1. Thus, the presence of simple sugars and sugar alcohols on young planets is possible under the assumption that at least a fraction of the original icy-dust material survives upon transfer to the early planet surface or, alternatively, is delivered by comets or other celestial bodies during the late bombardment stage of the early Earth. From this point of view, it should be noticed that the reaction scheme suggested in Figure 3.1 has to result in the formation of racemic mixtures of simple sugars and sugar alcohols, and the selection of D- over L-stereoisomers should occur at one of the later evolutionary stages.

BIBLIOGRAPHY

Abou Mrad, N., Duvernay, F., Chiavassa, T., & Danger, G. 2016, Mon. Not. R. Astron. Soc., 458, 1234

Allamandola, L. J., Sandford, S. A., & Valero, G. J. 1988, Icarus, 76, 225

Anton, R., Wiegner, T., Naumann, W., et al. 2000, Review of Scientific Instruments, 71, 1177

Baratta, G. A. & Palumbo, M. E. 1998, Journal of the Optical Society of America A, 15, 3076

Bertin, M., Romanzin, C., Doronin, M., et al. 2016, Astrophys. J. Lett., 817, L12

Biver, N., Bockelée-Morvan, D., Debout, V., et al. 2014, Astron. Astrophys., 566, L5

Boogert, A. C. A., Gerakines, P. A., & Whittet, D. C. B. 2015, Ann. Rev. Astron. Astrophys., 53, 541

Bottinelli, S., Boogert, A. C. A., Bouwman, J., et al. 2010, Astrophys. J., 718, 1100

Brittain, E. F. H., George, W. O., & Collins, G. C. S. 1971, J. Chem. Soc. B, 2414

Burke, D. J., Puletti, F., Brown, W. A., et al. 2015, Mon. Not. R. Astron. Soc., 447, 1444

Butscher, T., Duvernay, F., Theule, P., et al. 2015, Mon. Not. R. Astron. Soc., 453, 1587

Caselli, P. & Ceccarelli, C. 2012, Astron. Astrophys. Rev., 20, 56

Cernicharo, J., Kisiel, Z., Tercero, B., et al. 2016, Astron. Astrophys., 587, L4

Chang, Q. & Herbst, E. 2016, Astrophys. J., 819, 145

Charnley, S. B. & Rodgers, S. D. 2008, Space Science Reviews, 138, 59

Charnley, S. B., Rodgers, S. D., & Ehrenfreund, P. 2001, Astron. Astrophys., 378, 1024

Chuang, K.-J., Fedoseev, G., Ioppolo, S., van Dishoeck, E. F., & Linnartz, H. 2016, Mon. Not. R. Astron. Soc., 455, 1702

Chuang, K.-J., Fedoseev, G., Qasim, D., et al. 2017, Mon. Not. R. Astron. Soc., 467, 2552

Coutens, A., Persson, M. V., Jørgensen, J. K., Wampfler, S. F., & Lykke, J. M. 2015, Astron. Astrophys., 576, A5

Cuppen, H. M., Karssemeijer, L. J., & Lamberts, T. 2013, Chemical Reviews, 113, 8840

Cuppen, H. M., Penteado, E. M., Isokoski, K., van der Marel, N., & Linnartz, H. 2011, Mon. Not. R. Astron. Soc., 417, 2809

Cuppen, H. M., van Dishoeck, E. F., Herbst, E., & Tielens, A. G. G. M. 2009, Astron. Astrophys., 508, 275

Fedoseev, G., Chuang, K.-J., van Dishoeck, E. F., Ioppolo, S., & Linnartz, H. 2016, Mon. Not. R. Astron. Soc., 460, 4297

Fedoseev, G., Cuppen, H. M., Ioppolo, S., Lamberts, T., & Linnartz, H. 2015, Mon. Not. R. Astron. Soc., 448, 1288

Fuchs, G. W., Cuppen, H. M., Ioppolo, S., et al. 2009, Astron. Astrophys., 505, 629

Garrod, R., Park, I. H., Caselli, P., & Herbst, E. 2006, Faraday Discussions, 133, 51

Garrod, R. T., Belloche, A., Müller, H. S. P., & Menten, K. M. 2017, Astron. Astrophys., 601, A48

Garrod, R. T., Widicus Weaver, S. L., & Herbst, E. 2008, Astrophys. J., 682, 283

Geppert, W. D., Hellberg, F., Österdahl, F., et al. 2005, in IAU Symposium, Vol. 231, Astrochemistry: Recent Successes and Current Challenges, ed. D. C. Lis, G. A. Blake, & E. Herbst, 117–124

Goesmann, F., Rosenbauer, H., Bredehöft, J. H., et al. 2015, Science, 349

Halfen, D. T., Ilyushin, V. V., & Ziurys, L. M. 2015, Astrophys. J. Lett., 812, L5

Henderson, B. L. & Gudipati, M. S. 2015, Astrophys. J., 800, 66

Herbst, E. & van Dishoeck, E. F. 2009, Ann. Rev. Astron. Astrophys., 47, 427

Hidaka, H., Watanabe, M., Kouchi, A., & Watanabe, N. 2009, Astrophys. J., 702, 291

Hiraoka, K., Ohashi, N., Kihara, Y., et al. 1994, Chemical Physics Letters, 229, 408

Hollis, J. M., Lovas, F. J., & Jewell, P. R. 2000, Astrophys. J. Lett., 540, L107

Hollis, J. M., Lovas, F. J., Jewell, P. R., & Coudert, L. H. 2002, Astrophys. J. Lett., 571, L59

Hudson, R. L. & Moore, M. H. 2000, Icarus, 145, 661

Ioppolo, S., Fedoseev, G., Lamberts, T., Romanzin, C., & Linnartz, H. 2013, Review of Scientific Instruments, 84, 073112

Jheeta, S., Domaracka, A., Ptasinska, S., Sivaraman, B., & Mason, N. J. 2013, Chemical Physics Letters, 556, 359

Jiménez-Serra, I., Vasyunin, A. I., Caselli, P., et al. 2016, Astrophys. J. Lett., 830, L6

Jørgensen, J. K., Favre, C., Bisschop, S. E., et al. 2012, Astrophys. J. Lett., 757, L4

Jørgensen, J. K., van der Wiel, M. H. D., Coutens, A., et al. 2016, Astron. Astrophys., 595, A117

Kaiser, R. I., Maity, S., & Jones, B. M. 2015, Angewandte Chemie International Edition, 54, 195

Lamberts, T., Samanta, P. K., Köhn, A., & Kästner, J. 2016, Phys. Chem. Chem. Phys., 18, 33021

Le Roy, L., Altwegg, K., Balsiger, H., et al. 2015, Astron. Astrophys., 583, A1

Linnartz, H., Ioppolo, S., & Fedoseev, G. 2015, International Reviews in Physical Chemistry, 34, 205

Maity, S., Kaiser, R. I., & Jones, B. M. 2015, Phys. Chem. Chem. Phys., 17, 3081

McGuire, B. A., Carroll, P. B., Loomis, R. A., et al. 2016, Science, 352, 1449

McManus, J. R. 2014, PhD thesis, University of Pennsylvania

Meinert, C., Myrgorodska, I., de Marcellus, P., et al. 2016, Science, 352, 208

Modica, P. & Palumbo, M. E. 2010, Astron. Astrophys., 519, A22

Oba, Y., Takano, Y., Watanabe, N., & Kouchi, A. 2016, Astrophys. J. Lett., 827, L18

Öberg, K. I. 2016, Chemical Reviews, 116, 9631

Öberg, K. I., Garrod, R. T., van Dishoeck, E. F., & Linnartz, H. 2009, Astron. Astrophys., 504, 891

Paardekooper, D. M., Bossa, J.-B., & Linnartz, H. 2016a, Astron. Astrophys., 592, A67

Paardekooper, D. M., Fedoseev, G., Riedo, A., & Linnartz, H. 2016b, Astron. Astrophys., 596, A72

Patel, A., Yamashita, N., Ascaño, M., et al. 2015, Nature Communications, 6, 10119

Pontoppidan, K. M. 2006, Astron. Astrophys., 453, L47

Pontoppidan, K. M., Fraser, H. J., Dartois, E., et al. 2003, Astron. Astrophys., 408, 981

Prasad, S. S. & Tarafdar, S. P. 1983, Astrophys. J., 267, 603

Ritson, D. & Sutherland, J. D. 2012, Nature Chemistry, 4, 895

Rivilla, V. M., Beltrán, M. T., Cesaroni, R., et al. 2017, Astron. Astrophys., 598, A59

Shalabiea, O. M. & Greenberg, J. M. 1994, Astron. Astrophys., 290, 266

Sutherland, J. D. 2017, Nature Reviews Chemistry, 1, 0012

Taquet, V., López-Sepulcre, A., Ceccarelli, C., et al. 2015, Astrophys. J., 804, 81

Taquet, V., Wirström, E. S., & Charnley, S. B. 2016, Astrophys. J., 821, 46

Tielens, A. G. G. M. & Hagen, W. 1982, Astron. Astrophys., 114, 245

Tielens, A. G. G. M., Tokunaga, A. T., Geballe, T. R., & Baas, F. 1991, Astrophys. J., 381, 181

Tschersich, K. G. 2000, Journal of Applied Physics, 87, 2565

Vasyunin, A. I. & Herbst, E. 2013a, Astrophys. J., 762, 86

Vasyunin, A. I. & Herbst, E. 2013b, Astrophys. J., 769, 34

Walsh, C., Herbst, E., Nomura, H., Millar, T. J., & Weaver, S. W. 2014a, Faraday Discussions, 168, 389

Walsh, C., Millar, T. J., Nomura, H., et al. 2014b, Astron. Astrophys., 563, A33

Watanabe, N. & Kouchi, A. 2002, Astrophys. J. Lett., 571, L173

Woods, P. M., Kelly, G., Viti, S., et al. 2012, Astrophys. J., 750, 19

Zhitnikov, R. A. & Dmitriev, Y. A. 2002, Astron. Astrophys., 386, 1129

PRODUCTION OF COMPLEX ORGANIC MOLECULES: H-ATOM ADDITION VERSUS UV IRRADIATION

Complex organic molecules (COMs) have been identified in different environments in star forming regions. Laboratory studies show that COMs form in the solid state, on icy grains, typically following a 'non-energetic' (atom-addition) or 'energetic' (UV-photon absorption) trigger. So far, such studies have been largely performed for single processes. Here, we present the first work that quantitatively investigates both the relative importance and the cumulative effect of '(non-)energetic' processing. We focus on astronomically relevant $CO:CH_3OH$ = 4:1 ice analogues exposed to doses relevant for the collapse stage of dense clouds. Hydrogenation experiments result in the formation of methyl formate (MF; $HC(O)OCH_3$), glycolaldehyde (GA; $HC(O)CH_2OH$) and ethylene glycol (EG; $H_2C(OH)CH_2OH$) at 14 K. The absolute abundances and the abundance fractions are found to be dependent on the H-atom/$CO:CH_3OH$ molecule ratios and on the overall deposition rate. In the case that ices are exposed to UV photons only, several different COMs are found. Typically, the abundance fractions are 0.2 for MF, 0.3 for GA and 0.5 for EG as opposed to the values found in pure hydrogenation experiments without UV in which MF is largely absent: 0.0, 0.2 − 0.6 and 0.8 − 0.4, respectively. In experiments where both are applied, overall COM abundances drop to about half of those found in the pure UV irradiation experiments, but the composition fractions are very similar. This implies COM ratios can be used as a diagnostic tool to derive the processing history of an ice. Solid-state branching ratios derived here for GA and EG compare well with observations, while the MF case cannot be explained by solid-state conditions investigated here.

4.1 INTRODUCTION

Complex organic molecules (COMs) are regarded as the building blocks of species that are inherent to life. In space, COMs have been unambiguously identified in very different environments (Herbst & van Dishoeck 2009), such as toward the Galactic Centre in hot cores and giant molecular clouds (Hollis et al. 2000; Martín-Pintado et al. 2001; Requena-Torres et al. 2006, 2008; Belloche et al. 2013), toward low- and high-mass proto-stars (Blake et al. 1987; Neill et al. 2014; Tercero et al. 2015; Jørgensen et al. 2012, 2016; Caselli & Ceccarelli 2012; Coutens et al. 2015; Taquet et al. 2015; Rivilla et al. 2016), molecular outflows (Arce et al. 2008; Codella et al. 2015), photon-dominated regions (Guzmán et al. 2013), as well as toward dark cloud cores and pre-stellar cores (Marcelino et al. 2007; Bacmann et al. 2012; Öberg et al. 2010, 2011b; Cernicharo et al. 2012; Vastel et al. 2014; Jiménez-Serra et al. 2016). With eight and ten atoms, the simplest sugar, glycolaldehyde (HC(O)CH$_2$OH, hereafter GA), and the simplest sugar alcohol, ethylene glycol (H$_2$C(OH)CH$_2$OH, hereafter EG), can be considered amongst the largest organic molecules detected so far in the interstellar medium (ISM). GA has been observed toward solar-mass proto-stars (Jørgensen et al. 2012, 2016; Coutens et al. 2015) and in comets (Crovisier et al. 2004; Biver et al. 2014; Goesmann et al. 2015; Le Roy et al. 2015) together with chemically related species, such as EG or methyl formate (CH(O)OCH$_3$, hereafter MF), one of the corresponding isomers. It is generally accepted that these species form in the solid state, on icy dust grains and are often found chemically linked to other O-bearing COMs in star-forming regions (Rivilla et al. 2016). Recent work on the spatial distribution of COMs in the L1544 pre-stellar core (with T<10 K) revealed that O-bearing gas-phase COMs are more abundant toward a low-density (A$_V$~7.5 − 8 mag) shell, where gas-phase methanol also peaks, than toward the denser (A$_V \geqslant$30 mag) continuum peak (Jiménez-Serra et al. 2016). At A$_V$~7-8 mag, CO molecules start freezing-out onto the grains (Pontoppidan 2006; Boogert et al. 2015). An enhancement of factors ~2 − 10 in the abundance of O-bearing COMs in the outer shell of L1544 can be explained by the surface formation of COMs in a CO-rich ice environment followed by non-thermal desorption. In the outer shell, visual extinctions are indeed high enough for COMs to avoid photo-dissociation by the external interstellar radiation field, but they are not high enough for COMs to be completely accreted onto the ice grains (Jiménez-Serra et al. 2016). In such environments, both 'non-energetic' (atom bombardment) and 'energetic' (cosmic rays (CR) induced UV photons) formation routes can result in the formation of COMs.

In dense clouds, CO is the second most abundant ice species along with CO$_2$ on grain surfaces with a relative abundance ranging from 20 to 45 per cent with respect to water ice (Boogert et al. 2015). Most of the CO ice is formed through accretion from the gas-phase during the so-called catastrophic CO freeze-out stage, when it accretes onto layers of preformed water ice, resulting in a CO-rich apolar ice coating (Tielens et al. 1991; Pontoppidan 2006; Gibb et al. 2004; Öberg et al. 2011a; Mathews et al. 2013; Boogert et al. 2015). At this stage, CO is the starting point in hydrogenation schemes that result in H$_2$CO and CH$_3$OH formation through successive ('non-energetic') H-atom addition reactions. This surface reaction scheme is generally considered as the pathway to explain the observed gaseous CH$_3$OH abundances in space (Geppert et al. 2005), a conclusion that is supported by theoretical and modelling studies (Tielens & Hagen 1982; Shalabiea & Greenberg 1994; Cuppen et al. 2009; Vasyunin & Herbst 2013a) as well as compelling laboratory experiments (Hiraoka et al. 1994; Watanabe & Kouchi 2002; Zhitnikov & Dmitriev 2002; Fuchs et al. 2009; Linnartz et al. 2015). CH$_3$OH ice has been detected with abundances ranging from 1 to 25 per cent with respect to water ice (Bottinelli et al. 2010; Boogert et al. 2015). Indeed, spectroscopic studies of CO ice, comparing astronomical spectra (Pontoppidan et al. 2003; Penteado et al. 2015) and laboratory spectro-

scopic ice data (LDI[4.1]), confirm that CH_3OH and CO are intimately mixed in interstellar ices (Cuppen et al. 2011; Penteado et al. 2015). In the follow-up studies (Fedoseev et al. 2015; Butscher et al. 2015; Chuang et al. 2016), it was shown that these 'non-energetic' reactions also offer pathways toward COM formation at temperatures as low as 10 K along steps of the $CO \xrightarrow{2H} H_2CO \xrightarrow{2H} CH_3OH$ reaction scheme, through recombination reactions of reactive intermediates, e.g., HCO, CH_2OH and CH_3O, that form both in addition and abstraction reactions. This results in the unambiguous formation of GA, EG and MF, fully in line with astrochemical models that hint at COM formation early in the cosmochemical cycle, namely in dark interstellar clouds (Charnley & Rodgers 2005; Woods et al. 2012).

Laboratory studies involving 'energetic' processing of CH_3OH ice, e.g., UV photolysis (Gerakines et al. 1996; Öberg et al. 2009; Paardekooper et al. 2016a; Öberg 2016), electron impact (Henderson & Gudipati 2015; Maity et al. 2015) and ion bombardment (Moore & Hudson 2005; Modica & Palumbo 2010), show that it is also possible to form GA, EG and MF as well as a several other COMs in CH_3OH-rich interstellar ice analogues. Upon irradiation, for example, the methanol dissociates, and the reactive free radicals recombine, forming larger species, such as acetaldehyde, ethanol and dimethyl ether, as well as the three COMs that are investigated here.

Clearly, completely different triggers, involving similar reactive intermediates, result in the formation of similar species, but not necessarily with comparable (relative) abundances, and this knowledge may be used as a tool to relate the role of specific chemical processes to specific astronomical environments. In dark and dense clouds, impacting H atoms are the dominating process and thermal processing can be fully neglected. However, the internal UV radiation field, which is due to cosmic-ray excitation of molecular hydrogen, can influence the ice chemistry. In translucent clouds, hot cores, and proto-planetary disks, the 'energetic' processing will be much more relevant; thermal effects are at play for the higher temperatures and particularly UV radiation fields are much more intense than in dense cold quiescent regions.Moreover, further gas-phase chemistry leads to the formation of COMs upon sublimation of second-generation species from icy dust grains (Charnley et al. 1992; see also Herbst & van Dishoeck (2009) for a review). Recently, Vasyunin & Herbst (2013b), Balucani et al. (2015) and Taquet et al. (2016) proposed that MF and other complex species may also be produced through low temperature gas-phase routes. However, the abundances derived from their models do not always match the observational data. Finally, COMs have also been identified mass spectrometrically in cometary objects (Goesmann et al. 2015; Le Roy et al. 2015) that consist of the planetesimals built during the proto-planetary stage. The investigation of the chemical connection between interstellar and cometary ices is an important future goal (Mumma & Charnley 2011) that has become further within reach through all recent data for 67P and the launch of JWST in 2018.

In this paper, we present for the first time laboratory studies that allow to quantitatively compare COM formation through hydrogenation and UV-induced reactions as well as their cumulative effect in interstellar ice analogues. The combined experiments are relevant to conditions in dark interstellar clouds as described above and have been applied in the past for other systems. Watanabe et al. (2007) investigated the competition between hydrogenation and photolysis in a pre-deposited H_2O:CO ice mixture. Another more recent study showed that, for the case of NO hydrogenation and UV photolysis, hydroxylamine (NH_2OH) is efficiently formed upon hydrogenation of NO molecules, but once UV photons are added, the presence of NH_2OH in the ice diminishes and the available nitrogen gets locked in three

---

[4.1]See the Leiden Database for Ice at http://icedb.strw.leidenuniv.nl/, which is maintained by the Sackler Laboratory for Astrophysics.

chemically linked species: HNCO, OCN$^-$ and H$_2$NCHO (Congiu et al. 2012; Fedoseev et al. 2016). This finding has been taken as one of the arguments for the non-detection of NH$_2$OH in space despite a number of dedicated surveys and to explain the observed correlation between HNCO and H$_2$NCHO abundances (Pulliam et al. 2012; McGuire et al. 2015).

Here, we focus on three specific COMs: GA, EG and MF. As stated, these three COMs are amongst the most commonly produced complex species in both 'energetic' and 'non-energetic' ice processing. We compare the laboratory findings for the MF/EG, MF/GA and GA/EG solid-state abundance ratios for different experiments with those found for the gas-phase abundance ratios in different astronomical environments. In this approach, we make two assumptions: first, we consider EG, GA and MF as representative products in the COM formation schemes, realizing that we neglect other (higher generation) COMs that form, but typically with lower abundances; second, it is not a priori clear that solid-state and gas-phase abundance ratios scale one to one. This depends on the sublimation process that bridges the grain-gas gap and that may be triggered by shocks, heat or chemical, reactive and photo-desorption processes (Garrod et al. 2008; Herbst & van Dishoeck 2009; Öberg et al. 2009; Fayolle et al. 2011; Minissale et al. 2016). Moreover, the sublimated species could subsequently participate in further chemical reactions in the gas phase. Whereas thermal desorption is a smooth and fast process leaving the ice molecules intact, photo-desorption tends to dissociate COMs upon excitation. This will be discussed in the final section. First the experimental procedure is described and subsequently the results are discussed.

4.2   EXPERIMENTAL PROCEDURE

4.2.1   *Experimental set-up*

All experiments are performed under ultra-high vacuum (UHV) conditions, using SURFRESID-E^2. Details of this set-up and measurement procedures have been described by Ioppolo et al. (2013). The experiments are performed in a main chamber with a base pressure of $\sim$10^{-10} mbar. In its centre, a gold-coated copper substrate is positioned so that it is connected to a closed-cycle helium cryostat, reaching temperatures as low as 13 K and onto which ices are grown. Resistive heating allows temperatures up to 330 K. In order to perform hydrogenation and UV irradiation experiments simultaneously, the icy substrate can be exposed to H atoms formed in a Hydrogen Atom Beam Source (HABS; Tschersich 2000, mounted in a second UHV chamber, and UV photons generated by a Microwave Discharge Hydrogen flowing Lamp (MDHL) that is directly attached to the main chamber (see Fedoseev et al. 2016 for more details). The UV light is guided through an MgF$_2$ window and hits the substrate at normal incidence, covering the whole area of the gold substrate (2.5 $\times$ 2.5 cm^2). The optical axis of the lamp intersects the surface at a 45° angle with the H-atom beam and at a 22° angle with the two available molecular deposition lines. The H-atom flux of the HABS and UV-photon flux as well as the spectrum of the MDHL have been well calibrated in a number of previous experiments (see Ioppolo et al. 2013; Ligterink et al. 2015). The UV spectrum ranging between 114 and 220 nm consists of a main peak at 121.6 nm (Ly-α, 33 per cent of the total flux) and a series of other peaks between 155 and 165 nm (H$_2$ emission, 20 per cent of the total flux) superposed on a broad continuum (47 per cent of the total flux) with the total UV flux estimated to be $(4.1 \pm 0.5) \times 10^{12}$ photons cm^{-2} s^{-1}, with $\sim$13 per cent of relative uncertainty. The laboratory UV spectrum resembles quite accurately the spectrum produced by CRs interacting with H$_2$ in dense clouds. H-atom fluxes applied here are 6$\times$10^{12} and 1$\times$10^{12} atoms cm^{-2} s^{-1} in high and low co-deposition rate experiments, respectively. In dense clouds, icy dust grains experience both atom addition and UV irradiation. This results in a 3 : 2 H-atom to

UV-photon exposure; the H-atom flux ($\sim 10^4$ atoms cm^{-2} s^{-1}) is either comparable or higher than that of the UV photons (CR-induced UV-photon flux $(1\text{-}10) \times 10^3$ photons cm^{-2} s^{-1}; see Prasad & Tarafdar 1983; Mennella et al. 2003; Shen et al. 2004). It should be noted that an absolute H-atom flux is given. The effective H-atom flux can be significantly lower. This is due to the difference in sticking probability between room temperature H atoms as used in the laboratory and 10-20 K cold H atoms as expected in dense clouds. Furthermore, the ~ 10 orders of magnitude higher H-atom flux used in the laboratory results in a significantly higher H-atom recombination rate, reducing the amount of H atoms available for the reaction with CO.

4.2.2 *Experimental methods*

All performed experiments utilize a co-deposition technique, which is the simultaneous deposition of ices with H atoms and/or UV photons. This overcomes the problem of a limited H-atom penetration depth into the bulk of the ice compared to the larger UV-photon penetration depth and, also, is more representative of the actual processes taking place in the ISM, where atoms and molecules continuously adsorb onto grains. The chosen CO:CH$_3$OH = 4:1 ratio is a representative value for ice ratios found in quiescent dense clouds observations toward background stars and observations of low-mass young stellar objects (YSOs) (see Boogert2015), although it should be stressed that other mixing ratios have been observed as well (Pontoppidan et al. 2004; Cuppen et al. 2011). The CO:CH$_3$OH ice mixtures are grown by simultaneous deposition of CO and CH$_3$OH on top of a pre-deposited (10 Langmuir) argon (Ar) ice. The Ar layer further prevents direct interactions between deposited molecules and photo-electrons potentially produced by the interaction between the incident UV photons and the gold substrate (gold work function > 4.7 eV; see Hopkins & Riviere 1964). CO (Linde 2.0) is used for ice deposition and H$_2$ (Praxair 5.0) is used for the H-atom source and MDHL. Liquid CH$_3$OH (Sigma-Aldrich, 99.8 per cent) is purified through three freeze-pump-thaw cycles before it is used as a mixture component. The ice thickness is derived using a modified Beer's law with a calibrated absorbance strength that is measured by He-Ne laser interference experiments during ice growth on SURFRESIDE^2, following a similar procedure as described by Paardekooper et al. (2016b).

Ices are monitored in situ by Fourier Transform Reflection-Absorption InfraRed Spectroscopy (FT-RAIRS) in the range from 700 to 4000 cm^{-1}, with 1 cm^{-1} resolution. After completion of a co-deposition experiment, a temperature-programmed desorption experiment using a Quadrupole Mass Spectrometer (TPD QMS) is performed. For each species, the desorption temperature and ionized fragment pattern are unique and used to identify the resulting COMs. In order to compare GA, EG and MF yields, the desorption QMS signals are integrated, then normalized to the total column density of the most abundant carbon-bearing species observed by RAIRS at the end of the co-deposition (see Fedoseev et al. 2015; Chuang et al. 2016). Then, the obtained values for GA, EG and MF are calibrated using the available literature ionisation cross-section values (Hudson et al. 2003, 2006; Bull & Harland 2008). The uncertainty in the abundance determination is statistically derived by averaging the result from a number of identical experiments. The lack of HCO, CH$_3$O and CH$_2$OH observations at the end of the hydrogenation experiments (Chuang et al. 2016) shows that the radical recombination during the heating process is negligible under our experimental conditions. Table 4.1 lists the relevant experiments performed for this work.

Table 4.1: Overview of the performed experiments.

No.	Experiments	T_{sample} (K)	Ratio (CO:CH$_3$OH)	Flux$_{(CO+CH_3OH)}$ (cm^{-2} s^{-1})	Flux$_H$ (cm^{-2} s^{-1})	Flux$_{UV}$ (cm^{-2} s^{-1})	Time (s)	COM Composition Fraction MF	GA	EG
1	CO+CH$_3$OH+H	14	4:1	1.2E+13	6.0E+12	-	3600	0	0.2	0.8
2	CO+CH$_3$OH+hν	14	4:1	1.2E+13	-	4.0E+12	3600	0.2	0.3	0.5
3	CO+CH$_3$OH+H+hν	14	4:1	1.2E+13	6.0E+12	4.0E+12	3600	0.2	0.3	0.5

No.	Control Experiments	T_{sample} (K)	Ratio (CO:CH$_3$OH)	Flux$_{(CO+CH_3OH)}$ (cm^{-2} s^{-1})	Flux$_H$ (cm^{-2} s^{-1})	Flux$_{UV}$ (cm^{-2} s^{-1})	Time (s)	COM Composition Fraction MF	GA	EG
1.1	CO+CH$_3$OH+H$_2$	14	4:1	1.2E+13	-	-	3600	-	-	-
1.2	CO+CH$_3$OH+H	14	4:1	2.0E+12	1.0E+12	-	21600	<0.05	0.4	0.6
1.3	CO+CH$_3$OH+H	14	4:1	2.0E+12	6.0E+12	-	21600	<0.05	0.6	0.4
3.1	CO+CH$_3$OH+H$_2$	14	4:1	1.2E+13	-	-	3600	-	-	-
3.2	CO+CH$_3$OH+H$_2$(100%)+hν	14	4:1	1.2E+13	-	4.0E+12	3600	0.2	0.3	0.5
3.3	CO+CH$_3$OH+ H$_2$(70%)+hν	14	4:1	1.2E+13	-	4.0E+12	3600	0.2	0.3	0.5
4.1	CO+CH$_3$OH+Ar(100%)+hν	14	4:1	1.2E+13	-	4.0E+12	3600	0.2	0.25	0.55
4.2	CO+CH$_3$OH+Ar(70%)+hν	14	4:1	1.2E+13	-	4.0E+12	3600	0.2	0.3	0.5
4.3	CO+CH$_3$OH+Ar(30%)+hν	14	4:1	1.2E+13	-	4.0E+12	3600	0.2	0.3	0.5

Note. MF=HC(O)OCH$_3$, GA=HC(O)CH$_2$OH, and EG=H$_2$C(OH)CH$_2$OH

4.3 RESULTS AND DISCUSSION

Experiments 1-3 are performed to study and compare the isolated effect of hydrogenation and UV photolysis and the combined effect of both, respectively, on the formation of COMs in a co-deposited $CO:CH_3OH = 4:1$ mixture at 14 K. All three experiments are intentionally performed under the same experimental conditions and for well-chosen parameter settings in order to compare the different formation/destruction mechanisms. Also control experiments are performed, directly linked to exps. 1 (1.1-1.3) and 3 (3.1-3.3) or for other settings (4.1-4.3). The details are summarized in Table 4.1.

The results are summarized in Figure 4.1 that shows the absolute abundances (upper panel) and composition fractions (lower panel) for MF, GA and EG resulting from experiments 1-3. A comparison of the absolute abundances for the three experiments reveals that under the selected and identical experimental conditions (i) H-atom addition induced surface reactions lead to the lowest values for the three COMs. It should be noted that to select an astrophysical relevant H-atom/UV-photon flux of ~1, a high H-atom flux is used for this set of experiment. However, by performing an experiment that has the same overall H-atom fluence of exps. 1 and 3 in the longer timescale (i.e., lower flux and longer exposition time; exp. 1.2), the COM yields resemble those of the pure UV-photolysis experiment except for MF. A lower H-atom flux is closer to the conditions in the ISM. These flux-dependent experiments are discussed in Section 3.1.1; (ii) the highest amount of COMs comes from pure UV photolysis of the ice; (iii) the combination of hydrogenation and UV photons leads to lower amounts of COMs than in the case of pure UV photolysis. These findings are briefly introduced and discussed in more detail from Section 4.3.1 onward.

In exp. 1, smaller absolute amounts of GA and EG are detected from TPD QMS data and the composition fraction of the three COMs is given as 0.0 for MF, 0.2 for GA and 0.8 for EG, respectively. In this case, the formation of MF in detectable amounts is only unambiguously confirmed when UV light is used. Indeed, H-atom-induced abstraction from CH_3OH results in the preferential formation of CH_2OH rather than CH_3O radicals (Hidaka et al. 2009; Chuang et al. 2016). The CH_3O radical can be produced by the hydrogenation of H_2CO that, however, is not one of the initial components of the ice mixture and therefore mainly builds-up upon hydrogenation of CO molecules. On the contrary, CH_3O is abundantly formed upon photolysis of CH_3OH ice. The COM formation yields obtained in exp. 2 are the highest of the three selected experiments and are ~50 per cent higher than those found in exp. 3. This is not surprising because the impinging UV photons can efficiently release their energy to both the surface and bulk of the ice. As a consequence, many molecular bonds are broken and, in timescales of picoseconds, the molecular fragments can recombine giving rise to a rearrangement of the chemical structure that leads to the formation of new and often more complex molecular species. In exp. 3, an overabundance of H atoms can reduce COM formation rates through their recombination with the HCO, CH_2OH and CH_3O radicals produced by UV photons. This favours the production of simpler species and rather uniformly reduces the formation of more complex ones. As discussed later in the text, segregation by H_2 molecules, i.e., the case in which free radicals produced by photo-dissociation are spatially separated by abundantly present H_2 molecules, also reduces COM yield rates. It should be noted that although the cumulative effect of 'energetic' and 'non-energetic' processes frustrates COM formation, this should not be generalized. For instance, in Fedoseev et al. (2016), NH_2OH is formed by the hydrogenation of NO and simultaneously destroyed by UV photolysis to form HNCO, OCN^- and NH_2CHO, when the initial NO ice is mixed in $CO/H_2CO/CH_3OH$-rich environments. In the work presented here, the composition fractions of COMs for exps. 2 and 3 are similar and amount to ~0.2 for MF, ~0.3 for GA and ~0.5 for EG. This indicates that the larger amount of
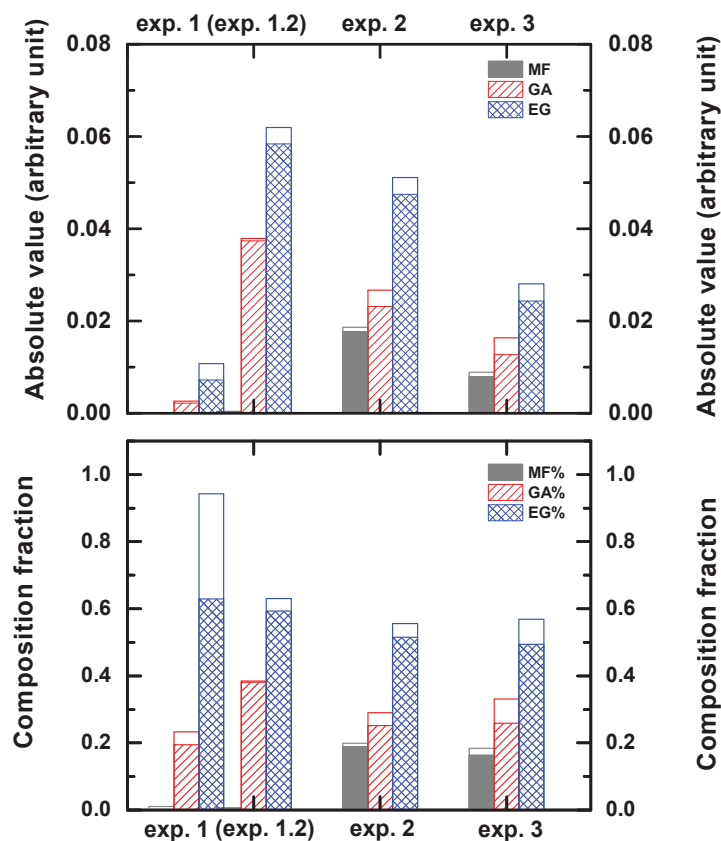
Figure 4.1: Absolute abundances (upper panel) and composition fractions (lower panel) for MF, GA and EG as obtained in QMS TPD experiments for pure hydrogenation (exps. 1 and 1.2), pure UV photolysis (exp. 2) and simultaneous UV-photon irradiation and H-atom addition (exp. 3), all for 14 K CO:CH$_3$OH = 4:1 ice mixtures. Experiment 1.2 is performed under the same experimental conditions and overall fluence as exp. 1, except its timescale is six times longer. Values are calibrated using the corresponding ionization cross-sections and are normalized for the total amount of carbon-bearing molecules observed before performing the TPD experiment. White bars show the standard errors estimated from independent experiments.
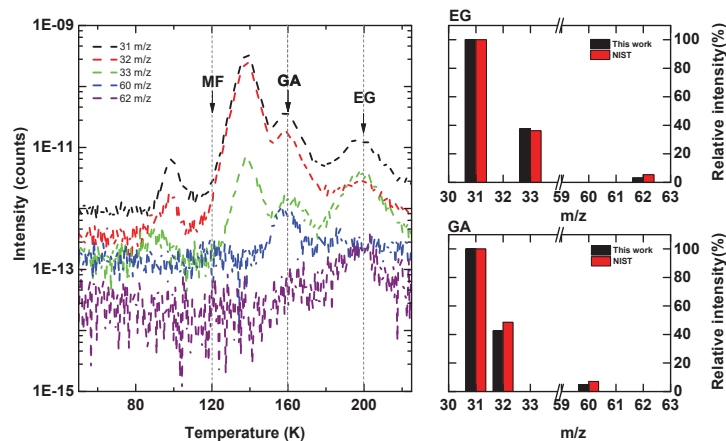
Figure 4.2: The left-hand panel shows part of TPD QMS spectra obtained after co-deposition of CO:CH$_3$OH = 4:1 ice mixtures with H-atom flux 6.0×10^{12} atoms cm^{-2} s^{-1} at 14 K (exp. 1.3) for m/z = 31, 32, 33, 60, 62 amu. Peaks at T ~120, 160 and 200 K correspond to MF, GA and EG. For the latter two species, their fragmentation patterns upon 70 eV electron impact ionization are compared to the available literature values on the right-hand panels.

COMs still originates from UV-induced reactions even for exp. 3 under our experimental conditions. Below, a detailed discussion of the results from exps. 1-3 is presented, as well as from a series of selected control experiments (exps. 1.1-4.3) performed to constrain the chemistry and physics at play.

4.3.1   Hydrogenation of CO:CH$_3$OH ice mixtures

A set of experiments (exps. 1 and 1.1-1.3) is performed to study the hydrogenation of CO:CH$_3$OH ice mixtures for different overall deposition rates and H/ices ratio settings. Figure 4.2 presents the results of a typical experiment (exp. 1.3). Here QMS TPD spectra are shown and obtained after hydrogenation of a CO:CH$_3$OH ice mixture at 14 K. Previous laboratory studies have shown that upon CO ice hydrogenation not only H$_2$CO and CH$_3$OH form (Watanabe & Kouchi 2002; Fuchs et al. 2009), but also GA and EG are produced (Fedoseev et al. 2015). The experiments presented here are fully consistent with this finding. Two of the TPD peaks desorbing at lower temperature are due to H$_2$CO (~100K) and CH$_3$OH (~140 K). Two other peaks at higher temperatures can be assigned to species with heavier masses. The first peak is located around 160 K, and the second one around 200 K. Based on the available desorption values reported by Öberg et al. (2009), and in recent work by Fedoseev et al. (2015) and Maity et al. (2015), these two peaks are assigned to GA and EG, respectively. In addition, their QMS spectra for 70 eV electron ionization energy are largely consistent with the corresponding
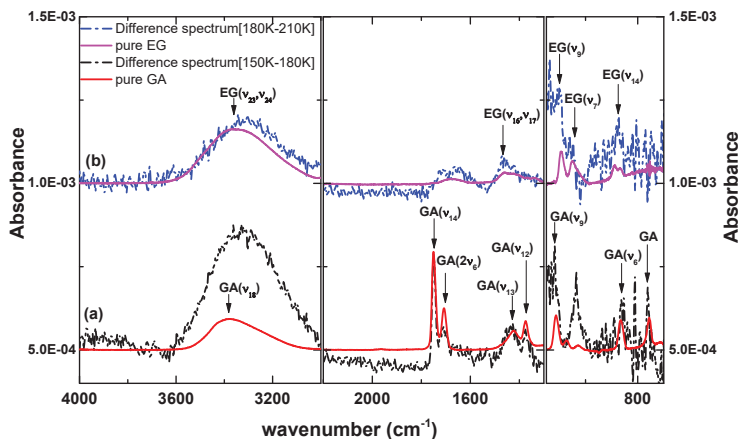
Figure 4.3: RAIR difference spectra (dash-dotted lines) are presented for the experiment of CO:CH$_3$OH = 4:1 ice mixtures with H-atom flux 6.0×10^{12} atoms cm^{-2} s^{-1} at 14 K (exp. 1.3) during TPD between 150 and 180 K (a) as well as between 180 and 210 K (b). These are compared to pure GA and EG RAIR spectra (solid lines), respectively. The arrows indicate the IR absorption peaks of the corresponding COMs.

NIST database values (see footnote 4.2). Only traces of MF (a peak of 60 *m/z* centred around 120 K) can be observed in this experiment.

Furthermore, in Figure 4.3, the comparison between the difference spectra (dash dotted lines) obtained for chosen temperature ranges during TPD and the spectra of pure GA and EG ice (solid lines) provides additional evidence that both GA, sublimating between 150 and 180 K (a), and EG, sublimating between 180 and 210 K (b), are formed. Two absorption peaks around 1036 and 3320 cm^{-1} are likely due to thermal co-desorption of trapped CH$_3$OH with the aforementioned COMs.

The presence of COMs in the ice upon H-atom addition can be explained through two mechanisms that may take place simultaneously. The first one has been previously discussed by Woods et al. (2012) and experimentally verified by Fedoseev et al. (2015). First, the hydrogenation of CO leads to the formation of HCO intermediate radicals. Their recombination, in turn, yields glyoxal (HC(O)CHO) as a side product. The latter one is subsequently hydrogenated to form GA and EG via

$$HCO + HCO \longrightarrow HC(O)CHO \xrightarrow{2H} HC(O)CH_2OH \xrightarrow{2H} H_2C(OH)CH_2OH. \quad (20)$$

The second mechanism has been described by Chuang(2016). H-atom additions and H-atom-induced abstractions in the CO $\longleftrightarrow$ H$_2$CO $\longleftrightarrow$ CH$_3$OH reaction network result in the formation of HCO, CH$_3$O and CH$_2$OH intermediate radicals. Subsequent radical-radical recom-

---

[4.2] NIST Mass Spec Data Center, S.E. Stein, director, 'Mass Spectra' in NIST Chemistry WebBook, NIST Standard Reference Database Number 69, Eds. P.J. Linstrom and W.G. Mallard, National Institute of Standards and Technology, Gaithersburg MD, 20899, http://webbook.nist.gov.
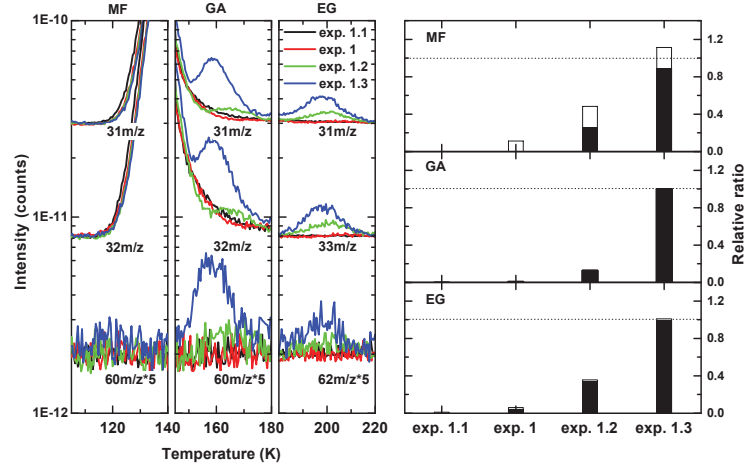
Figure 4.4: Left-hand panels: the TPD QMS spectra obtained after co-deposition of CO:CH$_3$OH = 4:1 ice mixtures with H atoms (exps. 1, 1.2 and 1.3) and blank experiment (exp. 1.1) at 14 K; *m/z* channels are shifted for clarity. The H-atom fluxes in exps. 1, 1.2 and 1.3 amount to 6.0×10^{12}, 1.0×10^{12} and 6.0×10^{12} atoms cm^{-2} s^{-1}, while the total H-atom fluences are 2.2×10^{16}, 2.2×10^{16} and 1.3×10^{17} atoms cm^{-2}, respectively. The total amount of deposited CO and CH$_3$OH molecules is kept constant in all four experiments. Only the relevant *m/z* numbers and selected desorbing temperatures are shown for MF, GA and EG. Right-hand panels: relative comparison of the integrated intensities of MF (upper panel), GA (middle panel) and EG (lower panel) obtained by TPD QMS and normalized for the total amount of CO, H$_2$CO and CH$_3$OH observed prior to the TPD experiment. Subsequently, each signal is normalized to its maximum yield. The white bars indicate the standard errors derived statistically from an independent set of experiments.

bination leads to the formation of GA and further hydrogenation results in the formation of EG:

$$HCO + CH_2OH \longrightarrow HC(O)CH_2OH \xrightarrow{2H} H_2C(OH)CH_2OH. \tag{21}$$
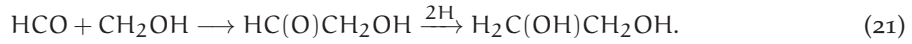
The successive formation of HC(O)CH$_2$OH by recombination of HCO and CH$_2$OH radicals was also reported by Butscher et al. (2015). EG can also be formed by the recombination of two CH$_2$OH radicals. Although not found in the IR spectra due to its low production yield and the limited detection sensitivity of RAIRS, MF is formed through the radical-radical recombination of HCO and CH$_3$O radicals. Here, only traces of MF can be observed by means of TPD QMS (e.g., exp. 1.3).

4.3.1.1   *Overall deposition rate and H-atom/ice ratio dependences*

In this paragraph, we focus on the influence of the overall H-atom and CO:CH$_3$OH deposition rates as well as H-atom to CO:CH$_3$OH co-deposition ratios on the formation efficiency of MF, EG and GA. In Figure 4.4, zoom-in views of the TPD QMS spectra of CO:CH$_3$OH ice mixtures

co-deposited with H atoms are shown for different experimental conditions, i.e., for the same H-atom to CO:CH$_3$OH co-deposition ratio, but for two different overall combined deposition rates (exps. 1 versus 1.2); and for the same number of deposited CO:CH$_3$OH molecules, but for two different H-atom fluxes (exp. 1.2 versus. 1.3). The H-atom and CO:CH$_3$OH fluxes in exp. 1 amount to 6.0×10^{12} atoms cm^{-2} s^{-1} and 1.2×10^{13} molecules cm^{-2} s^{-1} during 60 minutes of co-deposition. In exp. 1.2, these values are 1.0×10^{12} atoms cm^{-2} s^{-1} and 2.0×10^{12} molecules cm^{-2} s^{-1} during 360 minutes of co-deposition, i.e., the same final fluences of $\sim 2.2 \times 10^{16}$ atoms cm^{-2} and $\sim 4.4 \times 10^{16}$ molecules cm^{-2} are obtained. In exp. 1.3, the same flux of H atoms as in exp. 1 is applied (6.0×10^{12} atoms cm^{-2} s^{-1}), while the CO:CH$_3$OH flux is kept the same as in exp. 1.2 (2.0×10^{12} molecules cm^{-2} s^{-1}) for the duration of 360 minutes, resulting in a six times higher fluence of H atoms ($\sim 1.3 \times 10^{17}$ atoms cm^{-2}) and an unchanged number of deposited CO:CH$_3$OH molecules ($\sim 4.4 \times 10^{16}$ molecules cm^{-2}) in exps. 1 and 1.2-1.3. The blank experiment (exp. 1.1) is shown for reference. The three left-hand panels in Figure 4.4 show the selected TPD QMS spectra and the relevant m/z signals for our three COMs. For MF, the sublimation temperature is around 120 K, and mass scans for the two strongest m/z fragment signals, i.e., CH$_3$O$^+$ (31 m/z) and CH$_3$OH$^+$ (32 m/z), as well as the precursor signal HC(O)OCH$_3$$^+$ (60 m/z) are presented. The desorbing peaks around 160 K assigned to GA are found for three (isomer) mass signals, i.e., CH$_2$OH$^+$ (31 m/z), CH$_3$OH$^+$ (32m/z) and HC(O)CH$_2$OH$^+$ (60 m/z). For EG, the sublimating peak is around 200 K, and its ionization fragments are CH$_2$OH$^+$ (31m/z), CH$_3$OH$_2$$^+$ (33 m/z) and the molecular precursor signal H$_2$C(OH)CH$_2$OH$^+$ (62 m/z).

Besides the qualitative identification of the newly formed COMs through their TPD QMS spectra, also quantitative information can be retrieved by integrating their desorption profiles and normalizing them for the total amount of CO, H$_2$CO and CH$_3$OH, i.e., those species that carry the largest amount of carbon in the ice. The results are shown on the right-hand panels of Figure 4.4 and presented as MF, GA and EG, each normalized to its maximum yield.

The blank experiment (CO + CH$_3$OH + H$_2$, exp. 1.1) exhibits, as one expects, no evidence for COM formation. In experiment 1, GA and EG are produced but in much smaller amounts compared to exps. 1.2 and 1.3. The formation follows the mechanisms mentioned before, and the ineffective formation of MF in exps. 1, 1.2 and 1.3 is consistent with previous studies that link this observation to the lack of the intermediate CH$_3$O radicals in the ice bulk, when a CO:CH$_3$OH mixture is co-deposited with H atoms (Chuang et al. 2016). In experiment 1.2, the H-atom and CO:CH$_3$OH fluxes are both reduced by a factor of 6 compared to exp. 1, but the total H-atom and CO:CH$_3$OH fluence in exps. 1 and 1.2 remains the same. It is found that in exp. 1.2 the amount of produced GA and EG is 15 and 7 times higher than in exp. 1, respectively. This is an important experimental finding as the higher production efficiency comes with a lower overall deposition rate. Moreover, traces of MF are found in exp. 1.2. Finally, exp. 1.3 has the same molecule flux as exp. 1.2, but six times higher H-atom flux, i.e., identical to exp. 1. Thus, exp. 1.3 results in the same number of exposed molecules as in experiment 1 and 1.2 but is performed with six times higher total H-atom fluence. The measured abundances of GA, EG and MF in exp. 1.3 are now 8, 3 and 3 times higher, respectively, in comparison to exp. 1.2 resulting in GA/EG ratios changing from 0.6 to 2.

Experiment 1.2, i.e., with a lower H-atom and CO:CH$_3$OH deposition rate than exp. 1, aims to better mimic the grain surface reactions under dense cloud conditions. The decrease of overall co-deposition flux and the corresponding increase in reaction time reduce the number of barrierless H-H recombination events that fully dominate the surface chemistry when high H-fluxes are applied at short laboratory time-scales. Here, the low accretion rates of H atoms allow them to scan a larger part of an ice surface before meeting another H atom (Fuchs et al. 2009). Thus, a lower H-atom deposition rate enhances the possibility of H-atom addition and

abstraction reactions, which, in turn, increases the amount of formed intermediate radicals and COM formation efficiencies. The purpose of exp. 1.3 is to further enhance the number of effective interactions between H atoms and $CO:CH_3OH$ molecules by increasing the H-atom flux with a factor of six compared to exp. 1.2 but keeping the $CO:CH_3OH$ deposition rate as used in exp. 1.2; this way molecules and radicals will be exposed to multiple interactions with H atoms before the limited H-atom penetration depth in the ice will prevent species to be further (de)hydrogenated (Cuppen et al. 2009; Fuchs et al. 2009). Again differences in the COM composition fractions are observed, as a function of overall deposition rate (comparison between exps. 1 and 1.2) and of H atom/ice ratio (comparison between exps. 1.2 and 1.3). The ratio of GA/EG changes from 0.3 to 0.6 to 2 in exps. 1.1, 1.2 and 1.3, respectively. The possible explanation for the enhanced GA/EG ratio is the fact that the formation of GA requires two times less H-atom addition events than the formation of EG (see reactions 20 and 21). These larger amounts of GA with respect to EG follow the increase in the overall COM formation yields. Only traces of MF can be detected in exps. 1.2 and 1.3. This is explained by the lack of CH_3O radicals that are mainly formed through the hydrogenation of H_2CO, a species formed in the ice and not present in the initial sample (Chuang et al. 2016). To sum up, three COMs can be formed upon hydrogenation of CO-rich ices and the relative formation efficiencies depend not only on effective H-atom/($CO:CH_3OH$) deposition ratio, but also on the overall accretion rate of the involved species. MF is not abundantly formed in these experiments.

4.3.2   *UV photolysis and combined UV and H-atom exposure of $CO:CH_3OH$ ice mixtures*

Experiment 2 is performed to study the effect of UV photolysis of $CO:CH_3OH$ ice mixtures on the formation of COMs in the ice. Experiment 3 focusses on the effect of simultaneous hydrogenation and UV irradiation of the same initial ice, while exps. 3.1-4.3 are mainly performed to control that the undissociated H_2 molecules present in the H-atom beam and those recombined on the surface of the ice do not participate in the reaction network. Figure 4.5 (three left-hand panels) shows the TPD QMS spectra for exps. 2, 3 and 3.2 (i.e., simultaneous deposition of UV photons and H_2 molecules). The results for the blank experiment (exp. 3.1) are also shown. In particular, the left-hand panels of Figure 4.5 show the relevant *m/z* signals for MF (31, 32 and 60 *m/z*), GA (31, 32 and 60 *m/z*) and EG (31, 33 and 62 *m/z*) at 120, 160 and 200 K, respectively, that can be interpreted as discussed in Section 4.3.1. In an identical way, the COM abundances obtained by integrating TPD QMS spectra are normalized for the final amount of the carbon-bearing CO, H_2CO, CH_3OH and CH_4 molecules (right-hand panels of Figure 4.5), and MF, GA and EG are each normalized to their maximum yield. The reason for also including CH_4 here, in contrast to exps. 1 and 1.1-1.3, is that only in the UV-photolysis experiments (exps. 2, 3 and 3.1-4.3), methane formation $((0.5-1)\times10^{15}$ molecules cm$^{-2})$ is expected and confirmed by RAIR spectra obtained at the end of the co-deposition. Note that the highest yields for the three COMs under investigation here are found in the pure UV experiment (exp. 2), whereas in the two other experiments (exps. 3 and 3.2) the simultaneous use of UV irradiation and H-atom bombardment substantially reduces the formation rate. In exp. 3.2, the COM yields with respect to those in exp. 2 amount to ∼0.7, which is slightly higher than $0.5-0.6$ found in exp. 3. As expected, the blank experiment (CO + CH_3OH + H_2, exp. 3.1) shows no evidence for COM formation.

Given the low gas-phase CH_3OH abundances during deposition we can exclude that any UV-triggered gas-phase processes substantially affect the solid-state reactions that are studied here. Öberg et al. (2009) published the results of an experiment for a pre-deposited $CO:CH_3-OH$ = 1:1 ice mixture exposed to UV photons at 20 K, and identified the formation of MF, EG,
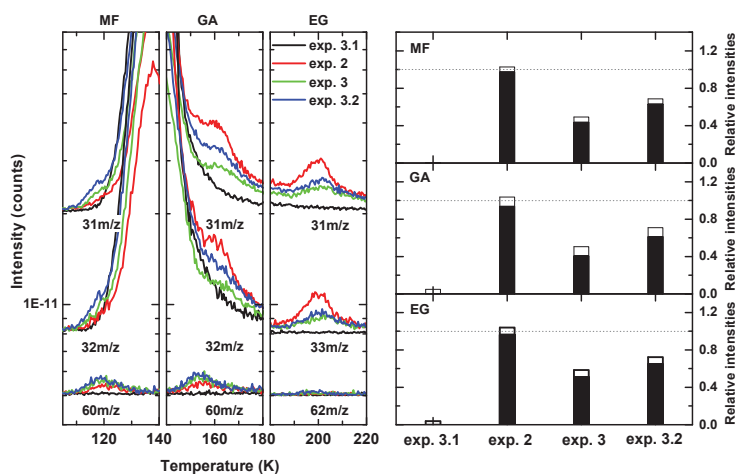
Figure 4.5: Left-hand panels: TPD QMS spectra obtained after co-deposition of CO:CH$_3$OH ice mixtures in a ratio of 4:1 with UV-photons (exp. 2), simultaneous UV photons and H atoms (exp. 3), UV photons and H$_2$ molecules (exp. 3.2), as well as a blank experiment (exp. 3.1) at 14 K. The *m/z* channels are presented with offsets for clarity. The UV-photon flux amounts to 4.0×10^{12} photons cm^{-2} s^{-1} for exps. 2, 3 and 3.2. Only relevant *m/z* numbers and selected desorbing temperatures are shown for MF, GA and EG. Right-hand panels: relative comparison of the integrated intensities of MF (upper panel), GA (middle panel) and EG (lower panel) obtained by TPD QMS and normalized for the total amount of carbon-bearing molecules observed prior to TPD. Subsequently, each signal is normalized to its maximum yield. White bars show the standard errors estimated statistically from a set of independent experiments.

GA as well as other COMs. The present set of experiments is different, as the irradiation takes place during the deposition, with a different $CO:CH_3OH = 4:1$ ratio, and at lower temperature (14 K; e.g., exp. 2). The deposited molecules are irradiated by the incoming UV photons with an energy up to 10.2 eV, which is enough to photo-dissociate CH_3OH into radicals, i.e. CH_2OH, CH_3O, CH_3, OH, etc., but not enough to directly photodissociate CO molecules. The newly formed intermediate radicals recombine directly to form COMs in the bulk of the ice, resulting in the formation of MF, GA and EG via

$$HCO + CH_3O \longrightarrow HC(O)OCH_3 \tag{22}$$

$$HCO + CH_2OH \longrightarrow HC(O)CH_2OH \tag{23}$$

$$CH_2OH + CH_2OH \longrightarrow H_2C(OH)CH_2OH \tag{24}$$

or other COMs Öberg et al. (2009).

In dense clouds, the H-atom flux is larger than the UV-photon flux. However, from a comparison between the published H_2CO formation rate values upon UV photolysis of CH_3OH ice and hydrogenation of CO ice (Gerakines et al. 1996; Fuchs et al. 2009; Öberg et al. 2009), it becomes clear that the efficiency of producing radicals by photo-dissociation is (much) larger than by hydrogenation. Moreover, Öberg et al. (2009) discussed the possibility that the presence of H atoms on the grain surface consumes 'frozen-in' radicals, leading to the formation of smaller products before they can grow larger species. In their pre-deposition experiment, this effect is not very significant because the H-atom penetration depth is limited to a few (top) monolayers and H atoms formed upon UV photolysis will mostly leave the surface because of the higher temperature. In the present work, we co-deposit ice constituents with H atoms and H_2 molecules during UV-irradiation (exps. 3 and 3.2, respectively). The recombination of H atoms and radicals produced upon photolysis, therefore, will be more prominent, increasing the efficiency of this chemical pathway. For instance, in exp. 3, the abundant H atoms recombine with the photo-induced radicals instead of participating in further hydrogenation of the parent ice mixtures. This results in an enhancement of products, such as CH_4 and H_2O, as confirmed by RAIR spectra, through the reactions:

$$H + CH_3 \longrightarrow CH_4 \tag{25}$$

$$H + OH \longrightarrow H_2O, \tag{26}$$

and that have been studied before, see e.g., Cuppen et al. (2010).

The results presented in Figure 4.5 focus on the formation of MF, GA and EG. These are also the main COM products upon pure H-atom addition reactions, but their formation efficiency is influenced as a result of the competition between COM formation (reactions 22—24) and competing hydrogenation reactions (reactions 25—26). In both exps. 3 and 3.2, molecular hydrogen is co-deposited with $CO:CH_3OH$ during UV irradiation, in exp. 3.2 as a main constituent and in exp. 3 mainly as a result of an incomplete dissociation process, which amounts

to ~70 per cent of the hydrogen molecules deposited in exp. 3.2 (Tschersich et al. 2008). In previous studies (Fuchs et al. 2009; Lamberts et al. 2013), it was shown that the role of H_2 in surface chemical processes is rather limited as the involved activation barriers with H_2 cannot be easily overcome for temperatures below 15 K. However, in exp. 3.2, we find a clear COM reduction which is less than that found in exp. 3. To understand the role of H_2 in the reaction network, Ar is used instead of H_2 in co-deposition with UV photons impacting on CO:CH_3OH in a series of control experiments (exps. 4.1-4.3, details are discussed in the Appendix).

Finally, it is also important to consider the role of UV-induced photo-desorption. A large number of laboratory studies have been performed on the photo-desorption rates of CO and CH_3OH ice (Öberg et al. 2007, 2009; Fayolle et al. 2011; Muñoz Caro et al. 2010; Chen et al. 2014; Bertin et al. 2016; Paardekooper et al. 2016a; Cruz-Diaz et al. 2016), and even though there exist some discrepancies between the exact values, roughly within an order of 10, this does not prevent the ability to assess the role of photo-desorption in the present experiment. With photo-desorption rates of the order of 1×10^{-2} (1×10^{-3}) for pure CO ice and less than 1×10^{-4} for pure CH_3OH ice, typically for ices with temperatures around $15 - 20$ K, an estimate can be made. Applying these rates to the total UV-photon fluence, which is 1.3×10^{16} photons cm^{-2}, results in upper limits of photo-desorbed molecules of ~0.1 (0.01) ML for CO and ~0.001 ML for CH_3OH. This effect will not influence our results, specifically as the photodesorption rates in mixed ices are expected to further decrease Bertin et al. (2016).

4.3.3   *Summary of laboratory results*

Figure 4.6 compares the laboratory data taken in this work (left-hand panels) with some selected literature data (right-hand panels) of (i) hydrogenation of ice mixtures including CO/H_2CO/C-H_3OH at 15 K by Chuang et al. (2016), (ii) UV irradiation of pre-deposited CH_3OH and CH_3OH:CO ice at 20 K by Öberg et al. (2009), studied by RAIR and QMS techniques and (iii) UV exposure of pre-deposited pure CH_3OH ice at 20 K by Paardekooper et al. (2016a), studied by laser desorption post-ionization mass spectrometry.

For the hydrogenation experiment of CO:CH_3OH ice mixtures presented here (exp. 1.2), the MF/EG, MF/GA and GA/EG at 14 K values are 7×10^{-3}, 1×10^{-2} and 0.6, respectively. These values agree within a factor of 2 with those of similar experiments as reported in Chuang et al. (2016) (i.e., MF/EG = 4×10^{-3}, MF/GA = 1×10^{-2} and GA/EG=0.4). In the ice mixture experiments containing H_2CO molecules (Chuang et al. 2016), i.e., CO:H_2CO + H, and H_2CO:CH_3OH + H, the MF/EG and MF/GA values are enhanced by a factor of ~30, while the GA/EG value remains the same. This shows that, as previously discussed, the MF yields in the final COM compositions are substantially increased if the initial ice mixtures contain H_2CO. For the hydrogenation experiments of pure ice, i.e., CO + H and H_2CO + H, the final COM compositions are GA dominated over the other COMs, most likely because GA is the first product of the glyoxal (HC(O)HCO) hydrogenation reaction or of the HCO and CH_2OH radical-radical recombination. A similar GA/EG ratio is found in exp. 1.3, where H_2CO is also clearly detected.

The MF/EG, MF/GA and GA/EG 14 K values for pure UV photolysis (exp. 2) amount to 0.4, 0.7 and 0.5, respectively, in reasonable agreement with the values reported in Paardekooper et al. (2016a) (i.e., MF/EG = 0.4, MF/GA = 0.6 and GA/EG = 0.7 derived from their figure. 11). The deviation from the Öberg et al. (2009) values of pure CH_3OH ice (CO:CH_3OH ice mixtures) is much larger, namely, upper limit MF/EG = 0.1, MF/GA = 0.8 (2 for CO:CH_3OH ice mixtures) and upper limit GA/EG = 0.1. However, there exist experimental differences that may explain these different values. In Öberg et al. (2009) pre-deposition is used, but as the selected ices are not very thick, this is not expected to be the determining factor. Instead the
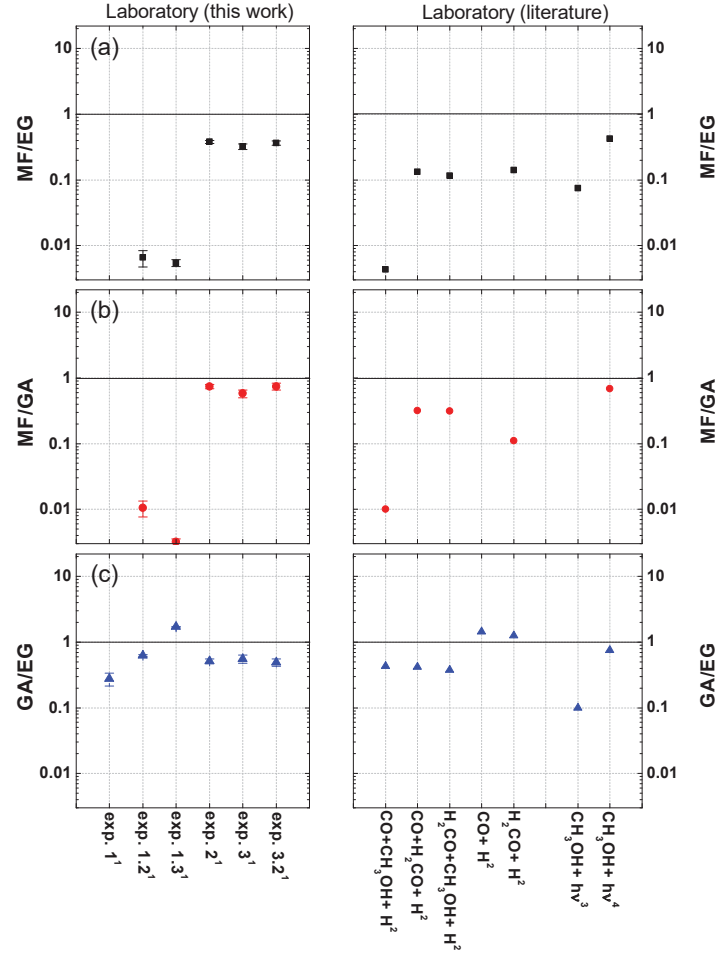
Figure 4.6: An overview of the relative ratios of MF/EG (a), MF/GA (b) and GA/EG (c), derived from laboratory data reported in the literature: (1) this work, (2) Chuang et al. (2016), (3) Öberg et al. (2009) and (4) Paardekooper et al. (2016a).

much higher UV-photon fluence of 2.4×10^{17} photons cm^{-2} likely pushes photochemistry beyond the point studied in our study and by Paardekooper et al. (2016a). So, this hints for a clear UV fluence dependence as well. Also the spectral emission characteristics of the H_2 discharge lamp differ from one experimental set-up to another. For instance, a higher H_2 flow pressure is used in our lamp settings resulting in a larger broadband H_2-emission contribution than just Ly-α (see Ligterink et al. 2015).

4.4 ASTROPHYSICAL IMPLICATIONS

It is widely accepted that COMs mainly form in the solid state. This is in agreement with a long list of experiments including those presented here that show how different ('energetic' and 'non-energetic') triggers result in the formation of rather similar species. However, as the underlying formation mechanisms differ, it is to be expected that the final COM abundance ratios in the solid state will vary. In the ISM, MF, EG and GA have only been directly observed in the gas phase. The experiments presented here show clear differences in relative MF, EG and GA ratios for pure hydrogenation, pure UV and combined hydrogenation and UV irradiation experiments. This is an interesting result and a comparison of the relative ratios of MF/GA, MF/EG and GA/EG offers - in principle - a further constraint to investigate the role of these processes during the chemical evolution of COMs in the ISM. In order to investigate this option, Figure 4.7 compares the laboratory data with astronomical values as derived from observations in different astronomical environments.

Observations used in Figure 4.7 include several comets (i.e., Hale-Bopp, Lemmon, Lovejoy and 67P/C6) and hot cores of low-mass proto-stars (i.e., IRAS16293-2422B, NGC1333 IRAS2A and NGC1333 IRAS4A) where ices are thermally desorbed. High-mass proto-stars are here excluded because they are generally characterized by a more intense UV field and higher temperatures resulting in further gas-phase chemistry. Comets form at large radii and are thought to harbour the most pristine chemical composition of earlier star-forming regions; in other words, they should preserve the initial pre-stellar ice abundances. Therefore, it is not surprising to find that the MF/EG and GA/EG ratios for the selected comets and low-mass proto-stars are roughly within an order of magnitude with respect to each other (Figure 4.7).

A first comparison of these data to our laboratory results shows that (i) observational MF/EG and MF/GA ratios are up to 3 orders of magnitude higher than found in laboratory hydrogenation experiments of $CO:CH_3OH$ mixtures and up to an order of magnitude higher than experiments that include UV processing; (ii) the observational GA/EG ratio is found in good agreement (i.e., within an order of magnitude) with our ('energetic'/'non-energetic') laboratory data, although hydrogenation experiments seem to reproduce better observations. As stated in previous sections, the lack of formed MF in the hydrogenation experiments comes from the chosen initial ice composition that does not include H_2CO. Results from Chuang et al. (2016) show that the MF/EG and MF/GA ratios obtained from hydrogenation experiments of H_2CO-containing ices are similar to those from the experiments involving UV photolysis shown here. Therefore, COM relative ratios are ice composition dependent in laboratory hydrogenation experiments, more so than for UV-photolysis studies because of the higher amount of radicals formed in the latter process. Simple cold cloud astrochemical models can then be used as a tool to better compare hydrogenation experiments with observations. The astrochemical models described in Cuppen et al. (2009) and Fedoseev et al. (2015) extend the CO hydrogenation scheme as studied in laboratories to dense cloud timescales and conditions. Fedoseev et al. (2015) in their model included the formation of simple ice molecules as well as GA and EG, but not MF. Their results on GA/H_2CO and EG/CH_3OH ratios were concluded to be in good agreement with observations of a solar-type proto-star (IRAS 16293-
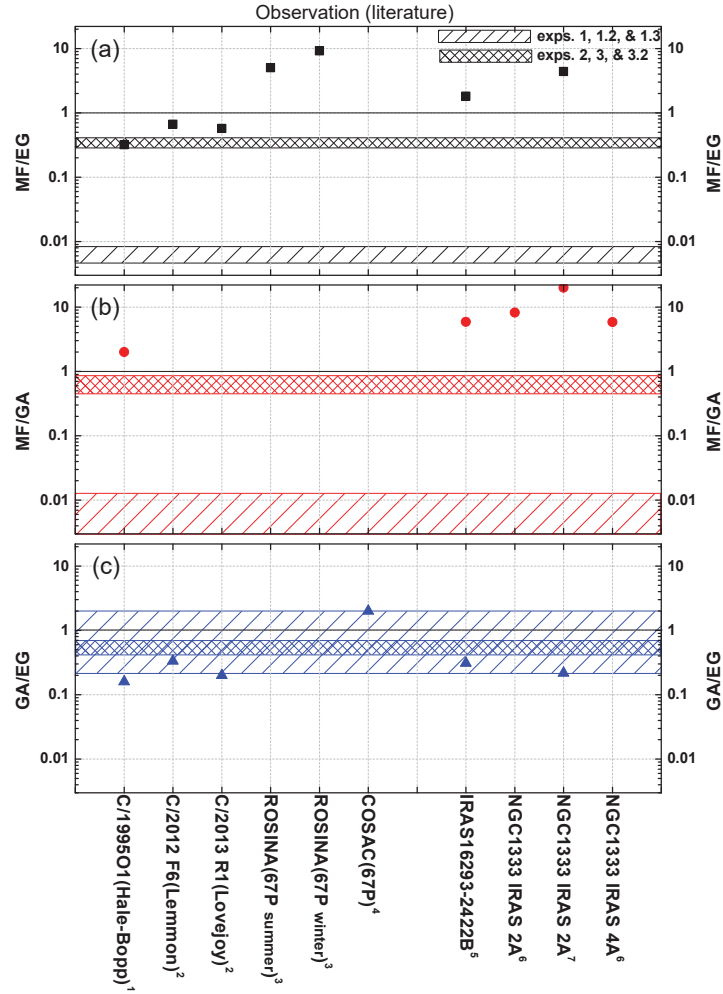
Figure 4.7: An overview of the relative ratios of MF/EG (a), MF/GA (b) and GA/EG (c), derived from astronomical observations reported in the literature. Observational data are taken from (1) Crovisier et al. (2004), (2) Biver et al. (2014), (3) Le Roy et al. (2015), (4) Goesmann et al. (2015), (5) Jørgensen et al. (2016), (6) Taquet et al. (2015) and (7) Coutens et al. (2015). The values of GA/EG and MF/EG for comets are presented as upper limits. In the case of MF/GA this is a lower limit. The shadow areas indicate the ranges of relative ratios taken from exps. 1, 1.2 and 1.3 (hydrogenation only) and exps. 2, 3 and 3.2 (including UV), respectively.

2422). This is a strong indication that GA and EG are efficiently formed in the solid phase through 'non-energetic' surface reactions in CO-rich ices, while MF formation most likely involves both 'energetic' and 'non-energetic' mechanisms in the solid phase and may even require some additional gas-phase route (Taquet et al. 2015).

A closer look at Figure 4.7 shows that ground-based observations, i.e., C/1995 O1-(Hale-Bopp) in Crovisier et al. (2004), C/2012 F6 (Lemmon) and C/2013 R1 (Lovejoy) in Biver et al. (2014), yield upper limit MF/EG ratios of $0.3 - 0.7$ and an upper limit of GA/EG of $0.1 - 0.2$ that are in good agreement as found in the UV-photon irradiation experiments by a factor of $\sim$3 (exps. 2-3 and 3.2, MF/EG = $0.3 - 0.4$ and GA/EG = $0.5 - 0.6$). The MF/GA = 2 value for comet Hale-Bopp is higher than the experimental UV irradiation results ($0.6 - 0.7$), by a factor of $\sim$3. Although speculative, such a difference may be due to a detection issue; Crovisier et al. (2004) indicated that their upper GA limit may have been underestimated. Another possible explanation is linked to the higher gas-phase reactive nature of GA (Hollis et al. 2001). This would cause GA to be further consumed, decreasing its overall abundance. However, in situ detections, like with ROSINA (Le Roy et al. 2015) or COSAC (Goesmann et al. 2015), measuring coma abundances and surface dust compositions for comet 67P provide complementary data. The resulting MF/EG = $5 - 9$ value indicates that MF is more abundant than EG, which is not consistent with other comet observations. Given the different desorption temperatures of MF, EG and other COMs, Le Roy et al. (2015) proposed that the detection of the coma composition depends on the comet surface temperature. This value varies with the comet's orbit and therefore it is not a good reference; MF, for example, desorbs at lower temperatures than EG. In the COSAC passive measurements, the GA/EG value is $\sim$2 (with an accuracy factor of $\sim$2). A similar value is only found in our study for the pure hydrogenation result in exp. 1.3 (GA/EG = 2). This is consistent with the picture that comets preserve their pre-stellar COM composition as formed upon hydrogenation reactions in the solid phase. The unambiguous MF detection by COSAC still needs to be confirmed. More recently, cometary ice models, including reactions proposed here, suggest that the abundance of GA is larger than that of MF (Drozdovskaya et al. 2016). The MF/GA ratios in the COM Torus model by Drozdovskaya et al. (2015) consider GA formation routes via H-atom additions.

GA, MF and EG, were detected for the first time toward a solar-mass proto-star by Jørgensen et al. (2012) using ALMA. Observations toward IRAS 2A and 4A also report the presence of these three COMs (Coutens et al. 2015; Taquet et al. 2015). The abundance of MF in these low-mass proto-stars is found to be higher than GA and EG, resulting in ratios of MF/GA and MF/EG larger than 1, i.e., roughly one order of magnitude higher than the experimental results presented here. The aforementioned GA gas-phase destruction rate and the MF enrichment through gas-phase chemistry upon CH_3OH sublimation could contribute to the observed enhanced MF/GA ratio (Balucani et al. 2015; Taquet et al. 2016). Concerning the GA/EG ratio in low-mass proto-stars, Coutens et al. (2015) proposed a value of 0.2 for IRAS 2A, which is of the same order of magnitude as found in exps. 2, 3 and 3.2 ($0.5 - 0.6$). The latest updated IRAS 16923B observations (Jørgensen et al. 2016) show a GA/EG ratio of 0.3, consistent with our UV-photon experiments, while still keeping a high abundance of MF.

As stated in Section 4.1, the comparisons discussed here have to be considered with care. It should be stressed that an abundance ratio in the gas phase does not necessarily reflect that from precursor species in the solid state, especially in cold clouds where thermal desorption, a relatively smooth process, is not possible and other processes are at play. Photodesorption, for example, can induce substantial fragmentation (Bertin et al. 2016). This will hold for most COMs; however, the ratio of the species that are desorbed without dissociation, in the end, may be representative again. Species may also desorb upon local hot spot formation, due to reactive desorption, i.e., using excess energy generated in a surface reaction, or

upon the interaction between the ice grain and a CR. This will clearly influence abundances of species that are formed in first or higher order reaction steps. Moreover, we have focussed here on CO:CH_3OH = 4:1 ices, neglecting H_2CO in the initial mixtures. It has been shown that formaldehyde-enriched ices are more effective in the formation of MF and that other astronomically relevant mixing ratios can lead to different COM formation ratios. Nevertheless, our results strongly support the hypothesis that interstellar solid MF, GA and EG (as well as probably other O-rich COMs) are formed at the same time in a CO ice during and after the catastrophic freeze-out of CO molecules in star-forming regions through a combination of 'energetic' and 'non-energetic' mechanisms.

4.5   CONCLUSIONS

In this work, we present for the first time a quantitative study that compares the influence of pure hydrogenation, pure UV irradiation and both hydrogenation and UV irradiation of CO:CH_3OH = 4:1 ice mixtures at experimental settings and exposure doses typical for the timeframes associated with the CO freeze out stage during the dense cloud collapse. We derive from the laboratory experiments a number of physical chemical dependences:

- Upon hydrogenation of CO-rich ices, MF, GA and EG are formed and their relative formation efficiencies depend on the effective H-atom/(CO:CH_3OH) deposition ratio as well as the used accretion rate of the involved species.
- Whereas GA and EG are formed quite efficiently, MF is produced in much lower abundances in experiments without UV, mainly because the amounts of H_2CO are low. As a consequence, the formation of the CH_3O radical is limited, whereas this has been found to be a primary precursor in the formation of MF.
- Upon UV irradiation, MF, GA and EG are formed (as well as several other COMs), but now MF is produced more efficiently as in this energetic scheme additional reaction pathways become accessible.
- In the combined H-atom and UV-photon exposure study, radicals formed upon photolysis are further hydrogenated; this decreases the overall formation efficiency but does not qualitatively affect the relative abundances.
- The formation ratios for MF:GA:EG for the three different types of experiments and a number of selected settings are summarized in Table 4.1 and Figure 4.1. These roughly range from 0:0.2 − 0.4:0.8 − 0.6 for pure hydrogenation to 0.2:0.3:0.5 for pure UV photolysis and combined hydrogenation and UV photolysis.

The astronomical take home message of these findings is that

- The different formation ratios for MF:GA:EG offer a diagnostic potential to derive the formation origin of these species in the solid state in different environments in space (Figure 4.7).
- Specifically, the GA/EG ratio observed in comets and in solar-mass proto-stars is consistent with the laboratory values derived for CO-rich ices in the hydrogenation, UV photolysis and combined experiments, and hints at pure solid-state formation pathways.
- Observed ratios involving MF (MF/GA and MF/EG) are not well reproduced in the laboratory experiments; typically we see less MF formed in the solid state than observed astronomically in the gas phase.
- Future experiments also adding H_2CO in the CO:CH_3OH mixture may result in MF/GA and MF/EG ratios that are closer to the astronomically data currently available. If not, this

may imply that MF in the ISM may also be formed in other ways, e.g., by gas-phase reactions.

4.6 APPENDIX

The substitution of Ar by H_2 results in similar formation yields for MF, EG and GA with relative abundances, 0.71, 0.74 and 0.66, respectively, that are slightly higher (i.e., within their experimental errors) than those in exp. 3.2 (right-hand panels in Figure 4.5). Therefore, the most likely explanation for a clear COM reduction in exps. 3.2 and 4.1 is that the presence of H_2 (or Ar) causes physical segregation of the reactants reducing the recombination probability of HCO, CH_2OH and CH_3O radicals to form complex molecules. Furthermore, the segregation effect seen when using Ar instead of H_2 is confirmed by varying the Ar deposition rate, i.e., 100, 70 and 30 per cent of the Ar flux used in exp. 4.1, respectively (see Figure 4.8; exps. 4.1-4.3). As shown in Figure 4.8, the higher Ar flux gives less COM production efficiency. In exps. 4.2 and 3.3, the chosen Ar and H_2 flux is the same as the flux of incomplete dissociated H_2 in exp. 3. The difference in COM yields shown in Figure 4.8 between exps. 3 and 4.2 as well as 3.3 is purely due to the H-radical recombination forming simple species through reactions (25—26). Although less likely, minor differences between exps. 3.2 and 4.1 can be due to H atoms produced by the photo-dissociation of H_2. However, in the gas phase, the direct photo-dissociation of H_2 does not occur for photon energies below 11.27 eV. This makes the photo-dissociation of H_2 an unlikely scenario under our experimental conditions.
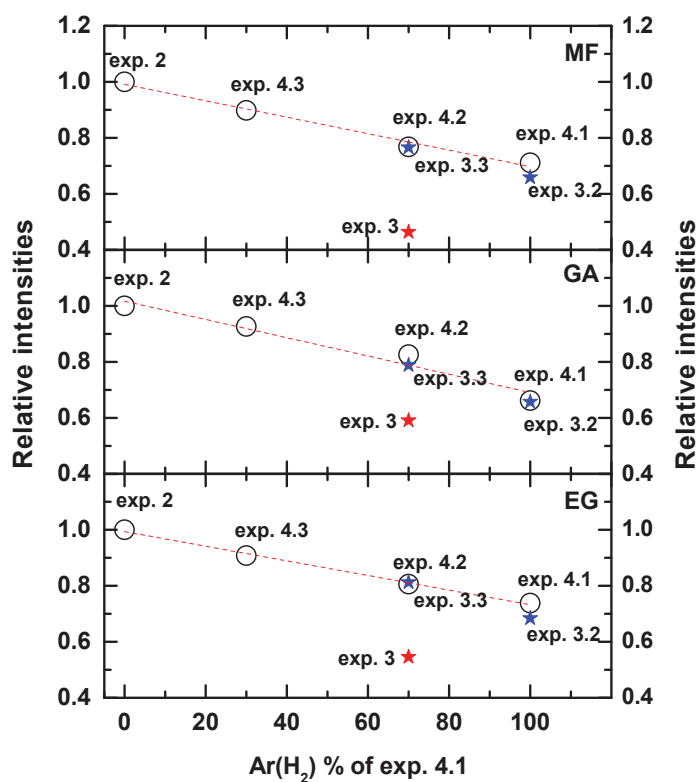
Figure 4.8: Comparison of the integrated intensities of MF (upper panel), GA(middle panel) and EG (lower panel) obtained by TPD QMS for different Ar (H_2) flux in exps. 2, 3, 3.2 and 3.3 and for the controlled experiments of CO + CH_3OH + Ar + UV (exps. 4.1-4.3). The integrated intensities are normalized for the total amount of carbon-bearing molecules observed prior to TPD and then each of them is normalized to their maximum yield.

BIBLIOGRAPHY

Arce, H. G., Santiago-García, J., Jørgensen, J. K., Tafalla, M., & Bachiller, R. 2008, Astrophys. J. Lett., 681, L21

Bacmann, A., Taquet, V., Faure, A., Kahane, C., & Ceccarelli, C. 2012, Astron. Astrophys., 541, L12

Balucani, N., Ceccarelli, C., & Taquet, V. 2015, Mon. Not. R. Astron. Soc., 449, L16

Belloche, A., Müller, H. S. P., Menten, K. M., Schilke, P., & Comito, C. 2013, Astron. Astrophys., 559, A47

Bertin, M., Romanzin, C., Doronin, M., et al. 2016, Astrophys. J. Lett., 817, L12

Biver, N., Bockelée-Morvan, D., Debout, V., et al. 2014, Astron. Astrophys., 566, L5

Blake, G. A., Sutton, E. C., Masson, C. R., & Phillips, T. G. 1987, Astrophys. J., 315, 621

Boogert, A. C. A., Gerakines, P. A., & Whittet, D. C. B. 2015, Ann. Rev. Astron. Astrophys., 53, 541

Bottinelli, S., Boogert, A. C. A., Bouwman, J., et al. 2010, Astrophys. J., 718, 1100

Bull, J. N. & Harland, P. W. 2008, International Journal of Mass Spectrometry, 273, 53

Butscher, T., Duvernay, F., Theule, P., et al. 2015, Mon. Not. R. Astron. Soc., 453, 1587

Caselli, P. & Ceccarelli, C. 2012, Astron. Astrophys. Rev., 20, 56

Cernicharo, J., Marcelino, N., Roueff, E., et al. 2012, Astrophys. J. Lett., 759, L43

Charnley, S. B. & Rodgers, S. D. 2005, in IAU Symposium, Vol. 231, Astrochemistry: Recent Successes and Current Challenges, ed. D. C. Lis, G. A. Blake, & E. Herbst, 237

Charnley, S. B., Tielens, A. G. G. M., & Millar, T. J. 1992, Astrophys. J. Lett., 399, L71

Chen, Y.-J., Chuang, K.-J., Muñoz Caro, G. M., et al. 2014, Astrophys. J., 781, 15

Chuang, K.-J., Fedoseev, G., Ioppolo, S., van Dishoeck, E. F., & Linnartz, H. 2016, Mon. Not. R. Astron. Soc., 455, 1702

Codella, C., Fontani, F., Ceccarelli, C., et al. 2015, Mon. Not. R. Astron. Soc., 449, L11

Congiu, E., Fedoseev, G., Ioppolo, S., et al. 2012, Astrophys. J. Lett., 750, L12

Coutens, A., Persson, M. V., Jørgensen, J. K., Wampfler, S. F., & Lykke, J. M. 2015, Astron. Astrophys., 576, A5

Crovisier, J., Bockelée-Morvan, D., Colom, P., et al. 2004, Astron. Astrophys., 418, 1141

Cruz-Diaz, G. A., Martín-Doménech, R., Muñoz Caro, G. M., & Chen, Y.-J. 2016, Astron. Astrophys., 592, A68

Cuppen, H. M., Ioppolo, S., Romanzin, C., & Linnartz, H. 2010, Phys. Chem. Chem. Phys., 12, 12077

Cuppen, H. M., Penteado, E. M., Isokoski, K., van der Marel, N., & Linnartz, H. 2011, Mon. Not. R. Astron. Soc., 417, 2809

Cuppen, H. M., van Dishoeck, E. F., Herbst, E., & Tielens, A. G. G. M. 2009, Astron. Astrophys., 508, 275

Drozdovskaya, M. N., Walsh, C., van Dishoeck, E. F., et al. 2016, Mon. Not. R. Astron. Soc., 462, 977

Drozdovskaya, M. N., Walsh, C., Visser, R., Harsono, D., & van Dishoeck, E. F. 2015, Mon. Not. R. Astron. Soc., 451, 3836

Fayolle, E. C., Bertin, M., Romanzin, C., et al. 2011, Astrophys. J. Lett., 739, L36

Fedoseev, G., Chuang, K.-J., van Dishoeck, E. F., Ioppolo, S., & Linnartz, H. 2016, Mon. Not. R. Astron. Soc., 460, 4297

Fedoseev, G., Cuppen, H. M., Ioppolo, S., Lamberts, T., & Linnartz, H. 2015, Mon. Not. R. Astron. Soc., 448, 1288

Fuchs, G. W., Cuppen, H. M., Ioppolo, S., et al. 2009, Astron. Astrophys., 505, 629

Garrod, R. T., Widicus Weaver, S. L., & Herbst, E. 2008, Astrophys. J., 682, 283

Geppert, W. D., Hellberg, F., Österdahl, F., et al. 2005, in IAU Symposium, Vol. 231, Astrochemistry: Recent Successes and Current Challenges, ed. D. C. Lis, G. A. Blake, & E. Herbst, 117–124

Gerakines, P. A., Schutte, W. A., & Ehrenfreund, P. 1996, Astron. Astrophys., 312, 289

Gibb, E. L., Whittet, D. C. B., Boogert, A. C. A., & Tielens, A. G. G. M. 2004, Astrophys. J. Suppl. Ser., 151, 35

Goesmann, F., Rosenbauer, H., Bredehöft, J. H., et al. 2015, Science, 349

Guzmán, V. V., Goicoechea, J. R., Pety, J., et al. 2013, Astron. Astrophys., 560, A73

Henderson, B. L. & Gudipati, M. S. 2015, Astrophys. J., 800, 66

Herbst, E. & van Dishoeck, E. F. 2009, Ann. Rev. Astron. Astrophys., 47, 427

Hidaka, H., Watanabe, M., Kouchi, A., & Watanabe, N. 2009, Astrophys. J., 702, 291

Hiraoka, K., Ohashi, N., Kihara, Y., et al. 1994, Chemical Physics Letters, 229, 408

Hollis, J. M., Lovas, F. J., & Jewell, P. R. 2000, Astrophys. J. Lett., 540, L107

Hollis, J. M., Vogel, S. N., Snyder, L. E., Jewell, P. R., & Lovas, F. J. 2001, Astrophys. J. Lett., 554, L81

Hopkins, B. J. & Riviere, J. C. 1964, British Journal of Applied Physics, 15, 941

Hudson, J. E., Hamilton, M. L., Vallance, C., & Harland, P. W. 2003, Phys. Chem. Chem. Phys., 5, 3162

Hudson, J. E., Weng, Z. F., Vallance, C., & Harland, P. W. 2006, International Journal of Mass Spectrometry, 248, 42

Ioppolo, S., Fedoseev, G., Lamberts, T., Romanzin, C., & Linnartz, H. 2013, Review of Scientific Instruments, 84, 073112

Jiménez-Serra, I., Vasyunin, A. I., Caselli, P., et al. 2016, Astrophys. J. Lett., 830, L6

Jørgensen, J. K., Favre, C., Bisschop, S. E., et al. 2012, Astrophys. J. Lett., 757, L4

Jørgensen, J. K., van der Wiel, M. H. D., Coutens, A., et al. 2016, Astron. Astrophys., 595, A117

Lamberts, T., Cuppen, H. M., Ioppolo, S., & Linnartz, H. 2013, Phys. Chem. Chem. Phys., 15, 8287

Le Roy, L., Altwegg, K., Balsiger, H., et al. 2015, Astron. Astrophys., 583, A1

Ligterink, N. F. W., Paardekooper, D. M., Chuang, K.-J., et al. 2015, Astron. Astrophys., 584, A56

Linnartz, H., Ioppolo, S., & Fedoseev, G. 2015, International Reviews in Physical Chemistry, 34, 205

Maity, S., Kaiser, R. I., & Jones, B. M. 2015, Phys. Chem. Chem. Phys., 17, 3081

Marcelino, N., Cernicharo, J., Agúndez, M., et al. 2007, Astrophys. J. Lett., 665, L127

Martín-Pintado, J., Rizzo, J. R., de Vicente, P., Rodríguez-Fernández, N. J., & Fuente, A. 2001, Astrophys. J. Lett., 548, L65

Mathews, G. S., Klaassen, P. D., Juhász, A., et al. 2013, Astron. Astrophys., 557, A132

McGuire, B. A., Carroll, P. B., Dollhopf, N. M., et al. 2015, Astrophys. J., 812, 76

Mennella, V., Baratta, G. A., Esposito, A., Ferini, G., & Pendleton, Y. J. 2003, Astrophys. J., 587, 727

Minissale, M., Congiu, E., & Dulieu, F. 2016, Astron. Astrophys., 585, A146

Modica, P. & Palumbo, M. E. 2010, Astron. Astrophys., 519, A22

Moore, M. H. & Hudson, R. L. 2005, in IAU Symposium, Vol. 231, Astrochemistry: Recent Successes and Current Challenges, ed. D. C. Lis, G. A. Blake, & E. Herbst, 247–260

Muñoz Caro, G. M., Jiménez-Escobar, A., Martín-Gago, J. Á., et al. 2010, Astron. Astrophys., 522, A108

Mumma, M. J. & Charnley, S. B. 2011, Ann. Rev. Astron. Astrophys., 49, 471

Neill, J. L., Bergin, E. A., Lis, D. C., et al. 2014, Astrophys. J., 789, 8

Öberg, K. I. 2016, Chemical Reviews, 116, 9631

Öberg, K. I., Boogert, A. C. A., Pontoppidan, K. M., et al. 2011a, Astrophys. J., 740, 109

Öberg, K. I., Bottinelli, S., Jørgensen, J. K., & van Dishoeck, E. F. 2010, Astrophys. J., 716, 825

Öberg, K. I., Fuchs, G. W., Awad, Z., et al. 2007, Astrophys. J. Lett., 662, L23

Öberg, K. I., Garrod, R. T., van Dishoeck, E. F., & Linnartz, H. 2009, Astron. Astrophys., 504, 891

Öberg, K. I., van der Marel, N., Kristensen, L. E., & van Dishoeck, E. F. 2011b, Astrophys. J., 740, 14

Paardekooper, D. M., Bossa, J.-B., & Linnartz, H. 2016a, Astron. Astrophys., 592, A67

Paardekooper, D. M., Fedoseev, G., Riedo, A., & Linnartz, H. 2016b, Astron. Astrophys., 596, A72

Penteado, E. M., Boogert, A. C. A., Pontoppidan, K. M., et al. 2015, Mon. Not. R. Astron. Soc., 454, 531

Pontoppidan, K. M. 2006, Astron. Astrophys., 453, L47

Pontoppidan, K. M., Fraser, H. J., Dartois, E., et al. 2003, Astron. Astrophys., 408, 981

Pontoppidan, K. M., van Dishoeck, E. F., & Dartois, E. 2004, Astron. Astrophys., 426, 925

Prasad, S. S. & Tarafdar, S. P. 1983, Astrophys. J., 267, 603

Pulliam, R. L., McGuire, B. A., & Remijan, A. J. 2012, Astrophys. J., 751, 1

Requena-Torres, M. A., Martín-Pintado, J., Martín, S., & Morris, M. R. 2008, Astrophys. J., 672, 352

Requena-Torres, M. A., Martín-Pintado, J., Rodríguez-Franco, A., et al. 2006, Astron. Astrophys., 455, 971

Rivilla, V. M., Fontani, F., Beltrán, M. T., et al. 2016, Astrophys. J., 826, 161

Shalabiea, O. M. & Greenberg, J. M. 1994, Astron. Astrophys., 290, 266

Shen, C. J., Greenberg, J. M., Schutte, W. A., & van Dishoeck, E. F. 2004, Astron. Astrophys., 415, 203

Taquet, V., López-Sepulcre, A., Ceccarelli, C., et al. 2015, Astrophys. J., 804, 81

Taquet, V., Wirström, E. S., & Charnley, S. B. 2016, Astrophys. J., 821, 46

Tercero, B., Cernicharo, J., López, A., et al. 2015, Astron. Astrophys., 582, L1

Tielens, A. G. G. M. & Hagen, W. 1982, Astron. Astrophys., 114, 245

Tielens, A. G. G. M., Tokunaga, A. T., Geballe, T. R., & Baas, F. 1991, Astrophys. J., 381, 181

Tschersich, K. G. 2000, Journal of Applied Physics, 87, 2565

Tschersich, K. G., Fleischhauer, J. P., & Schuler, H. 2008, Journal of Applied Physics, 104, 034908

Vastel, C., Ceccarelli, C., Lefloch, B., & Bachiller, R. 2014, Astrophys. J. Lett., 795, L2

Vasyunin, A. I. & Herbst, E. 2013a, Astrophys. J., 762, 86

Vasyunin, A. I. & Herbst, E. 2013b, Astrophys. J., 769, 34

Watanabe, N. & Kouchi, A. 2002, Astrophys. J. Lett., 571, L173

Watanabe, N., Mouri, O., Nagaoka, A., et al. 2007, Astrophys. J., 668, 1001

Woods, P. M., Kelly, G., Viti, S., et al. 2012, Astrophys. J., 750, 19

Zhitnikov, R. A. & Dmitriev, Y. A. 2002, Astron. Astrophys., 386, 1129

5

SIMULTANEOUS HYDROGENATION AND UV-PHOTOLYSIS EXPERIMENTS OF NO IN CO-RICH INTERSTELLAR ICE ANALOGUES; LINKING HNCO, OCN⁻, NH₂CHO, AND NH₂OH

The laboratory work presented here simulates the chemistry on icy dust grains as typical for the 'CO freeze-out stage' in dark molecular clouds. It differs from previous studies in that solid-state hydrogenation and vacuum UV photoprocessing are applied simultaneously to co-depositing molecules. In parallel, the reactions at play are described for fully characterized laboratory conditions. The focus is on the formation of molecules containing both carbon and nitrogen atoms, starting with NO in CO-, H_2CO-, and CH_3OH-rich ices at 13 K. The experiments yield three important conclusions. (1) Without UV processing hydroxylamine (NH_2OH) is formed, as reported previously. (2) With UV processing (energetic) NH_2 is formed through photodissociation of NH_2OH. This radical is key in the formation of species with an N-C bond. (3) The formation of three N-C bearing species, HNCO, OCN^-, and NH_2CHO, is observed. The experiments put a clear chemical link between these species; OCN^- is found to be a direct derivative of HNCO and the latter is shown to have the same precursor as formamide (NH_2CHO). Moreover, the addition of VUV competing channels decreases the amount of NO molecules converted into NH_2OH by at least one order of magnitude. Consequently, this decrease in NH_2OH formation yield directly influences the amount of NO molecules that can be converted into HNCO, OCN^-, and NH_2CHO.

5.1 INTRODUCTION

Isocyanic acid (HNCO) and formamide (NH_2CHO) have been detected in the gas phase in a number of massive hot molecular cores (Bisschop et al. 2007; Ligterink et al. 2015b), low- and intermediate-mass pre-stellar and protostellar objects (Kahane et al. 2013; López-Sepulcre et al. 2015) and in the outflow shock regions L1157-B1 and B2 (Mendoza et al. 2014). In these regions, the gaseous molecules are thought to be directly desorbed from the ice grain mantles. Recently, both species have been searched for during the *Rosetta* mission on comet 67P/Churyumov-Gerasimenko. The analysis of the volatile coma composition by the ROSINA instrument yielded HNCO abundances ranging from 0.016 to 0.031 per cent with respect to H_2O and an upper limit of 0.001 per cent was derived for NH_2CHO (Le Roy et al. 2015). An *in situ* analysis of the comet's surface by the COSAC instrument on board of the Philae lander reported higher values for both HNCO (0.3 per cent) and NH_2CHO (1.8 per cent) with respect to water ice (Goesmann et al. 2015). Although solid HNCO and NH_2CHO in interstellar ice have not yet been detected, the direct derivative of HNCO, the cyanate ion (OCN^-), has been found in the solid state towards both low- and high-mass young stellar objects (YSOs) with abundances of $0.3 - 0.8$ per cent with respect to that of H_2O (van Broekhuizen et al. 2004; Öberg et al. 2011; Boogert et al. 2015). This makes HNCO a strong candidate to be present in interstellar ices during the YSO formation stage. The growing astronomical interest for HNCO and NH_2CHO molecules is not surprising, since both molecules have direct links to astrobiology, HNCO and NH_2CHO are the simplest molecules that comprise of the four most abundant elements associated with living organisms, and therefore both species are often considered as possible starting points in the formation of biologically important molecules like amino acids.

Mendoza et al. (2014) and López-Sepulcre et al. (2015) found a correlation between the observed HNCO and NH_2CHO abundances, which hints for chemical links between the two species (i.e., the formation of one from the other or the formation of both from a common precursor molecule). Both studies suggested a solid-state origin of NH_2CHO, and surface hydrogenation of HNCO was proposed as a likely source of NH_2CHO formation. However, recent laboratory work by Noble et al. (2015) contradicted HNCO hydrogenation as a direct route towards NH_2CHO, requiring an alternative solid-state mechanism to explain the observed chemical link between NH_2CHO and HNCO.

Hereby we present this possible formation route with nitric oxide (NO) as a starting molecule. NO is one of the most abundant nitrogen-bearing molecu-les detected in dark molecular clouds and YSOs with abundances with respect to H_2 ranging from $\sim10^{-9}$ to $\sim10^{-7}$ (Liszt & Turner 1978; Pwa & Pottasch 1986; McGonagle et al. 1990; Gerin et al. 1992). Although less abundant than NH_3 and N_2, NO has generated much astrochemical interest in the past few years because of its higher chemical reactivity compared to other N-bearing species. The open shell configuration of an NO molecule, i.e., the presence of an unpaired valence electron, substantially increases its chemical reactivity towards other species. This is particularly important under the extremely cold conditions of the interstellar medium (ISM), where gas phase and surface reactions are strongly affected by even small endothermicity or the presence of an activation barrier. Recently, frozen NO molecules have been linked to the formation of other species, like NH_2OH, NO_2, N_2O, and HNO_2 (Congiu et al. 2012a,b; Fedoseev et al. 2012; Joshi et al. 2012; Minissale et al. 2014; Ioppolo et al. 2014a; Linnartz et al. 2015).

In space, NO molecules are primarily formed in the gas phase through the reaction:

$$N^{(g)} + OH^{(g)} \longrightarrow NO^{(g)} + H^{(g)} \tag{27}$$
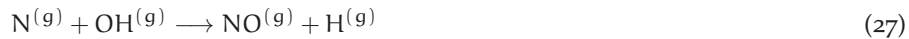
(see Herbst & Klemperer 1973; McGonagle et al. 1990; Gerin et al. 1992). Then, in dense regions of the ISM, NO molecules accrete onto the surface of submicrometer-sized interstellar grains, where they in turn can react with other accreting species, like H, N, and O atoms and/or be processed by impacting UV-photons and cosmic rays (see Charnley et al. 2001; Congiu et al. 2012b). Among all the possible solid-state reactions involving NO and the aforementioned atoms, those with hydrogen are the most important ones due to the great overabundance of hydrogen in comparison to other atomic species. Thus, hydrogenation of NO has been the subject of recent theoretical (Charnley et al. 2001; Blagojevic et al. 2003) and experimental (Congiu et al. 2012a,b; Fedoseev et al. 2012) studies, and was shown to result in the formation of hydroxylamine (NH_2OH) through three sequential steps:

$$NO + H \longrightarrow HNO \tag{28}$$

$$HNO + H \longrightarrow H_2NO/HNOH \tag{29}$$

$$H_2NO/HNOH + H \longrightarrow NH_2OH \tag{30}$$
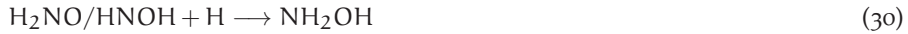
that all proceed with either no or very low activation barriers. Very recently also another formation route of hydroxylamine through O-atom addition to ammonia was discussed (He et al. 2015), but despite these laboratory findings dedicated astronomical searches for NH_2OH towards the molecular outflow L1157 (McGuire et al. 2015) did only result in upper limits, so far. A possible explanation is that hydroxylamine is easily photodissociated and that the resulting photofragments like NH_2 are rapidly consumed in reactions with other species present in the ice. According to this picture, NH_2OH is therefore a candidate precursor of more complex organic species, also including N-C bond-bearing species. One of the aims of this work is to experimentally verify this hypothesis.

In Congiu et al. (2012a) and Fedoseev et al. (2012), hydrogenation of NO has been investigated both in the submonolayer and multilayer regime, respectively. In the first case, pure NO molecules were deposited on amorphous silicates with the aim to simulate the hydrogenation of NO on the surface of bare interstellar grains (Congiu et al. 2012a). In the second case, the simultaneous accretion of NO and H_2O or CO molecules (Fedoseev et al. 2012) aims at reproducing the polar (water-rich) and apolar (water-poor) layers of ice mantles growing at different stages of dark molecular cloud evolution (Boogert et al. 2015). The CO-rich apolar layer is of greater astrochemical interest because according to current models the formation of NO in the gas phase through reaction (27) peaks when a significant amount of water-rich ice is already formed on the surface of the grains, and the abundance of OH in the gas-phase increases (Charnley et al. 2001; Visser et al. 2011; Congiu et al. 2012b; Vasyunina et al. 2012). As a consequence, the accretion of NO on the ice surface should correspond to the freeze out of CO. Recently, Fedoseev et al. (2012) studied the possible interaction between the NO-hydrogenation reaction network and CO molecules that can potentially be followed by the formation of N-C bearing species. However, in this laboratory study, no sign of N-C bond formation was found upon H-atom bombardment or UV photolysis of NO in a CO-rich environment.

A possible explanation for the lack of C-N bond formation in the aforementioned experiments is the inability to study atom bombardment and UV photolysis during a single experiment. A recent modification of our SURFRESIDE^2 ultrahigh vacuum (UHV) setup allows now investigation of both processes, sequentially and simultaneously in the same ice (Ioppolo et al. 2013). This is made possible by the addition of a H$_2$-flow microwave discharge UV lamp to the main chamber in addition to the two existing atom beam lines. Furthermore, two independent molecular deposition lines allow for the simultaneous accretion of a selected molecule (NO) with another species, simulating a more realistic interstellar analogue composition of the bulk of the ice. The details are described in Section 5.2.

This work presents the first simultaneous hydrogenation and UV photolysis experiments of accreting NO molecules in three distinct molecular environments: CO-, H$_2$CO-, and CH$_3$OH-rich ices. The choice of CO is motivated by the fact that, as previously mentioned, the peak of NO accretion onto grains is expected to overlap with the accretion peak of CO (Charnley et al. 2001; Congiu et al. 2012b; Vasyunina et al. 2012). H$_2$CO and CH$_3$OH are the most abundant products of CO hydrogenation and therefore are expected to be present in the same ice layer according to a large number of experimental, theoretical, and observational studies (Hiraoka et al. 1994; Watanabe & Kouchi 2002; Zhitnikov & Dmitriev 2002; Fuchs et al. 2009; Cuppen et al. 2011; Boogert et al. 2015; Linnartz et al. 2015; Penteado et al. 2015). It should be noted that another ice constituent abundantly observed in CO-rich interstellar ice mantles is CO$_2$ that can be formed via the CO+OH pathway (Oba et al. 2010; Ioppolo et al. 2011; Noble et al. 2011). However, because of the high chemical inertness of CO$_2$ in comparison to CO, H$_2$CO, and CH$_3$OH molecules, we do not include carbon dioxide in our experiments. Moreover, special care is taken to control the ratio between the used H-atom and UV-photon fluxes in an attempt to get as close as possible to the mean ratios expected for the life time of dark molecular clouds (Mathis et al. 1983; Prasad & Tarafdar 1983; Duley & Williams 1984; Goldsmith & Li 2005; Fuchs et al. 2009). It should be noted, though, that the main focus of the present study is on the formation of various N-C bearing molecules and the photochemistry of NO hydrogenation products and not on the photochemistry of CO, H$_2$CO, and CH$_3$OH ices that leads to the formation of carbon-bearing complex organic molecules (Öberg et al. 2011; Henderson & Gudipati 2015; Maity et al. 2015; Paardekooper et al. 2016).

The next section describes the extended setup and the experimental procedures. The results section summarizes our findings and is followed by the discussion section that focuses on the possible reaction mechanisms responsible for the formation of each of the detected N-C bearing molecules. The paper concludes with the astrochemical implications and the astrobiological importance of the newly formed molecules.

5.2   EXPERIMENTAL PROCEDURE

5.2.1   *Experimental setup*

All experiments are performed using a modified version of the SURFace REaction SImulation DEvice (SURFRESIDE^2) UHV setup (Ioppolo et al. 2013; Linnartz et al. 2015). The original design has been described in detail by Ioppolo et al. (2013). The setup consists of three distinct UHV chambers separated by shutters. A gold-coated substrate is mounted on top of the cold head of a He close-cycle cryostat placed in the centre of the main UHV chamber (base pressure $\sim 10^{-10}$ mbar). The ices are grown on the substrate with monolayer (ML) precision (where 1 ML is assumed to be 1×10^{15} mol cm^{-2}). The temperature control is realized by means of heating wires. The absolute temperature precision is <2 K while the relative precision between experiments is as low as 0.5 K. Two other UHV chambers ($10^{-9} - 10^{-10}$ mbar) contain two

atom beam sources. Two different atom sources are used to produce a number of atoms and radicals (i.e., H, D, N, O, OH, NH, and NH_2). These are a hydrogen atom beam source (Dr. EberlMBE-Komponenten GmbH, see Tschersich 2000) that generates atoms by cracking the parent molecules that pass through the hot (1850°C) tungsten capillary, and a microwave atom source (Oxford Scientific Ltd, see Anton et al. 2000) that generates atoms and radicals by using a capacitively coupled microwave discharge (125 − 300 W at 2.45 GHz). The sample surface is exposed to two atom beams with controllable fluxes and incidence angles of 45° and 135°. A nose-shaped quartz pipe is placed along the path of each of the atom beams to quench excited electronic and rovibrational states of atoms and non-dissociated molecules through collisions with its walls before they reach the sample. Details on the H-atom flux calibration can be found in Ioppolo et al. (2013).

In addition to the two atom beam lines, two separate molecular dosing lines are available for the deposition of stable species. These lines can be operated independently and are used to simulate different molecular environments corresponding to different stages during the interstellar ice evolution. In this work, NO (Linde 2.5), CO (Linde 2.0), and H_2 (Praxair 5.0) are used as gas supplies during our experiments. H_2CO is obtained by thermal decomposition of paraformaldehyde (Sigma-Aldrich, 95 per cent) at 80°C under vacuum. Liquid CH_3OH sample (Sigma-Aldrich, 99.8 per cent) is frozen-pumped-thawed three times before it is used as a mixture component. Gas mixtures are prepared in the pre-pumped ($<10^{-4}$ mbar) full-metal dosing line by introducing NO and a second gas component into the two distinct parts of the dosing line with a known volume ratio and by letting gases mix with each other over time. A high-precision full metal leak valve is used to introduce this gas mixture into the main chamber. The molecular masses of NO and CO (30 and 28 amu) and, therefore, the corresponding mean thermal velocities of both molecules are in close proximity. The desorption temperatures of both molecules are also close. Thus, we assume the ratio between NO and CO fluxes at the surface of the sample to be nearly equal to the NO:CO ratio in the dosing line. Although mean thermal velocities of H_2CO (30 amu) and CH_3OH (32 amu) are also similar to that of NO, the desorption temperatures of H_2CO and CH_3OH are considerably higher than that of nitric oxide and well above the temperature of the thermal shield around the sample. This will lead to a decrease of the actual H_2CO and CH_3OH deposition rates because some H_2CO and CH_3OH can deposit onto the shield as well, resulting into a somewhat higher effective NO:H_2CO and NO:CH_3OH deposition ratios, i.e., a higher fraction of NO in the resulting ice mixture compared to that in the dosing line.

Deposition proceeds under 68° and 158° incidence angles, different from the original SURF-RESIDE[2] design where the second line was mounted at 90°. The cleared port normal to the substrate surface is now used to expose the sample to a UV-photon beam. UV-photons are generated by a broad-band hydrogen microwave discharge (0.5 mbar, 100 W) that peak at 121 nm (Ly-α) and ~160 nm (Ligterink et al. 2015a). The UV lamp is connected and separated from the UHV chamber through a MgF_2 window. The divergence of the beam guarantees that the whole area of the gold substrate (2.5×2.5 cm) is exposed to UV-photons. This results in a configuration in which ices grown through two independent deposition lines can be bombarded by radical species from two atom beam lines and can be irradiated by UV-photons, sequentially or simultaneously.

The method used to evaluate the UV-photon flux at the substrate is based on a simple extrapolation of the UV-photon flux measurements performed by Ligterink et al. (2015a) using a National Institute of Standards and Technology (NIST) calibrated photodiode (AXUV-100) for the same lamp configuration, microwave cavity, and power supply. Assuming the UV lamp to be a point source and taking into account the difference in distance between UV source and ice target for SURFRESIDE[2] and the setup used in Ligterink et al. (2015a), a lower limit of

~$1.3{\times}10^{13}$ photons cm^{-2} s^{-1} is obtained. This value is used to derive exposure ratios and total UV-photon fluences summarized in Table 5.1.

5.2.2   *Experimental methods*

Two different experimental procedures are used to study the UV-induced photochemistry of the NO hydrogenation surface reaction products: sequential UV (seq-exposure, i.e., after completion of the hydrogenation) and simultaneous UV exposure (co-exposure, i.e., during hydrogenation) of the ice. Furthermore, all the experiments are divided into two main sets that work with either pure NO or NO mixed with CO, H_2CO, and CH_3OH. All the relevant experiments are summarized in Table 5.1.

The sequential UV exposure experiments are performed in three steps. First, a 10 L (Langmuir) layer of Ar ice is deposited on top of a bare gold sample. This is done to avoid possible interactions on the inter phase between the gold surface and the ice molecules upon UV exposure. Second, a co-deposition of NO molecules with an overabundance of H-atoms is performed at 13 K. Alternatively, to reproduce a CO-rich interstellar ice analogue, a mixture of NO and CO is co-deposited with H-atoms to form a layer of CO ice containing isolated NH_2OH as well as non-fully hydrogenated HNO and NO molecules. To better compare the experimental results with each other, the same exposure dose of NO equal to 8.5 L is set for all the experiments and a total H-atom fluence equal to $6{\times}10^{16}$ atoms cm^{-2} is used. Co-deposition of NO with CO, H_2CO, and CH_3OH molecules is performed by introducing a pre-made gas mixture in a 1:12 ratio through a single molecular dosing line. This 1:12 ratio is used to guarantee that each depositing NO molecule will have at least 12 surrounding CO molecules. This corresponds to the number of neighbours for each of the molecules in a pure CO crystal (Kohin 1960). The same 1:12 ratio is then applied to H_2CO and CH_3OH molecules. Furthermore, the NO:CO ratio of 1:12 is close to that expected astronomically on a grain surface based on astrochemical model predictions; see for example the surface abundances of NO and CO determined for $1{\times}10^3 - 1{\times}10^5$ years in Charnley et al. (2001) and Congiu et al. (2012b). During the third and final step of a sequential UV exposure experiment, the resulting ice is exposed to the UV light of the lamp. A Reflection Absorption InfraRed (RAIR) spectrum in the range from 700 to 4000 cm^{-1} is recorded with 1 cm^{-1} resolution after deposition of the Ar ice layer. This spectrum is used as a reference for a series of RAIR spectra acquired every 5 min during the full time of the NO (or NO:CO) + H co-deposition. Once this step is completed, another reference spectrum is obtained and a second series of RAIR spectra is acquired every 2 min for the full time of the UV exposure.

The experiment is completed by performing a temperature programmed desorption (TPD) measurement by means of a quadrupole mass spectrometer (QMS) of the photoprocessed ice as a complementary analytical tool. The following procedure is systematically performed. First, an ice is desorbed with a constant rate of 2 K min^{-1} up to 50 K to gently remove volatile species from the ice. Then a 5 K min^{-1} rate is used until 225 K is reached to provide a better peak-to-noise ratio in the QMS signal. Every 6 s, a mass scan is taken. Simultaneously, RAIR spectra are acquired every 2 min for the full time of the TPD. It should be noted that the simultaneous recording of RAIRS and TPD spectra offers a highly effective tool to unambiguously identify molecules formed in the ice (see Öberg et al. 2009 and Ioppolo et al. 2014b).

The UV co-exposure experiment consists of two steps. The first step is the same as for the sequential UV exposure experiments (i.e., a deposition of 10 L of Ar ice on the bare substrate). During the second step, a simultaneous co-exposure of H-atoms and UV-photons with 8.5 L of NO molecules is performed. In the case of CO-, H_2CO-, and CH_3OH-rich interstellar ice analogues; mixtures of NO:CO (NO:H_2CO or NO:CH_3OH) are co-deposited with H-atoms and

Table 5.1: List of discussed experiments.

Ref. N	Experiment	UV-exposure	Ratio[a]	T_{sample} (K)	NO_{dep} ($L \, s^{-1}$)	second Molecule$_{dep}$ ($L \, s^{-1}$)	H-atom flux ($10^{13} \, cm^{-2} \, s^{-1}$)	UV-flux ($10^{13} \, cm^{-2} \, s^{-1}$)	Time (s)	TPD
1.1	NO	-	-	13	0.0017	-			5000	QMS/RAIR
1.2	NO:H	-	1:7	13	0.0017	-	1.2		5000	QMS/RAIR
1.3	NO:H+hν	seq-exposure	1:7	13	0.0017	-	1.2	1.3	5000+1200	QMS/RAIR
1.4	NO:H:UV	co-exposure	1:7:8	13	0.0017	-	1.2	1.3	5000	QMS/RAIR
						CO_{dep}				
2.1	NO:CO:H	-	1:12:7	13	0.0017	0.02	1.2		5000	QMS/RAIR
2.2	NO:CO:H+hν	seq-exposure	1:12:7	13	0.0017	0.02	1.2	1.3	5000+1200	QMS/RAIR
2.3	NO:CO:H:UV	co-exposure	1:12:7:8	13	0.0017	0.02	1.2	1.3	5000	QMS/RAIR
						H_2CO_{dep}				
3.1	NO:H$_2$CO	-	1:12	13	0.0017	0.02			5000	QMS/RAIR
3.2	NO:H$_2$CO:H	-	1:12:7	13	0.0017	0.02	1.2		5000	QMS/RAIR
3.3	NO:H$_2$CO:H:UV	co-exposure	1:12:7:8	13	0.0017	0.02	1.2	1.3	5000	QMS/RAIR
						CH_3OH_{dep}				
4.1	NO:CH$_3$OH	-	1:12	13	0.0017	0.02			5000	QMS/RAIR
4.2	NO:CH$_3$OH:H	-	1:12:7	13	0.0017	0.02	1.2		5000	QMS/RAIR
4.3	NO:CH$_3$OH:H:UV	co-exposure	1:12:7:8	13	0.0017	0.02	1.2	1.3	5000	QMS/RAIR

Note. [a] Under the assumption that 1 L (Langmuir) exposure leads to the surface coverage of 1 ML $\approx 10^{15}$ particles cm^{-2}.
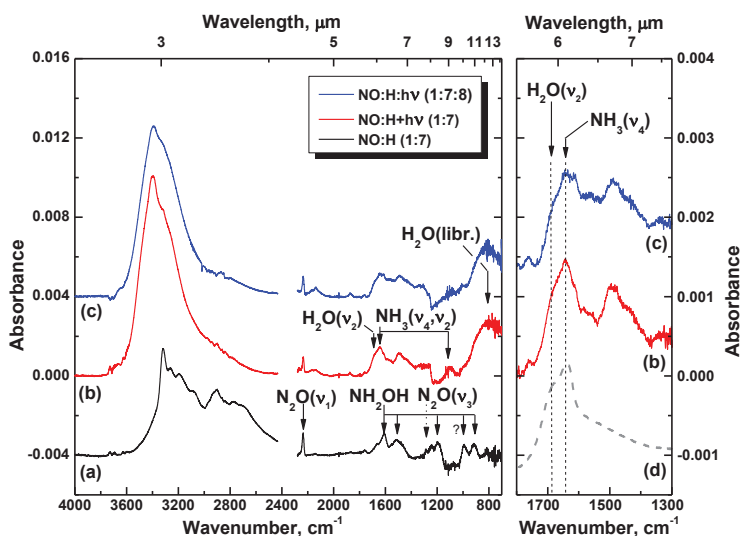
Figure 5.1: Left-hand panel: RAIR spectra obtained after (a) co-deposition of NO molecules with H-atoms (experiment 1.2); (b) co-deposition of NO molecules with H-atoms followed by UV-photon exposure of $\sim 1.6 \times 10^{16}$ photons cm^{-2} (experiment 1.3); (c) co-deposition of NO molecules and H-atoms with simultaneous UV-photon exposure of $\sim 6.5 \times 10^{16}$ photons cm^{-2} (experiment 1.4). Right-hand panel: zoom-in of the spectral range $1800 - 1300$ cm^{-1} that shows the presence of newly formed NH$_3$ and H$_2$O in the ice compared to a spectrum of a NH$_3$:H$_2$O = 1:4 mixture taken from figure 11.14 of Oberg 2009 (d). The total exposure dose of NO molecules is estimated to be 8.5 L in all three experiments. The total H-atom fluence is 6×10^{16} atoms cm^{-2}.

UV-photons. Similar to the sequential UV exposure procedure, a reference RAIR spectrum is obtained after Ar deposition and a series of RAIR spectra is acquired every 5 min for the full time of co-exposure with UV-photons. The experiments are completed by performing a QMS-TPD in the very same way as for sequential UV exposure experiments. The main aim of the UV co-exposure experiments is to study the effect of UV-photons on all the NO hydrogenation reaction products, including intermediates. These experiments are actually closer to the conditions observed in the ISM, where accreting NO molecules are simultaneously exposed to H-atoms and UV-photons.

A number of control experiments are performed to verify that the formed products are the result of UV-induced photochemistry (see Table 5.1). With this purpose in mind, all the experiments are repeated under the very same experimental conditions, but without UV-exposure. In this way, the obtained RAIR and QMS-TPD spectra can be used as a reference for comparison and the assignment of photochemistry products can be further constrained.

5.3   RESULTS

5.3.1   *Simultaneous hydrogenation and UV processing of pure NO*

A set of experiments (experiments 1.1-1.4 in Table 5.1) is performed to investigate the effect of UV photolysis on the non-energetic NO hydrogenation reaction route. Figure 5.1 compares the

RAIR spectrum obtained after NO co-deposition with H-atoms (Figure 5.1(a)), the RAIR spectrum obtained after NO co-deposition with H-atoms followed by UV-photon sequential exposure (Figure 5.1(b)), and the RAIR spectrum obtained after simultaneous NO co-deposition with H-atoms and co-exposure by UV-photons (Figure 5.1(c)). The RAIR spectrum obtained after co-deposition of pure NO with H-atoms is similar to the spectra obtained in previous studies of surface NO hydrogenation reactions (e.g., Congiu et al. 2012b; Fedoseev et al. 2012). The main product of NO hydrogenation is hydroxylamine, NH_2OH, a potential glycine precursor (Blagojevic et al. 2003; Congiu et al. 2012b). The formation of NH_2OH is confirmed in our experiments through the presence of wide absorption bands in the range of the O-H and N-H stretching vibrations ($2600 - 3400$ cm^{-1}) and mostly through the more isolated and sharper absorption bands in the bending vibrational mode range ($1700 - 900$ cm^{-1}). These are the peaks centred around 1607, 1514, 1196, 914, and possibly 990 cm^{-1} (see figure 1 of Nightingale & Wagner 1954 and figure. 1 of Congiu et al. 2012b for comparison). Another species whose absorption features are observed in Figure 5.1(a) is N_2O (2235 and 1283 cm^{-1}). The presence of N_2O can be explained at least partially by intrinsic contaminations in the NO gas cylinder. No signs of monomeric NO and only traces of cis-$(NO)_2$ dimer are observed around 1865 and 1761 cm^{-1} (see Congiu et al. 2012b; Fedoseev et al. 2012).

The RAIR spectra obtained after UV processing of the ice (Figure 5.1(b)) clearly show that a visible fraction of the solid NH_2OH is consumed and that new species form. These are NH_3, which can be tentatively assigned through its two absorption bands around 1641 and 1112 cm^{-1} (Reding & Hornig 1955; Bertie & Shehata 1985, and figure 11.14 of Öberg 2009), and H_2O, confirmed by the detection of its bending mode centred around 1680 cm^{-1} (see zoom-in panel in Figure 5.1(b)), its libration mode (broad-band below 980 cm^{-1}), and by a shift in the wide absorption band between 2600 and 3400 cm^{-1} towards higher wavenumbers. The latter is due to the disappearance of a weaker N-H stretching vibration mode of NH_2OH and the consequent appearance of a stronger O-H stretching vibration mode of H_2O. The assignment of NH_3 and H_2O is further constrained by the comparison of our RAIR data (Figure 5.1(b)) with a spectrum of a NH_3:H_2O = 1:4 mixture in the $1800 - 1300$ cm^{-1} spectral range taken from Öberg 2009 (Figure 5.1(d)). Another species that is abundantly formed upon UV processing, but cannot be detected by means of RAIRS, is N_2. Its presence in irradiated ice samples is confirmed by means of TPD, the QMS shows a broad N_2 desorption feature that starts at 29 K and peaks around 40 K (Hiraoka et al. 1995, see also Figure 5.2 for more details on TPD-QMS data). Along with traces of cis-$(NO)_2$, also weak signals due to NO monomers can be resolved after UV processing of the ice through their characteristic absorption at 1875 cm^{-1} (Fateley et al. 1959; Fedoseev et al. 2012; Minissale et al. 2014).

Co-exposure of UV irradiation and H-atoms during deposition of NO molecules (Figure 5.1(c)) results in a significant decrease in the amount of formed NH_2OH (i.e., only traces can be detected) and the formation of H_2O. Although NH_3 absorption features cannot be well distinguished in Figure 5.1(c), the corresponding TPD-QMS data indicate that the total area of m/z = 15 (NH^+), m/z = 16 (NH_2^+) or m/z = 17 (NH_3^+) signals of NH_3 desorbing between 100 and 140 K is nearly equal to those observed in the sequential exposure experiment; the values are within 10 per cent. Furthermore, the m/z = 15:16:17 signal ratio is equal to 0.06:0.84:1 at the desorption maximum. This is in good agreement with the values available from the NIST mass spectrometry database, confirming the assignment of this desorption peak to NH_3. Similarly, N_2 TPD areas (m/z = 28) do not reveal any major difference between the two experiments. TPD results for m/z = 28 and m/z = 16 are presented in Figure 5.2. Along with the desorption peak of NH_3 itself (between 100 and 140 K), the m/z = 16 spectrum illustrates the desorption of two other species that can be clearly resolved by their characteristic desorption temperatures. These are H_2O (a desorption feature between 140 and 160 K) and
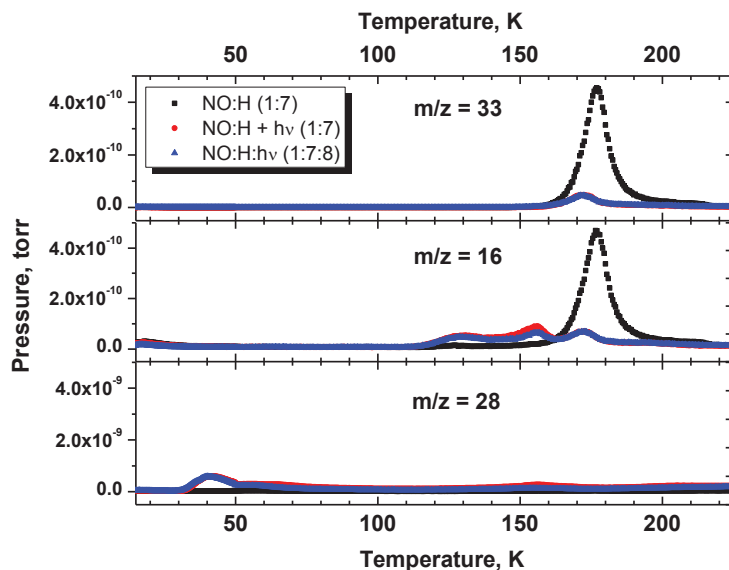
Figure 5.2: TPD spectra for three selected m/z values obtained after: black squares — co-deposition of NO molecules with H-atoms (experiment 1.2); red circles — co-deposition of NO molecules with H-atoms followed by UV-photon exposure of $\sim 1.6 \times 10^{16}$ photons cm^{-2} (experiment 1.3); blue triangles — co-deposition of NO molecules and H-atoms with simultaneous UV-photon exposure of $\sim 6.5 \times 10^{16}$ photons cm^{-2} (experiment 1.4). The total exposure dose of NO molecules is estimated to be 8.5 L in all three experiments. The total H-atom fluence is 6×10^{16} atoms cm^{-2}. The $m/z = 33$ signal corresponds to the NH$_2$OH$^+$ cation obtained by ionization of NH$_2$OH; the $m/z = 16$ signal corresponds to the NH$_2^+$ cation obtained by dissociative ionization of NH$_3$ and NH$_2$OH, or O$^+$ cation obtained by dissociative ionization of H$_2$O; the $m/z = 28$ signal corresponds to N$_2^+$.

NH$_2$OH (a desorption feature between 160 and 200 K). The latter becomes possible because of the higher detection sensitivity of TPD-QMS. Unfortunately, the RAIR data cannot be used to determine the NH$_2$OH formation/destruction yield ratio in the experiments presented in Figure 5.1 (experiments 1.2-1.4), because of the overlap of the hydroxylamine absorption features with those of water and ammonia. However, the same information can be obtained from QMS TPD spectra (see Figure 5.2). The integration of the area of $m/z = 33$ signal in the range between 140 and 225 K (with a peak at 170 K) in both sequential and co-exposure experiments reveals that the final NH$_2$OH yield is 10 times lower than in the case of co-deposition of NO and H-atoms without UV irradiation.

5.3.2   *Simultaneous hydrogenation and UV processing of NO molecules co-deposited in a CO-rich environment*

Three sets of experiments are performed to investigate the co-exposure of UV-photons and H-atoms to NO molecules in CO ices. Experiments 2.1-2.3 presented in Figure 5.3 are comparable to experiments 1.2-1.4 (shown in Figure 5.1) with the exception that CO is added to the accreting gas mixture. Figure 5.3(a) shows a selected region of the acquired RAIR spectrum
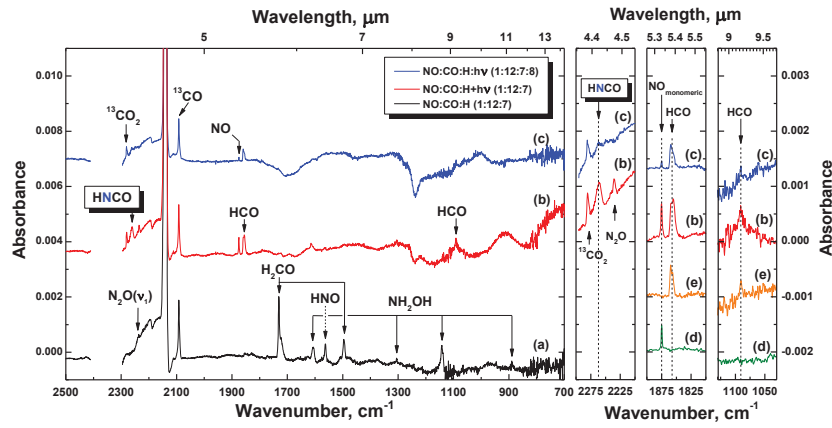
Figure 5.3: Left-hand panel: RAIR spectra obtained after (a) co-deposition of NO:CO = 1:12 molecular mixture with H-atoms for the total ratio of 1:12:7 (experiment 2.1); (b) co-deposition of NO:CO = 1:12 molecular mixture with H-atoms followed by the UV-photon exposure of $\sim 1.6 \times 10^{16}$ photons cm^{-2} (experiment 2.2); and (c) co-deposition of NO:CO = 1:12 molecular mixture and H-atoms with simultaneous UV-photon exposure of $\sim 6.5 \times 10^{16}$ photons cm^{-2} (experiment 2.3). Right-hand panels: zoom-in of the spectral ranges around 2250, 1850, and 1100 cm^{-1} that show (from left to right) the presence of newly formed $^{13}CO_2$, HNCO, NO monomers, and HCO through comparison with the spectrum of the isolated HCO obtained by UV photoprocessing of H_2 entrapped in a solid CO matrix (e) and the spectrum of isolated NO taken from Minissale(2014) (d). The total dose of NO molecules is estimated to be 8.5 L in all three experiments. The total estimated H-atom fluence is $\sim 6 \times 10^{16}$ atoms cm^{-2}.

obtained after NO:CO = 1:12 gas-mixture deposition with H-atoms. As for the RAIR spectrum in Figure 5.1(a), infrared absorption features of NH_2OH in Figure 5.3(a) can be clearly identified. The abundant presence of CO in the ice acts as a matrix, isolating the formed NH_2OH molecules and preventing intermolecular (H-bond) interactions. Therefore, the NH_2OH absorption bands are narrower and also somewhat shifted compared to those observed in Figure 5.1(a) and, in accordance with Withnall & Andrews (1988) and Yeo & Ford (1990), these bands peak at 1606, 1375, 1142, and 889 cm^{-1}. As shown by Fedoseev et al. (2012), besides the fully saturated NH_2OH, also intermediate products of the hydrogenation scheme, such as HNO (1563 cm^{-1}), can be observed in the spectrum. This can be explained by the selected amount of co-deposited CO (12 times higher rate than NO) that may cause the trapping of intermediates like HNO in the bulk of the ice along with a suppression of ongoing hydrogenation.

In addition to the isolation effect of CO on NO and its hydrogenation products, CO can participate in H-atom addition reactions. Therefore, besides the strong absorption band of CO (centred at 2142 cm^{-1}) and its broad left shoulder presumably caused by lattice interactions, H_2CO —a product of two H-atom additions to CO— can be successfully assigned through the absorption features centred at 1730 and 1496 cm^{-1}. As concluded in many previous studies (summarized in Hama & Watanabe 2013 and Linnartz et al. 2015), the CO hydrogenation results in the formation of methanol. In this study, methanol is not observed in the RAIRS data, but a QMS-TPD confirms its formation. As stated before, the presence of N_2O in the spectrum is mainly caused by intrinsic contaminations in the NO gas bottle. No N-C bearing species are detected within the sensitivity range of our RAIR technique. Similar results were presented in Fedoseev et al. (2012).

The UV irradiation of this ice (Figure 5.3(b)) results in the disappearance of NH_2OH, HNO, and H_2CO absorption features, consistent with their photodestruction, and the simultaneous appearance of new absorption features, originating from newly formed photoproducts. Besides the formation of HCO radicals and NO monomers, assigned by absorption bands centred at 1859, 1091 Ewing et al. (1960), and 1875 cm^{-1} (Fateley et al. 1959; Minissale et al. 2014), respectively, the UV ice processing now results in the formation of N-C bearing molecules, such as HNCO. The latter is assigned through its strong absorption feature at 2261 cm^{-1} (Teles et al. 1989). Additional spectroscopic information is added in Figure 5.3 (right-hand panels) to further constrain the assignments through comparison with spectra of HCO (obtained by UV photoprocessing of H_2 entrapped in the solid CO matrix at similar experimental conditions) and NO monomers (Minissale et al. 2014). QMS data obtained from TPD experiments further support this assignment by detecting the HNCO desorption starting at 135 K and peaking at 160 K (see Figure 5.4 for more details on the TPD-QMS data). The TPD-QMS spectrum also shows UV photoproducts that cannot be identified by means of RAIRS. This is N_2 (note that the $m/z = 14$ signal is used instead of $m/z = 28$ that overlaps with the signal from CO) and a large desorption peak of CO_2 starting at around 68 K with its maximum peak at 81 K. Although CO_2 has strong absorption bands in the infrared, its assignment is challenged by the presence of absorption features from residual atmospheric CO_2 along the purged path of the IR beam outside the main chamber of the setup. The relative abundance of CO_2 in the irradiated ice sample, however, can be derived through the observation of $^{13}CO_2$ absorption at 2280 cm^{-1} (see the corresponding zoom-in shown in Figure 5.3). A natural isotope fractionation of roughly 1.1 per cent with respect to regular ^{12}C is assumed. No clear signs of NH_3 and only traces of NH_2OH are detected by means of QMS during TPD.

As opposed to the experiment involving solely NO (Figure 5.1), the addition of CO molecules results in a different final ice composition in the case of the co-exposure experiment when compared to the sequential exposure experiment discussed above (see Figure 5.3(b) and (c) for comparison). The simultaneous UV-photon and H-atom exposure of the co-deposited NO:CO
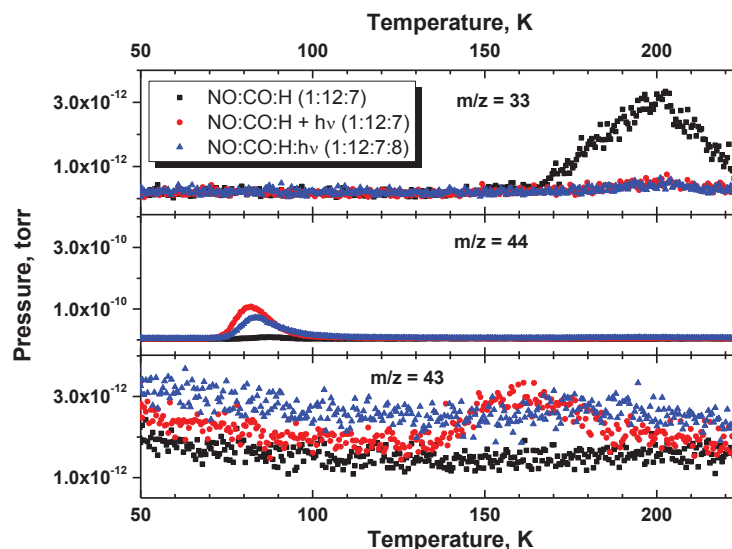
Figure 5.4: TPD spectra for three selected m/z values obtained after black squares— co-deposition of NO:CO = 1:12 molecular mixture with H-atoms for the total ratio of 1:12:7 (experiment 2.1); red circles— co-deposition of NO:CO = 1:12 molecular mixture with H-atoms followed by the UV-photon exposure of $\sim 1.6 \times 10^{16}$ photons cm^{-2} (experiment 2.2); blue triangles— co-deposition of NO:CO = 1:12 molecular mixture and H-atoms with simultaneous UV-photon exposure of $\sim 6.5 \times 10^{16}$ photons cm^{-2} (experiment 2.3). The total dose of NO molecules is estimated to be 8.5 L in all three experiments. The total H-atom fluence is 6×10^{16} atoms cm^{-2}. Here $m/z = 33$, $m/z = 44$, and $m/z = 43$ correspond to NH_2OH^+, $CO_2{}^+$, and $HNCO^+$, respectively.

gas mixture results in a significant reduction of the HNCO yield, as well as in a visual decrease of HCO and NO absorption features. The reduction of the HNCO yield is also confirmed by a decrease of the corresponding QMS integrated area ($m/z = 43$) obtained during TPD. Lower yields for HCO and NO can be expected. The co-exposure of the ice to UV-photons and H-atoms allows the species formed through the interaction with UV-photons to react with H-atoms. Thus, the decrease in the formation yield of the species that are highly reactive towards H-atoms is not surprising. HNCO, however, exhibits an activation barrier in the reaction with hydrogen atoms (Nguyen et al. 1996), so its decrease must be explained in a different way, e.g., by the consumption of the intermediate species involved in its formation.

Integrating the area under the $m/z = 33$ (NH_2OH) signal in the range between 140 and 225 K for experiments 2.1-2.3 reveals a decrease of the NH_2OH yield of about 10 times in the experiments 2.2 and 2.3 with respect to the yield measured in experiment 2.1. This is similar to what was found in experiments 1.2-1.4, i.e., independent of the addition of CO.

5.3.3   Simultaneous hydrogenation and UV processing of NO molecules co-deposited in H_2CO and CH_3OH-rich environments

Figure 5.5 presents the RAIR spectra obtained for experiments 3.2-3.3 (top panel) and 4.2-4.3 (bottom panel), where a CO environment (as in experiments 2.1-2.3) is replaced by H_2CO
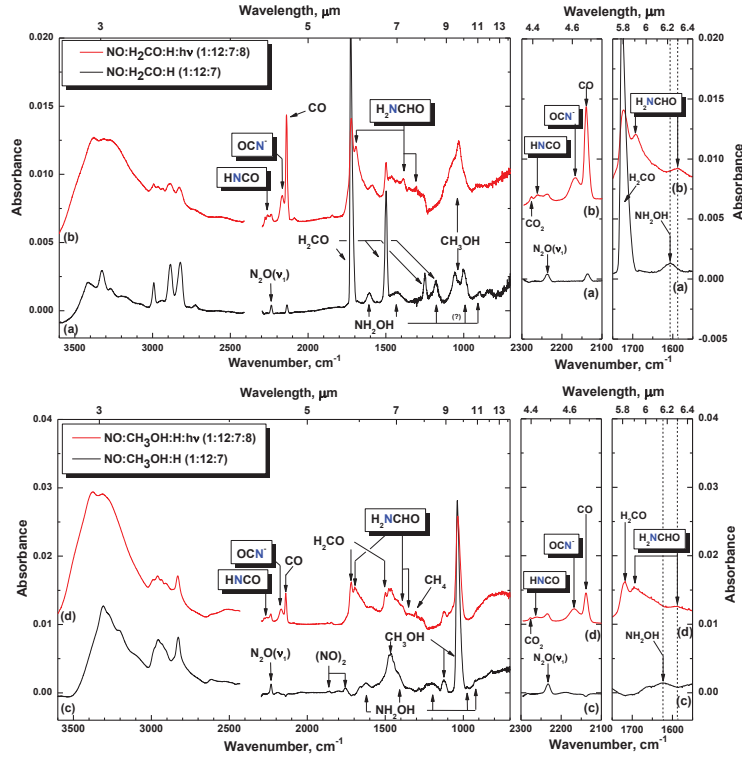
Figure 5.5: Top panel: RAIR spectra for NO in H_2CO obtained after (a) co-deposition of $NO:H_2CO$ = 1:12 molecular mixture with H-atoms (experiment 3.2); (b) co-deposition of $NO:H_2CO$ = 1:12 molecular mixture and H-atoms with simultaneous UV-photon exposure (experiment 3.3). Bottom panel: RAIR spectra for NO in CH_3OH mixtures, obtained after (c) co-deposition of $NO:CH_3OH$ = 1:12 molecular mixture with H-atoms (experiment 4.2); (d) co-deposition of $NO:CH_3OH$ = 1:12 molecular mixture with simultaneous exposure of H-atoms and UV-photons (experiment 4.3). The total exposure dose of NO molecules is estimated to be 8.5 L in all the experiments. The total estimated H-atom and UV-photon fluences are $\sim6\times10^{16}$ atoms cm^{-2} and $\sim6.5\times10^{16}$ photons cm^{-2}, respectively. The two right-hand panels on top and bottom panel present a zoom-in of spectra in the 2200 and 1650 cm^{-1} regions, where HNCO, OCN$^-$, and H_2NCHO absorptions can be seen.

(experiments 3.2-3.3) and then by CH_3OH (experiments 4.2-4.3). In both the top and bottom panel, the results for the co-exposure experiments with and without UV irradiation are compared to each other. In Figure 5.5(a), the RAIR spectrum obtained after co-deposition of an $NO:H_2CO$ mixture with only H-atoms shows the appearance of several new species. Along with the expected NH_2OH (see Figure 5.1(a) for comparison) and H_2CO bands (1730, 1498, 1248, and 1178 cm^{-1}), absorption features of CH_3OH (see Öberg et al. 2009) can be successfully assigned in the spectrum. These are associated with the broad absorption in the range $1500 - 1400$ cm^{-1}, caused by several ($\nu6, \nu4, \nu5, \nu10$) vibrational modes, and the strongest absorption of CH_3OH in the range between 1000 and 1070 cm^{-1}, caused by the C-O stretching vibration mode. It is not clear whether both of the absorption features in this spectral range are due to CH_3OH molecules in different environments or whether CH_3OH is responsible for only one of these features. Furthermore, carbon monoxide, an abstraction product of H-atom interaction with H_2CO, as found by Hidaka et al. (2004) and recently extensively discussed by Chuang et al. (2016), is also found (2136 cm^{-1}).

The simultaneous UV processing of the ice (Figure 5.5(b)) results in a significant decrease of H_2CO and NH_2OH absorption features and in the increase of CH_3OH and CO absorption bands. Simultaneously, new species are formed. These are N-C bearing species: HNCO (2261 cm^{-1}), which was already observed in the photolysis experiments involving CO (Figs 5.3(b) and (c)); OCN^- (2167 cm^{-1}; van Broekhuizen et al. 2004; and most importantly formamide, NH_2CHO (1693, 1590, 1388, and 1350 cm^{-1}; King 1971; Sivaraman et al. 2013. Other irradiation products that can be assigned by means of RAIRS are CH_4 (1303 cm^{-1}) and $^{13}CO_2$ (2276 cm^{-1}). QMS data obtained during the TPD confirm a significant production of CO_2 during the photolysis as well. The CH_4 assignment is confirmed through QMS data by observing CH_4 desorption starting at 48 and peaking at 57 K with a $m/z = 15$ to $m/z = 16$ ratio of 0.9. Unfortunately, the broad and overlapping co-desorbing profiles of H_2CO, CH_3OH, and NH_2OH do not allow for a clear deconvolution of the HNCO and NH_2CHO desorption features. Furthermore, it should be noted that thermal processing of this ice results in a rich chemistry, since H_2CO exhibits strong chemical activity upon heating in the presence of a base like NH_3 (see for example Schutte et al. 1993; Duvernay et al. 2014). In this study, NH_2OH may play the role of interacting base. The most intense m/z signal of HNCO ($m/z = 43$) rises at 180 K and exhibits a maximum at 205 K (van Broekhuizen et al. 2004), while NH_2CHO ($m/z = 45$) has at least two broad peaks in the TPD spectra with maxima at 165 and 215 K, confirming that both species may be present in the solid phase. The measured desorption peak is also in agreement with the desorption temperature of pure NH_2CHO, as reported by Dawley et al. (2014). On the other hand, RAIRS data show that formamide and isocyanic acid form efficiently already at 13 K, and well before thermal processing occurs during TPD.

The RAIR was obtained after NO hydrogenation in CH_3OH ice (Figure 5.5(c)) shows the presence of CH_3OH (1037 cm^{-1} and the broad absorption feature centred at 1465 cm^{-1}, see Öberg et al. 2009) and NH_2OH (see Figure 5.1(a) for comparison). Furthermore, non-hydrogenated NO in the form of cis-$(NO)_2$ can be assigned in the spectrum through absorptions at 1857 and 1756 cm^{-1}. The presence of NO indicates that HNO should also be found in the ice; however, its detection is not straightforward because of the overlap between the strongest absorption band of HNO at 1562 cm^{-1} and some CH_3OH absorption features. The coaddition of UV-photons in a similar experiment (Figure 5.5(d)) results in the expected decrease of CH_3OH and NH_2OH absorption bands. The photoprocessing products are similar to those discussed in the case of H_2CO-rich ices. Besides the formation of H_2CO, CO, and CH_4 that may solely originate from CH_3OH photoprocessing, three N-C bearing species are detected: OCN^-, HNCO, and NH_2CHO (see Figure 5.5(b) for comparison). It should be noted that the integrated areas under the absorption bands of OCN^-, HNCO, and NH_2CHO are

lower than in the case of H_2CO-rich ices. However, the final yields of these species are significantly higher than in the case of a CO-rich environment, where NH_2CHO is not observed.

Similarly as in the case of H_2CO-rich ices, a broad desorption feature of CH_3OH entrapping H_2CO and NH_2OH and eventual thermally induced chemistry do not allow to confidently assign HNCO and NH_2CHO desorbing peaks in the QMS data. Nevertheless, at least three peaks with *m/z* = 43 and *m/z* = 45 signals are present in the TPD spectra with desorption maxima at 135, 165, and 215 K, fully consistent with such an assignment. To further constrain the detection of NH_2CHO, the top panel of Figure 5.6 compares a co-deposition of $NO:H_2CO$ = 1:12 mixture with H-atoms and UV-photons (experiment 3.3) with RAIR difference spectra obtained between 210 and 240 K during the TPD after experiment 3.3, and the NIST reference spectrum of liquid NH_2CHO. The bottom panel of Figure 5.6 shows the analogue case for the $NO:CH_3OH$ = 1:12 mixture with H-atoms and UV-photons (experiment 4.3) compared to RAIR difference spectra obtained between 210 and 240 K during the TPD after experiment 4.3, and the NIST reference spectrum of liquid NH_2CHO. In both cases, the RAIR different spectra acquired at higher temperatures resemble closely the profile of the NIST spectrum of liquid NH_2CHO, confirming that NH_2CHO is formed at low temperatures and that right before its desorption, a nearly pure NH_2CHO ice is present on the gold substrate.

5.4 DISCUSSION

The main products observed after UV photolysis of hydrogenated NO ice, i.e., N_2, NH_3, and H_2O, are similar to the main products observed during NH_2OH gas-phase photolysis (Betts & Back 1965). Furthermore, no major differences are found between sequential and co-exposure experiments in terms of photoproducts of NH_2OH ice. Therefore, it is concluded that the UV-photons dissociate NH_2OH and the resulting radicals can react with other ice components to form new species, while the UV-photons impinging on NO and its unsaturated hydrogenation products do not result in the formation/detection of new molecules. Betts & Back (1965) investigated a series of high-pressure gas-phase reactions that may have an equivalent in the solid phase and could be relevant to the experiments discussed here. In their work, Betts & Back 1965 showed that the photodissociation of NH_2OH leads mainly to the formation of NH_2 and OH radicals. These radicals are then involved in further reactions:

$$NH_2OH + h\nu \longrightarrow NH_2 + OH \tag{31}$$

$$NH_2 + NH_2OH \longrightarrow NH_3 + NHOH \tag{32}$$

$$OH + NH_2OH \longrightarrow H_2O + NHOH \tag{33}$$

$$NHOH + NHOH \longrightarrow N_2 + 2H_2O \tag{34}$$

Our experimental results do not contradict these routes (reactions 31-34). It should be noted that the energy of the N-O bond in NH_2OH (2.7 eV; Hettema & Yarkony 1995) is significantly lower than the energy of the UV-photons produced by our H_2-discharge lamp (10.2 and ~7.7 eV; Ligterink et al. 2015a). Therefore, if photodissociation of NH_2OH proceeds through reaction (31), one or even both of the formed NH_2 and OH radicals could be in their electronically
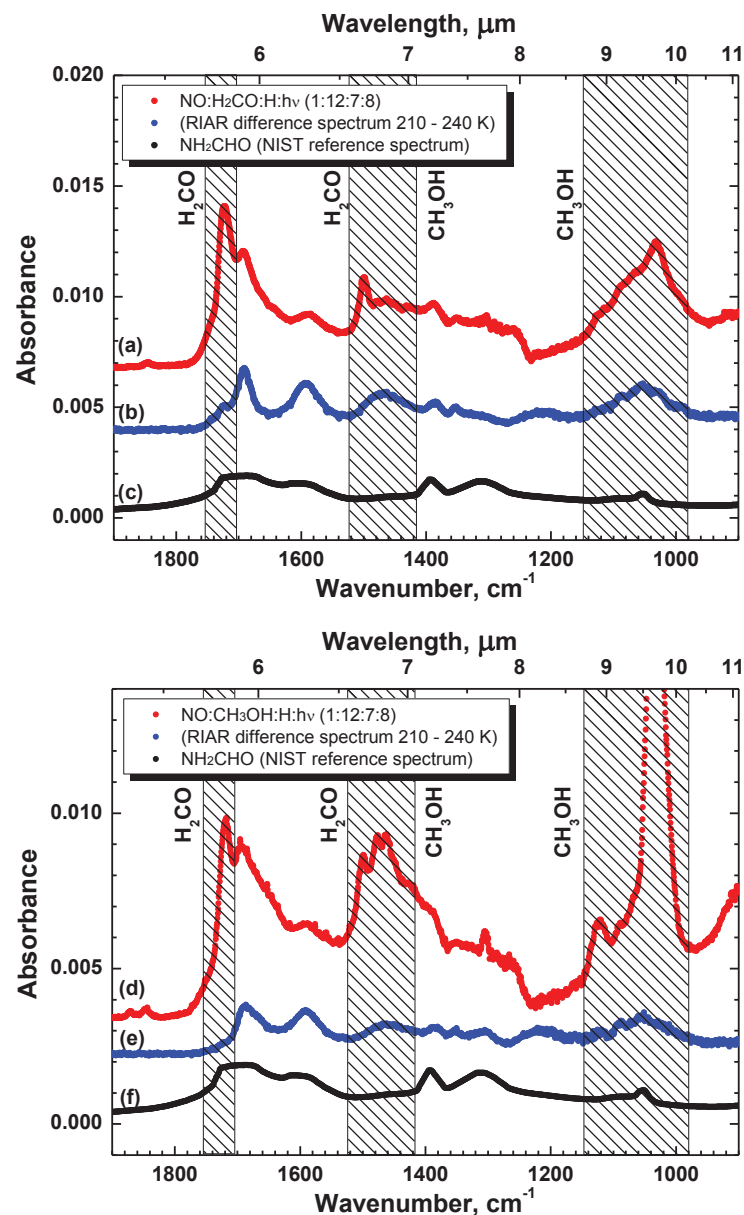
Figure 5.6: Top panel: RAIR spectra for (a) co-deposition of NO:H$_2$CO = 1:12 mixture with H-atoms and UV-photons (experiment 3.3); (b) RAIR difference spectra obtained between 210 and 240 K during the TPD after experiment 3.3; (c) NIST reference spectra of liquid NH$_2$CHO. Bottom panel: (d) co-deposition of NO:CH$_3$OH = 1:12 mixture with H-atoms and UV-photons (experiment 4.3); (e) RAIR difference spectra obtained between 210 and 240 K during the TPD after experiment 4.3; panel (f) same as panel (c). Dashed areas indicate spectral regions where IR features from trapped H$_2$CO and CH$_3$OH at high temperatures are expected.

and vibrationally excited states (Gericke et al. 1994; Luckhaus et al. 1999) or have excess translational energy. This, in turn, may promote reactions (32) and (33) that both require activation barriers to proceed in the solid phase. Moreover, the absence of a significant HNO and NO yield indicates that the photodissociation of NH_2OH into HNO and two H-atoms (Gericke et al. 1994) is an overall less efficient pathway:

$$NH_2OH + h\nu \longrightarrow HNO + 2H \tag{35}$$

$$HNO + h\nu \longrightarrow NO + H \tag{36}$$

The photodissociation of NH_2OH into NH_2 and OH (reaction 31) finds further confirmation when CO molecules are added into the chemical network. Both HNCO and CO_2 molecules observed in the experiments 2.2-2.3 can be formed by the interaction of NH_2 and OH radicals with the abundantly present CO molecules:

$$OH + CO \longrightarrow CO_2 + H \tag{37}$$

$$NH_2 + CO \longrightarrow HNCO + H \tag{38}$$
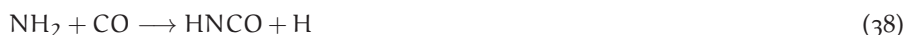
The formation of CO_2 as a result of CO interaction with OH is reported in a number of experimental studies and is expected to proceed through the HOCO complex as an intermediate that has a low activation barrier and can therefore be formed through reaction (37) with OH in its ground electronic state (Goumans et al. 2008; Oba et al. 2010; Ioppolo et al. 2011; Noble et al. 2011). Recent molecular dynamics calculations (Arasa et al. 2013) showed that the spontaneous dissociation of the HOCO complex requires an activation barrier to occur. Thus, in the formation of CO_2, a two-step mechanism may be involved in which a HOCO complex is formed by interaction of CO with a hydroxyl radical followed by an interaction with H-atoms or UV-photons. Calculations show that reaction (38) is endothermic by 0.41 eV and that it has an activation barrier of 1.39 eV (Nguyen et al. 1996). Thus, it requires NH_2 to be in a vibrationally or electronically excited state (or NH_2 with a very high translational energy) as will be discussed below, and reaction (38) to proceed before deexcitation of NH_2 occurs. The consumption of OH and NH_2 in reactions (37) and (38) also explains the decrease in the NH_3, H_2O, and consequently N_2 final yields as observed in the photolysis experiments involving CO, compared to the values found in the corresponding photolysis experiments of pure NO-hydrogenation products.

The addition of H_2CO or CH_3OH into the photolysis scheme complicates the reaction network because H_2CO and CH_3OH are also easily photodissociated resulting in efficient formation of several other photoproducts. The two possible H_2CO photodissociation channels are as follows:

$$H_2CO + h\nu \longrightarrow HCO + H \tag{39}$$

$$H_2CO + h\nu \longrightarrow CO + H_2 \tag{40}$$

(see McQuigg & Calvert 1969; Moore & Weisshaar 1983; Rhee et al. 2007). HCO and CO, both H_2CO photodissociation products, are chemically active towards NH_2 and OH. Interactions

with CO result in the formation of HNCO and CO_2 following reactions (37) and (38), as discussed earlier in this section. HNCO and CO_2 are indeed among the products observed during the simultaneous photolysis and hydrogenation of NO in H_2CO-rich ice.

Formamide is another product observed in this study that may be formed through the interaction of NH_2 and HCO:

$$NH_2 + HCO \longrightarrow H_2NCHO \tag{41a}$$

This radical-radical recombination should proceed without any activation barrier; however, a competing reaction should not be neglected:

$$NH_2 + HCO \longrightarrow NH_3 + CO \tag{41b}$$

Similarly to NH_2, the interaction of OH with HCO may proceed through two different pathways:

$$OH + HCO \longrightarrow HC(O)OH \tag{42a}$$

$$OH + HCO \longrightarrow H_2O + CO \tag{42b}$$

Although no HCOOH and NH_3 detections are possible in this study (see Section 5.3.3), their formation cannot be disproven due to the overlap of typical RAIR absorption features with those of other more abundant molecules. Thus, no solid conclusion can be made on the efficiency and branching ratio of reactions (41) and (42).

NH_2 and OH radicals formed in reaction (31) should be produced with significant excess energy. This excess energy could contribute to overcoming of activation barriers for the reactions of NH_2 and OH with H_2CO. In the first case, NH_2CHO should be formed (Barone et al. 2015):

$$NH_2 + H_2CO \longrightarrow H_2NCHO + H \tag{43a}$$

However, similar to reactions (41) and (42), a competing abstraction reaction may occur:

$$NH_2 + H_2CO \longrightarrow NH_3 + HCO \tag{43b}$$

The interaction of OH with H_2CO likely results in the abstraction reaction (Hudson et al. 2006):

$$OH + H_2CO \longrightarrow H_2O + HCO \tag{44}$$
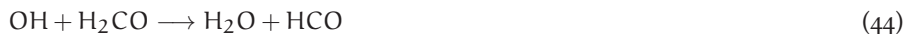
Recent calculations by Barone et al. (2015) suggested that reaction (43a) is nearly barrierless and can be efficient even at very low temperatures. If this is indeed the case, formamide production via reaction (31) followed by reaction (43a) should be overall more efficient than through a pathway involving reactions (31), (39), and (41a).

OCN^- observed in this study is a direct derivate of HNCO and can be formed in a number of proton transfer reactions. Along with H_2O and NH_3 that both can act as a base in interaction with isocyanic acid (Grim et al. 1989; Theule et al. 2011; Mispelaer et al. 2012), NH_2OH and NH_2CHO can act as a base as well:

$$NH_2OH(NH_3, H_2O, NH_2CHO) + HNCO \longrightarrow \tag{45}$$
$$NH_3OH^+(NH_3^+, H_3O^+, NH_3^+CHO)NCO^-$$
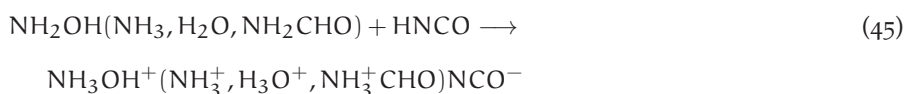
This can explain the detection of OCN^- in our RAIR data. The excess energy of HNCO produced through reaction (38) or through other possible mechanisms should help to overcome the activation barrier of reaction (45). A ratio between HNCO and OCN^- transmission band strengths of 1.7 is known from the literature (van Broekhuizen et al. 2005) and indicates that most of the isocyanic acid is in the form of its anion (see Figures 5.5(b) and (d)).

Simultaneous photolysis and hydrogenation of NO in a CH_3OH environment results in the same products observed in the two previous discussed cases, i.e., the photolysis and hydrogenation of NO in a CO and H_2CO-rich environment. This is not surprising because photoprocessing of CH_3OH leads to the dehydrogenation products H_2CO and CO and thus to the two cases already discussed before. The detection of methane among the photolysis products shows that part of the methanol is also photodissociated into OH and CH_3 to yield CH_4. Moreover, the interaction of CH_3OH with the photoproducts of reaction (31), i.e., energetically excited NH_2 and OH, should lead to H-atom abstraction reactions from methanol, due to the saturated nature of CH_3OH molecules. The lower formation yields of HNCO, OCN^-, and NH_2CHO in comparison to the case of H_2CO-rich ice is in agreement with the picture that the interaction of NH_2 and OH with H_2CO and CO is responsible for the observed reaction products rather than the direct interaction of NH_2 with CH_3OH molecules. Similar to the sequential and co-exposure experiments in H_2CO-rich ices, most of the HNCO ends up in its anionic form, OCN^-.

To conclude this discussion section, we mention another aspect of CH_3OH-related photochemistry. The photodissociation of CH_3OH also can lead to the formation of three distinct carbon-bearing radicals, i.e., CH_3, CH_2OH, and CH_3O. The formation of CH_3 finds direct confirmation through the detection of CH_4 that is formed in the reaction

$$CH_3 + H \longrightarrow CH_4 \tag{46}$$

or through the abstraction of H-atoms by CH_3 radicals from the other species present in the ice. Interactions of CH_3, CH_2OH, and CH_3O with NH_2 radicals, formed in the reaction (31), may in turn yield methylamine:

$$CH_3 + NH_2 \longrightarrow CH_3NH_2 \tag{47}$$

and two other rather exotic species. These are aminomethanol

$$CH_2OH + NH_2 \longrightarrow NH_2CH_2OH \tag{48}$$

and methoxyamine:

$$CH_3O + NH_2 \longrightarrow CH_3ONH_2 \tag{49}$$

Unfortunately, none of these complex molecules can be confidently detected in our RAIR spectra at 13 K. There is a significant overlap between the main infrared absorption features of CH_3NH_2 and CH_3ONH_2 (Gray & Lord 1957; Nelson 1970) with infrared bands of other species clearly present in the ice. As far as we know, IR spectra are not available in the literature for H_2NCH_2OH obtained by direct deposition due to the high instability of this species at room temperature. Nevertheless, based on other work, predictions can be made. Recent work by Paardekooper et al. (2016) report effective branching ratios of CH_3OH photodissociation with $CH_2OH:CH_3:CH_3O$ equal to 8:3:2 for UV sources similar to that used in this study. This makes H_2NCH_2OH (reaction 48) and to a lesser extent CH_3NH_2 (reaction 47) other likely candidates to be formed in experiments involving simultaneous hydrogenation and photolysis of NO in a CH_3OH environment.

5.5   ASTROCHEMICAL IMPLICATION AND CONCLUSIONS

Various astrochemical models show that a maximum in the gas-phase NO abundance is reached during the late stages of dark molecular cloud evolution (Charnley et al. 2001; Congiu et al. 2012b; Vasyunina et al. 2012), when the so-called CO freeze out occurs (Tielens et al. 1991; Gibb et al. 2004; Pontoppidan 2006; Öberg et al. 2011; Visser et al. 2011; Boogert et al. 2015). Thus, a peak of NO accretion on the grain surface is expected simultaneously with CO accretion and the chemical environment around depositing NO molecules should be rich in molecules observed in the CO-rich layer of the ice mantle. CH_3OH and H_2CO, i.e., the main hydrogenation surface reaction products of solid CO, are also expected to be present in the same interstellar ice layer (Cuppen et al. 2011; Penteado et al. 2015).

Here we show that the accretion of NO molecules under physical-chemical conditions that are similar to those observed in dark molecular clouds (i.e., $T \leqslant 15$ K, simultaneous H-atom accretion and UV-photon exposure, ice layers rich in CO, H_2CO, and CH_3OH molecules) results in the efficient formation of three N-C bearing species: HNCO, OCN^-, and NH_2CHO. OCN^- is usually assigned to the full or at least part of the XCN band that is observed in interstellar ices towards both low- and high-mass YSOs with abundances ranging from 0.3 to 0.8 per cent with respect to water ice (Öberg et al. 2011; Boogert et al. 2015). Although HNCO has not been observed in the solid phase, it is referred to as a direct precursor for OCN^- (van Broekhuizen et al. 2005; Boogert et al. 2015). The higher abundance of OCN^- over HNCO in our experiments is consistent with astronomical observations. Another important outcome of our study is the formation of NH_2CHO. If accretion of NO molecules onto grain surfaces is partially responsible for the OCN^- observations in ice mantles, then our work shows that NH_2CHO should also be present as a product of combined NO hydrogenation and photolysis in CO-rich ices and therefore linked to the formation of HNCO and OCN^-. Correlations between HNCO:OCN^-:NH_2CHO abundances in the solid state will result in the observation of HNCO:NH_2CHO ratio in the gas phase upon sublimation of the ice. This result is fully in line with the observed gas-phase correlation of HNCO and NH_2CHO abundances in the protostellar shock regions L1157-B1 and L1157-B2 (López-Sepulcre et al. 2015) as well as in low- and high-mass pre-stellar and protostellar objects (Bisschop et al. 2008; Mendoza et al. 2014). Moreover, it should be noted that although solid-state detections of HNCO and NH_2CHO in interstellar ices are lacking and only upper limits have been derived (Schutte et al. 1999; van Broekhuizen et al. 2004), both of these species have been observed in cometary ices with abundances of about 0.02 and 0.002 with respect to water ice (Mumma & Charnley 2011; Goesmann et al. 2015; Le Roy et al. 2015).

Figure 5.7 summarizes all findings in a reaction network illustrating how the aforementioned N-C bearing complex molecules HNCO, OCN^-, and NH_2CHO can be formed. The central role NH_2 plays is clear from this figure. In the experiments described here it is formed through the photodissociation of hydroxylamine, formed upon NO hydrogenation, but in interstellar clouds NH_2 radical could also originate from the photodissociation of NH_3, or from hydrogenation of atomic N. In the latter case, the NH_2 would not be energetic, reducing the probability to react with CO to form HNCO. Laboratory experiments showed that non-energetic reaction routes to HNCO and NH_2CHO are NH + CO, NH_2 + HCO and, possibly, NH_2 + H_2CO (see discussion here and Fedoseev et al. 2015). However, as interstellar NH_3 will be mostly mixed with H_2O in water-rich layers, and N hydrogenation is largely expected to occur in such polar ices (i.e., CO-poor ices), the present scheme, starting from NO, remains the most likely one that shows a chemical link among HNCO, OCN^-, and NH_2CHO.

The formation of two other complex organic species —aminomethanol (NH_2CH_2OH) and methylamine (CH_3NH_2)— is indicated in Figure 5.7 as well. The intermediate free radicals re-
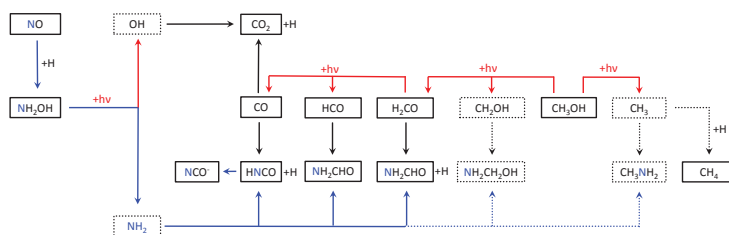
Figure 5.7: Proposed solid-state reaction network obtained from this study showing how various N-C bearing complex organic molecules are formed starting from hydrogenation and UV irradiation of NO ice. Solid boxes mark molecules and free radicals detected in this study, while dotted boxes indicate species for which direct laboratory detections are still missing. Blue arrows indicate nitrogen-bearing species formation routes. Red arrows indicate photodissociation routes.

quired to form these species are present in the ice. Nevertheless, the detection of aminomethanol and methylamine in our experiments has not been successful yet.

Besides aforementioned formation of N-C bearing complex molecules, co-exposure of NO molecules to UV-photons and H-atoms results in a significant decrease of NH_2OH in the ice. In particular, a drop of one order of magnitude in NH_2OH abundance is observed under our experimental conditions, when NH_2OH is exposed to UV-photons. This also puts an upper limit on the amount of accreted NO molecules that can be converted into HNCO, OCN^-, and NH_2CHO; this value has to be less or equal than the loss in NH_2OH abundance. Moreover, the efficient photodissociation of NH_2OH and the observed reactivity of its photofragments in CO, H_2CO, and CH_3OH-rich ices may account for a lower NH_2OH abundance in interstellar ices than expected on the basis of hydrogenation experiments only (Congiu et al. 2012b) and can be one of the reasons responsible for the so far unsuccessful efforts to identify this molecule in the ISM (Pulliam et al. 2012; McGuire et al. 2015).

The last point that is stressed here is the astrobiological importance of our findings. The general role that molecules containing an N-C bond could play in the synthesis of amino acids and nucleobases is well illustrated by the example of HCN polymerization (see for instance figure1 of Matthews & Minard 2008). In turn, a [-(H)NC(O)-] functional group is a necessary constituent of all peptides—oligomers and polymers consisting of amino-acids that are crucial for life on Earth. Thus, the formation of molecules with an [-(H)NC(O)-] structural backbone, such as HNCO and NH_2CHO, is interesting from an astrobiological point of view because these molecules are potentially involved in the synthesis of fragments of peptides as schematically illustrated in figure 6 of Fedoseev et al. (2015). Clearly, the detection of interstellar ice constituents with peptide (-(H)NC(O)-) or just N-C bonds with the James Webb Space Telescope would provide new insights in chemical processes that are considered to provide the building blocks of biologically relevant molecules. Also in the laboratory, ices rich in HNCO (OCN^-), NH_2CHO, and CH_3OH offer a starting point for studies that focus on the formation of 'heavier' species. Such work reaches beyond the potential importance of interstellar ices, as HNCO and NH_2CHO delivered to primordial terrestrial oceans through cometary impacts may also play a role in cometary ices, full in line with recent studies analyzing the constituents of comet 67P/Churyumov-Gerasimenko (Goesmann et al. 2015; Le Roy et al. 2015).

BIBLIOGRAPHY

Anton, R., Wiegner, T., Naumann, W., et al. 2000, Review of Scientific Instruments, 71, 1177

Arasa, C., van Hemert, M. C., van Dishoeck, E. F., & Kroes, G. J. 2013, Journal of Physical Chemistry A, 117, 7064

Barone, V., Latouche, C., Skouteris, D., et al. 2015, Mon. Not. R. Astron. Soc., 453, L31

Bertie, J. E. & Shehata, M. R. 1985, J. Chem. Phys., 83, 1449

Betts, J. & Back, R. A. 1965, Canadian Journal of Chemistry, 43, 2678

Bisschop, S. E., Jørgensen, J. K., Bourke, T. L., Bottinelli, S., & van Dishoeck, E. F. 2008, Astron. Astrophys., 488, 959

Bisschop, S. E., Jørgensen, J. K., van Dishoeck, E. F., & de Wachter, E. B. M. 2007, Astron. Astrophys., 465, 913

Blagojevic, V., Petrie, S., & Bohme, D. K. 2003, Mon. Not. R. Astron. Soc., 339, L7

Boogert, A. C. A., Gerakines, P. A., & Whittet, D. C. B. 2015, Ann. Rev. Astron. Astrophys., 53, 541

Charnley, S. B., Rodgers, S. D., & Ehrenfreund, P. 2001, Astron. Astrophys., 378, 1024

Chuang, K.-J., Fedoseev, G., Ioppolo, S., van Dishoeck, E. F., & Linnartz, H. 2016, Mon. Not. R. Astron. Soc., 455, 1702

Congiu, E., Chaabouni, H., Laffon, C., et al. 2012a, J. Chem. Phys., 137, 054713

Congiu, E., Fedoseev, G., Ioppolo, S., et al. 2012b, Astrophys. J. Lett., 750, L12

Cuppen, H. M., Penteado, E. M., Isokoski, K., van der Marel, N., & Linnartz, H. 2011, Mon. Not. R. Astron. Soc., 417, 2809

Dawley, M. M., Pirim, C., & Orlando, T. M. 2014, Journal of Physical Chemistry A, 118, 1228

Duley, W. W. & Williams, D. A. 1984, Inorganic Chemistry

Duvernay, F., Danger, G., Theulé, P., Chiavassa, T., & Rimola, A. 2014, Astrophys. J., 791, 75

Ewing, G. E., Thompson, W. E., & Pimentel, G. C. 1960, J. Chem. Phys., 32, 927

Fateley, W. G., Bent, H. A., & Crawford, Jr., B. 1959, J. Chem. Phys., 31, 204

Fedoseev, G., Cuppen, H. M., Ioppolo, S., Lamberts, T., & Linnartz, H. 2015, Mon. Not. R. Astron. Soc., 448, 1288

Fedoseev, G., Ioppolo, S., Lamberts, T., et al. 2012, J. Chem. Phys., 137, 054714

Fuchs, G. W., Cuppen, H. M., Ioppolo, S., et al. 2009, Astron. Astrophys., 505, 629

Gericke, K.-H., Lock, M., Schmidt, F., & Comes, F. J. 1994, J. Chem. Phys., 101, 1988

Gerin, M., Viala, Y., Pauzat, F., & Ellinger, Y. 1992, Astron. Astrophys., 266, 463

Gibb, E. L., Whittet, D. C. B., Boogert, A. C. A., & Tielens, A. G. G. M. 2004, Astrophys. J. Suppl. Ser., 151, 35

Goesmann, F., Rosenbauer, H., Bredehöft, J. H., et al. 2015, Science, 349

Goldsmith, P. F. & Li, D. 2005, Astrophys. J., 622, 938

Goumans, T. P. M., Uppal, M. A., & Brown, W. A. 2008, Mon. Not. R. Astron. Soc., 384, 1158

Gray, A. P. & Lord, R. C. 1957, J. Chem. Phys., 26, 690

Grim, R. J. A., Greenberg, J. M., de Groot, M. S., et al. 1989, Astron. Astrophys. Suppl., 78, 161

Hama, T. & Watanabe, N. 2013, Chemical Reviews, 113, 8783

He, J., Vidali, G., Lemaire, J.-L., & Garrod, R. T. 2015, Astrophys. J., 799, 49

Henderson, B. L. & Gudipati, M. S. 2015, Astrophys. J., 800, 66

Herbst, E. & Klemperer, W. 1973, Astrophys. J., 185, 505

Hettema, H. & Yarkony, D. R. 1995, J. Chem. Phys., 102, 8431

Hidaka, H., Watanabe, N., Shiraki, T., Nagaoka, A., & Kouchi, A. 2004, Astrophys. J., 614, 1124

Hiraoka, K., Ohashi, N., Kihara, Y., et al. 1994, Chemical Physics Letters, 229, 408

Hiraoka, K., Yamashita, A., Yachi, Y., et al. 1995, Astrophys. J., 443, 363

Hudson, J. E., Weng, Z. F., Vallance, C., & Harland, P. W. 2006, International Journal of Mass Spectrometry, 248, 42

Ioppolo, S., Fedoseev, G., Lamberts, T., Romanzin, C., & Linnartz, H. 2013, Review of Scientific Instruments, 84, 073112

Ioppolo, S., Fedoseev, G., Minissale, M., et al. 2014a, Phys. Chem. Chem. Phys., 16, 8270

Ioppolo, S., Öberg, K. I., & Linnartz, H. 2014b, Laboratory Astrochemistry - FromMolecules Through Nanoparticles to Grains, Wiley, New York, 289

Ioppolo, S., van Boheemen, Y., Cuppen, H. M., van Dishoeck, E. F., & Linnartz, H. 2011, Mon. Not. R. Astron. Soc., 413, 2281

Joshi, P. R., Zins, E.-L., & Krim, L. 2012, Mon. Not. R. Astron. Soc., 419, 1713

Kahane, C., Ceccarelli, C., Faure, A., & Caux, E. 2013, Astrophys. J. Lett., 763, L38

King, S.-T. 1971, Journal of Physical Chemistry, 75, 405

Kohin, B. C. 1960, J. Chem. Phys., 33, 882

Le Roy, L., Altwegg, K., Balsiger, H., et al. 2015, Astron. Astrophys., 583, A1

Ligterink, N. F. W., Paardekooper, D. M., Chuang, K.-J., et al. 2015a, Astron. Astrophys., 584, A56

Ligterink, N. F. W., Tenenbaum, E. D., & van Dishoeck, E. F. 2015b, Astron. Astrophys., 576, A35

Linnartz, H., Ioppolo, S., & Fedoseev, G. 2015, International Reviews in Physical Chemistry, 34, 205

Liszt, H. S. & Turner, B. E. 1978, Astrophys. J. Lett., 224, L73

López-Sepulcre, A., Jaber, A. A., Mendoza, E., et al. 2015, Mon. Not. R. Astron. Soc., 449, 2438

Luckhaus, D., Scott, J. L., & Fleming Crim, F. 1999, J. Chem. Phys., 110, 1533

Maity, S., Kaiser, R. I., & Jones, B. M. 2015, Phys. Chem. Chem. Phys., 17, 3081

Mathis, J. S., Mezger, P. G., & Panagia, N. 1983, Astron. Astrophys., 128, 212

Matthews, C. N. & Minard, R. D. 2008, in IAU Symposium, Vol. 251, Organic Matter in Space, ed. S. Kwok & S. Sanford, 453–458

McGonagle, D., Irvine, W. M., Minh, Y. C., & Ziurys, L. M. 1990, Astrophys. J., 359, 121

McGuire, B. A., Carroll, P. B., Dollhopf, N. M., et al. 2015, Astrophys. J., 812, 76

McQuigg, R. D. & Calvert, J. G. 1969, Journal of the American Chemical Society, 91, 1590

Mendoza, E., Lefloch, B., López-Sepulcre, A., et al. 2014, Mon. Not. R. Astron. Soc., 445, 151

Minissale, M., Fedoseev, G., Congiu, E., et al. 2014, Phys. Chem. Chem. Phys., 16, 8257

Mispelaer, F., Theule, P., Duvernay, F., Roubin, P., & Chiavassa, T. 2012, Astron. Astrophys., 540, A40

Moore, C. B. & Weisshaar, J. C. 1983, Annual Review of Physical Chemistry, 34, 525

Mumma, M. J. & Charnley, S. B. 2011, Ann. Rev. Astron. Astrophys., 49, 471

Nelson, H. M. 1970, J. Chem. Phys., 53, 1433

Nguyen, M. T., Sengupta, D., Vereecken, L., Peeters, J., & Vanquickenborne, L. G. 1996, Journal of Physical Chemistry, 100, 1615

Nightingale, R. E. & Wagner, E. L. 1954, J. Chem. Phys., 22, 203

Noble, J. A., Dulieu, F., Congiu, E., & Fraser, H. J. 2011, Astrophys. J., 735, 121

Noble, J. A., Theule, P., Congiu, E., et al. 2015, Astron. Astrophys., 576, A91

Oba, Y., Watanabe, N., Kouchi, A., Hama, T., & Pirronello, V. 2010, Astrophys. J. Lett., 712, L174

Öberg, K. I. 2009, PhD thesis, Leiden University

Öberg, K. I., Garrod, R. T., van Dishoeck, E. F., & Linnartz, H. 2009, Astron. Astrophys., 504, 891

Öberg, K. I., van der Marel, N., Kristensen, L. E., & van Dishoeck, E. F. 2011, Astrophys. J., 740, 14

Paardekooper, D. M., Bossa, J.-B., & Linnartz, H. 2016, Astron. Astrophys., 592, A67

Penteado, E. M., Boogert, A. C. A., Pontoppidan, K. M., et al. 2015, Mon. Not. R. Astron. Soc., 454, 531

Pontoppidan, K. M. 2006, Astron. Astrophys., 453, L47

Prasad, S. S. & Tarafdar, S. P. 1983, Astrophys. J., 267, 603

Pulliam, R. L., McGuire, B. A., & Remijan, A. J. 2012, Astrophys. J., 751, 1

Pwa, T. H. & Pottasch, S. R. 1986, Astron. Astrophys., 164, 116

Reding, F. P. & Hornig, D. F. 1955, J. Chem. Phys., 23, 1053

Rhee, T. S., Brenninkmeijer, C. A. M., & Röckmann, T. 2007, Atmospheric Chemistry & Physics Discussions, 7, 12715

Schutte, W. A., Allamandola, L. J., & Sandford, S. A. 1993, Science, 259, 1143

Schutte, W. A., Boogert, A. C. A., Tielens, A. G. G. M., et al. 1999, Astron. Astrophys., 343, 966

Sivaraman, B., Raja Sekhar, B. N., Nair, B. G., Hatode, V., & Mason, N. J. 2013, Spectrochimica Acta Part A: Molecular Spectroscopy, 105, 238

Teles, J. H., Maier, G., Andes Hess, B., et al. 1989, Chemische Berichte, 122, 753

Theule, P., Duvernay, F., Ilmane, A., et al. 2011, Astron. Astrophys., 530, A96

Tielens, A. G. G. M., Tokunaga, A. T., Geballe, T. R., & Baas, F. 1991, Astrophys. J., 381, 181

Tschersich, K. G. 2000, Journal of Applied Physics, 87, 2565

van Broekhuizen, F. A., Keane, J. V., & Schutte, W. A. 2004, Astron. Astrophys., 415, 425

van Broekhuizen, F. A., Pontoppidan, K. M., Fraser, H. J., & van Dishoeck, E. F. 2005, Astron. Astrophys., 441, 249

Vasyunina, T., Vasyunin, A. I., Herbst, E., & Linz, H. 2012, Astrophys. J., 751, 105

Visser, R., Doty, S. D., & van Dishoeck, E. F. 2011, Astron. Astrophys., 534, A132

Watanabe, N. & Kouchi, A. 2002, Astrophys. J. Lett., 571, L173

Withnall, R. & Andrews, L. 1988, Journal of Physical Chemistry, 92, 2155

Yeo, G. A. & Ford, T. A. 1990, Journal of Molecular Structure, 217, 307

Zhitnikov, R. A. & Dmitriev, Y. A. 2002, Astron. Astrophys., 386, 1129

6

REACTIVE DESORPTION OF CO HYDROGENATION PRODUCTS UNDER COLD PRE-STELLAR CORE CONDITIONS

The astronomical gas-phase detection of simple species and small organic molecules in cold pre-stellar cores, with abundances as high as $\sim 10^{-8} - 10^{-9}$ n_H, contradicts the generally accepted idea that at 10 K, such species should be fully frozen out on grain surfaces. A physical or chemical mechanism that results in a net transfer from solid-state species into the gas phase offers a possible explanation. Reactive desorption, i.e., desorption following the exothermic formation of a species, is one of the options that has been proposed. In astronomical models, the fraction of molecules desorbed through this process is handled as a free parameter, as experimental studies quantifying the impact of exothermicity on desorption efficiencies are largely lacking. In this work, we present a detailed laboratory study with the goal of deriving an upper limit for the reactive desorption efficiency of species involved in the $CO-H_2CO-CH_3OH$ solid-state hydrogenation reaction chain. The limit for the overall reactive desorption fraction is derived by precisely investigating the solid-state elemental carbon budget, using reflection absorption infrared spectroscopy and the calibrated solid-state band-strength values for CO, H_2CO and CH_3OH. We find that for temperatures in the range of 10 to 14 K, an upper limit of 0.24 ± 0.02 for the overall elemental carbon loss upon CO conversion into CH_3OH. This corresponds with an effective reaction desorption fraction of $\leqslant 0.07$ per hydrogenation step, or $\leqslant 0.02$ per H-atom induced reaction, assuming that H-atom addition and abstraction reactions equally contribute to the overall reactive desorption fraction along the hydrogenation sequence. The astronomical relevance of this finding is discussed.

6.1   INTRODUCTION

Surface chemistry in the earliest phase of molecular cloud evolution is determined by a rather low particle density ($\sim 10^3 - 10^4$ cm^{-3}) at temperatures around 15 K. In such environments, chemical processes on dust grains are largely dominated by H-atom addition reactions, forming an H_2O-rich polar ice layer on silicate dust grains by recombining oxygen and hydrogen atoms (Tielens & Hagen 1982; Tielens et al. 1991; Ioppolo et al. 2008, 2010; Miyauchi et al. 2008; Cuppen et al. 2010; Öberg et al. 2011; van Dishoeck et al. 2013; Boogert et al. 2015; Linnartz et al. 2015). During this stage, other molecules, like NH_3 and CH_4, also form in N+H and C+H addition reactions (Hasegawa et al. 1992; Hiraoka et al. 1995, 1998; Hidaka et al. 2011; Fedoseev et al. 2015b). In the next phase, temperatures become as low as ~ 10 K and densities increase ($\sim 10^{4-5}$ cm^{-3}); gaseous CO accretes onto the pre-formed H_2O-rich ice and forms a CO-rich apolar ice coating (Pontoppidan 2006), an event often referred to as the 'catastrophic CO freeze-out stage.' The timescale for the CO freeze-out phase is about 10^{4-5} years ($1 \times 10^9/n_H$ years where $n_H = 2n(H_2) + n(H)$, Willacy & Millar 1998), which is shorter than the typical lifetime of a low-mass prestellar core ($\sim 4.5 \times 10^5$ years, Enoch et al. 2008). The CO coating is regarded as a starting point in the hydrogenation scheme that leads primarily to the formation of H_2CO and CH_3OH through successive H-atom additions. This reaction scheme has been studied in much detail before, in a gas-grain model by Tielens & Hagen (1982), in astrochemical simulations and theoretical studies (Charnley 1997; Cuppen et al. 2009; Chang & Herbst 2012)) and in a number of systematic laboratory experiments (Hiraoka et al. 1994; Watanabe & Kouchi 2002; Zhitnikov & Dmitriev 2002; Fuchs et al. 2009). The solid-state laboratory and astrochemical modeling conclusions are in agreement with the observed CH_3OH ice and gas abundances in star-forming regions that cannot be explained through a pure gas-phase radiative association route (Garrod et al. 2006; Geppert et al. 2006). Analysis of Very Large Telescope ice data shows that CH_3OH and CO must be mixed in interstellar ices and exist in a water poor environment (Cuppen et al. 2011; Penteado et al. 2015), fully consistent with the picture that methanol is formed via sequential hydrogenation of accreted CO molecules. Moreover, recent theoretical and laboratory studies revealed that recombination of the reactive intermediates, HCO, CH_3O, and CH_2OH formed through H-atom addition and abstraction reactions along the CO-H_2CO-CH_3OH chain, also result in the formation of larger complex organic molecules (COMs), like ethylene glycol, glycolaldehyde, methyl formate, and even glycerol in the solid state (Garrod et al. 2006; Woods et al. 2012; Butscher et al. 2015; Fedoseev et al. 2015a, 2017; Chuang et al. 2016, 2017).

For the typical pressure and temperature conditions in dark and dense clouds, all of these species except H_2 and He are expected to be fully depleted into the solid state. However, astronomical observations show unexpectedly large abundances of gaseous CH_3OH and COMs (Öberg et al. 2010; Bacmann et al. 2012; Cernicharo et al. 2012; Jiménez-Serra et al. 2016). In dark and pre-stellar clouds, it is too cold for thermal desorption to take place; thus, nonthermal mechanisms need to be considered to explain the observed gas-phase abundances, but effective low-temperature desorption processes remain poorly understood.

Different mechanisms have been proposed, investigated, and discussed, to explain how frozen species can sublimate. Until recently, UV induced photodesorption was considered to be an efficient process for both non-dissociative desorption, i.e., CO photodesorption, and dissociative processes eventually followed by fragment recombination in the ice or kick-out processes, i.e., H_2O photodesorption (Andersson & van Dishoeck 2008; Arasa et al. 2015). However, experiments on methanol ice exhibit substantial molecular fragmentation, including CH_3O, CH_2OH, and CH_3, and with photodesorption rates far too low to transfer substantial amounts of intact CH_3OH into the gas phase (Bertin et al. 2016; Cruz-Diaz et al. 2016). It is

expected that this will also apply to COMs larger than methanol; photodesorption and photodissociation are here clearly connected. A possible way to circumvent fragmentation upon photo-excitation is UV induced codesorption; the excitation of one species results in desorption of another species. For mixed CO and N_2 ices, N_2 photocodesorption rate (defined as indirect DIET photodesorption rate) was found to be a highly effective process, i.e., $\sim 10^{-2}$ molecule cm^{-2} $photon^{-1}$ for photon energies between 7.9 and 9.5 eV (Bertin et al. 2013), but in ice mixtures of CO and CH_3OH no methanol could be detected upon CO excitation (Bertin et al. 2016). In a similar way, low-temperature thermal codesorption of a less volatile species like methanol with CO was only found to yield very low upper limits of 7×10^{-7} molecules per CO (Ligterink et al. 2018). Local heating of an ice mantle induced by the impacting cosmic rays offers another possible mechanism (Leger et al. 1985; Ivlev et al. 2015), but given the high energies involved, it is rather unlikely that this would be a less destructive process than photodesorption, and this process is generally less effective for strongly bound molecules like CH_3OH than for CO. An interesting alternative is reactive desorption.

Reactive desorption may contribute to the gas-phase enrichment of both simple and complex species; directly, upon formation, formaldehyde, methanol or other COMs are instantly released into the gas phase because of the available excess energy of several eV, or indirectly, by releasing intermediates that cannot be efficiently formed in gas-phase chemical networks, but may act as precursor in COM gas-phase networks. A reactive codesorption process cannot be excluded either, but the excess energy upon bond formation may rapidly dissipate into the ice lattice before being absorbed by another species. These three scenarios may take place simultaneously, but with different efficiencies.

In astrochemical models, the reactive desorption fraction, i.e., the efficiency of product desorption from the surface after reaction, is usually a free parameter, chosen in a range of $0.01 - 0.1$ to account for the steady-state gas-phase abundances of simple species as observed in the later stages of dense clouds (Garrod et al. 2007; Vasyunin & Herbst 2013). The initial focus was on energy release upon H_2 formation (Duley & Williams 1993), and later extended to other reactions (Garrod et al. 2007; Vasyunin & Herbst 2013; Cazaux et al. 2015; Minissale et al. 2016b; Fredon et al. 2017). In the latter work, reactive desorption of species was also proposed as a starting point for low-temperature gas-phase formation of COMs (see also Balucani et al. 2015; Taquet et al. 2016; Rivilla et al. 2017; Vasyunin et al. 2017). Currently, the relative solid-state and gas-phase formation efficiencies for dark cloud conditions are under renewed debate.

So far, there have been few attempts to experimentally study the reactive desorption of the two main CO hydrogenation products, H_2CO and CH_3OH. There is a reason for this: the simultaneous occurrence of H-atom induced addition and abstraction reactions, i.e., forward and backward steps along the reaction chain (Figure 6.1), make it hard to de-convolute the individual reaction steps.

Previously reported experimental desorption fractions for reactive steps in the CO hydrogenation chain are high. Hidaka et al. (2004) stated that the H_2CO reactive desorption fraction during hydrogenation could be as high as 60% to rationalize their finding that the column density of the newly formed CH_3OH product was less than the consumed column density of the pre-deposited H_2CO, i.e., $\Delta N(CH_3OH) / \Delta N(H_2CO) < 1$. Minissale et al. (2016b) found a reactive desorption fraction of 40% for the single reaction $HCO + H \longrightarrow CO + H_2$. This reaction was studied in the sub-monolayer region on a bar of oxidized highly oriented pyrolytic graphite substrate using quadrupole mass spectrometry. For a more astronomically relevant thick ice (several tens of monolayers) these conditions are likely not fully representative and therefore reactive desorption fractions may be substantially different as well.
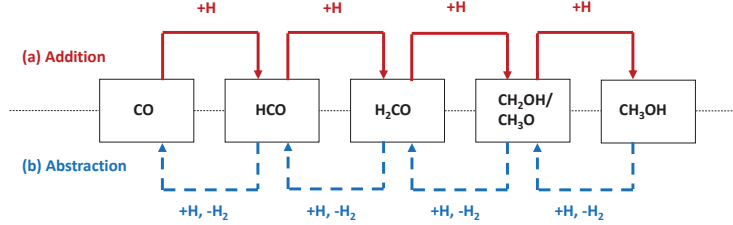
Figure 6.1: CO-H$_2$CO-CH$_3$OH hydrogenation sequence scheme. The solid line and dashed line are for H-atom (a) addition and (b) abstraction reactions, respectively.

The work presented here is motivated by the lack of experimentally determined reactive desorption fractions for hydrogenation reactions in multi-layered CO-rich interstellar ice analogs, i.e., for an astrochemically relevant ice thickness of $\sim$0.01 μm (Boogert et al. 2015). Rather than trying to disentangle the individual reactions and to measure the individual reaction products in the gas phase, we focus on the full CO-H$_2$CO-CH$_3$OH hydrogenation sequence. This is realized by estimating as precisely as possible, the difference in solid-state elemental carbon budget between the amount available from the original species and the resulting solid-state hydrogenation products. We assume that the observed difference is fully or at least partially due to reactive desorption, i.e., the resulting value reflects an upper limit. To perform such experiments, it is necessary to derive setup specific band-strength values in cm molecule^{-1} for each of the involved species and their ice mixtures.

In the following section the experimental procedure is described. The results are presented in Section 6.3. In the final section the astronomical relevance of the data and conclusions are presented.

6.2   EXPERIMENTAL

6.2.1   *Approach*

The total consumption of elemental carbon of the original species should be equal to the total amount of elemental carbon of the formed species, both in the solid state and, after reactive desorption, in the gas phase:

$$N_{\text{consumed}}(\text{C}) = \Delta N_{\text{solid}}(\text{CO}) = \Delta N_{\text{solid}}(\text{H}_2\text{CO}) + \Delta N_{\text{solid}}(\text{CH}_3\text{OH}) + N_{\text{RD}}(\text{C}) \quad (50)$$

where $\Delta N_{\text{solid}}(\text{CO})$ is the column density of CO consumption, $\Delta N_{\text{solid}}(\text{H}_2\text{CO})(\Delta N_{\text{solid}}(\text{CH}_3\text{OH}))$ is the net column density of the H$_2$CO (CH$_3$OH) formation, and $N_{\text{RD}}(\text{C})$ is the column density of carbon-bearing species upon reactive desorption mechanism after H-atom bombardment. This means that an upper limit for $N_{\text{RD}}(\text{C})/N_{\text{consumed}}(\text{C})$ can be derived by comparing accurately the total difference in CO abundance and H$_2$CO and CH$_3$OH abundances. In practice, Equation (50) is only an approximation, as it does not take into account other loss channels, such as the formation of other products than H$_2$CO and CH$_3$OH; reactive intermediates can recombine and form COMs larger than methanol, as recently shown by Chuang

et al. (2016) and Fedoseev et al. (2017). The impact of this restriction is discussed in Section 6.3.

6.2.2 *Experimental Setup*

All experiments are performed using SURFRESIDE[2], an ultra-high vacuum setup fully optimized to study non-energetic atom addition reactions in interstellar ice analogs at cryogenic temperatures. Details of the design and operation of SURFRESIDE[2] are available from Ioppolo et al. (2013) and Fedoseev et al. (2016). The base pressure in the main chamber is $\sim 10^{-10}$ mbar, and the corresponding H_2O contamination through background gas accretion is negligible ($< 6.3 \times 10^{10}$ molecule cm^{-2} s^{-1}). A gold-plated copper substrate is mounted in the center of the main chamber and cooled by a recently upgraded closed-cycle helium cryostat that allows to vary the substrate temperature between 8 and 450 K. A silicon diode is used to monitor the temperature with 0.5 K absolute accuracy. It should be noted that the temperatures used in the present manuscript are about ~ 2 K lower than the corresponding numbers used in Fuchs et al. (2009) new and more precise thermal sensors were installed on the substrate. Gaseous species, i.e., H_2CO obtained by thermal decomposition of paraformaldehyde (Sigma-Aldrich, 95%) at 60 °C—80 °C under vacuum, CH_3OH purified through multiple freeze-pump-thaw cycles and CO (Linde 2.0), are admitted into the UHV chamber through high-precision leak valves mounted under an angle of 22° from the substrate surface normal. The ices are grown with sub-monolayer precision with CO, H_2CO and CH_3OH deposition rates of $\sim 1.7 \times 10^{12}$, $\sim 1.4 \times 10^{12}$ and $\sim 2.2 \times 10^{12}$ molecules cm^{-2} s^{-1}, respectively. The corresponding ice column densities for CO, H_2CO, and CH_3OH are $\sim 6.0 \times 10^{15}$, $\sim 5.0 \times 10^{15}$, and $\sim 8.0 \times 10^{15}$ molecules cm^{-2}, respectively. The details of the exact deposition rate calculations are provided later.

After a preset ice thickness of the precursor species is realized, H-atoms are introduced using a Hydrogen Atom Beam Source (Tschersich 2000), mounted in a second UHV chamber. A nose-shape quartz pipe is placed along the path to efficiently quench and thermalize excited H-atoms and nondissociated molecules through multiple collisions with the walls of the pipe. The used H-atom flux in this work amounts to $\sim 8 \times 10^{12}$ atoms cm^{-2} s^{-1} with an absolute uncertainty of $< 50\%$ (Ioppolo et al. 2013) and H-atoms reach the surface under an incident angle of 45° from the substrate surface normal.

The ice composition is monitored in situ, before and during H-atom bombardment by Fourier Transform Reflection-Absorption InfraRed Spectroscopy in the range from 700 to 4000 cm^{-1}, with 1 cm^{-1} resolution. The ice column density N in cm^{-2} is derived from a modified Beer's law:

$$N = \frac{\log 10 \cdot \int Abs(\nu) \, d\nu}{A'} \tag{51}$$

where $Abs(\nu)$ is the band absorbance, $d\nu$ is the wavenumber differential in cm^{-1}, and A' is the calibrated band strength in cm molecule^{-1} in reflection mode. This RAIR band strength cannot be taken from the literature data available for the IR transmission spectroscopy, as the signals obtained in reflection are enhanced through substrate dipole couplings. Moreover, the determination of RAIR band strengths from transmission values cannot be realized by only compensating for different effective IR pathways in the ice. Therefore, a series of extra experiments (see Section 6.2.3) has been performed to determine the band strength for each of the involved species for our specific experimental settings by using the interference pattern of a HeNe laser that is reflected from the growing ice sample at 10 K (Baratta & Palumbo

1998; Brunetto et al. 2008; Fulvio et al. 2009; Bouilloud et al. 2015). For pure ice the absolute column density is calculated by the equation:

$$N = \frac{d \cdot \rho \cdot N_a}{M} \tag{52}$$

where d is the thickness of ice in nm, ρ is the density in g cm^{-3}, N_a is the Avogadro's constant $(6.022 \times 10^{23}$ mol$^{-1})$, and M is the molar mass of the species. The ice thickness ($D_{growing}$) is experimentally determined by laser refractive interference,

$$N = k \frac{\lambda}{2n \cdot \cos(\theta_f)} \tag{53}$$

where λ = 632.8 nm is the HeNe laser wavelength, n is the refractive index of a specific ice, $\theta_f \cong 3$ is the angle of refraction in the ice in degrees, and k is the number of involved fringes (Hollenberg & Dows 1961; Westley et al. 1998). The exact band-strength values may vary with changing ice composition, structure, and temperature. The reported absolute uncertainty of this method is 5%, a value that is largely determined by the density and refractive index uncertainty (Baratta & Palumbo 1998; Fulvio et al. 2009). Moreover, as the same technique is used to determine CO, H_2CO and CH_3OH band strengths, the relative error between values is expected to be lower. This makes it possible, in principle, to establish the obtained $N_{RD}(C)/N_{consumed}(C)$ with high confidence, even when chemistry changes relative ice compositions.

6.2.3   Band strength measurement for pure ices

The left-hand panel of Figures 6.2(a)-(c) shows the HeNe laser interference pattern that changes with time as the ice thickness increases upon deposition of CO, H_2CO, and CH_3OH onto the 10 K substrate. One single fringe is typically observed for the low-deposition rates used in this study. Ice density (ρ) and refractive index (n) may vary for different conditions (Bossa et al. 2015). It is important to note that the precise ice density in the amorphous phase is generally unknown for the species studied in this work. Here, the commonly accepted values in literature are taken as good approximate values. For CO, the ice density reported by (Roux et al. 1980) at 20 K is used. Their deposition conditions may have been different from those in our work. For H_2CO, no density value has been reported in the solid phase, thus the value measured in liquid phase is employed (Weast & Astle 1985). For CH_3OH, the ice density is derived from the value available for its crystalline structure (Mate2009). Based on the density and refractive index values summarized in (Bouilloud et al. 2015) 0.80±0.01 g cm^{-3} and 1.25±0.03 for CO, 0.81±0.03 g cm^{-3} and 1.33±0.04 for H_2CO, and 1.01±0.03 g cm^{-3} and 1.33±0.04 for CH_3OH — CO, H_2CO, and CH_3OH deposition rates are derived with values of $\sim(1.3\pm0.1)\times10^{14}$, $\sim(4.7\pm0.4)\times10^{13}$, and $\sim(5.6\pm0.5)\times10^{13}$ molecules cm^{-2} s^{-1}. Note that these values differ in these experiments from the regular hydrogenation settings. The choice of the applied density and refractive index values is not ideal, but given the lack of more precise values, this is the best we can provide. If better values become available, the final ratio of $N_{RD}(C)/N_{consumed}(C)$ can be easily re-evaluated.

The corresponding CO, H_2CO, and CH_3OH plots, showing the column density upon ice deposition (horizontal axis) and the increasing IR absorption area (vertical axis) over time are presented in the right-hand panels of Figures 6.2(d)-(e). As explained in Section 6.2 (Equation 51), from these plots the A', band-strength value, can be derived from molecule specific RAIR bands, following a linear fit. The fitted slopes for (d) CO (2142 cm^{-1}), (e) H_2CO (1497 cm^{-1}), and (f) CH_3OH (1030 cm^{-1}) yield absorption strength values A' of $(5.2\pm0.3)\times10^{-17}$,
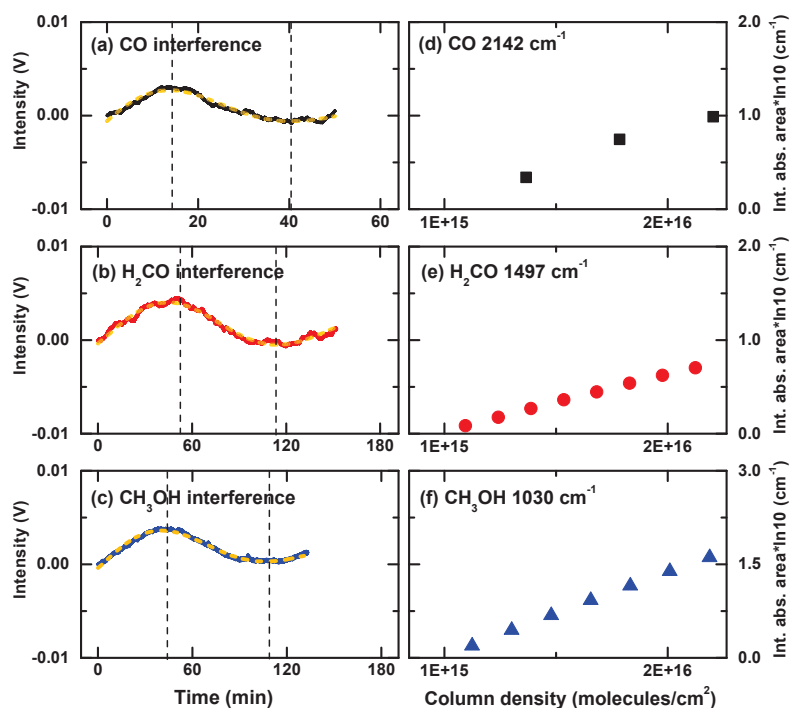
Figure 6.2: Left: typical examples of the obtained interference fringes as function of time and their corresponding sinusoidal fittings (yellow dashed line) during 10 K substrate deposition of pure (a) CO, (b) H_2CO, and (c) CH_3OH. The vertical dashed lines (black) indicate the time for maximum and minimum amplitude. Right: the integrated absorption area for deposited (d) CO (2142 cm^{-1} band), (e) H_2CO (1497 cm^{-1} band) and (f) CH_3OH (1030 cm^{-1} band) as a function of column density for the first 7 minutes of deposition.

$(3.2\pm0.3)\times10^{-17}$, and $(7.1\pm0.6)\times10^{-17}$ cm molecule^{-1}, respectively. It should be noted that these values are only safe to use for identical experimental circumstances, i.e., identical IR incident angles, surface materials, etc.

Kerkhof et al. (1999) showed that the band strength of methanol in an ice mixture of CH_3OH:CO_2(1:1) and in pure CH_3OH ice does not vary. We checked this by performing a set of control experiments in which the CO, H_2CO, and CH_3OH band-strength values are compared with those derived in CO:H_2CO (1:1), CO:CH_3OH (1:1), and CO:H_2CO:CH_3OH (1:1:1) mixed ices. This is realized in the following way. At first, a constant deposition rate of CO molecules is used through one of the dosing lines. Then, sequentially, H_2CO and CH_3OH are introduced through other dosing lines growing an ice mixture during co-deposition. Each time a new species is allowed into the main chamber, and any changes in the CO absorbance integral area are carefully monitored. Then, in a similar way, changes in the H_2CO and CH_3OH absorbance integral area are measured. These changes are linearly correlated with their increasing column densities. From this, it is found that the CO, H_2CO, and CH_3OH band strengths are rather constant, with variations that do not exceed 2% in CO, CO:H_2CO (1:1), CO:CH_3OH (1:1), and CO:H_2CO:CH_3OH (1:1:1) ices. RAIR spectra are used only as long as signals are far from saturation, to guarantee a linear correlation with the corresponding column densities (Teolis et al. 2007).

6.3 RESULTS AND DISCUSSION

6.3.1 *Elemental carbon budget in CO hydrogenation experiments*

Figure 6.3 presents RAIR difference spectra obtained after hydrogenation of pre-deposited CO ice for 180 minutes by an H-atom flux of $\sim8\times10^{12}$ atoms cm^{-2} s^{-1} at (a) 10 K, (b) 12 K, and (c) 14 K, respectively. The negative peak at 2142 cm^{-1} shows the consumption of the originally predeposited CO ice, and the positive peaks indicate the formation of two newly formed main products, i.e., H_2CO (1727, 1497, and 1250 cm^{-1}) and CH_3OH (1030 cm^{-1}). Very similar results have been reported and discussed extensively in previous studies of Watanabe & Kouchi (2002) and Fuchs et al. (2009). No entrapment of the formed intermediate radicals such as HCO, CH_3O, and CH_2OH is found, as these easily react with free H-atoms or other radical species.

Figure 6.4 shows the changing column density obtained from the integrated RAIR absorption areas of the CO (2142 cm^{-1}), H_2CO (1497 cm^{-1}), and CH_3OH (1030 cm^{-1}) signals during H-atom accretion. The negative CO consumption peak at 10 K clearly saturates due to the limited penetration depth of H-atoms impacting on the surface. This observation is in agreement with previous findings (Fuchs et al. 2009), indicating that the CO consumption rate exhibits a strong temperature dependence; a lower temperature results in a higher CO conversion rate, fully in line with the proposed CO-H_2CO-CH_3OH reaction findings presented in the literature (Watanabe et al. 2004; Fuchs et al. 2009). This temperature dependence is explained by the different life (i.e., residence) time of H-atoms on the ice surface before desorbing from the ice surface or recombining to H_2 through interactions with other H-atoms. At 10 K and after 120 minutes of H-atom exposure, the CO depletion behavior starts slowing down, reaching a maximum value at approximately 2×10^{15} molecules cm^{-2} (180 minutes), reflecting that only the few upper layers of CO molecules are accessible to accreting H-atoms.

In Figure 6.5, the effective RD related column densities are shown for three different ice temperatures for 180 minutes H-atom bombardment. The increasing loss reflects that the sum of H_2CO and CH_3OH abundances is less than the amount of consumed CO molecules. At 180 minutes, the N_{RD} (C) value reaches $\sim4.5\times10^{14}$, $\sim3.9\times10^{14}$, and $\sim1.7\times10^{14}$ molecules

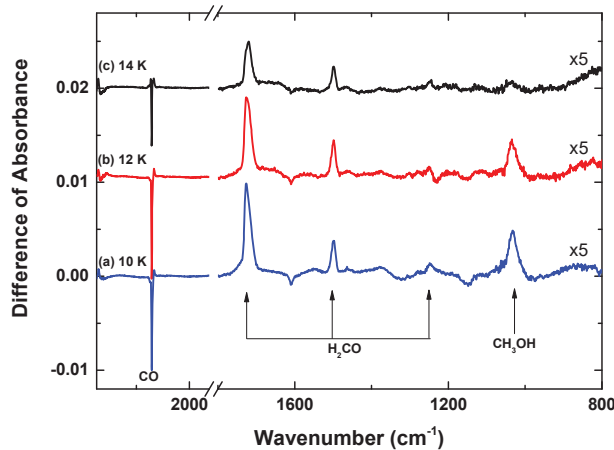Figure 6.3: RAIR difference spectra obtained after the exposure of 6×10^{15} molecules cm^{-2} pre-deposited CO to an H-atom flux of $\sim8\times10^{12}$ atoms cm^{-2} s^{-1} for 180 minutes at (a) 10 K, (b) 12 K, and (c) 14 K. Negative and positive signals reflect net consumption and formation, respectively.

cm^{-2} for 10 K, 12 K, and 14 K, respectively. As discussed in Equation (50), $N_{RD}(C)$ reflects all products that are not recorded by the RAIRS technique in the solid state, i.e., this variable includes both the effect of reactive desorption and other elemental carbon loss channels, such as the formation of COMs with two, three, or more carbon atoms. However, the expected final abundances of these COMs cannot account for more than a few percent of the consumed CO molecules, as discussed in Fedoseev et al. (2017). Moreover, their CO stretching vibration modes are very similar to the CO stretching vibration modes used here for the CH$_3$OH column densities calculations; the smaller fraction of carbon atoms conserved in the formed larger COMs is actually already contributing to the CH$_3$OH column densities. Non-overlapping (and generally weaker) IR absorption features of COMs, i.e., around 860 cm^{-1} for glycolaldehyde and ethylene glycol are not visible, yielding upper limits of the order of $\sim5\times10^{13}$ molecules cm^{-2} s^{-1}, i.e., <3% of the consumed CO column density. It should be noted that previous studies on solid state COM formation by Chuang et al. (2016, 2017) and Fedoseev et al. (2017) were performed in co-deposition modus that are assumed to simulate interstellar ice conditions in a more representative way.

In Figure 6.6, the obtained upper limits of $N_{RD}(C)/N_{consumed}(C)$ ratios are summarized for two different time periods: from the start to the end ($0-180$ minutes) and from $60-180$ minutes. These ratios must be strictly treated as upper limits of the reactive desorption fraction for the performed hydrogenation experiments. The abundances obtained at the end of the CO ice hydrogenation experiments after 180 minutes of H-atom bombardment are used for the calculations (black column in Figure 6.6), as here the largest amounts with reaction products are reached. This results in the best peak-to-noise ratios and therefore the lowest uncertainties. The resulting $N_{RD}(C)/N_{consumed}(C)$ fractions are 0.23±0.02, 0.22±0.02 and 0.28±0.05 for 10 K, 12 K, and 14 K, respectively. The averaged RD fraction ($N_{RD}(C)/N_{consumed}(C)_{10-14K}$) amounts to 0.24±0.02 for overall 180 minutes.
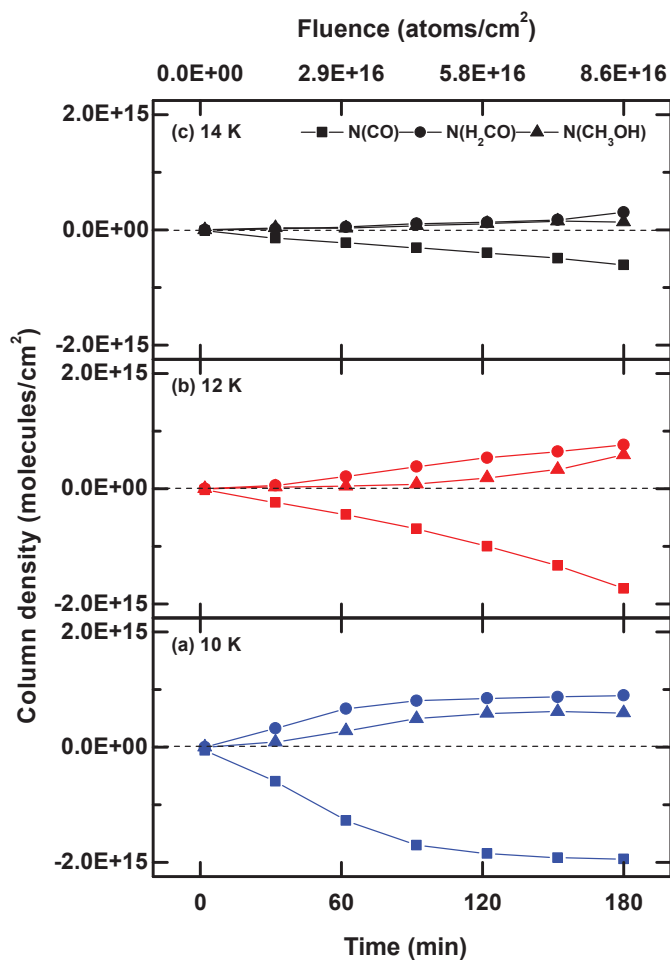
Figure 6.4: Evolution of the surface column density of CO, H_2CO, and CH_3OH during a CO hydrogenation experiment with an H-atom flux of $\sim 8 \times 10^{12}$ atoms $cm^{-2}\,s^{-1}$ over 180 minutes at (a) 10 K, (b) 12 K, and (c) 14 K, respectively.
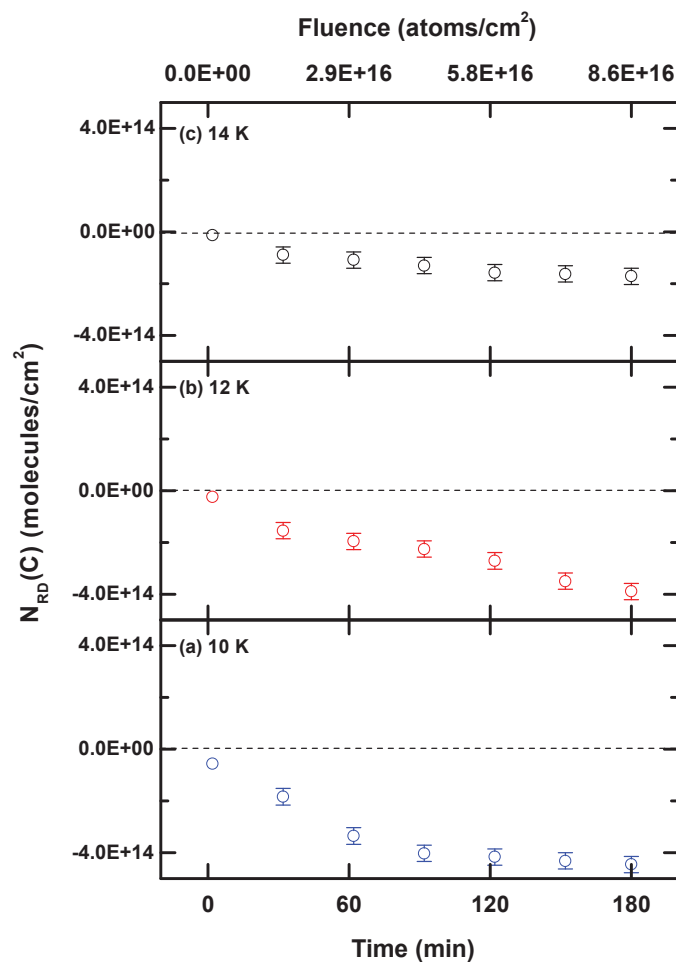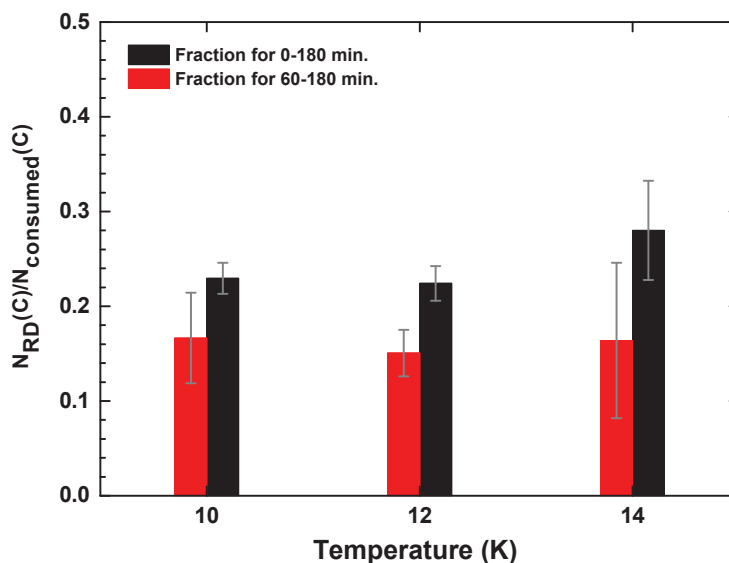
Figure 6.5: Evolution of the column density of the reactive desorption species, $N_{RD}(C)$, during a CO hydrogenation experiment with an H-atom flux of $\sim 8 \times 10^{12}$ atoms cm^{-2} s^{-1} over 180 minutes at (a) 10 K, (b) 12 K, and (c) 14 K, respectively.

Figure 6.6: $N_{RD}(C)/N_{consumed}(C)$ ratios obtained after the bombardment of prede-posited CO ice with ~8×10^{12} H-atoms cm^{-2} s^{-1} for the full 180 minutes (black column) and the data recorded between 60 and 180 minutes (red column) at 10, 12, or 14 K, respectively.

A detailed analysis of the data presented in Figure 6.5 shows that $N_{RD}(C)$ does not decrease linearly with time; roughly during the first 60 minutes, the decrease is faster (for all three investigated temperatures). This may hint at startup effects, linked to structural weaknesses in the top surface layers because of any loosely bound CO molecules that get off much easier without the need of reactive desorption, for example, upon a collisional impact. For the period from 60 to 180 minutes, the $N_{RD}(C)$ decrease is much more linear. To exclude any perturbing contributions, therefore, the elemental carbon loss fraction is also calculated for the values derived between 60 and 180 minutes of H-atom bombardment (red column in Figure 6.6) resulting in somewhat lower upper values: 0.17±0.05, 0.15±0.02, and 0.16±0.08 for 10 K, 12 K, and 14 K, respectively. The resulting averaged value (0.16±0.03) amounts to ~70% of the overall value. The latter value is likely more precise, as it does not include startup effects. However, to stay on the safe side, we report here the overall averaged RD fraction.

6.3.2   *Elemental carbon budget in H_2CO and CH_3OH hydrogenation experiments*

A very similar set of experiments is used to investigate reactive desorption upon H_2CO and CH_3OH hydrogenation. Figure 6.7 (left panel) presents the RAIR difference spectra obtained after hydrogenation of pre-deposited (a) H_2CO and (b) CH_3OH ice for an H-atom flux of ~8×10^{12} atoms cm^{-2} s^{-1} for 180 minutes at 10 K. In spectrum (a), the negative peaks at 1727, 1497, and 1250 cm^{-1} show the depletion of the initially deposited H_2CO, while the positive peaks indicate the formation of newly formed products, i.e., CO (2142 cm^{-1}) and CH_3OH (1030 cm^{-1}). The formation of CO through H-atom abstraction reactions from H_2CO and of CH_3OH through H-atom addition reactions to H_2CO have been reported previously by Hidaka et al. (2004) and Chuang et al. (2016).

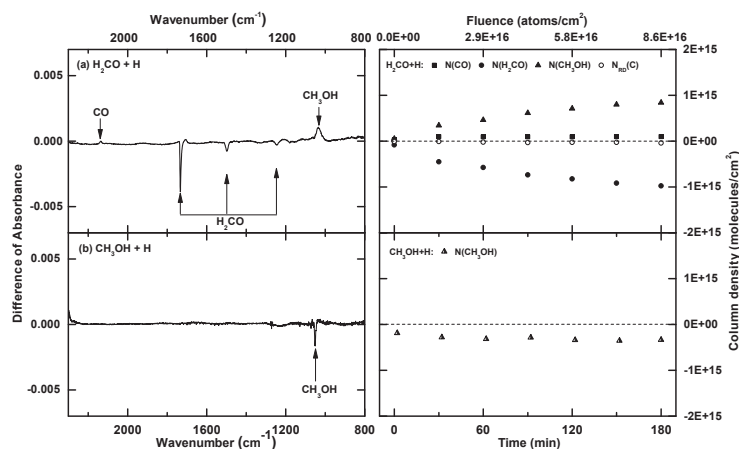Figure 6.7: Left: RAIR difference spectra obtained after the exposure of 5×10^{15} molecules cm^{-2} pre-deposited (a) H$_2$CO and 8×10^{15} molecules cm^{-2} pre-deposited (b) CH$_3$OH to ~8×10^{12} H-atoms cm^{-2} s^{-1} for 180 minutes at 10 K. Right: evolution of the surface column density of CO, H$_2$CO, and CH$_3$OH during H$_2$CO and CH$_3$OH hydrogenation over 180 minutes at 10 K.

In contrast, the CH$_3$OH hydrogenation experiments (Figure 6.7(b)) do not result in any efficient consumption of CH$_3$OH and the formation of hydrogenation products. Only a small negative CH$_3$OH peak (1050 cm^{-1}) is observed, while no secure identification of other carbon-bearing species can be made. Moreover, the consumption peak accumulates at the very beginning of the H-atom bombardment and as discussed above; this may be due to other processes than reactive desorption. As in the CO hydrogenation experiments, there is no spectroscopic evidence for radical entrapments due to high reactivity.

The evolving column density of CO, H$_2$CO, and CH$_3$OH during H-atom exposure with time is shown in the right-hand panel of Figure 6.7. The consumed N(H$_2$CO) saturates at ~1×10^{15} molecules cm^{-2} and is possibly limited by the H-atom penetration depth as discussed before. However, N(CH$_3$OH) saturates immediately, indicating the structural ice changes described before occurring on the surface comprising of CH$_3$OH molecules. As discussed for the CO hydrogenation experiments, the column density of the missing carbon during the first 60 minutes of H-atom bombardment likely includes other unwanted desorption processes. Following the same approach as described in Section 6.3.2, an extended calculation of the H$_2$CO hydrogenation experiment shows that the sum of the consumption of H$_2$CO and the production of CO and CH$_3$OH is very small; ~2.0×10^{13} molecules cm^{-2}, i.e., 4% with respect to the CO hydrogenation experiments at 10 K. In the CH$_3$OH hydrogenation experiments, the N_{RD}(C) originates only from the consumption of N(CH$_3$OH) due to a poor detection of H$_2$CO and results in 4% with respect to the CO hydrogenation experiments at 10 K. These small signals with large uncertainty complicate the determination of reactive desorption fractions. Future work is needed to provide more precise RD efficiencies for H$_2$CO and CH$_3$OH.

6.4 ASTROPHYSICAL IMPLICATION AND CONCLUSIONS

The astronomical relevance of this work is that the RD fraction used in astrochemical models (for CO hydrogenation, but likely also more general) can be based on an experimentally determined value. The laboratory data obtained here indicate that the sum of consumption and production of carbon-bearing species along the CO hydrogenation in the solid state is not zero. The overall reactive desorption fraction $f_{overall} = N_{RD}(C) / N_{consumed}(C)_{10-14k} = 0.24\pm0.02$ for CO hydrogenation into CH_3OH is obtained under the assumption that the missing carbon fraction is fully or largely explained by the reactive desorption of hydrogenation products into the gas phase. This value is in the best case an upper limit and the actual effect of reactive desorption may be much smaller, in line with value derived from $60-180$ minutes experiments.

The obtained upper limit is the cumulative effect of all involved reactions. This includes H-atom addition and H-atom abstraction reactions with the stable species (CO, H_2CO, and CH_3OH) as well as H-atom reactions with intermediate radicals (HCO, CH_3O, CH_2OH). Although the resulting number is an overall value, it is possible to derive the effective desorption fraction for a single H-atom reaction (f_{single}) by assuming an identical efficiency for each reaction in the hydrogenation process (Garrod et al. 2007). The total fraction of the species left on the surface, i.e., $(1 - f_{overall})$, is equal to the left fraction of a single reaction, i.e., (f_{single}), to the power n:

$$(1-f_{single})^n = 1 - f_{overall} \tag{54}$$

where n is the number of reactions in the hydrogenation scheme. f_{single} can be obtained from the $f_{overall}$ measured in our experiments and depends on the average number of H-atom addition and abstraction steps occurring upon conversion of CO into CH_3OH (see Figure 6.1). For an astrochemical simulation in which only H-atom addition reactions are taken into account, the number of steps resulting in the conversion of CO molecules into CH_3OH is four ($n = 4$):

$$CO \longrightarrow HCO \longrightarrow H_2CO \longrightarrow CH_3O \longrightarrow CH_3OH \tag{55}$$
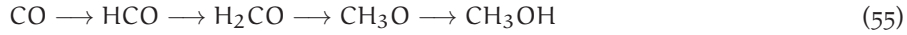
According to Equation (54), this gives f_{single} is $\leqslant 0.066\pm0.006$. This value can be treated as the upper limit for the effective reactive desorption fraction at each of the H-atom addition steps. For a scenario in which H-atom induced abstraction reactions are also considered, this value further decreases. Assuming that both addition and abstraction reactions contributed equally efficient to the overall reactive desorption fraction along the hydrogenation sequence, e.g.,

$$CO \longrightarrow HCO \longrightarrow CO \longrightarrow HCO \longrightarrow H_2CO \longrightarrow HCO \longrightarrow H_2CO \longrightarrow \tag{56}$$

$$CH_3O \longrightarrow H_2CO \longrightarrow CH_3O \longrightarrow CH_3OH \longrightarrow CH_2OH \longrightarrow CH_3OH.$$
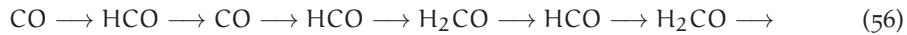
The effective reactive desorption fraction per reaction of f_{single} is $\leqslant 0.023\pm0.002$, taking $n = 12$. Such effective reactive desorption fractions per hydrogenation reaction can be utilized in the models where both H-atom addition and abstraction steps are incorporated. It should be noted that at the current stage no clear understanding on the number of the involved reaction steps is achieved (Nagaoka et al. 2005; Hidaka et al. 2009; Minissale et al. 2016a). In general, a higher number of reaction steps will yield a lower effective reactive desorption fraction per single reaction. Clear data on the relative contribution of the involved H-atom addition and abstraction steps do not exist in the literature and cannot be reliably concluded from the current study.

The effective reactive desorption fractions concluded in both the aforementioned scenarios are well within the $0.01-0.10$ range of reactive desorption fractions currently used as a free

parameter in astrochemical models to explain the transfer of species into the gas phase follow-
ing their formation in the solid state (Garrod et al. 2007; Vasyunin & Herbst 2013; Balucani
et al. 2015; Chang & Herbst 2016). These values are clearly much lower than the 40%—60%
values reported earlier for other surfaces, but as discussed before, these involved experiments
in the sub-monolayer regime. Values of the order of $0.01 - 0.1$, however, are large enough
to support a solid-state mechanism enhancing abundances of small carbon-bearing species
into the gas phase. This is relevant from two points of view. On one hand, it provides an
intrinsic non-thermal desorption mechanism that may explain the gas-phase observation of
molecules that should be fully frozen out for the low temperatures in cold clouds. Garrod
et al. (2007) show that models including chemical desorption only induced by association
reactions require a reactive desorption fraction of 0.03 to optimally represent the observed
gaseous CH_3OH abundances for L134N (Dickens et al. 2000). On the other hand, RD may
offer the necessary precursors for proposed gas-phase reaction networks that result in the
formation of complex molecules in addition to COMs already formed in the solid state.

The astronomical take home message is that the experimental results presented here yield
an effective reactive desorption fraction for CO hydrogenation that constrain the desorption
efficiency previously used in astrochemical simulations to explain astronomical observations
toward pre-stellar cores. The derived values give upper limits and the real effect of RD may
be smaller.

BIBLIOGRAPHY

Andersson, S. & van Dishoeck, E. F. 2008, Astron. Astrophys., 491, 907

Arasa, C., Koning, J., Kroes, G.-J., Walsh, C., & van Dishoeck, E. F. 2015, Astron. Astrophys., 575, A121

Bacmann, A., Taquet, V., Faure, A., Kahane, C., & Ceccarelli, C. 2012, Astron. Astrophys., 541, L12

Balucani, N., Ceccarelli, C., & Taquet, V. 2015, Mon. Not. R. Astron. Soc., 449, L16

Baratta, G. A. & Palumbo, M. E. 1998, Journal of the Optical Society of America A, 15, 3076

Bertin, M., Fayolle, E. C., Romanzin, C., et al. 2013, Astrophys. J., 779, 120

Bertin, M., Romanzin, C., Doronin, M., et al. 2016, Astrophys. J. Lett., 817, L12

Boogert, A. C. A., Gerakines, P. A., & Whittet, D. C. B. 2015, Ann. Rev. Astron. Astrophys., 53, 541

Bossa, J.-B., Maté, B., Fransen, C., et al. 2015, Astrophys. J., 814, 47

Bouilloud, M., Fray, N., Bénilan, Y., et al. 2015, Mon. Not. R. Astron. Soc., 451, 2145

Brunetto, R., Caniglia, G., Baratta, G. A., & Palumbo, M. E. 2008, Astrophys. J., 686, 1480

Butscher, T., Duvernay, F., Theule, P., et al. 2015, Mon. Not. R. Astron. Soc., 453, 1587

Cazaux, S., Bossa, J.-B., Linnartz, H., & Tielens, A. G. G. M. 2015, Astron. Astrophys., 573, A16

Cernicharo, J., Marcelino, N., Roueff, E., et al. 2012, Astrophys. J. Lett., 759, L43

Chang, Q. & Herbst, E. 2012, Astrophys. J., 759, 147

Chang, Q. & Herbst, E. 2016, Astrophys. J., 819, 145

Charnley, S. B. 1997, Mon. Not. R. Astron. Soc., 291, 455

Chuang, K.-J., Fedoseev, G., Ioppolo, S., van Dishoeck, E. F., & Linnartz, H. 2016, Mon. Not. R. Astron. Soc., 455, 1702

Chuang, K.-J., Fedoseev, G., Qasim, D., et al. 2017, Mon. Not. R. Astron. Soc., 467, 2552

Cruz-Diaz, G. A., Martín-Doménech, R., Muñoz Caro, G. M., & Chen, Y.-J. 2016, Astron. Astrophys., 592, A68

Cuppen, H. M., Ioppolo, S., Romanzin, C., & Linnartz, H. 2010, Phys. Chem. Chem. Phys., 12, 12077

Cuppen, H. M., Penteado, E. M., Isokoski, K., van der Marel, N., & Linnartz, H. 2011, Mon. Not. R. Astron. Soc., 417, 2809

Cuppen, H. M., van Dishoeck, E. F., Herbst, E., & Tielens, A. G. G. M. 2009, Astron. Astrophys., 508, 275

Dickens, J. E., Irvine, W. M., Snell, R. L., et al. 2000, Astrophys. J., 542, 870

Duley, W. W. & Williams, D. A. 1993, Mon. Not. R. Astron. Soc., 260, 37

Enoch, M. L., Evans, II, N. J., Sargent, A. I., et al. 2008, Astrophys. J., 684, 1240

Fedoseev, G., Chuang, K.-J., Ioppolo, S., et al. 2017, Astrophys. J., 842, 52

Fedoseev, G., Chuang, K.-J., van Dishoeck, E. F., Ioppolo, S., & Linnartz, H. 2016, Mon. Not. R. Astron. Soc., 460, 4297

Fedoseev, G., Cuppen, H. M., Ioppolo, S., Lamberts, T., & Linnartz, H. 2015a, Mon. Not. R. Astron. Soc., 448, 1288

Fedoseev, G., Ioppolo, S., & Linnartz, H. 2015b, Mon. Not. R. Astron. Soc., 446, 449

Fredon, A., Lamberts, T., & Cuppen, H. M. 2017, Astrophys. J., 849, 125

Fuchs, G. W., Cuppen, H. M., Ioppolo, S., et al. 2009, Astron. Astrophys., 505, 629

Fulvio, D., Sivaraman, B., Baratta, G. A., Palumbo, M. E., & Mason, N. J. 2009, Spectrochimica Acta Part A: Molecular Spectroscopy, 72, 1007

Garrod, R., Park, I. H., Caselli, P., & Herbst, E. 2006, Faraday Discussions, 133, 51

Garrod, R. T., Wakelam, V., & Herbst, E. 2007, Astron. Astrophys., 467, 1103

Geppert, W. D., Hamberg, M., Thomas, R. D., et al. 2006, Faraday Discussions, 133, 177

Hasegawa, T. I., Herbst, E., & Leung, C. M. 1992, Astrophys. J. Suppl. Ser., 82, 167

Hidaka, H., Watanabe, M., Kouchi, A., & Watanabe, N. 2009, Astrophys. J., 702, 291

Hidaka, H., Watanabe, M., Kouchi, A., & Watanabe, N. 2011, Phys. Chem. Chem. Phys., 13, 15798

Hidaka, H., Watanabe, N., Shiraki, T., Nagaoka, A., & Kouchi, A. 2004, Astrophys. J., 614, 1124

Hiraoka, K., Miyagoshi, T., Takayama, T., Yamamoto, K., & Kihara, Y. 1998, Astrophys. J., 498, 710

Hiraoka, K., Ohashi, N., Kihara, Y., et al. 1994, Chemical Physics Letters, 229, 408

Hiraoka, K., Yamashita, A., Yachi, Y., et al. 1995, Astrophys. J., 443, 363

Hollenberg, J. L. & Dows, D. A. 1961, J. Chem. Phys., 34, 1061

Ioppolo, S., Cuppen, H. M., Romanzin, C., van Dishoeck, E. F., & Linnartz, H. 2008, Astrophys. J., 686, 1474

Ioppolo, S., Cuppen, H. M., Romanzin, C., van Dishoeck, E. F., & Linnartz, H. 2010, Phys. Chem. Chem. Phys., 12, 12065

Ioppolo, S., Fedoseev, G., Lamberts, T., Romanzin, C., & Linnartz, H. 2013, Review of Scientific Instruments, 84, 073112

Ivlev, A. V., Padovani, M., Galli, D., & Caselli, P. 2015, Astrophys. J., 812, 135

Jiménez-Serra, I., Vasyunin, A. I., Caselli, P., et al. 2016, Astrophys. J. Lett., 830, L6

Kerkhof, O., Schutte, W. A., & Ehrenfreund, P. 1999, Astron. Astrophys., 346, 990

Leger, A., Jura, M., & Omont, A. 1985, Astron. Astrophys., 144, 147

Ligterink, N., Walsh, C., Bhuin, R., et al. 2018, Astronomy & Astrophysics, 612, A88

Linnartz, H., Ioppolo, S., & Fedoseev, G. 2015, International Reviews in Physical Chemistry, 34, 205

Minissale, M., Congiu, E., & Dulieu, F. 2016a, Astron. Astrophys., 585, A146

Minissale, M., Moudens, A., Baouche, S., Chaabouni, H., & Dulieu, F. 2016b, Mon. Not. R. Astron. Soc., 458, 2953

Miyauchi, N., Hidaka, H., Chigai, T., et al. 2008, Chemical Physics Letters, 456, 27

Nagaoka, A., Watanabe, N., & Kouchi, A. 2005, Astrophys. J. Lett., 624, L29

Öberg, K. I., Bottinelli, S., Jørgensen, J. K., & van Dishoeck, E. F. 2010, Astrophys. J., 716, 825

Öberg, K. I., van der Marel, N., Kristensen, L. E., & van Dishoeck, E. F. 2011, Astrophys. J., 740, 14

Penteado, E. M., Boogert, A. C. A., Pontoppidan, K. M., et al. 2015, Mon. Not. R. Astron. Soc., 454, 531

Pontoppidan, K. M. 2006, Astron. Astrophys., 453, L47

Rivilla, V. M., Beltrán, M. T., Cesaroni, R., et al. 2017, Astron. Astrophys., 598, A59

Roux, J. A., Wood, B. E., Smith, A. M., & Plyer, R. R. 1980, Infrared optical properties of thin CO, NO, CH4, HC1, N2O, O2, AR, and air cryofilms, Tech. rep.

Taquet, V., Wirström, E. S., & Charnley, S. B. 2016, Astrophys. J., 821, 46

Teolis, B. D., Loeffler, M. J., Raut, U., Famá, M., & Baragiola, R. A. 2007, Icarus, 190, 274

Tielens, A. G. G. M. & Hagen, W. 1982, Astron. Astrophys., 114, 245

Tielens, A. G. G. M., Tokunaga, A. T., Geballe, T. R., & Baas, F. 1991, Astrophys. J., 381, 181

Tschersich, K. G. 2000, Journal of Applied Physics, 87, 2565

van Dishoeck, E. F., Herbst, E., & Neufeld, D. A. 2013, Chemical Reviews, 113, 9043

Vasyunin, A. I., Caselli, P., Dulieu, F., & Jiménez-Serra, I. 2017, Astrophys. J., 842, 33

Vasyunin, A. I. & Herbst, E. 2013, Astrophys. J., 769, 34

Watanabe, N. & Kouchi, A. 2002, Astrophys. J. Lett., 571, L173

Watanabe, N., Nagaoka, A., Shiraki, T., & Kouchi, A. 2004, Astrophys. J., 616, 638

Weast, R. C. & Astle, M. J. 1985, CRC Handbook of Data on Organic Compounds (Boca Raton, FL: CRC Press), 968

Westley, M. S., Baratta, G. A., & Baragiola, R. A. 1998, J. Chem. Phys., 108, 3321

Willacy, K. & Millar, T. J. 1998, Mon. Not. R. Astron. Soc., 298, 562

Woods, P. M., Kelly, G., Viti, S., et al. 2012, Astrophys. J., 750, 19

Zhitnikov, R. A. & Dmitriev, Y. A. 2002, Astron. Astrophys., 386, 1129

H_2 CHEMISTRY IN INTERSTELLAR ICES: THE CASE OF CO ICE HYDROGENATION IN UV IRRADIATED CO:H_2 ICE MIXTURES

In dense clouds, hydrogenation reactions on icy dust grains are key in the formation of molecules, like formaldehyde, methanol and complex organic molecules (COMs). These species form through the sequential hydrogenation of CO ice. Although molecular hydrogen (H_2) abundances can be four orders of magnitude higher than those of free H-atoms in dense clouds, H_2 surface chemistry has been largely ignored; several laboratory studies show that H_2 does not actively participate in 'non-energetic' ice chemistry because of the high activation energies required. For the example of CO ice hydrogenation, we investigate experimentally the potential role of H_2 molecules on the surface chemistry when 'energetic' processing (i.e., UV photolysis) is involved. We test whether additional hydrogenation pathways become available upon UV irradiation of a CO:H_2 ice mixture and whether this reaction mechanism also applies to other chemical systems. UHV experiments are performed at $8 - 20$ K. A pre-deposited solid mixture of CO:H_2 is irradiated with UV-photons. Reflection absorption infrared spectroscopy (RAIRS) is used as an *in situ* diagnostic tool. Single reaction steps and possible isotopic effects are studied by comparing results from CO:H_2 and CO:D_2 ice mixtures. After UV-irradiation of a CO:H_2 ice mixture, two photon-induced products, HCO and H_2CO, are unambiguously detected. The proposed reaction mechanism involves electronically excited CO in the following reaction steps: $CO + h\nu \longrightarrow CO^*$, $CO^* + H_2 \longrightarrow HCO + H$ where newly formed H-atoms are then available for further hydrogenation reactions. The HCO formation yields have a strong temperature dependence for the investigated regime, which is most likely linked to the H_2 sticking coefficient. Moreover, the derived formation cross section reflects a cumulative reaction rate determined by both the H-atom diffusion rate and initial concentration of H_2 at $8 - 20$ K and that is largely determined by the H_2 sticking coefficient. Finally, the astronomical relevance of this photo-induced reaction channel is discussed.

In dense molecular clouds, carbon monoxide starts heavily accreting on H_2O-rich ice mantles when densities (i.e., $n_H = 2n(H_2) + n(H)$) increase to $\sim 10^{4-5}$ cm^{-3}, and temperatures drop to ~ 10 K. This results in a CO-rich ice coating with a thickness of ~ 0.01 μm (Pontoppidan 2006; Boogert et al. 2015) and is known as the 'CO catastrophic freeze-out stage'. During this stage, the simultaneous accretion of H-atoms and CO leads primarily to the formation of H_2CO and CH_3OH via successive H-atom addition reactions $CO \xrightarrow{H} HCO \xrightarrow{H} H_2CO \xrightarrow{H} CH_3O \xrightarrow{H} CH_3OH$ as introduced in gas-grain models by Tielens & Hagen (1982). These hydrogenation reactions have been investigated in a number of systematic laboratory experiments (Watanabe & Kouchi 2002; Fuchs et al. 2009, see reviews by Watanabe & Kouchi 2008; Hama & Watanabe 2013; Linnartz et al. 2015) as well as astrochemical simulations and theoretical studies (Charnley 1997; Cuppen et al. 2009; Chang & Herbst 2012). The CO+H channel is also regarded as a starting point in the formation of various complex organic molecules (COMs) in dense clouds; recombination of reactive intermediates, i.e., HCO, CH_2OH, and CH_3O, formed in H-atom addition and abstraction reactions with each other or with other reaction products results in the low temperature solid-state formation of larger COMs, like glycolaldehyde, ethylene glycol, glycerol and likely glyceraldehyde (Garrod et al. 2006; Woods et al. 2012; Butscher et al. 2015, 2016; Fedoseev et al. 2015, 2017; Chuang et al. 2016, 2017). The astronomical gas-phase detection of a number of COMs in cold dark regions, i.e., environments in which (UV) photo-processing is not dominant, has been explained in this way (Öberg et al. 2010; Bacmann et al. 2012; Cernicharo et al. 2012; Jiménez-Serra et al. 2016), even though the mechanism transferring the solid COMs into the gas phase is still not fully understood (Bertin et al. 2016; Chuang et al. 2018; Ligterink et al. 2018; Balucani et al. 2015). Key in all this work is the important role of accreting H-atoms.

Molecular hydrogen, H_2, is the most abundant molecule in the Universe (Wooden et al. 2004). Particularly in molecular clouds, the gaseous abundance of H_2 is about four orders of magnitude higher than that of CO and H-atoms. Molecular hydrogen may freeze out and the direct observation of H_2 ice was claimed by Sandford et al. (1993) in the infrared spectrum of WL5 in the ρ Oph molecular cloud, thanks to a small induced dipole as a result of H_2 interacting with surrounding ice species (Warren et al. 1980). Later on this observation was questioned (Kristensen et al. 2011). It is widely accepted though, that H_2 is abundantly formed in the solid state through H-H recombination on silicate or carbonaceous dust grains or amorphous water ice, through photolysis of hydrogenated amorphous carbon or water, or H_2 abstraction from polycyclic aromatic hydrocarbons (see reviews by Vidali 2013; Wakelam et al. 2017, and references therein). Which of these formation mechanisms dominates, depends on the environmental conditions (Wakelam et al. 2017).

H_2 is extremely volatile, and its sticking coefficient, which is defined as the ratio of 'adsorbed-species'/'total incident-species' for a given period of time, is a function of several properties, e.g., binding energy of adsorbed species on a surface, species coverage, and substrate temperature (Hama & Watanabe 2013). This coefficient also depends on the incident energy and angle of impacting species (Matar et al. 2010). Given the very small binding energy ($E_b \sim 100$ K) of H_2 accreting on a preformed H_2 ice layer, multi-layer 'pure' H_2 ice is not expected under dense cloud conditions (Lee 1972). However, in space, ice mantles formed by condensation on grain surfaces are typically amorphous, resulting in a distribution of binding energies. In a three-dimensional off-lattice Monte Carlo simulation, Garrod (2013) found that the water ice formation on grain surfaces exhibits a highly porous (creviced) structure. Sites with relatively high binding energies in these pores can be a place where H_2 sticks (Buch & Devlin 1994). Laboratory results by Dissly et al. (1994) showed that H_2 can accrete together with other in-

terstellar species, such as H_2O, under dense cloud conditions with an ice ratio (H_2/H_2O) of ~0.3. However, a gas phase co-deposition of H_2O and H_2 in the interstellar medium (ISM) is unlikely due to the low density of gaseous H_2O for the temperatures at which H_2 starts freezing-out. Moreover, it is well established that H_2O is mainly produced *in situ* on grain surfaces through the hydrogenation of oxygen allotropes accreting from the gas phase prior to gaseous CO condensation (Hiraoka et al. 1998; Dulieu et al. 2010; Miyauchi et al. 2008; Ioppolo et al. 2008, 2010; Oba et al. 2009, 2012; Cuppen et al. 2010; Lamberts et al. 2013). In recent laboratory studies, the reported H_2 sticking coefficients in a sub-monolayer regime on an olivine sample (i.e., a magnesium iron silicate) showed an unexpectedly high value of ~0.7 at 10 K (Acharyya 2014). This hints for the possibility that gaseous H_2 could co-deposit with other species on dust grains at low temperature and in particular with CO, forming $CO:H_2$ ice mantles, during its 'catastrophic freeze-out stage'. In principle, this could facilitate reactions between CO and H_2, however, as ground-state molecule-molecule reactions typically have a very high activation energy, even the four orders of magnitude higher H_2 abundance compared to atomic hydrogen is not expected to compensate for the high reaction barriers.

At high visual extinctions (A_V), dark clouds are shielded from external UV radiation by the dust. Only cosmic rays are expected to penetrate the cloud and react with the abundant gaseous H_2, resulting in the emission of UV photons. The internal cloud UV-photon flux is $(1-10)\times10^3$ photons cm^{-2} s^{-1}, which is a few times lower than the typical H-atom flux in the same regions (Prasad & Tarafdar 1983; Mennella et al. 2003; Shen et al. 2004). However, UV-photons have a larger penetration depth in interstellar ice analogues, e.g., 830 ML in H_2O and 640 ML in CO, with 95% absorption for $120-160$ nm (Cruz-Diaz et al. 2014). The energy of these UV-photons (mainly located around 160 and at 121.6 nm, i.e., Lyα) is not high enough to directly dissociate H_2 or CO, but is sufficient to radiatively pump CO (i.e., $A^1\Pi \longleftarrow X^1\Sigma^+$) into a vibronically excited state, CO* (Tobias et al. 1960). This energy can be transferred from subsurface layers to eject CO molecules located in the first few top-layers resulting in a CO photo-desorption event, following a so called DIET (Desorption Induced by Electronic Transition) mechanism (Fayolle et al. 2011; Bertin et al. 2013; van Hemert et al. 2015). Alternatively, this energy can be used to overcome the activation energy of the involved barriers resulting in the formation of photo-products, e.g., CO_2 (Gerakines et al. 1996; Gerakines & Moore 2001; Loeffler et al. 2005).

The present work is motivated by our limited understanding of the impact of UV-photons interacting with H_2-containing ices under dense cloud conditions. The idea of studying the role of molecular hydrogen in grain surface chemistry is not new. Previous work, like Fuchs et al. (2009) excluded the direct role of H_2 in the formation of H_2CO and CH_3OH. Oba et al. (2012) proposed a H_2O formation mechanism through the reactions between H_2 and OH radical, and found isotope effects when using D_2 instead of H_2 (see also Meisner et al. 2017). Recently, Lamberts et al. (2014) experimentally studied the reaction between H_2 and O in the ground state to form H_2O on grain surfaces, and this only resulted in a rather low upper limit for H_2O formation for this channel in dense clouds. A similar mechanism was also studied to explain the HCN formation through the reaction H_2+CN in an H_2 matrix experiment (Borget et al. 2017). Here, we focus on the UV irradiation of a $CO:H_2$ ice mixture studied for temperatures ranging from 8 to 20 K. The aim is to investigate whether cosmic ray induced UV-photons can trigger surface reactions between an electronically excited species, e.g., CO in this work, and H_2, the two most abundant molecules in prestellar cores, and how this compares to the regular CO ice H-atom addition reaction scheme.

All experiments are performed by using SURFRESIDE[2], an ultra-high vacuum (UHV) setup, which has been described in detail in Ioppolo et al. (2013). The base pressure of the main chamber is $\sim 10^{-10}$ mbar, and the H_2O contamination from the residual gas accretion, which is observed by its monomer IR feature at 1600 cm^{-1}, is estimated to be $<3\times10^{10}$ molecule cm^{-2} s^{-1}. A gold-plated copper substrate is centered in the chamber and cooled by a closed-cycle helium cryostat that allows for variation of the substrate temperature between 8 and 450 K, which is monitored by two silicon diode thermal sensors with 0.5 K absolute accuracy. Gaseous species, i.e., H_2 (D_2) (Linde 5.0) and CO (Linde 2.0), are separately introduced into the UHV chamber through the Hydrogen Atom-Beam Source line (filament is off and at room temperature) and a molecule dosing line, respectively. The ice sample is monitored *in situ*, before and during UV-photon irradiation by Fourier Transform Reflection-Absorption InfraRed Spectroscopy (FT-RAIRS) in the range from 700 to 4000 cm^{-1}, with 1 cm^{-1} resolution. The RAIR band strength value of CO and possible formation products, like H_2CO is obtained from the laser interference experiments described by Chuang et al. (2018). The HCO radical band strength value for RAIRS is calibrated from the averaged transmission value estimated by Bennett et al. (2007) and Gerakines et al. (1996) multiplying a conversion factor (i.e., 'reflection mode'/'transmission mode'=2.05 for present IR setting). The conversion factor is based on the assumption that the band strength ratio of HCO/CO is constant in both transmission and reflection IR spectroscopy (Öberg et al. 2009). Since the DCO band strength has not been reported in the literature, it is estimated by multiplying the HCO band strength value with a factor of 0.74. This conversion factor is obtained under the assumption that the band strength ratio in C=O stretching mode of DCO/HCO is similar to the ratio of D_2CO/H_2CO (i.e., 0.74) reported in Hidaka et al. (2009) . The used IR band strengths in this work are 2.26×10^{-17}, 2.49×10^{-17}, 3.36×10^{-17}, and 3.59×10^{-17} cm molecule^{-1} for CO (2142 cm^{-1}), HCO (1859 cm^{-1}), DCO (1798 cm^{-1}), and H_2CO (1737 cm^{-1}), respectively. The deposition rate of CO ice is 1.7×10^{13} molecules cm^{-2} s^{-1} determined by using a modified Beer-Lambert law for the IR absorbance at 2142 cm^{-1}. As H_2 (D_2) is an IR inactive molecule, the H_2 (D_2) flow rate is obtained by the Langmuir estimation (i.e., 1×10^6 torr· s=1 L) resulting in a gas-phase flux of 7.3×10^{14} molecules cm^{-2} s^{-1}. The H_2 sticking coefficient (*f*) on pure CO ice is not available from the literature, and is expected to depend strongly on temperatures in the range of $8-20$ K. Moreover, not all the H_2 that gets temporarily stuck will stay on the surface long enough to get also trapped in the bulk of the ice; the residence time of H_2 on the surface is short which causes a fraction to return into the gas phase. Therefore, the estimated concentration of H_2 ice is an upper limit and expected to be less than CO due to the very small binding energy for multi-layer H_2 ice. The ice deposition time is 60 minutes resulting in a very similar column density of CO in all experiments.

After the simultaneous deposition of a CO:H_2 ice mixture, UV photons generated by a Microwave Discharge Hydrogen flowing Lamp (MDHL) are guided through a MgF_2 window onto the ice sample at a 90 degrees angle w.r.t. the ice layer covering the entire substrate area (2.5×2.5 cm^2). The spectral emission pattern and fluxes have been characterized in detail in previous work (Ligterink et al. 2015; Fedoseev et al. 2016; Chuang et al. 2017). The used H_2 pressure amounts to ~1 mbar which corresponds to a ratio of 'Lyα'/'H_2-emission (~160 nm)'$\cong1.7$ and UV-photon flux of $\sim6\times10^{12}$ photons cm^{-2} s^{-1} (Ligterink et al. 2015).
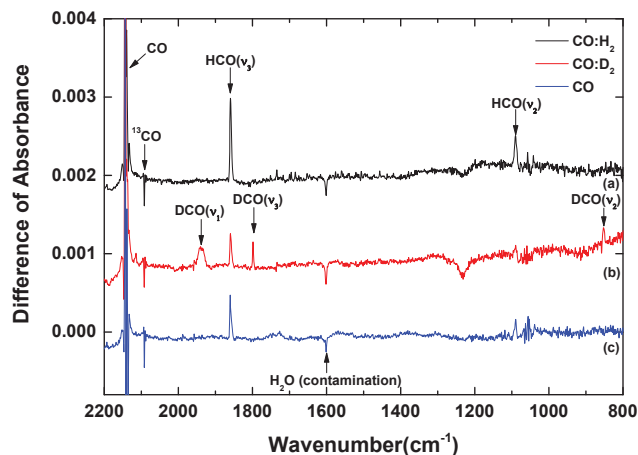
Figure 7.1: The IR spectra of the UV photolysis experiments in pre-deposited (a) CO:H_2, (b) CO:D_2 and (c) CO ice with a photon-flux of 6×10^{12} photons cm^{-2} s^{-1} over 60 minutes at 8 K.

7.3   RESULTS

HCO formation: Figure 7.1 presents the RAIR difference spectra obtained after UV-photon irradiation of pre-deposited (a) CO:H_2, (b) CO:D_2 and (c) pure CO ice at 8 K with a photon-flux of 6×10^{12} photons cm^{-2} s^{-1} for 60 minutes. The negative peaks visible at 2142 and 2091 cm^{-1} are due to CO and its natural isotope ^{13}CO, respectively, and reflect that their initial ice abundances decrease through photo-desorption and photo-chemistry. H_2 consumption cannot be monitored by using RAIRS; in the infrared, frozen H_2 can only be made visible through transitions at 4137 and 4144 cm^{-1} that are the result of a small dipole moment induced through interactions with CO ice (Warren et al. 1980). The estimated band strength, however, is extremely small, i.e., $\sim 10^{-19}$ cm molecule^{-1} and about two orders of magnitude smaller than for CO ice (Sandford & Allamandola 1993). For the relatively thin ices studied in our experiments, therefore, it is not possible to monitor H_2 directly.

The positive peaks at 1859, 1090, and 2488 cm^{-1} (the latter is not shown in Figure 7.1) in the CO:H_2 experiment indicate the formation of HCO, and originate from its C-O stretching (ν_3), bending (ν_2), and C-H stretching (ν_1) vibration mode, respectively (Ewing et al. 1960; Milligan & Jacox 1964). The corresponding isotopic product of the formyl radical (DCO) in the CO:D_2 experiment is identified by absorption signals at 1798, 852, and 1938 cm^{-1} due to its C-O stretching (ν_3) and bending (ν_2), and C-D stretching (ν_1) vibrational modes, respectively (Ewing et al. 1960; Milligan & Jacox 1964). In experiments (b) and (c), HCO peaks can also be observed. The HCO features in (b) and (c) are weaker than in (a) and can be explained by the presence of H_2 or H_2O as background residual gases in the UHV chamber. This is confirmed by the fact that the HCO feature strengths are identical in experiments (b) and (c). Since no DCO signal is found in experiment (a) we confirm the formation of HCO/DCO upon UV irradiation of a CO:H_2/CO:D_2 ices. The estimated H_2O column density, i.e., $N(H_2O)$, is below $\sim 0.1 \times 10^{15}$ molecule cm^{-2} in all three experiments and the ratio of $N(H_2O)/N_{\mathrm{deposited}}(CO) < 0.002$ after CO:H_2 ice mixture preparation. Other photolysis prod-
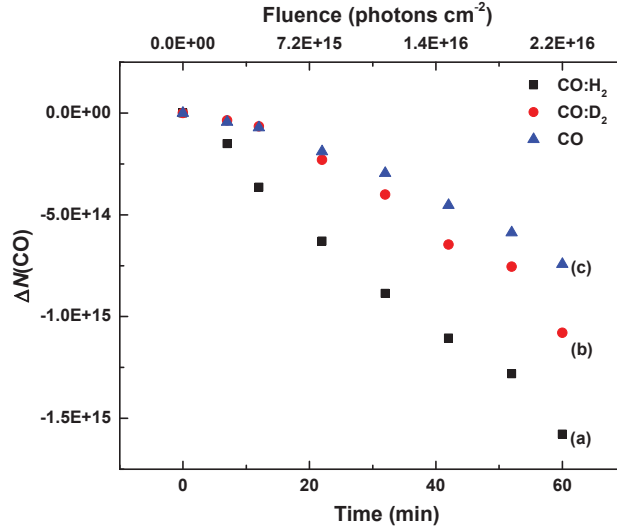
Figure 7.2: The evolution of the ΔN(CO) depletion over 60 min of UV-photon irradiation with a photon-flux of 6×10^{12} photons cm^{-2} s^{-1} at 8 K for (a) CO:H$_2$, (b) CO:D$_2$ and (c) CO ice. The ΔN(CO) has been calibrated by the initial ^{13}CO ice thickness.

ucts, like CO$_2$ (2346 cm^{-1}) and its isotope ^{13}CO$_2$ (2280 cm^{-1}) are also detected in all three experiments (not shown in Figure 7.1). Their formation has been reported in previous UV-photon irradiation studies of pure CO ice (Gerakines et al. 1995; Gerakines & Moore 2001; Muñoz Caro et al. 2010; Chen et al. 2014; Paardekooper et al. 2016).

The initial ice thickness of CO is beyond the RAIRS saturation limit for our experimental conditions, making it difficult to quantify the CO column density directly from its IR absorbance signal at 2142 cm^{-1}. Given the constant CO/^{13}CO ratio (i.e., the natural abundance of CO:^{13}CO=98.9:1.1), the unsaturated ^{13}CO feature can also be used to derive the CO abundance. Figure 7.2 shows the relative intensity changes of the CO abundance during 60 minutes of UV-photon irradiation at 8 K for the three experiments shown in Figure 7.1, i.e., ΔN(CO), determined from the integrated IR absorbance area of ^{13}CO (2091 cm^{-1}). In all three experiments the CO abundance is clearly decreasing; after 60 minutes of UV photolysis which corresponds to a UV fluence of 2.2×10^{16} photons cm^{-2}, the depletion ΔN(CO) is 1.6×10^{15}, 1.1×10^{15}, and 0.7×10^{15} molecules cm^{-2} for (a) CO:H$_2$, (b) CO:D$_2$ and (c) CO ice, respectively.

The UV-photon irradiation of pure CO ice has been extensively studied; CO ice is mainly found to photo-desorb following a DIET mechanism and small amounts of CO$_2$ at the level of a few percent are formed in the ice (see for an overview Paardekooper et al. 2016). After calibrating the distance between the ice sample and MDHL, and assuming that the light acts as a point source, the absolute depletion rate per second of pure CO ice is derived as 4.9×10^{11} molecules cm^{-2} s^{-1}, comparable to the rate of $(3.2\pm1.7)\times10^{11}$ molecules cm^{-2} s^{-1} reported in Paardekooper et al. (2016) for very similar MDHL settings. The derived absolute CO photo-desorption rate is 3.2×10^{-2} molecules photon^{-1} by employing the photon flux used in this work. The experimental CO absolute depletion rates for CO:H$_2$ and CO:D$_2$ ices are ~2
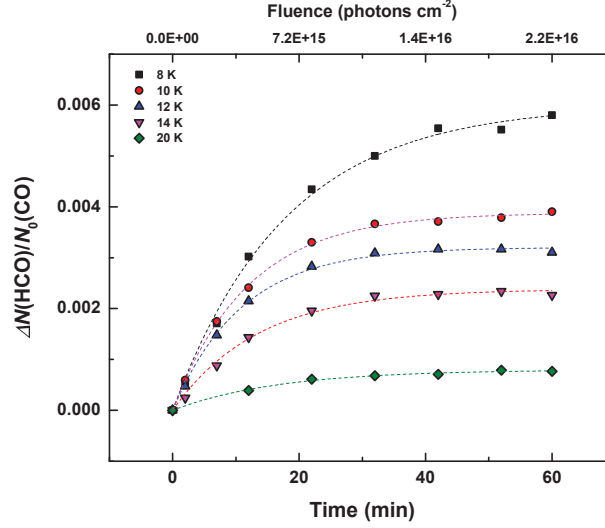
Figure 7.3: The evolution of the newly formed N(HCO) w.r.t. initially predeposited N_0(CO) over 60 min of UV-photon irradiation of CO+H$_2$ ice mixture with a photon-flux of 6×10^{12} photons cm^{-2} s^{-1} at 8, 10, 12, 14 and 20 K, respectively. The solid lines are the exponentially fitted results by using equation (57).

and ~1.5 times higher, respectively, indicating that more CO has been consumed than can be explained by photo-desorption only, i.e., this observation is fully consistent with additional CO losses because of involvement in photo-chemical reactions with H$_2$ (D$_2$) forming HCO (DCO), as shown in Figure 7.1.

Temperature dependence: Figure 7.3 presents the column density of N(HCO) which is obtained from the integration of the IR feature at 1859 cm^{-1} and that is normalized to the initial CO abundance, i.e., N_0(CO), for experiments of CO:H$_2$ ice over 60 minutes UV-photon irradiation at 8, 10, 12, 14 and 20 K. The HCO production grows with increasing UV-photon fluence impinging on the ice mixture, and reaches saturation around $30-60$ minutes (except at 8 K), which implies that a balance between HCO formation and destruction processes is eventually reached. The final HCO abundances after 60 min of UV-photon irradiation show a strong temperature dependence in the range of $8-20$ K; at 20 K, the yield of HCO is only ~10% of the production at 8 K. Because of the small absorption cross section reported for CO, i.e., 4.7×10^{-18} cm^2 (Cruz-Diaz et al. 2014), and as the energy dissipation lifetime is relatively short (~15 ns; Chervenak & Anderson 1971), here, we assume that the electronically excited CO triggered by impinging UV-photons is the limited reactant. Therefore, a pseudo-first-order reaction equation is used to fit the approximately steady-state formation curve of ΔN(HCO)/N_0(CO) for the sequential reactions (Watanabe et al. 2006; Hidaka et al. 2007):

$$\frac{\Delta N(\text{HCO})}{N_0(\text{CO})} = \alpha(1 - \exp(-N(\text{H}_2)\cdot \text{k}\cdot \text{t})) = \alpha(1-\exp(-\phi\cdot\sigma\cdot\text{t})), \qquad (57)$$

where N(H$_2$) is the column density of hydrogen molecules in molecules cm^{-2}, k is the rate constant in cm^2 molecules^{-1}s^{-1}, α is the saturation value (unitless), ϕ is the UV-photon
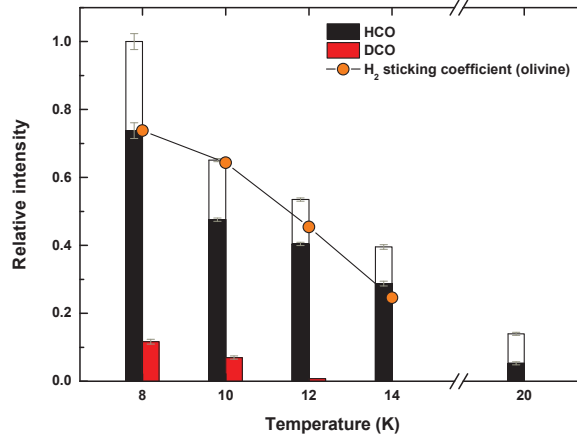
Figure 7.4: The relative intensity of the final yield for N(HCO) (black column) and N(DCO) (red column), i.e., the saturation value (α), obtained after CO:H_2 and CO:D_2 ice UV irradiation for 60 minutes with a flux of 6×10^{12} photons cm^{-2} s^{-1} at temperatures ranging from 8 to 20 K, respectively. The white columns are the initial N(HCO) before subtraction of the extra HCO contribution from the contamination of residual H_2 or H_2O in the UHV chamber. The column densities have been calibrated by the initial ^{13}CO ice thickness, and further normalized to the most abundant N(HCO) in the CO:H_2 experiment at 8 K. The orange points are the reported relative intensity of H_2 sticking coefficients on olivine substrate at $8-14$ K in Acharyya (2014).

flux in photons cm^{-2} s^{-1}, σ is the effective formation cross section in cm^2 photon^{-1}, and t is the experimental time in seconds. The rate constant (k) cannot be derived here due to the IR-inactive H_2, but the formation cross section (σ) is available from experimental results (Gerakines et al. 1996; Öberg et al. 2009; Oba et al. 2018). The derived fitting parameters are plotted in Figures 7.4 and 7.5.

In Figure 7.4, the relative intensity of the saturation value (α), i.e., the final yield of HCO (black column) and DCO (red column), is presented for experiments of CO:H_2 and CO:D_2, respectively, after 60 min of UV-photon irradiation for temperatures in the range from 8 to 20 K. The unwanted contributions of HCO (white column) from residual H_2 and H_2O gas in the UHV chamber (as shown in Figure 7.1) can be independently quantified in the CO:D_2 experiments and subtracted from the final HCO production in the CO:H_2 experiments. The derived relative HCO abundance with respect to the maximum yield, i.e., the total HCO abundance before subtracting the unwanted HCO contributions, obtained at 8 K is $\sim$0.74, $\sim$0.48, $\sim$0.40, $\sim$0.29 and $\sim$0.05 at 8, 10, 12, 14 and 20 K, respectively. The DCO abundance with respect to the HCO abundance at 8 K is $\sim$0.12 and $\sim$0.07 at 8 and 10 K, respectively. At 12 K, the DCO formation ratio, $\sim$0.01, is only regarded as an upper limit due to low S/N from the corresponding RAIRS signal.

In Figure 7.4, the calibrated HCO abundances show a strong temperature dependence at $8-20$ K that can be linked to the relative sticking coefficient of H_2 reported in literature, e.g., Acharyya (2014) on olivine substrate. This is also shown in the figure. Clearly our results
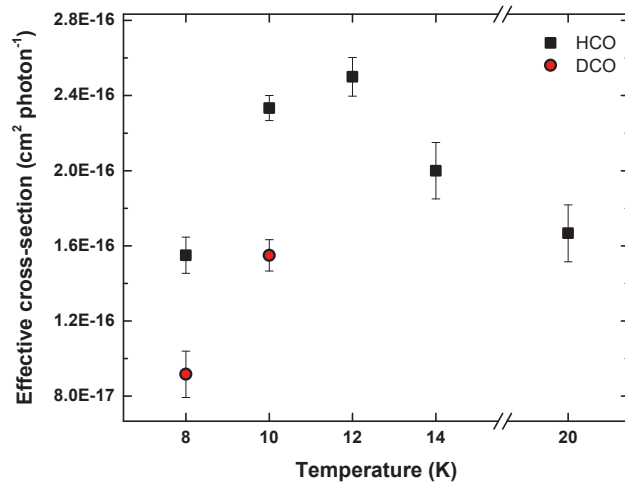
Figure 7.5: The derived effective formation cross-section (σ) obtained by fitting the kinetics of N(HCO) and N(DCO) formation over 60 minutes irradiation of UV-photons with a flux of 6×10^{12} photos cm^{-2} s^{-1} in experiments CO:H$_2$ and CO:D$_2$ at temperatures in the range from 8 to 20 K, respectively.

and the data points reported by Acharyya (2014) are very similar. It should be noted, though, that the surface in our work, CO ice, is different from the substrate used in Acharyya (2014). As aforementioned, due to the lack of H$_2$ sticking coefficients on pure CO ice, the value reported for a non-water surface is currently the best option to compare with our experimental results. It reflects that the HCO formation abundance is predominantly controlled by the initial H$_2$ abundance in the pre-deposited CO:H$_2$ ice mixture. The H$_2$ abundance decreases with increasing temperature due to the dramatic drop of the sticking coefficient while the CO abundance (sticking coefficient=unity) remains constant at all experimental temperatures below 20 K. Up to our knowledge, the D$_2$ sticking coefficient on any surfaces at temperatures in the range of $8 - 20$ K is not available from the literature. However, a similar correlation between the initial D$_2$ ice abundance and the final DCO yield is expected.

The formyl radical formation as result of UV-irradiation clearly shows an isotope effect in the overall formation yield; the amount of HCO formation for UV irradiated CO:H$_2$ ice is about $6 - 7$ times higher than the corresponding amount of DCO in CO:D$_2$ ices. This observation is not directly in line with the assumption of a higher sticking coefficient for D$_2$ compared to H$_2$, i.e., the initial amount of frozen D$_2$ for a specific temperature is expected to be higher than for H$_2$ due to the higher binding energies for D$_2$ (Amiaud et al. 2015). The observed difference in the formation yield between the CO:H$_2$ and CO:D$_2$ will be discussed in the next section.

Figure 7.5 presents the effective formation cross section (σ), which is derived by the single exponential fit (i.e., equation (57)) of HCO and DCO formation kinetics for product HCO (black squares) and DCO (red dots). The derived cross section is the cumulative outcome of multiple reaction channels of HCO (DCO), and is mainly controlled by two reaction parameters, e.g., diffusion rate and sticking coefficient (initial ice abundance). Figure 7.5 shows a
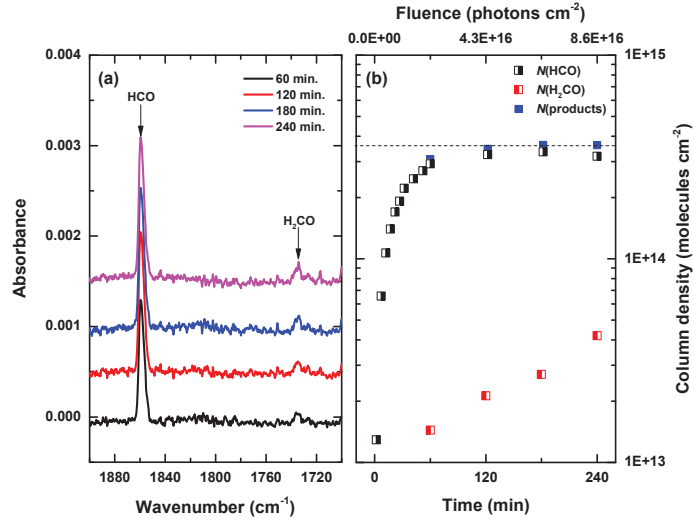
Figure 7.6: Left: the IR spectra of the UV photolysis experiments on pre-deposited CO:H$_2$ ice with a photon-flux of 6×10^{12} photons cm^{-2} s^{-1} for 240 min at 8 K. Right: the evolution of newly formed N(HCO), N(H$_2$CO) and total abundance of photolysis products over 240 min of UV-photon irradiation.

temperature dependency of the HCO formation rate in the range of $8 - 20$ K, with a maximum value at $\sim$12 K. A proportional correlation, i.e., increasing the ice sample temperature results in an increased formation cross section, in the range of $8 - 12$ K; at 12 K the effective cross section of HCO is 1.7 times higher than the value at 8 K. One of the possible interpretations is that this positive slope can be explained by the diffusion rate that is expected to be also temperature dependent, i.e., the higher the temperature, the higher the diffusion rate of H$_2$ (D$_2$) and H(D)-atoms is (Fuchs et al. 2009). However, at the same time, the formation cross section is also dominated by the available H$_2$ (D$_2$) ice abundance (species concentration in bulk ice) that is controlled by its sticking coefficient. At higher temperature, the concentration of H$_2$ (D$_2$) molecules in the CO ice is lower than that at low temperature. This results in a decreased effective cross section with increasing temperature from 2.5×10^{-16} at 12 K to 1.7×10^{-16} cm^2 photon^{-1} at 20 K (i.e., 68% less). A detailed temperature dependent study (e.g., a wider temperature range and a better temperature resolution) is needed for a more detailed picture. For DCO, as aforementioned, the absolute formation yield above 12 K cannot be derived from the IR spectrum due to the limited detection sensitivity. With much thicker ice than used in this work, the effective formation cross section for higher temperature can be measured and also for CO:D$_2$ ices but this is presently outside the scope of this work. A similar temperature dependence of the formation rate due to the different sticking coefficients was reported in previous laboratory studies of CO hydrogenation in the same temperature range of $8 - 20$ K (Watanabe et al. 2006).

H$_2$CO formation: Figure 7.6(a) shows the IR absorbance difference spectra for the photo-induced experiment of CO:H$_2$ for 240 min with a flux of 6×10^{12} photons cm^{-2} s^{-1} at 8 K. As aforementioned, HCO is observed at 1859 cm^{-1} along with 2488 and 1090 cm^{-1}, and its

absorbance is relatively constant from 60 to 240 min. The new IR feature appearing at 1737 cm^{-1} can be assigned to monomer H_2CO (ν_2), and becomes much clearer with longer UV-photon irradiation time (Khoshkhoo & Nixon 1973; Nelander 1980). In Figure 7.6(b), the product abundances obtained from the integration of HCO (1859 cm^{-1}) and H_2CO (1737 cm^{-1}) IR signals, respectively, are presented over 240 min. The HCO formation rate starts slowing down after 60 minutes and slightly decreases after passing the maximum column density of 3×10^{14} molecules cm^{-2}. The detectable abundance of H_2CO builds up after 60 minutes of UV-irradiation as the fluence amounts to 2.2×10^{16} photons cm^{-2}, and the final abundance ratio of $\Delta N(H_2CO)/\Delta N(HCO)$ is ~0.13 reflecting that H_2CO is a second generation product after HCO; the free H-atoms from HCO photodissociation can either react with HCO or diffuse away and then react with HCO forming H_2CO through barrierless recombination. Alternatively, Butscher et al. (2017) reported the H-atom abstraction from HCO by another HCO which could be an additional channel to form H_2CO and CO. The sum of $N(HCO)$ and $N(H_2CO)$ shows a relatively constant value of 3.6×10^{14} after 120 minutes suggesting a direct chemical link between these two products.

7.4 DISCUSSION

The UV-photon energy applied here is $\leqslant 10.2$ eV, and cannot directly dissociate CO or H_2 molecules; the required threshold dissociation energies of CO and H_2 in the gas phase are 11.09 and 11.20 eV, respectively (Field et al. 1966; Dalgarno & Stephens 1970; Okabe 1978). In the solid state these values can decrease, but with 0.13 eV decrease for CO the effect is negligible (Lu et al. 2005). However, CO has a strong absorption cross section in the $127 - 157$ nm range, coinciding with the wavelength of the impacting UV-photons. This allows to excite CO into its first electronic state ($A^1\Pi \longleftarrow X^1\Sigma^+$), i.e., CO* with excess energy $\geqslant 7.9$ eV (Lu et al. 2005; Mason et al. 2006; Cruz-Diaz et al. 2014);

$$CO + h\nu \longrightarrow CO^* \tag{58}$$

Subsurface CO* can transfer the energy to the top layer molecules leading to the CO non-thermal desorption at low temperature, as discussed by Fayolle et al. (2011) and van Hemert et al. (2015), and in the bulk it can further react with neighboring CO to form CO_2 (Bertin et al. 2013; Okabe 1978; Gerakines et al. 1996; Gerakines & Moore 2001; Loeffler et al. 2005; Chen et al. 2014);

$$CO^* + CO \longrightarrow CO_2 + C \tag{59}$$

Due to a small amount of H_2O contamination as shown in our IR spectrum at 1600 cm^{-1}, another reported CO_2 formation channel through the reaction between CO and OH radical, originating from H_2O photodissociation, cannot be excluded (Watanabe & Kouchi 2002; Watanabe et al. 2007; Oba et al. 2010; Ioppolo et al. 2011).

As mentioned, the H_2 (D_2) molecule cannot be directly dissociated in H-atoms (D-atoms) upon Lyα excitation, or electronically excited by an UV-photon ($\leqslant 10.2$ eV), however, an alternative channel may apply that is similar to the CO_2 formation scheme shown in equation (59):

$$CO^* + H_2 \longrightarrow HCO + H_{dis} \tag{60}$$
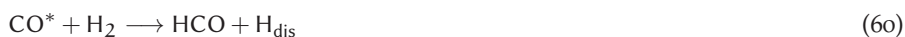
The lowest potential energy of the first electronic state of CO is 7.9 eV, and is larger than the reported enthalpy of $CO + H_2 \longrightarrow HCO + H$ in the gas phase, i.e., ~3.7 eV (Reilly et al. 1978).

Moreover, ab initio calculations show that the H_2 dissociation due to energy transfer from the electronically excited CO is a barrierless reaction (Sperlein et al. 1987). Therefore, we expect that the reaction shown in equation (60) proceeds without activation barrier in the solid state as well. The product HCO is likely thermally stabilized below 20 K, and preserved in the ice mixture. The free H-atom (H_{dis}) that is formed in equation (60) may react with the newly formed HCO radical in equation (60) yielding H_2CO or CO+H_2 through:

$$H_{dis} + HCO \longrightarrow H_2CO \tag{61a}$$

$$H_{dis} + HCO \longrightarrow CO + H_2 \tag{61b}$$

There is also a possibility that the H_{dis} diffuses in the bulk ice and reacts with CO to form HCO through direct H-atom addition reactions contributing to the total yield of HCO detected in the IR spectrum (Watanabe & Kouchi 2002; Fuchs et al. 2009):

$$H_{dis} + CO \longrightarrow HCO \tag{62}$$

or meets with other free radicals available in the ice, like HCO and H_{dis} forming H_2CO (equation 61a), H_2+CO (equation 61b) and H_2 through:

$$H_{dis} + H_{dis} \longrightarrow H_2 \tag{63}$$

The reaction channels of equations (61) and (62) compete with each other showing a strong temperature dependence due to the different diffusion rates; at higher ice temperatures, the mobile H-atom will diffuse away much quicker from the newly formed HCO in the bulk ice, and eventually react with CO forming HCO. This explains the increase of the observed HCO formation cross section in Figure 7.5 at temperatures from 8 to 12 K. Beyond 12 K, the substantial decrease of the effective concentration of H_2 leads to a lower cumulative formation rate.

For the final yield of HCO, it is important to note that the HCO formation in equation (60) induced by UV-photons is expected to proceed without activation barrier, but the hydrogenation of CO in equation (62) was shown before to exhibit a strong isotope effect due to the quantum tunneling of H(D)-atoms (Hidaka et al. 2007). This likely explains the difference in formation yield between HCO and DCO, and shows that secondary D(H)-atoms are indeed contributing to the overall abundances. Therefore, the derived formation cross section of formyl radical is concluded to be an effective value that is controlled by the reaction parameters, e.g., sticking coefficient, diffusion rate for H_2 and D_2 molecules, and an isotope effect that gets important in a secondary reaction step..

The possible formation mechanism of H_2CO is through the reaction HCO+H, of which the H-atom can be directly formed as shown in equation (61a) or be produced by photodissociation of HCO (Heays et al. 2017);

$$HCO + h\nu \longrightarrow CO + H \tag{64}$$

Alternatively, the recombination of two HCO radicals can result in H_2CO+CO formation through the reaction (Butscher et al. 2017):

$$HCO + HCO \longrightarrow H_2CO + CO \tag{65}$$

In this work, the observed H_2CO formation is found when HCO abundance passes its maximum yield and starts decreasing (Figure 7.6), implying that the HCO is a key precursor to form H_2CO or even more complex species, although, these are not found here.

7.5   ASTROCHEMICAL IMPLICATION

This laboratory work shows that electronically excited ice species induced by UV-photons can react with H_2 molecules adsorbed (or trapped) in interstellar ices at low temperatures to form new species. In space, cosmic rays, electrons and photons can all interact with ice grains transferring energy to the ice. Such events can lead to a series of different thermal and chemical processes depending on the energetic input and chemical composition of the ice. For instance, previous laboratory studies on UV-irradiation of CO ice showed that although UV-photons cannot photodissociate CO molecules, they can electronically excite CO* species that can then cause the non-thermal desorption of other CO molecules (Fayolle et al. 2011; van Hemert et al. 2015). This mechanism successfully explains the observed gaseous abundance of CO at low temperature and also, at least partially, the photo-excitation chemistry resulting in the formation of C_nO_m species in the solid phase, particularly CO_2 (Loeffler et al. 2005; Gerakines & Moore 2001). It also has been linked to the location of photo-induced snow lines in proto-planetary disks (Qi et al. 2015; Öberg et al. 2015).

In dense clouds, the H_2 abundance is four orders of magnitude higher than that of H-atoms. Therefore, since H_2 molecules are expected to be found in interstellar ices at low temperatures (Sandford et al. 1993; Buch & Devlin 1994; Dissly et al. 1994), it is possible that electronically excited species react with molecular hydrogen getting hydrogenated. The dissociation of H_2 induced by the excited species results in a free H-atom that can further hydrogenate other molecules forming hydrogen-saturated species, like CH_3OH and COMs. This mechanism may also apply to other reaction chains. For instance, water and hydrocarbons can be formed through reactions of hydrogen molecules with photo-excited oxygen-atoms (O*) and carbon-atoms (C*), respectively. Both have a strong UV-photon absorption cross section in the range of $120 - 160$ nm.

It should be noted that the solid state formation of hydrogen-rich species containing atomic C and O (e.g., H_2CO, and CH_3OH) is believed to occur predominantly through H-atom addition reactions to CO in dense clouds. In the present work we show for a first time that electronically excited species can react with frozen H_2 under dense cloud conditions, a process that is limitedly involved in current astrochemical networks. We propose a general mechanism on the example of $CO:H_2+h\nu$ as this system is well studied and has a minimum number of competing side-photochemical products. It offers an additional channel that holds the potential to form HCO radicals (and larger species) in interstellar ices, especially at very low temperatures. Since there is no proof of CH_3OH formation in our experiments, this hints at a lower efficiency of the CO*+H_2 compared to the regular CO+H hydrogenation chain. As UV light can penetrate deeper in ices than H-atoms, the mechanism studied here may increase the abundance of HCO radicals in the deeper layers of the ice, where CO and H_2 (depending on temperature) are preserved and H-atoms cannot penetrate. Ultimately, this may affect the efficiency with which COMs can be formed in the later stage when the ice mantle is gently heated by the central protostar. The work presented here should be considered as a case study, investigating a new process capable of triggering chemical reactions at low temperatures in interstellar ices. The process may be more generally relevant, and applicable to other reaction chains as well. To which extent it contributes to the full chemical picture, will be topic of future astrochemical modeling studies.

7.6   CONCLUSIONS

Below the main findings of this experimental study are given for frozen H$_2$ when absorbed or trapped in interstellar ice analogues upon UV irradiation:

1. UV-photons generated by cosmic rays in dense clouds may increase HCO (H$_2$CO and possibly larger COMs) abundances by triggering a solid-state reaction involving electronically excited CO* and H$_2$. The HCO formation is explained by two consecutive reaction steps CO*+H$_2 \longrightarrow$HCO+H$_{dis}$ and CO+H$_{dis} \longrightarrow$HCO.

2. The derived effective formation cross section shows a temperature dependence that is determined by the cumulative effect of the H-atom diffusion rate and initial H$_2$ concentration in the bulk ice that is determined by the sticking coefficient. For the investigated laboratory settings, we find a maximum at 12 K of 2.5$\times$10^{-16} cm^2 photon^{-1}.

3. The surface temperature between 8 and 20 K determines the photolysis product yield and this is due to the temperature dependent sticking efficiency of H$_2$.

4. The mechanism that involves reactions between electronically excited species and H$_2$ molecules on icy grains may be of more general importance in ISM chemistry. It will take more detailed astrochemical modeling to put this pathway into perspective and to check to which extent this contributes to the formation of H$_2$CO and eventual COMs in space. Based on the experiments performed here, the mechanism is found to contribute, but very likely at a level that is (substantially) lower than regular CO hydrogenation upon impacting H-atoms.

BIBLIOGRAPHY

Acharyya, K. 2014, Mon. Not. R. Astron. Soc., 443, 1301

Amiaud, L., Fillion, J.-H., Dulieu, F., Momeni, A., & Lemaire, J.-L. 2015, Phys. Chem. Chem. Phys., 17, 30148

Bacmann, A., Taquet, V., Faure, A., Kahane, C., & Ceccarelli, C. 2012, Astron. Astrophys., 541, L12

Balucani, N., Ceccarelli, C., & Taquet, V. 2015, Mon. Not. R. Astron. Soc., 449, L16

Bennett, C. J., Chen, S.-H., Sun, B.-J., Chang, A. H. H., & Kaiser, R. I. 2007, Astrophys. J., 660, 1588

Bertin, M., Fayolle, E. C., Romanzin, C., et al. 2013, Astrophys. J., 779, 120

Bertin, M., Romanzin, C., Doronin, M., et al. 2016, Astrophys. J. Lett., 817, L12

Boogert, A. C. A., Gerakines, P. A., & Whittet, D. C. B. 2015, Ann. Rev. Astron. Astrophys., 53, 541

Borget, F., Müller, S., Grote, D., et al. 2017, Astron. Astrophys., 598, A22

Buch, V. & Devlin, J. P. 1994, Astrophys. J. Lett., 431, L135

Butscher, T., Duvernay, F., Danger, G., & Chiavassa, T. 2016, Astron. Astrophys., 593, A60

Butscher, T., Duvernay, F., Rimola, A., Segado-Centellas, M., & Chiavassa, T. 2017, Phys. Chem. Chem. Phys., 19, 2857

Butscher, T., Duvernay, F., Theule, P., et al. 2015, Mon. Not. R. Astron. Soc., 453, 1587

Cernicharo, J., Marcelino, N., Roueff, E., et al. 2012, Astrophys. J. Lett., 759, L43

Chang, Q. & Herbst, E. 2012, Astrophys. J., 759, 147

Charnley, S. B. 1997, Mon. Not. R. Astron. Soc., 291, 455

Chen, Y.-J., Chuang, K.-J., Muñoz Caro, G. M., et al. 2014, Astrophys. J., 781, 15

Chervenak, J. & Anderson, R. 1971, JOSA, 61, 952

Chuang, K.-J., Fedoseev, G., Ioppolo, S., van Dishoeck, E. F., & Linnartz, H. 2016, Mon. Not. R. Astron. Soc., 455, 1702

Chuang, K.-J., Fedoseev, G., Qasim, D., et al. 2017, Mon. Not. R. Astron. Soc., 467, 2552

Chuang, K.-J., Fedoseev, G., Qasim, D., et al. 2018, Astrophys. J., 853, 102

Cruz-Diaz, G. A., Muñoz Caro, G. M., Chen, Y.-J., & Yih, T.-S. 2014, Astron. Astrophys., 562, A119

Cuppen, H. M., Ioppolo, S., Romanzin, C., & Linnartz, H. 2010, Phys. Chem. Chem. Phys., 12, 12077

Cuppen, H. M., van Dishoeck, E. F., Herbst, E., & Tielens, A. G. G. M. 2009, Astron. Astrophys., 508, 275

Dalgarno, A. & Stephens, T. L. 1970, Astrophys. J. Lett., 160, L107

Dissly, R. W., Allen, M., & Anicich, V. G. 1994, Astrophys. J., 435, 685

Dulieu, F., Amiaud, L., Congiu, E., et al. 2010, Astron. Astrophys., 512, A30

Ewing, G. E., Thompson, W. E., & Pimentel, G. C. 1960, J. Chem. Phys., 32, 927

Fayolle, E. C., Bertin, M., Romanzin, C., et al. 2011, Astrophys. J. Lett., 739, L36

Fedoseev, G., Chuang, K.-J., Ioppolo, S., et al. 2017, Astrophys. J., 842, 52

Fedoseev, G., Chuang, K.-J., van Dishoeck, E. F., Ioppolo, S., & Linnartz, H. 2016, Mon. Not. R. Astron. Soc., 460, 4297

Fedoseev, G., Cuppen, H. M., Ioppolo, S., Lamberts, T., & Linnartz, H. 2015, Mon. Not. R. Astron. Soc., 448, 1288

Field, G. B., Somerville, W. B., & Dressler, K. 1966, Ann. Rev. Astron. Astrophys., 4, 207

Fuchs, G. W., Cuppen, H. M., Ioppolo, S., et al. 2009, Astron. Astrophys., 505, 629

Garrod, R., Park, I. H., Caselli, P., & Herbst, E. 2006, Faraday Discussions, 133, 51

Garrod, R. T. 2013, Astrophys. J., 778, 158

Gerakines, P. A. & Moore, M. H. 2001, Icarus, 154, 372

Gerakines, P. A., Schutte, W. A., & Ehrenfreund, P. 1996, Astron. Astrophys., 312, 289

Gerakines, P. A., Schutte, W. A., Greenberg, J. M., & van Dishoeck, E. F. 1995, Astron. Astrophys., 296, 810

Hama, T. & Watanabe, N. 2013, Chemical Reviews, 113, 8783

Heays, A., Bosman, AD, v., & van Dishoeck, E. 2017, Astronomy & Astrophysics, 602, A105

Hidaka, H., Kouchi, A., & Watanabe, N. 2007, J. Chem. Phys., 126, 204707

Hidaka, H., Watanabe, M., Kouchi, A., & Watanabe, N. 2009, Astrophys. J., 702, 291

Hiraoka, K., Miyagoshi, T., Takayama, T., Yamamoto, K., & Kihara, Y. 1998, Astrophys. J., 498, 710

Ioppolo, S., Cuppen, H. M., Romanzin, C., van Dishoeck, E. F., & Linnartz, H. 2008, Astrophys. J., 686, 1474

Ioppolo, S., Cuppen, H. M., Romanzin, C., van Dishoeck, E. F., & Linnartz, H. 2010, Phys. Chem. Chem. Phys., 12, 12065

Ioppolo, S., Fedoseev, G., Lamberts, T., Romanzin, C., & Linnartz, H. 2013, Review of Scientific Instruments, 84, 073112

Ioppolo, S., van Boheemen, Y., Cuppen, H. M., van Dishoeck, E. F., & Linnartz, H. 2011, Mon. Not. R. Astron. Soc., 413, 2281

Jiménez-Serra, I., Vasyunin, A. I., Caselli, P., et al. 2016, Astrophys. J. Lett., 830, L6

Khoshkhoo, H. & Nixon, E. R. 1973, Spectrochimica Acta Part A: Molecular Spectroscopy, 29, 603

Kristensen, L., Amiaud, L., Fillion, J.-H., Dulieu, F., & Lemaire, J.-L. 2011, Astron. Astrophys., 527, A44

Lamberts, T., Cuppen, H. M., Fedoseev, G., et al. 2014, Astron. Astrophys., 570, A57

Lamberts, T., Cuppen, H. M., Ioppolo, S., & Linnartz, H. 2013, Phys. Chem. Chem. Phys., 15, 8287

Lee, T. J. 1972, Journal of Vacuum Science Technology, 9, 257

Ligterink, N., Walsh, C., Bhuin, R., et al. 2018, Astronomy & Astrophysics, 612, A88

Ligterink, N. F. W., Paardekooper, D. M., Chuang, K.-J., et al. 2015, Astron. Astrophys., 584, A56

Linnartz, H., Ioppolo, S., & Fedoseev, G. 2015, International Reviews in Physical Chemistry, 34, 205

Loeffler, M. J., Baratta, G. A., Palumbo, M. E., Strazzulla, G., & Baragiola, R. A. 2005, Astron. Astrophys., 435, 587

Lu, H.-C., Chen, H.-K., Cheng, B.-M., Kuo, Y.-P., & Ogilvie, J. F. 2005, Journal of Physics B Atomic Molecular Physics, 38, 3693

Mason, N. J., Dawes, A., Holtom, P. D., et al. 2006, Faraday discussions, 133, 311

Matar, E., Bergeron, H., Dulieu, F., et al. 2010, J. Chem. Phys., 133, 104507

Meisner, J., Lamberts, T., & Kaìĺstner, J. 2017, ACS Earth and Space Chemistry, 1, 399

Mennella, V., Baratta, G. A., Esposito, A., Ferini, G., & Pendleton, Y. J. 2003, Astrophys. J., 587, 727

Milligan, D. E. & Jacox, M. E. 1964, J. Chem. Phys., 41, 3032

Miyauchi, N., Hidaka, H., Chigai, T., et al. 2008, Chemical Physics Letters, 456, 27

Muñoz Caro, G. M., Jiménez-Escobar, A., Martín-Gago, J. Á., et al. 2010, Astron. Astrophys., 522, A108

Nelander, B. 1980, J. Chem. Phys., 73, 1026

Oba, Y., Miyauchi, N., Hidaka, H., et al. 2009, Astrophys. J., 701, 464

Oba, Y., Tomaru, T., Lamberts, T., Kouchi, A., & Watanabe, N. 2018, Nature Astronomy, 2, 228

Oba, Y., Watanabe, N., Hama, T., et al. 2012, Astrophys. J., 749, 67

Oba, Y., Watanabe, N., Kouchi, A., Hama, T., & Pirronello, V. 2010, Astrophys. J. Lett., 712, L174

Öberg, K. I., Bottinelli, S., Jørgensen, J. K., & van Dishoeck, E. F. 2010, Astrophys. J., 716, 825

Öberg, K. I., Furuya, K., Loomis, R., et al. 2015, Astrophys. J., 810, 112

Öberg, K. I., Garrod, R. T., van Dishoeck, E. F., & Linnartz, H. 2009, Astron. Astrophys., 504, 891

Okabe, H. 1978, Photochemistry of small molecules

Paardekooper, D. M., Fedoseev, G., Riedo, A., & Linnartz, H. 2016, Astron. Astrophys., 596, A72

Pontoppidan, K. M. 2006, Astron. Astrophys., 453, L47

Prasad, S. S. & Tarafdar, S. P. 1983, Astrophys. J., 267, 603

Qi, C., Öberg, K. I., Andrews, S. M., et al. 2015, Astrophys. J., 813, 128

Reilly, J., Clark, J., Moore, C. B., & Pimentel, G. C. 1978, The Journal of Chemical Physics, 69, 4381

Sandford, S. A. & Allamandola, L. J. 1993, Astrophys. J. Lett., 409, L65

Sandford, S. A., Allamandola, L. J., & Geballe, T. R. 1993, Science, 262, 400

Shen, C. J., Greenberg, J. M., Schutte, W. A., & van Dishoeck, E. F. 2004, Astron. Astrophys., 415, 203

Sperlein, R. F., Golde, M. F., & Jordan, K. D. 1987, Chemical physics letters, 142, 359

Tielens, A. G. G. M. & Hagen, W. 1982, Astron. Astrophys., 114, 245

Tobias, I., Fallon, R. J., & Vanderslice, J. T. 1960, J. Chem. Phys., 33, 1638

van Hemert, M. C., Takahashi, J., & van Dishoeck, E. F. 2015, J. Phys. Chem. A, 119, 6354

Vidali, G. 2013, Chemical reviews, 113, 8762

Wakelam, V., Bron, E., Cazaux, S., et al. 2017, Molecular Astrophysics, 9, 1

Warren, J. A., Smith, G. R., & Guillory, W. A. 1980, J. Chem. Phys., 72, 4901

Watanabe, N. & Kouchi, A. 2002, Astrophys. J. Lett., 571, L173

Watanabe, N. & Kouchi, A. 2008, Progress In Surface Science, 83, 439

Watanabe, N., Mouri, O., Nagaoka, A., et al. 2007, Astrophys. J., 668, 1001

Watanabe, N., Nagaoka, A., Hidaka, H., et al. 2006, Planet. Space Sci., 54, 1107

Wooden, D. H., Charnley, S. B., & Ehrenfreund, P. 2004, Composition and evolution of interstellar clouds, ed. G. W. Kronk, 33–66

Woods, P. M., Kelly, G., Viti, S., et al. 2012, Astrophys. J., 750, 19

SUMMARY

Large areas of space are filled by molecular clouds that consist of gas (mainly hydrogen) and (sub)-micron sized silicate and carbonaceous dust grains that are the remnants of dead stars. These interstellar clouds are optically opaque and cold as light penetration is hindered. With decreasing temperature and increasing density, gas starts accreting onto dust grain surfaces that act as highly effective cryopumps. This results in layered geometries of partially mixed ices on top of the grains. It has become clear that these icy dust grains act as molecule reservoirs and cryogenic catalysts on which both simple and complex molecules form in surface reactions, triggered by impacting atoms, electrons and cosmic rays or irradiation by vacuum UV light. Moreover, these grains form the material from which planetesimals and later larger celestial bodies —comets and planets and their moons —are formed. A good understanding of the elementary processes taking place in dark interstellar clouds is necessary to understand the chemical inventory of stellar systems, like our own Solar system.

This thesis focuses on laboratory studies investigating the surface chemistry of CO-rich ices on dust grains under dense interstellar cloud conditions. The formation mechanisms of complex organic molecules (COMs) are investigated by non-energetic processes (e.g., hydrogenation) and energetic processes (e.g., photolysis) of simple molecules, like CO and other interstellar relevant precursor species. Moreover, the net transfer of the newly formed hydrogenated species from grain surfaces into the gas phase through non-thermal desorption is investigated. All work described in the previous chapters has been performed in the Sackler Laboratory for Astrophysics at Leiden University.

INTERSTELLAR ICE IN DENSE CLOUDS

Astronomical observations show the presence of frozen molecules on dust grains, such as H_2O, CO, CO_2, and CH_3OH, through their vibrational transitions in the infrared. In dense clouds, the density (n_H) increases to 10^{4-5} cm^{-3} and temperature drops to ~10 K; carbon monoxide (CO), which is the second most abundant gaseous species (i.e., ~$10^{-4}n_H$) after H_2, abundantly condenses on the pre-formed H_2O-rich ice mantle. This stage is known as the 'catastrophic CO freeze-out stage'. The simultaneous accretion of CO and H-atoms primarily leads to hydrogenated species formation, e.g., H_2CO and CH_3OH, through successive H-atoms addition reactions forming a CO-rich apolar ice coating. This non-energetic mechanism (e.g., hydrogenation) dominating the ice chemistry on grain surfaces is widely considered as the pathway to explain the observed CH_3OH abundance in space. In this thesis it is shown that along this reaction chain also larger complex organic molecules (COMs), such as glycolaldehyde, ethylene glycol and glycerol can be formed.

In dense clouds, the moderate UV-photons induced by cosmic rays interacting with H_2 molecules also affect the surface chemistry of interstellar ices. The flux of the secondary UV-photons ($\leqslant$10.2 eV) is lower than the typical flux of H-atoms (~1×10^4 atoms cm^{-2} s^{-1}). However, such UV-photons can easily penetrate the entire ice mantle resulting in photolysis reactions. The energy of impinging UV-photons cannot dissociate simple molecules, e.g., CO and H_2, but is enough to photo-pump CO into its first electronically excited state or to photo-dissociate the CO hydrogenated species, e.g., H_2CO and CH_3OH. The photolysis of CH_3OH also leads to the formation of interstellar complex organic molecules through the photo-fragment recombination reactions.

The work presented in this thesis shows that molecules of prebiotic interest are already formed during the very first stages of star and planet formation. Complex organic molecules are generally believed to be precursors of the building blocks that are inherent to life and that may have been delivered to early Earth by impacting celestial bodies. Glycolaldehyde, for example, is an important ingredient for ribonucleic acid (RNA) and has been astronomically observed with methyl formate (one of its isomers) and ethylene glycol (a sugar alcohol) toward a number of high- and low-mass protostars. The formation mechanism of COMs is generally accepted to take place on icy dust grains through the recombination of radicals that are generated upon both energetic triggers (e.g., UV-photons, electrons, and ions) and non-energetic triggers (e.g., H-atoms). Recently, the 'cold' discovery of gaseous COMs in dense clouds and prestellar cores (at temperatures as low as 10 K) has challenged the conventional synthesis scenario where CH_3OH undergoes intense energetic particle bombardment and 'warm ice chemistry' forming COMs in high-mass protostars. In cold regions, therefore, hydrogenation starting from CO ice offers an alternative mechanism to explain the presence of COMs in the early phase of star formation. This mechanism is proven in this thesis.

The astronomical gas-phase observation of simple species and organic molecules in dense clouds, with abundance as high as $10^{-9} - 10^{-8} n_H$, contradicts the concept that at such low temperature all species (except H_2 and He) should condense onto dust grains. A physical or chemical mechanism that transfers the ice species from the solid state into the gas phase offers a possible explanation. A direct thermal desorption is forbidden due to the very low temperature ($\sim$10 K) at this stage. Therefore, different non-thermal desorption mechanisms have been proposed to bridge the grain-gas gap. Photo-desorption is an efficient mechanism to non-thermally desorb simple species, e.g., CO, CO_2, H_2O, and $CO:N_2$ ices. However, for the hydrogenated species CH_3OH, photo-dissociation becomes a dominating channel resulting in fragment formation, e.g., CH_3, CH_3O, and CH_2OH. For this reason, a different mechanism has been studied here; reactive desorption (RD) may offer a gas-phase enrichment of both simple species and organic molecules through desorption following exothermic reactions along the CO-H_2CO-CH_3OH hydrogenation scheme.

INTERSTELLAR ICE IN LABORATORY

The solid-state chemistry in interstellar ice analogues described in this thesis has been studied in the Sackler Laboratory for Astrophysics by using Surface Reaction Simulation Device[2] (SURFRESIDE[2]; Figure 1), an ultra-high vacuum system fully optimized to study atom reactions and UV-photolysis under dense cloud conditions, i.e. at very low temperatures. Two atom beam lines, i.e., a Hydrogen Atom Beam Source (HABS) and Microwave Atom Source (MWAS), are available to generate interstellar atomic (or molecular) radicals that are co- or pre-deposited with simple species from molecular dosing line onto a cryogenically cooled surface that mimics the grain surfaces in space. A Microwave Discharge Hydrogen-flow Lamp (MDHL) is used to simulate the secondary UV-photons induced by cosmic rays excited molecular hydrogen in dense clouds. The wide range of available substrate temperatures, which are set by the cryostat and resistive heating wire, makes it possible to study the cold surface chemistry that happens in interstellar cores at low temperatures and to simulate thermal desorption, when icy species sublimate into the gas phase, during the later stages of star evolution.

The interstellar ices in SURFRESIDE[2] are *in situ* monitored by means of Reflection-Absorption InfraRed Spectroscopy (RAIRS). The icy constituents are identified by their characteristic vibrational modes that are linked to the various chemical functional groups, and their abundances are derived by the IR absorption band strength (*A* value) that is carefully calibrated

Figure 1: A photo of SURFRESIDE[2].

by a HeNe laser interference technique. A Temperature Programmed Desorption (TPD) experiment in combination with Quadrupole Mass Spectrometry (QMS) providing a very high detection sensitivity is used as a complementary tool to identify the newly formed products. Species desorb at very specific temperatures and are relatively easily distinguished through their characteristic fragmentation patterns upon electron impact ionization. In the case of ambiguity, isotopically enriched species can be used. This all makes SURFRESIDE[2] a very versatile tool to investigate molecular complexity in interstellar ices, for settings that are fully controlled and with a precision that allows to quantitatively investigate the underlying physical/chemical processes on icy grain surfaces.

NON-ENERGETIC FORMATION MECHANISM OF COMS IN DENSE CLOUDS

The laboratory studies of the solid-state interaction between H_2CO and H-atoms not only leads to the hydrogenated species, i.e., CH_3OH, but also results in dehydrogenated species, i.e., CO, through HCO radical. The H-atom abstraction reactions are also found in CH_3OH ice interacting with H-atoms to form H_2CO through CH_2OH radical. The simultaneous forward (hydrogenation) and backward (dehydrogenation) reactions of CO-rich species increase the lifetime of the intermediate radicals on grain surfaces. As a consequence, a barrierless radical-radical recombination can explain the formation of oxygen-bearing complex organic molecules, e.g., methyl formate ($HC(O)OCH_3$), glycolaldehyde ($HC(O)CH_2OH$) and ethylene glycol ($H_2C(OH)CH_2OH$), on dust grains under dense cloud conditions without the presence of energetic particles (e.g., UV-photons, electrons, and ions) or the central star. The experimental findings presented here are in strong support of COM formation during the 'catastrophic CO freeze-out stage'. This formation scheme goes beyond the formation of two-carbon bearing species.

The formation of a three-carbon simple sugar, e.g., glyceraldehyde ($HOCH_2CH(OH)CHO$), and a three-carbon sugar alcohol, e.g., glycerol ($HOCH_2CH(OH)CH_2OH$), is demonstrated by recombining single- and double-carbon radicles under dense cloud conditions. From this it
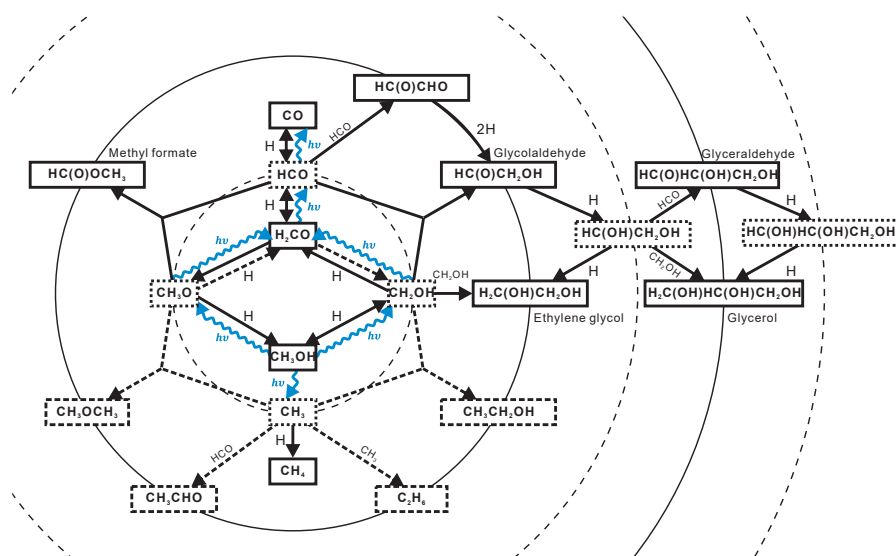
Figure 2: Proposed reaction diagram of COM formation.

is concluded that the non-energetic mechanism also holds much potential to form even larger complex organics in the space. The COM formation scheme is presented in Figure 2.

ICE CHEMISTRY INVOLVING UV-PHOTONS

In dense clouds, the interstellar ice chemistry is simultaneously triggered by both H-atom addition reactions and UV-photon irradiation on dust grains. A systematic experimental study presented in this Thesis shows a quantitative comparison between hydrogenation and UV-photolysis in interstellar relevant ice analogues resulting in different COM formation compositions. COM formation ratios derived from the laboratory results can be used as a diagnostic tool to determine how such species may have formed in interstellar ice. A comparison between laboratory data as discussed here and observational results toward comets and solar-mass protostars suggests that COMs, e.g., glycolaldehyde and ethylene glycol, have a solid-state formation pathway.

UV-photolysis can play an important role to associate a carbon- and nitrogen-bearing species forming prebiotic molecules (peptide-bearing compound). Nitric oxide (NO) has a very high chemical reactivity compared to other N-bearing simple species (e.g., N2) and accretes with H-atoms on grain surfaces in the CO freeze-out stage. Therefore, the fully saturated NH_2OH from NO hydrogenation is expected to be mixed with other CO-rich ices, e.g., H_2CO and CH_3OH. The UV-photons can efficiently dissociate the hydrogenated products resulting in photo-fragments, such as NH_2 and HCO. The experimental findings show that these energetic radicals can further undergo radical-radical recombinations forming NC-bearing biological species, such as HNCO and NH_2CHO that have been observed toward various star evolutionary and cometary objects.

Clearly, hydrogenation reactions involving CO ice on dust grains are important to form both smaller and larger complex organics, in dense clouds. However, molecular hydrogen (H_2), with an abundance four orders of magnitude higher than that of H-atoms, does not actively participate in non-energetic ice chemistry, despite its overabundance and this is due

to the high activation energy of the involved reactions. The experimental study of CO:H_2 ice photolysis results in the unambiguous identification of HCO and H_2CO under dense cloud conditions. It is concluded that the electronically excited carbon monoxide (CO*) induced by UV-photons can react with a ground-state H_2 molecule to form HCO and a free H-atom that then becomes available for H-atom addition reactions. The interaction between CO* and H_2 enhances the production of H_nCO species in the ice mantle and introduces a new solid-state channel involving electronically excited molecules and abundant H_2 in dense clouds.

NON-THERMAL DESORPTION IN DENSE CLOUDS

Reaction desorption (RD) is one of the crucial non-thermal desorption mechanisms to explain the net transfer of icy species from grain surfaces into gas phase at temperatures of which all molecules should be frozen out in the solid state. An accurate laboratory study of the solid-state elemental carbon budget monitored kinetically by RAIRS shows an upper limit of overall RD efficiency, i.e., 0.24, along the CO-H_2CO-CH_3OH hydrogenation scheme. Furthermore, the derived effective desorption fraction for single hydrogenation reaction and for each surface reaction induced by H-atoms (i.e., addition and abstraction) are $\leqslant 0.07$ and $\leqslant 0.02$, respectively, favoring the lower range of RD efficiencies of $0.01 - 0.10$ which is currently applied as a free parameter in astrochemical simulations.

This thesis experimentally demonstrates that the building blocks of life are already formed on icy dust grains at low temperatures before the presence of a protostar, and shows an unexpected molecular complexity following non-energetic processes in dense clouds. Upon UV irradiation this level of complexity is even enhanced. We clearly live in an icy universe and with the launch of the JWST, for the moment scheduled for 2020, a new tool will become available to study interstellar ices. Exciting times are ahead.

De ruimte is gevuld met grote, ijle wolken van gas (vooral waterstof) en micrometer grote stofdeeltjes die zijn overgebleven van exploderende sterren. Donkere interstellaire wolken zijn bijzonder koud, omdat ze grotendeels zijn afgeschermd voor licht van buitenaf. Deze wolken kunnen onder hun eigen gewicht in elkaar storten. Met dalende temperatuur en toenemende dichtheid, begint gas vast te vriezen op de stofdeeltjes. De laagjes ijs die daarbij ontstaan, vormen een molecuulreservoir en maken het mogelijk dat oppervlaktereacties gaan plaatsvinden. Deze worden getriggerd door ingevangen atomen, electronen en hoog geladen ionen of door UV licht. Het ijzige oppervlak fungeert daarbij als een 'derde lichaam'dat nodig is om energie die bij deze reacties vrijkomt te absorberen. Uiteindelijk vormen de moleculen die bij deze reacties onstaan het basismateriaal waaruit kleinere en grotere hemellichamen, brokken ruimtepuin, kometen, planeten en hun manen worden opgebouwd, wanneer de stofdeeltjes gaan samenklonteren op het moment dat in een proto-planetaire schijf een nieuwe ster en planeten ontstaan. Een goed begrip van de elementaire processen die plaatsvinden in donkere interstellaire wolken is dus van belang om de chemische samenstelling van sterstelsels, zoals van onze Zon en haar planeten te begrijpen.

Dit proefschrift gaat over het laboratoriumonderzoek naar de oppervlaktechemie van CO-rijk ijs op stofdeeltjes in donkere interstellaire wolken. Dit is een belangrijke fase in de evolutie van ijsdeeltjes in de ruimte. De mechanismen verantwoordelijk voor de vorming van complexe organische moleculen (COM's) door niet-energetische (hydrogenering, d.w.z. het toevoegen van een waterstofatoom) en energetische (fotolyse) bewerking van eenvoudige moleculen zijn onderzocht. Ook is de netto overdracht van nieuwgevormde reactieproducten van het stofoppervlak naar de gasfase door niet-thermische desorptie bekeken. Al het werk dat in de voorgaande hoofdstukken is beschreven, is uitgevoerd in het Sackler Laboratorium voor Astrofysica aan de Universiteit Leiden.

INTERSTELLAIR IJS IN DICHTE WOLKEN

Astronomische waarnemingen bevestigen de aanwezigheid van bevroren moleculen, zoals H_2O, CO, CO_2 en CH_3OH, op stofdeeltjes, via hun karakteristieke vibratie-overgangen in het infrarood. In dichte interstellaire wolken neemt de dichtheid (n_H) toe tot $1\times10^{4-5}$ cm^{-3} en daalt de temperatuur tot $\sim$10 K. Het zeer vluchtige koolmonoxide (CO), dat na moleculair waterstof (H_2) het tweede meest voorkomende gasvormige molecuul is ($\sim10^{-4}$ n_H), condenseert op een eerder gevormde H_2O-rijke ijsmantel. Deze belangrijke fase staat bekend als de 'catastrophic CO freeze-out stage'waardoor een stofdeeltje met een CO ijscoating wordt afgedekt. De gelijktijdige aangroei van CO en H-atomen leidt in de eerste plaats tot vorming van gehydrogeneerde moleculen, zoals formaldehyde (H_2CO) en methanol (CH_3OH), door opeenvolgende additiereacties van H-atomen. Dit niet-energetisch mechanisme dat de ijschemie op stofoppervlakken in donkere wolken domineert, wordt algemeen beschouwd als de manier om de astronomisch waargenomen hoeveelheden methanol in dichte wolken te verklaren. In dit proefschrift wordt aangetoond dat via dezelfde reactieketen ook grotere complexe organische moleculen, zoals glycolaldehyde, ethyleenglycol en glycerol kunnen ontstaan.

In dichte wolken kunnen naast H-atomen ook UV-fotonen de oppervlaktechemie van interstellair ijs beïnvloeden, zijhet in geringere mate dan bijvoorbeeld rondom een jonge ster. Deze fotonen worden uitgestraald door H_2-moleculen nadat deze door kosmische straling zijn

aangeslagen. De flux van deze UV-fotonen ($\leqslant$10.2 eV) is lager dan de typische H-atoom flux ($\sim1\times10^4$ atomen cm^{-2} s^{-1}), maar UV-fotonen kunnen wel gemakkelijker de gehele ijsmantel binnendringen. De energie van de UV-fotonen is te laag om eenvoudige moleculen, zoals CO en H$_2$, te dissociëren, maar is voldoende om CO te exciteren in zijn eerste aangeslagen electronische toestand, of om reactie product, zoals H$_2$CO of CH$_3$OH, uiteen te laten vallen. Het is reeds bekend, dat de fotolyse van methanol kan leiden tot de vorming van interstellaire COM's door recombinatie van de reactieve fotofragmenten die daarbij ontstaan.

COM's worden beschouwd als de voorlopers van de bouwstenen die inherent zijn aan het leven en die mogelijk zijn afgeleverd aan de jonge Aarde door invallende hemellichamen. Glycolaldehyde is bijvoorbeeld een belangrijk ingrediënt voor ribonucleïnezuur (RNA) en is astronomisch geïdentificeerd evenals methylformiaat (een van zijn isomeren) en ethyleenglycol (een suikeralcohol) in de omgeving van een aantal verschillende protosterren. Onlangs heeft de ontdekking van gasvormige COM's in koude wolken bij een temperatuur van slechts 10 K en in pre-stellaire kernen nogmaals bevestigd, dat de oorsprong van COM's niet alleen een gevolg kan zijn van UV bestraling van CH$_3$OH of 'warme ijschemie'zoals die plaatsvindt rondom protosterren. In koude gebieden is hydrogenering van CO-ijs een mechanisme waarmee de aanwezigheid van COM's al in de eerste fase van stervorming verklaard kan worden. Dit mechanisme is in dit proefschrift in detail onderzocht.

De astronomische waarneming van zowel eenvoudige als grotere organische moleculen in de gasfase in dichte wolken, met een hoeveelheid van $10^{-9} - 10^{-8}$ n$_H$, lijkt in tegenspraak met het feit dat bij dergelijke lage temperaturen alle moleculen (behalve H$_2$) op stofkorrels zouden moeten vastvriezen. Een fysisch of chemisch mechanisme dat ijsmoleculen van de vaste stof overbrengt in de gasfase biedt een mogelijke verklaring. Een directe thermische desorptie is zeer onwaarschijnlijk vanwege de zeer lage temperatuur ($\sim$10 K) in dit stadium. Daarom zijn verschillende niet-thermische desorptiemechanismen voorgesteld om de kloof tussen vaste stof en gasfase te overbruggen. Foto-desorptie is een efficiënt mechanisme voor het niet-thermisch desorberen van eenvoudige moleculen, zoals CO, CO$_2$, H$_2$O en CO:N$_2$-ijs. Voor CH$_3$OH overheerst echter foto-dissociatie, resulterend in fragmentvorming, bijvoorbeeld CH$_3$, CH$_3$O, en CH$_2$OH. Om deze reden is in dit proefschrift een ander mechanisme bestudeerd; reactieve desorptie (RD) kan een gasfase-verrijking bieden van zowel eenvoudige als organische moleculen door een thermische (hot-spot) desorptie volgend op exotherme reacties, zoals die bv. plaatsvinden in de opeenvolgende hydrogenerings stappen van CO en H$_2$CO naar CH$_3$OH.

INTERSTELLAIR IJS IN HET LABORATORIUM

De vaste-stof-chemie in interstellaire ijsanalogen die in dit proefschrift zijn beschreven, is onderzocht door gebruik te maken van het Surface Reaction Simulation Device2 (SURFRESIDE2; Figuur 1). Dit is een ultrahoog vacuümsysteem dat volledig is geoptimaliseerd om atoomreacties en UV-fotolyse van ijs onder dichte-wolk-omstandigheden te bestuderen, d.w.z. bij zeer lage temperaturen. Twee atoom bundels, een Hydrogen Atom Beam Source (HABS) en Microwave Atom Source (MWAS), zijn beschikbaar om interstellaire atomen en (moleculaire) radicalen te genereren die gelijktijdig met kleinere moleculen uit een doseringslijn op een cryogeen gekoeld oppervlak kunnen worden gedeponeerd. Een Microwave Discharge Hydrogen-flow Lamp (MDHL) wordt gebruikt voor het simuleren van de secundaire UV-fotonen die onstaan wanneer moleculair waterstof door kosmische straling wordt geraakt. Het grote bereik van mogelijke substraattemperaturen, maakt verschillende soorten experimenten mogelijk, variërend van de chemie van koude oppervlaken zoals in interstellaire kernen tot thermische

Figuur 1: Een foto van SURFRESIDE^2.

desorptie die optreedt wanneer bevroren stofen sublimeren later tijdens het stervormignsproces.

Het interstellaire ijs in SURFRESIDE2 wordt in situ gevolgd door middel van Reflection-Absorption InfraRed Spectroscopy (RAIRS). De ijzige bestanddelen worden geïdentificeerd door hun karakteristieke vibratiemodi die gekoppeld zijn aan de verschillende chemische functionele groepen. Hun hoeveelheden worden afgeleid door de IR-absorptiebandsterkte (A-waarde) te gebruiken, die zorgvuldig is gekalibreerd met een HeNe-laserinterferentietechniek. Een Temperature Programmed Desorption (TPD)-experiment in combinatie met zeer gevoelige Quadrupole Mass Spectrometry (QMS) detectie wordt gebruikt als een aanvullend hulpmiddel om de nieuwgevormde producten ondubbelzinnig te identificeren. Verschillende moleculen desorberen bij zeer specifieke temperaturen en zijn ook nog eens relatief gemakkelijk te onderscheiden door hun karakteristieke fragmentatiepatronen die het gevolg zijn van de ionisatie stap door botsende elektronen. Mocht dit nog steeds niet tot eenduidige resultaten leiden, dan kunnen isotoop-verrijkte uitgangsstoffen worden gebruikt. Dit alles maakt van SURFRESIDE2 een zeer veelzijdig hulpmiddel om moleculaire complexiteit in interstellair ijs te onderzoeken, voor instellingen die volledig worden gecontroleerd en met een precisie die het mogelijk maakt om de onderliggende fysische/chemische processen op ijzige stofdeeltjes kwantitatief te onderzoeken.

NIET-ENERGETISCH VORMINGSMECHANISME VAN COM'S IN DICHTE WOLKEN

De laboratoriumstudies van de vaste-stof-interactie tussen H_2CO en H-atomen leidt niet alleen tot meer gehydrogeneerde moleculen, zoals CH_3OH, maar resulteert ook in gedehydrogeneerde moleculen, zoals CO en het HCO-radicaal. Deze H-atoomabstractiereacties worden ook gevonden in CH_3OH-ijs, waarbij H_2CO en het CH_2OH-radicaal ontstaan. De gelijktijdige voorwaartse (additie/hydrogenering) en achterwaartse (abstractie/dehydrogenering) reacties verhogen de levensduur van de radicalen op stofoppervlakken. Deze kunnen vervolgens met andere radicalen of inmiddels gevormde tussenproducten reageren, hetgeen re-
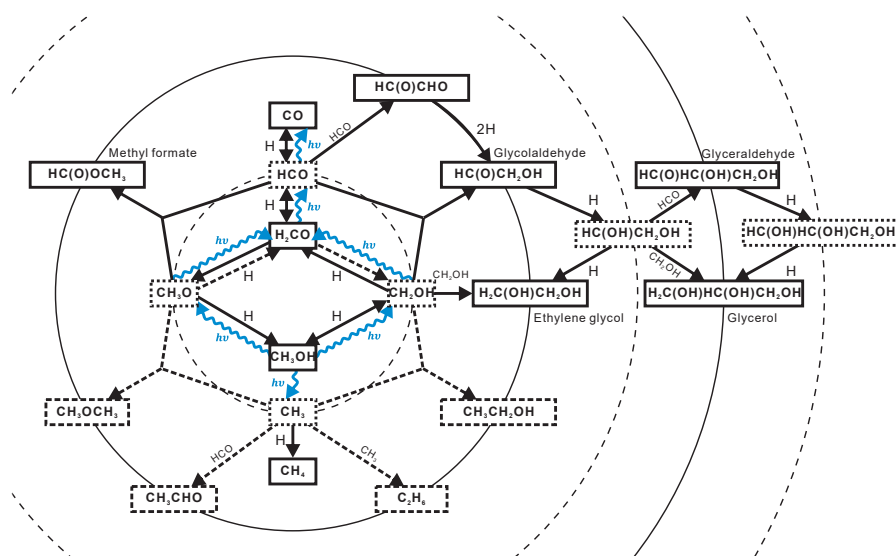
Figuur 2: Voorgesteld reactiediagram van de COM-formatie.

sulteert in de vorming van zuurstofhoudende COM's, zoals methylformiaat (HC(O)OCH$_3$), glycolaldehyde (HC(O)CH$_2$OH) en ethyleenglycol (H$_2$C(OH)CH$_2$OH) zonder dat daarvoor energetische deeltjes (bijv. UV-fotonen, elektronen en ionen) nodig zijn. De hier gepresenteerde experimentele conclusies ondersteunen COM-vorming tijdens de 'catastrofale CO-bevriezingsfase'. Het onderliggende reactieprincipe gaat echter verder dan de vorming van twee-koolstofhoudende soorten.

De vorming van een eenvoudige suiker met drie koolstofatomen, bijv. glyceraldehyde (HOCH$_2$CH(OH)CHO) en een suikeralcohol met drie koolstofatomen, bijv. glycerol (HOCH$_2$CH(OH)CH$_2$OH) is eveneens aangetoond in experimenten waarin enkelvoudige en dubbele koolstofradicalen onder gesimuleerde dichte-wolk-omstandigheden reageren. Hiermee wordt bevestigd dat een niet-energetische reactie mechanisme veel potentie heeft om grotere complexe organische stoffen in het heelal te vormen (Figuur 2).

IJSCHEMIE MET UV-FOTONEN

In dichte wolken vormen H-atoomtoevoegingsreacties het belangrijkste reactie mechanisme, maar bestraling met UV-fotonen als een secondair proces is ook mogelijk. Een systematische experimentele studie zoals in dit proefschrift beschreven is, toont een kwantitatieve vergelijking tussen hydrogenatie en UV-fotolyse in interstellaire relevante ijsanalogen, resulterend in verschillende COM-formatiesamenstellingen. COM-verhoudingen afgeleid uit deze laboratoriumresultaten zijn geschikt als een diagnostisch hulpmiddel om te bepalen wat de chemische oorsprong is van de moleculen die in de ruimte worden gevonden. Op basis van laboratoriumgegevens zoals hier besproken en observationele resultaten van kometen en protosterren vergelijkbaar met onze zon, wordt geconcludeerd dat COM's, zoals glycolaldehyde en ethyleenglycol, inderdaad op ijzige stofdeeltjes in de ruimte ontstaan.

UV-fotolyse kan ook een belangrijke rol spelen bij het associëren van koolstof- en stikstofhoudende moleculen waarbij prebiotische moleculen, met een peptide-bevattende verbinding, vormen. Stikstofmonoxide (NO) heeft een zeer hoge chemische reactiviteit vergeleken met an-

dere N-dragende moleculen (bijv. N_2) en deze neemt door wisselwerking met H-atomen op stofoppervlakken in de CO-bevriezingsfase nog verder toe. Daarom wordt verwacht dat het volledig verzadigde hydroxylamine (NH_2OH) a.g.v. NO-hydrogenering wordt gemengd met ander CO-rijk ijs, bijvoorbeeld H_2CO en CH_3OH. De UV-fotonen kunnen efficiënt de gehydrogeneerde producten dissociëren, resulterend in foto-fragmenten, zoals NH_2 en HCO. De experimentele bevindingen hier laten zien dat deze energetische radicalen verdere radicaal-radicaal recombinaties kunnen ondergaan die resulteren in NC-dragende moleculen, zoals HNCO en NH_2CHO, moleculen die een prebiotische rol spelen en ook al zijn waargenomen in de ruimte.

Het is duidelijk dat hydrogeneringsreacties met CO-ijs op stofkorrels belangrijk zijn om zowel kleinere als grotere complexe organische stoffen te vormen in dichte wolken. Echter, het veel meer voorkomende moleculaire waterstof (H_2), met dichtheden van vier orden van grootte hoger dan die van H-atomen, neemt niet actief deel in niet-energetische ijsprocessen. Dit is te wijten aan de hoge activeringsenergie die nodig is om H_2 in deze reacties te betrekken, echter een experimentele studie van CO:H_2-ijsfotolyse resulteert in de eenduidige identificatie van HCO en H_2CO. In dit proefschrift wordt geconcludeerd dat het elektronisch geëxciteerde koolmonoxide (CO*) geïnduceerd door UV-fotonen kan reageren met een H_2-molecuul in zijn grond toestand, waarbij HCO ontstaat en een vrij H-atoom dat vervolgens beschikbaar komt voor H-atoomtoevoegingsreacties. De interactie tussen CO* en H_2 verbetert de productie van HnCO-soorten in de ijsmantel en introduceert een niet eerder onderzocht vastestofkanaal met elektronisch geëxciteerde moleculen.

NIET-THERMISCHE DESORPTIE IN DICHTE WOLKEN

Reactieve-desorptie (RD) is een van de cruciale niet-thermische desorptiemechanismen om de netto overdracht van ijzige soorten van stofoppervlakken in gasfase te verklaren bij temperaturen waarbij alle moleculen in de vaste toestand bevroren zouden moeten zijn. Een nauwkeurig laboratoriumonderzoek van het vaste-stof elementaire koolstofbudget in een 'gesloten'CO-H_2CO-CH_3OH-hydrogeneringsschema, vertoont een bovengrens voor de RD-efficiëntie van 0.24. Hieruit kan de effectieve desorptiefractie voor een enkelvoudige hydrogeneringsreactie (additie en abstractie) worden overgeleid, resulterend in waarden van respectievelijk $\leqslant 0.07$ en $\leqslant 0.02$, in overeenstemming met RD-efficiënties van $0.01 - 0.10$ zoals die momenteel toegepast worden als een vrije parameter in astrochemische simulaties.

Dit proefschrift laat experimenteel zien dat de bouwstenen van het leven al gevormd worden op ijzige stofkorrels bij lage temperaturen vóór de aanwezigheid van een protoster, en toont een onverwachte moleculaire complexiteit na niet-energetische inwerking in dichte wolken. Bij UV-bestraling neemt de mate van complexitiet zelfs verder toe. Het is zeker dat ijs een belangrijke rol speelt in de chemische evolutie van ons universum. Met de lancering van de JWST, die op dit moment gepland staat voor de lente van 2020, zal een nieuw instrument beschikbaar komen om interstellair ijs en de processen zoals die hier beschreven zijn te bestuderen. Er komen spannende tijden aan.

SCIENTIFIC PUBLICATIONS

H_2 chemistry in interstellar ices: The case of CO ice hydrogenation in UV irradiated CO:H_2 ice mixtures
K.-J. Chuang, G. Fedoseev, D. Qasim, S. Ioppolo, E.F. van Dishoeck, and H. Linnartz,
submitted

Reactive desorption of CO hydrogenation products under cold pre-stellar core conditions
K.-J. Chuang, G. Fedoseev, D. Qasim, S. Ioppolo, E.F. van Dishoeck, and H. Linnartz,
Astrophys. J. 853 (2018) 102

Formation of interstellar methanol ice prior to the heavy CO freeze-out stage
D. Qasim, **K.-J. Chuang**, G. Fedoseev, S. Ioppolo, A.C. Boogert, and H. Linnartz,
Astron. Astrophys. 612 (2018) A83

Formation of glycerol through hydrogenation of CO ice under prestellar core conditions
G. Fedoseev, **K.-J. Chuang**, S. Ioppolo, D. Qasim, E.F. van Dishoeck, and H. Linnartz,
Astrophys. J. 842 (2017) 52

Production of complex organic molecules: atom addition versus UV irradiation
K.-J. Chuang, G. Fedoseev, S. Ioppolo, E.F. van Dishoeck, and H. Linnartz,
Mon. Not. R. Astron. Soc. 467 (2017) 2552

Simultaneous Hydrogenation and UV-photolysis Experiments of NO in CO-rich Interstellar ice Analogues; linking HNCO, OCN$^-$, NH_2CHO, and NH_2OH
G. Fedoseev, **K.-J. Chuang**, E.F. van Dishoeck, S. Ioppolo, and H. Linnartz,
Mon. Not. R. Astron. Soc. 460 (2016) 4297

H-atom addition and abstraction reactions in mixed CO, H_2CO and CH_3OH ices-an extended view on complex organic molecule formation
K.-J. Chuang, G. Fedoseev, S. Ioppolo, E.F. van Dishoeck, and H. Linnartz,
Mon. Not. R. Astron. Soc. 455 (2016) 1702

Chemical Evolution of a CO Ice Induced by Soft X-Rays
A. Ciaravella, Y. J. Chen, C. Cecchi-Pestellini, A. Jiménez-Escobar, G. M. Muñoz Caro, **K. J. Chuang**, and C. H. Huang,
Astrophys. J. 819 (2016) 38

Controlling the emission profile of an H_2 discharge lamp to simulate interstellar radiation fields
N. F. W. Ligterink, D. M. Paardekooper, **K.-J. Chuang**, M. L. Both, G. A. Cruz-Diaz, J. H. van Helden, and H. Linnartz,
Astron. Astrophys. 584 (2015) A56

Formation of S-bearing species by VUV/EUV Irradiation of H_2S-Containing Ice Mixtures: Photon Energy and Carbon Source Effects
Y.-J. Chen, **K. J. Chuang**, M. Nuevo, A. Jiménez-Escobar, G. M. Muñoz Caro, J.-M. Qiu, C.-C. Chu, T.-S. Yih, C.-Y. Wu, H.-S. Fung, and W.-H. Ip,

Astrophys. J. 798 (2015) 80

Vacuum-UV Emission Spectrum Measurement of a Microwave-Discharge Hydrogen-Flow Lamp in Several Configurations: Application to the Photodesorption of CO Ice
Y.-J. Chen, **K. J. Chuang**, G. M. Muñoz Caro, M. Nuevo, C.-C. Chu, T.-S. Yih, W.-H. Ip, and C.-Y. R. Wu,
Astrophys. J. 781 (2014) 15

Relevance of the H2 + O reaction pathway for the surface formation of interstellar water
T. Lamberts, H. M. Cuppen, G. Fedoseev, S. Ioppolo, **K. J. Chuang** and H. Linnartz,
Astron. Astrophys. 570 (2014) A57

Soft X-Ray Irradiation of Methanol Ice: Formation of Products as a Function of Photon Energy
Y.-J. Chen, A. Ciaravella, C. Cecchi-Pestellin, A. Jiménez-Escobar, G. M. Muñoz Caro, **K. J. Chuang** and T.-S. Yih,
Astrophys. J. 778 (2013) 162

CURRICULUM VITAE

On June 29, 1987, I was born in Hsinchu City in Taiwan. In 2002, I had a chance to start my scientific special education in Hsinchu Senior High school, a traditional all boy-school. Besides the science and literature training, I was also asked to learn music and arts. During these fruitful three years, I developed my interests in Physics. Subsequently, I continued my studies at the Department of Physics at National Central University (NCU), Taiwan, and learned the subject of astrophysics. In the last two years of my bachelor, I joined the Atomic and Molecular Spectroscopy Laboratory led by Prof. dr. T. Yi, and was trained to be a qualified experimentalist; first, start from the basics—making an ultra-high-vacuum Conflat Flange (CF). I graduated in four years with top grades that offered me a fellowship for a master degree at NCU. During the two-year master research, I specialized in laboratory astrophysics, supervised by Prof. dr. T. Yi and Prof. dr. J. Chen. I combined the experimental results performed at the large facility synchrotron light source (EUV-VUV) at NSRRC, Hsinchu, and at NCU leading to produce my master thesis, "The Formation Mechanism of the Sulfur-bearing species in H_2S+CO & H_2S+CO_2 photolysis Ice Mixtures". The work during my master resulted in four (co-authored) publications.

After my graduation from NCU (2011), I went through compulsory service in the military as a lieutenant specialized in political warfare and participated exercise. I was honorably discharged in 2012, and went back to science as an assistant researcher at Academia Sinica Institute of Astronomy and Astrophysics (ASIAA) in Taiwan for a few months. I decided to continue to pursue my research in laboratory molecular astrophysics at the Sackler Laboratory for Astrophysics in Leiden, the Netherlands, where the field originated. I had the opportunity to act as a guest researcher in the Sackler Lab for three months under the invitation from Prof. dr. H. Linnartz, and was offered to begin my doctoral studies supervised by Prof. dr. H. Linnartz and Prof. dr. E. van Dishoeck in 2014.

My doctoral work focuses on the experimental solid-state study of interstellar complex organic molecule formation mechanisms through energetic (UV-photolysis) and non-energetic ((de)-hydrogenation) processes in inter- and circumstellar ice analogues. I have upgraded and utilized SURFRESIDE^2, one of the UHV setups in the Sackler Laboratory for Astrophysics, to study the origin of building blocks of life. During my Ph.D., I have worked with many colleagues and collaborators: Dr. S. Ioppolo (UK), Dr. G. Fedoseev (Italy), M.Sc. D. Qasim (Netherlands), Prof. dr. H. Cuppen (Netherlands), and Dr. T. Lamberts (Netherlands), as well as presented my work at various conferences and scientific meetings in the Netherlands, United States, Spain, Germany, Taiwan, and Chile. My presentation at the International Astronomy Union (IAU) Symposium 332 was awarded a poster prize. Furthermore, I had the opportunity to spend one month as a visiting researcher at the Harvard-Smithsonian Center for Astrophysics hosted by Prof. dr. K. Öberg. The doctoral research resulted in five publications and one in preparation that are presented in this thesis.

ACKNOWLEDGEMENT

When I start reviewing how I completed my Ph.D. thesis, the memory train not only stops at the station indicating four-year-ago, it continues starting from earlier stations. I would like to thank my master supervisor Prof. T. Yi and co-promotor Prof. J. Chen (Asper), without their guidance, I never would have become a qualified experimentalist. I am grateful to A. Ciaravella and G. Munoz Caro who urged me to pursue a doctoral degree.

Finally, yet importantly, I would like to thank my family and friends in Taiwan and the Netherlands. I am grateful to Lu-Ting and his family hosting me on the first day I came to the Netherlands. Thanks to Liang-Yu, Chi-Lin, and Olivia for sharing the joyful life of a Ph.D. student— best wishes to their doctoral thesis writing. Pao-Yi, where you stay is the place I call home. I am an extremely lucky man to be able to experience life, work, traveling, and food with you. I thank my parents and sister for their unconditional support.